Refractory Body-Centred Cubic High-Entropy Alloys for Nuclear Fusion

John Christopher Waite

Supervised by

Prof. D.E.J. Armstrong and Prof. A.J. Wilkinson

September 2019

Abstract

In this work refractory High-Entropy Alloys (HEAs) have been investigated for application as Plasma Facing Components in nuclear fusion reactors. Sample fabrication was guided by optimising composition in order to maximise the Ω parameter, which has been previously identified as correlating with the stability of solid-solution microstructures. Arc melting was used to fabricate billets of TiVZrHfTa, TiVZrTa, and TiVTa, each of equiatomic and optimised compositions. These samples were analysed by XRD and SEM in the as-cast condition and after being annealed at 1400 °C for twenty four hours. The matrix of each sample was found to be BCC, and each contained secondary phases with either BCC, HCP, or rocksalt crystal structures. The latter of these phases was found to be a carbonitride, formed from an air leak that occurred during melting. Finite-Element Analysis of thermal transport in arc-melted billets has shown that cooling rates generated are rapid, and even more so in smaller billets. Smaller 10 g billets of equiatomic alloys were found to have much lower volume fractions of secondary phases than as-cast 50 g counterparts, and this has been attributed to the differences in solidification and cooling conditions. The modelling also demonstrated large variations in cooling rate throughout larger 50 g billets, and so the effect of this on as-cast microstructures was also investigated. It was found that the differences in cooling rate was sufficient to create variations in microstructures, with an increase of 10% volume fraction of the carbonitride phase between the bottom and top of the billet, along with a large increase in porosity. The main conclusion of this portion of the thesis is that arc melting plays a larger role in determining as-cast microstructures than previously thought. Two ion-implantation experiments were run into four different alloys of TiVZrHfTa up to damages of 0.6 and 3.5dpa. Nanoindentation has then been used to show there is no measurable change in hardness, despite a strong reaction being found in a vanadium control sample. Separately, these alloys were used to demonstrate the efficacy and limitation of using a new nanoindentation technique called Express indentation, which rapidly makes thousands of indents in order to map the hardness and modulus of materials.

Acknowledgements

Thanks must first and foremost go to Dave and Angus: your guidance has been the only thing that that helped me find my way through this project.

Thank you to Steve Roberts and Jonathan Yates, who spent untold hours turning me and so many others into proper scientists.

For their time, their expertise, and their company on long days and nights, thank you to Guillaume Matthews, Benjamin Jenkins, Christopher Magazzeni, and Phillip Gopon.

To all the members of office 18.02, past and present, thank you for friendship and support. Hopefully the office will get the fresh is start it needs.

To Carmen, Alex, and all of the CDT: we made it.

Thank you to my parents. You have always helped me, pushed me, and supported me. You have made me the person I am today. Without you I would be nowhere.

Contents

Chapter 1

Introduction

1.1 The Rising Demand for Energy

As the worlds population increases beyond 7.7 billion [1], and economic development of the global south leads to higher energy consumption per capita, the total energy requirement of the world is set to increase from 151 PW h in 2019 to between 186 and 267 PW h by 2040 [2], depending on the nature of energy transition that occurs. Although roughly half of this can be generated using renewables such as solar and wind [3], the remaining energy will have to come from either carbon based fuels or nuclear power.

1.2 The Feasibility of Nuclear Fission

The first nuclear fission reactor was developed in 1942, and since then has been deployed around the world to generate nearly 3.9 PW h in 2013 [4]. The advantages of nuclear fission over fossil fuels are primarily in the much reduced CO_2 emission and the improved safety record (when early deaths due to air pollution are taken into account [5]). The disadvantages of fission power is the lack of public support for nu-

clear energy, the generation of long-lived radioactive waste, and also the possibility of fissile materials being weaponised. None of these issues are relevant for reactors based on a fusion reaction, rather than a fission one.

1.3 The Potential of Nuclear Fusion

The most developed fusion reactor design is called the Tokamak, which is a type of Magnetic Confinement Fusion (MCF). This involves using strong magnetic fields to confine a plasma of hydrogen isotopes at temperatures and pressures that allow them to overcome the coulomb repulsion between them and fuse. The easiest energy-producing fusion reaction is between deuterium and tritium (called DT fusion), which results in the release of 17.6 MeV of energy distributed between a helium ion and a neutron, a schematic of which is shown in figure 1.1. The helium ion can be contained by the magnetic field, but the neutron will escape, and be absorbed by either deep in the wall, or by a Plasma Facing Component (PFC), which are indicated in figure 1.2.

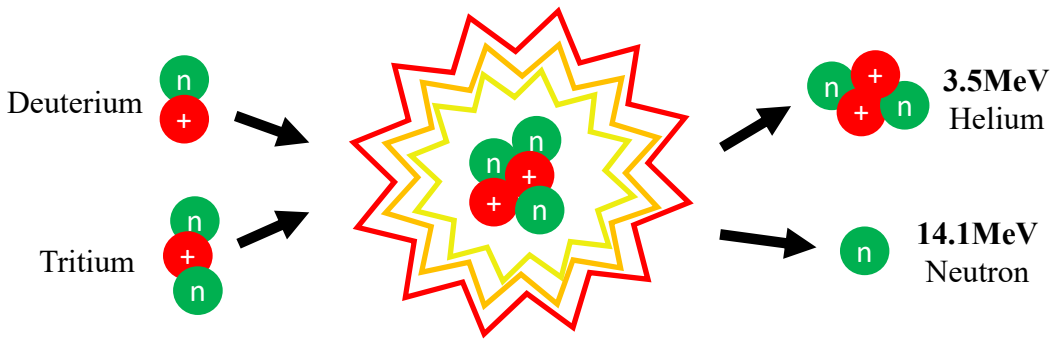

Figure 1.1: Schematic showing the DT reaction, including the products: a helium ion and a neutron.

1.4 The Requirements of Plasma Facing Materials

The temperatures generated in Tokamak plasmas are in the order of 150 MK, and while this is not directly felt by the wall, the nature of the geometry leads to high-energy hydrogen and helium particles being directed at the divertor: a component which acts as the reactors exhaust is shown in figure 1.2. Heat loads on the divertor are predicted to be as high as 10 to 20 $\mathrm{MW\,m^{-2}}$, and it will have to survive a minimum of two years in service in order for fusion to be economical [6]. Other challenges include transient loading due to plasma instabilities, heat cycling due to periods where the reactor must be switched off for maintenance, but arguably the most important are the interactions the wall has with the 14.1 MeV neutrons. These neutrons can interact with materials in two ways: inelastic scattering whereby the neutron is absorbed, or elastic scattering, whereby the lattice atoms are displaced.

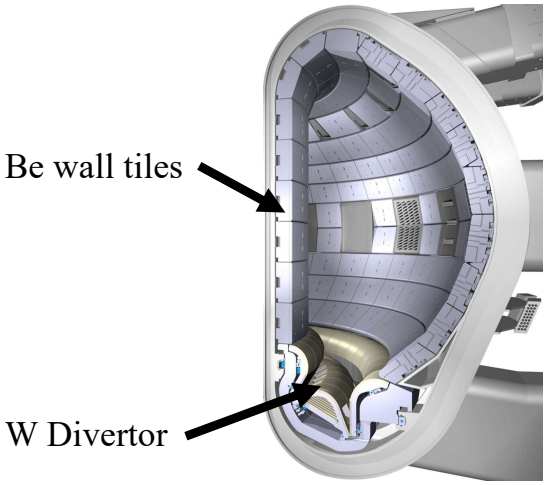

Figure 1.2: Schematic showing a poloidal cross-section of a Tokamak, with the PFC components labelled.

1.4.1 Inelastic Scattering

Inelastic scattering causes atomic transmutations; where the mass of nuclei change, become unstable, and subsequently evolve into different elements. This results in the alloy composition changing, sometimes to include radioactive elements which will produce their own decay heat after the fusion reaction is stopped. In order to ease the possible regulatory burden on future fusion reactors, only "low-activation" elements are being considered; these are defined as elements which can be classed as low-level waste after 100 years [7]. This means that common alloying elements such as Ni, Co, and Mo cannot be used in fusion materials, as can be seen from figure 1.3, which shows the change in activity of certain elements over time and has been reproduced from reference [8].

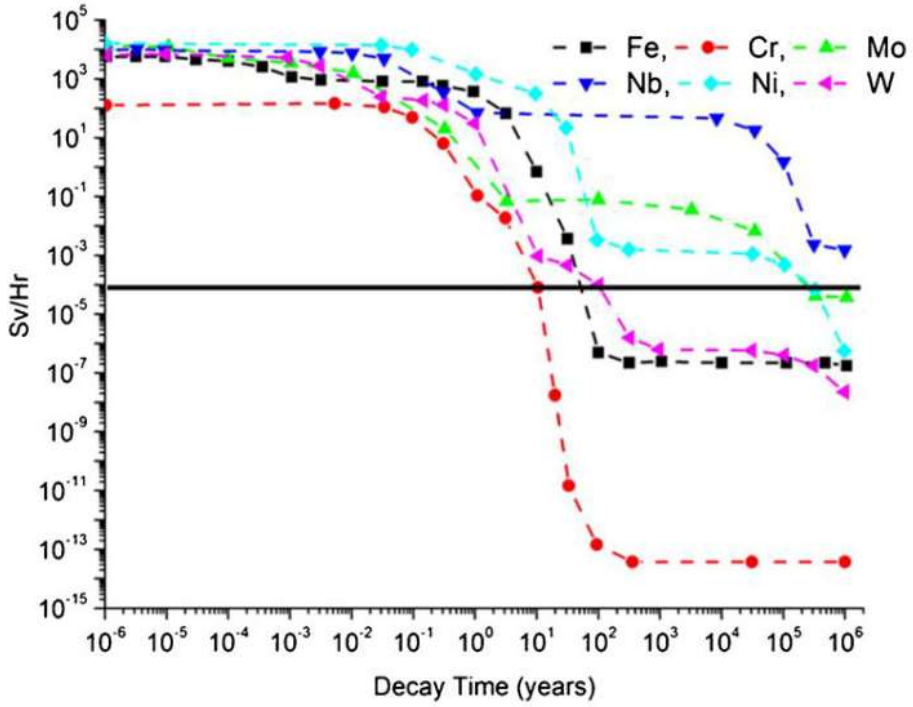

Figure 1.3: Graph taken from reference [8] showing activation against decay time for common structural elements. The thick black line represents acceptable activation, and so it can be seen that Cr, Fe, and W are all considered safe within 100 years (low activation), whereas Ni, Mo, and Nb are not.

1.4.2 Elastic Scattering

The elastic scattering caused by the neutrons results in cascades where millions of atoms are knocked out of their equilibrium positions. Although the majority of this damage can be healed as the material recrystallises, some vacancy and self-interstitial pairs are created. Over time these can build up and lead to a deterioration in the properties of the material. One of the most visually striking ways this can happen is through swelling; self-interstitials diffuse to a free surface, and the component slowly grows. It has been found that face-centered cubic structures (FCC) are more prone to this than body-centred cubic ones (BCC), and so for future fusion reactors BCC materials are of primary interest [9]. Vacancies are also able to diffuse

through the material, and often they group together in order to lower their surface to volume ratio; becoming either voids or stacking faults. The former of these is easier to conceptualise, as a roughly spheroidal structure where no lattice sites are filled. Gaseous atoms such as hydrogen and helium are also known to diffuse into these voids and form high-pressure bubbles. Stacking faults are harder to conceptualise, but represent a disc-shaped disruption of the lattice, that acts to break the regular order of lattice planes, which is akin to introducing a loop of dislocation line. This is shown as a schematic in figure 1.4, which is reproduced from reference [10].

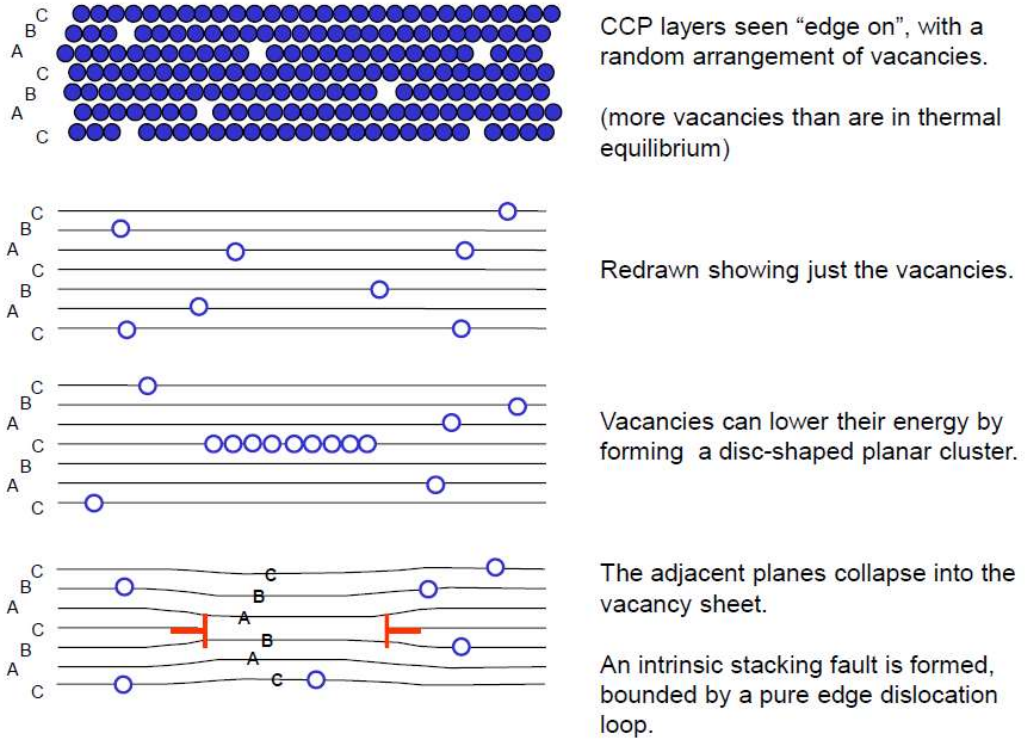

Figure 1.4: Schematic demonstrating how a disc-shaped formation of vacancies can form a stacking fault, which is effectively a loop of dislocation line. This is reproduced from reference [10].

These loops are not mobile, and they along with voids, act to block the motion of mobile dislocations, resulting in a decrease in the plastic capability of materials. This means that over time reactor materials will become more brittle. The inser-

tion of crystal defects acts to degrade the mechanical properties of PFCs, to a point where they are potentially unsafe for use, and a key aim of materials scientists is to design around this and ensure that components are able to survive in such an extreme environment.

1.4.3 Candidate materials for Fusion

As outlined previously, the ideal PFC is a BCC metal able to operate as structural material at high temperatures (refractory), to be comprised of low-activation elements, and to be able to resist the deleterious effects of the 14.1MeV neutrons. There are several candidate materials such as Tungsten [6], Oxide Dispersion Strengthened (ODS) steels [11], or Silicon Carbide [12]. Another set of potentially paradigm-shifting candidate materials are High-Entropy Alloys (HEAs).

These are a form of multicomponent alloy which are characterised as having more than three or more components in roughly equal proportions, whilst maintaining a simple crystal structure (BCC, FCC, etc.). The primary advantage of this class of alloy comes from their compositional flexibility; they can be comprised of almost any metallic element, meaning there are a wide variety of possible alloys that are entirely comprised of low-activation elements, which are BCC refractory metals when in their pure or alloyed form. In addition to this, studies have shown that High-Entropy Alloys have an as of yet unexplained resistance to radiation damage. It has been primarily shown on FCC systems that they are able to resist hardening, chemical segregation, and swelling better than conventional alloys [13, 14]. At the time of writing there are multiple theories as to why High-Entropy Alloys show this resistance, but none have been confirmed.

The purpose of this thesis is to develop understanding on the formation of High-

Entropy Alloys, on their resistance to radiation damage, and to try and develop an alloy that may find application as a PFC in a future fusion reactor. It is structured into five key chapters, next is a literature review focussing on the background of HEAs, the various attempt to predict HEA microstructures, and work that has been done to quantify the reaction of HEAs to ion irradiation. Following on from this the methods used and the novel work conducted in this thesis are presented: chapter 4 describes the various microstructures that were encountered, chapter 5 compares different methods of achieving a single-phase microstructure, chapter 6 is an examination of the variation within an arc-melted billet, whilst chapter 7 focusses on the ion-implantation experiments conducted and the testing of a new nanoindentation technique called the Express Method.

Chapter 2

Literature Review

2.1 Introduction to High-Entropy Alloys

2.1.1 Origin

Whereas almost all traditional structural engineering alloys are based on either Fe, Al, Ni, Ti, etc., and contain usually more than 80% of these elements, multicomponent alloys are characterised as having multiple elements in near-equiatomic proportions. Within this relatively unexplored region of phase space are several different classes of alloys including Bulk Metallic Glasses (BMGs), intermetallics, and High-Entropy Alloys (HEAs). High-entropy Alloys were developed separately by B. Cantor [15] and J.W. Yeh [16] in 2004. Both authors combined upwards of 5 elements in equal proportions and found that instead of forming a complex microstructure with many phases (including intermetallics), most had very few phases, and that these were simple, being either Face-Centred Cubic (FCC) or Body-Centred Cubic (BCC). Yeh concluded that the stable phases were disordered solid solutions, and that they were thermodynamically stabilised by their high configurational entropy. It should be noted that the alloy first created by Cantor, CrMnFeCoNi, is the most

commony studied and is often simply referred to as the 'Cantor alloy'.

This literature review begins by discussing the "four core effects", which were originally proposed by Yeh to explain some of the physical properties of HEAs, then moves on to examine thermodynamic predictors of HEA microstructures, the formation of secondary phases in refractory HEAs, and finally summarises current understanding of the resistance to radiation damage displayed by some HEAs.

2.1.2 The four core effects

In 2006 J.W. Yeh proposed four core effects that underpin the formation and properties of HEAs [17]. These were the "high-entropy effect", "severe lattice distortion", "sluggish diffusion", and the "cocktail effect". This section discusses each of these effects and the experimental evidence for their existence. Reviews of the HEA field by both Pickering [18] and Miracle [19] have criticised the lack of experimental validation of these effects, however, the papers which initially proposed the four core effects have been cited more than 500 times as of August 2019 [17, 20], and so discussing them is still very much pertinent to the current science.

2.1.2.1 The High Entropy Effect

The most thermodynamically stable phase will have the lowest free energy, normally this is achieved by minimising enthalpy; either through specific bond formation in compounds, or through ordering in intermetallic phases [21]. In high-entropy phases however (as the alloy name suggests), it is the high entropy that minimises the free energy. How various terms relate to Gibbs free energy is described by equation 2.1.

$$G = H - TS \tag{2.1}$$

G : Gibbs free energy (J mol^{-1})
H : Enthalpy (J mol^{-1})
T : Temperature (K)
S : Entropy (J K^{-1} mol^{-1})

This quation shows that free energy can be minimised by either minimising the enthalpy (H) or maximising the entropy (S). Additionally, the ability of entropy to decrease free energy is more pronounced at higher temperatures. This has led many authors to conclude that HEAs are thermally stable, and for this reason they are proposed for several high-temperature applications such as turbine blades and cladding for nuclear fuel [20].

In HEAs it is thought that it is the configurational entropy that is dominant, and as such it is typically the only form that is considered (contributions such as vibrational and magnetic are treated as negligible [22]). For equiatomic alloys the configurational entropy is shown to increase logarithmically with the number of components in the alloy, as shown in equation 2.2.

$$S_{\text{config}} = R \ln N \tag{2.2}$$

S_{config} : Configurational entropy (J K^{-1} mol^{-1})
R : Molar gas constant (8.31 J K^{-1} mol^{-1})
N : Number of components

The logarithmic nature of equation 2.2 means that increasing the number of components above a certain point begins to have a reduced impact on the magnitude of S_{config}, which led Yeh to suggest a practical number of HEA components between 5

and 13; however, high-entropy systems have been reported outside of this window [15, 23], and the guideline serves no real purpose. Further evidence against the formal definitions of HEAs is provided by Laurent-Brocq [24], where it was shown that a stable single-phase solid solution existed through a composition range which violated the concentration limits of 5 and 35at% for each element, originally suggested by Yeh [25].

There are two unanswered questions which overhang the high-entropy effect. The first is whether entropy's ability to stabilise new phases is as much as early authors anticipated, which is assessed during this thesis. The second is whether only considering configurational entropy is underestimating the total entropy of the alloys by non-negligible amounts. Ma et al. used ab initio methods to calculate all the electronic, magnetic, vibrational, as well as configurational entropies for the CrMnFeCoNi system, and found that the non-configurational terms added to just over a third of the total [26]. This shows that the high-entropy effect, despite underpinning the entire field of HEAs, is still not well understood.

2.1.2.2 Severe Lattice Distortion

The second core effect is severe lattice distortion, whereby the disordered structure of the alloy acts to to distort the lattice planes locally around every atom, creating a highly strained crystal. This distortion is shown schematically in figure 2.1.

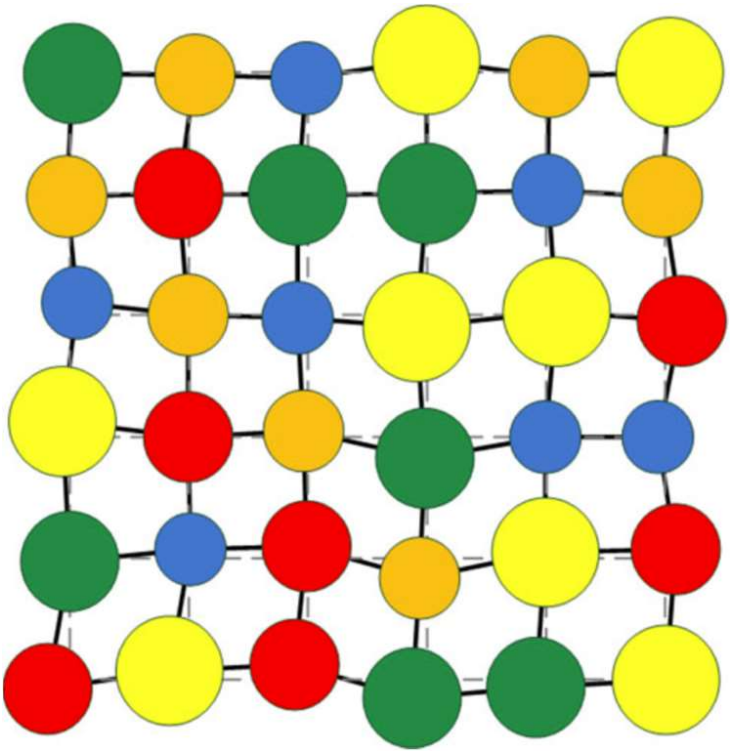

Figure 2.1: Two-dimensional schematic of a disordered and highly strained lattice, designed to aid in the conceptualisation of the severe lattice distortion predicted in HEAs. The figure is reproduced from reference [20].

Severe lattice distortion is easy to conceptualise in high-entropy structures, and has been used by many authors to explain the properties of their materials [27–41]. However, what is often not taken account of is what effect precipitation and other microstructural features are having. Experimental evidence such as reduced peak intensities in X-Ray Diffraction data (XRD) and observed lattice fringes in High Resolution Transmission Electron Microscopy (HR-TEM) has been suggested in

support of atomic length-scale lattice distortion [27, 42], but there is not compelling evidence to show a deconvolution of the effects of either phonons, or stress due to crystal defects such as dislocations [18].

Recent work has cast even more doubt on the hypothesis of severe lattice distortion. Todo-Caraballo et al. [43] used Density Functional Theory (DFT) to show that for BCC VNbMoTaW, which has a room temperature yield stress of 1GPa [23], the nearest neighbour strain is less than 5%; a level of strain comparable to many binary alloys [44]. In addition to this, neutron scatting experiments conducted by Owen et al. [45] have shown that atomic length-scale lattice strain in CrMnFeCoNi to be comparable to that of a CrCoNi ternary alloy, and even a CrNi binary alloy. More work is needed to investigate the lattice distortion of HEAs, but current evidence suggests that although it may be high in *some* alloys, it does not qualify as severe, and is not common to all HEAs.

2.1.2.3 Sluggish Diffusion

The disordered structure of HEAs is not only predicted to cause severe lattice distortion, but also to cause any diffusing species to see fluctuations in potential energies of lattice sites. This will act to regularly trap species, slowing transport within the alloy, to the point of "sluggish diffusion". The effect of slow diffusion on the properties of HEAs would be beneficial, particularly at elevated temperatures. It would slow grain growth and increase recrystallisation temperature, make it easier to achieve supersaturated solutions and nanometre scale precipitates, and most importantly it would reduce the rate of diffusion controlled creep. All these factors could lead to HEAs displacing Ni-based superalloys as the foremost high-temperature structural materials.

Just like with the severe lattice distortion this effect is easy to conceptualise and is used many times to explain observed microstructures and properties [41, 46–55]. The rate of diffusion in HEAs is now being actively investigated, and began with Tsai et al. in 2013 [56]. Their paper compared diffusion couples of CrMnFeCoNi HEA with ternary alloys and some pure elemental systems, the results of which can be seen in figure 2.2.

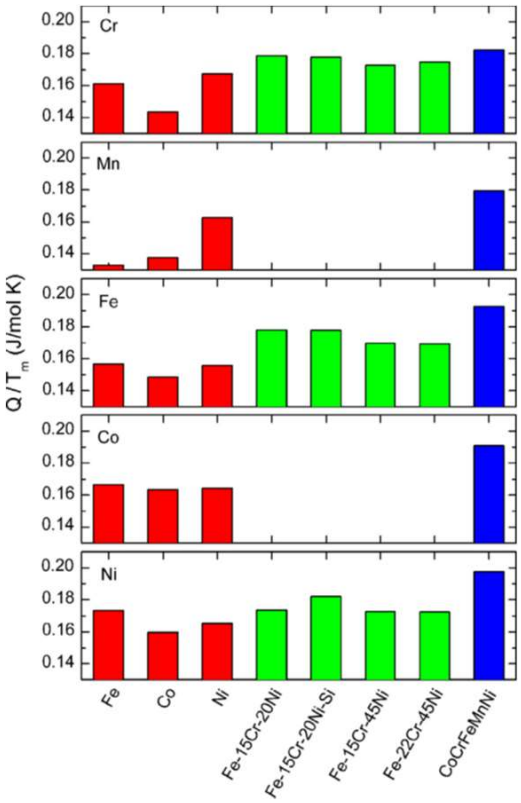

Figure 2.2: Comparison of normalised activation energies for diffusion in several systems, including pure elements (red), ternary alloys (green), and an HEA system (blue). Reproduced from reference [56].

For context in the following discussion the Arrhenius equation for diffusion is given in equation 2.3

$$D = D_0 \exp\left(\frac{Q}{RT}\right) \tag{2.3}$$

D	:	Diffusion coefficient ($m^2\ s^{-1}$)
D_0	:	Pre-exponential factor ($m^2\ s^{-1}$)
Q	:	Activation energy for diffusion (J)
T_m	:	Melting Temperature (K)

Tsai et al. found that the normalised activation energy, Q/T_m, of the HEA was higher than in the reference alloys (see figrue 2.2), and so concluded that diffusion in the HEA systems was sluggish. Reviews by Pickering [18] and Miracle [19] both take issue with this assessment, the former pointing out that although Q/T_m is higher in the HEA, the pre-exponential factor, D_0, is not, and that this could be sufficient to cancel one other out. Miracle observes that diffusion in the HEA system is actually *faster* when compared to the reference alloys at the same temperature - for example D_{Ni} is lower in austenitic stainless steels than in CrMnFeCoNi [19], and that the high Q/T_m values are as much a product of the HEA having a higher melting point when calculated according to the rule of mixtures.

Further to this, the author who inspired Tsai et al. to use the quasi-binary diffusion model in their investigation has criticised their methodology, suggesting that they have miscalculated the diffusion coefficients and that their analysis must be repeated in order to be accurate [57]. Tsai et al. hit back arguing that their methodology was correct [58], although other work on these systems since then has not corroborated their findings, or found diffusion to be sluggish [59–61].

In conclusion, sluggish diffusion is similar to severe lattice distortion, in so far as it is a satisfying idea which lacks validation. As so many HEA systems have been

shown to show precipitation, including the Cantor alloy, it is not possible to describe their diffusion as “sluggish”.

2.1.2.4 Cocktail Effect

The cocktail effect is the hardest of the four core effects to both describe and quantify. Yeh claims that its origins lie in cocktail drugs, that were shown to be more effective than standard drugs when treating AIDS [20], whereas Zhang claims it comes from the “the cocktail-party effect” whereby one can pick out an individual voice despite there being a clamour of overriding conversation [62]. What is even less clear than the origin of the name is what the cocktail effect actually describes: Lu states that the cocktail effect is little more than the application of the rule of mixtures [63], whereas Zhang states it is when *“unexpected properties can be obtained after mixing many elements, which could not be obtained from any one independent element”* [62]. It is this final description that is most concerning, as it has been used to justify broad and unverified generalities about HEAs, for example the statement that HEAs have good corrosion resistance, which is regularly repeated [30, 36, 37, 40, 64–66]. Lee et al. [67] did show that BAlCrFeCoNiCu can be more noble than 304 stainless steel when the composition is carefully controlled, but other papers have shown the opposite for other systems [68, 69]. This makes this generalisation misleading at best, and dangerous at worst.

If the cocktail effect is no more than the rule of mixtures, then it is not unique to HEAs and should not be listed as a core effect. If it is intended to be more than this then a realistic explanation must be presented for it. If it cannot be improved upon then it should be abandoned immediately.

2.1.2.5 Summary of the Core Effects

The four core effects are hypotheses, but due to their ease of conceptualisation and because early publications did not offer evidence that directly contradicted them, they were taken as facts. It was only a decade after their introduction that serious work began on testing these hypotheses, and ascertaining whether the fore core effects are real, and whether HEAs exhibit them as a general rule or not.

2.2 Predicting single phased HEAs

The general definition of HEAs is so broad that the total number of possible HEAs is greater than the number of atoms in the known universe [70]. It is clear that if HEAs of engineering significance are to be found then alloy design will have to guided by some form of predictive simulations - either thermodynamic in nature; showing which element palettes will form preferable microstructures, or mechanical in nature; accurately predicting which HEAs will have the most advantageous properties. This section aims to assess the current state of modelling of HEAs, which, at the time of writing, focuses almost exclusively on trying to predict the formation of single-phase HEAs. The next section is a justification of this design paradigm, whilst the following sections focus on some of the methods employed through the literature to predict HEA microstructures.

2.2.1 The ideal HEA microstructure

Early literature on HEAs was focussed on isolating single-phase microstructures, the underlying theory being that a single-phase solid solution would maximise the strength of the four core effects. In 2016, reviews by both Miracle and Pickering [18, 19] highlighted that almost all engineering materials utilise at least one secondary

phase in order to strengthen the material, often a network of precipitates such as in 2000 or 7000 series Aluminium alloys, or a bi-modal microstructure consisting of a brittle and a ductile phase, such as the pearlite microstructure in steels. These authors are correct in trying to move research away from single-phased HEAs, as any HEA that sees application will undoubtedly have a multiphase microstructure, however the importance of single-phased materials should not be ignored.

For any researcher trying to develop a framework with which to predict the formation of HEA microstructures, correctly predicting element palettes and compositions that form a single phase is the first step in understanding the underlying principles of HEAs, in order to eventually be able to identify the most beneficial microstructures in terms of optimising physical and structural properties. In addition, for the experimentalist, understanding the origin of specific properties of a new alloy can be made simpler by analysing simple microstructure: when testing the strength of a multi-phase system it is hard to isolate whether the properties observed are due to the primary phase, or due to the interactions with any of the secondary phases. It is only by isolating phases can their individual properties be tested. Successfully predicting and synthesising single-phased alloys will be an important part of HEA development for both modellers and experimentalists.

2.2.2 The Omega parameter

The most common parameters used for predicting the formation of single phase HEAs are Ω and δ, the formulations for which were suggested by Zhang [38] and Yang [71]. The δ parameter is the root mean square of atomic radii in the alloy, and is discussed in section 2.2.2.4. The Ω parameter attempts to quantify the competition between entropy and enthalpy as follows:

$$\Omega = \frac{T_{\mathrm{m}} \Delta S_{\mathrm{mix}}}{|\Delta H_{\mathrm{mix}}|} \tag{2.4}$$

Ω	:	The Ω parameter
T_{m}	:	Melting temperature (K)
ΔS_{mix}	:	Entropy of mixing (J K^{-1} mol^{-1})
ΔH_{mix}	:	Enthalpy of mixing of the solid solution (J mol^{-1})

Equation 2.4 shows that Ω is based on several assumption. Firstly, the use of T_{m} implies that the thermodynamics at the point of solidification determine the final microstructure of the cast material, and that the thermodynamics at lower temperatures are either consistent, or unimportant. This means that the temperature used in the equation is the melting point of the alloy, most usually determined using the rule of mixtures.

2.2.2.1 Entropy Formalism

The next assumption is that all contributions to entropy other than configurational can be ignored. This means that one can use equation 2.2 for equiatomic alloys, but this is more commonly expanded to take account of alloy composition as:

$$\Delta S_{\mathrm{mix}} = \Delta S_{\mathrm{config}} = -R \sum_{i=1}^{N} c_i \ln c_i \tag{2.5}$$

c_i : Composition of component i (at%)

If the alloys are assumed to have no long or short range order then the assumption means Ω should slightly underestimate the total entropy of the system. However, assuming zero ordering within the alloy is ill advised, as any amount of short-range order would dramatically reduce the configurational entropy. It is important there-

fore to attempt to understand how much ordering is occurring in these alloys, rather than assuming total disorder.

Long range order can be relatively easily assessed as shown by Bragg and Williams [72]. Short Range Order (SRO) on the other hand is harder to quantify; it can be assessed using various diffraction techniques, for details see [73], but an alternative approach that has been utilised for HEAs is to use Density Functional Theory (DFT) to predict the chemical SRO firstly in binary and ternary alloys, and then in well studied HEA systems. In the study in question [74] they found that the SRO in AlCrFeCoNi system was in line with earlier predictions. The authors note, however, that experimentally measuring SRO is difficult, and that their model should only be used to predictively guide future studies. The question of what the *actual* entropy is of HEAs is still being debated, but the ease of use and high through-put nature of equation 2.5 makes it the best choice for current predictive parameters.

2.2.2.2 Enthalpy Formalism

The denominator of Ω is the modulus of the mixing enthalpy. A stable HEA should have a high value of Ω, and therefore a small value of ΔH_{mix}; highly positive values will signal immiscibility, while highly negative values would suggest that there is likely to be stable intermetallics that may form in preference to the single phase solid solution, although they would not in themselves lead to phase separation.

Yang and Zhang followed the approach of Takeuchi and Inoue when they developed a similar model predicting the formation of BMGs [75, 76] whereby the Miedema model is used to quantify the binary interactions, and then to sum these according to equation 2.6.

$$\Delta H_{\text{mix}} = \sum_{i=1, j\neq 1}^{N} \left(4\Delta H_{\text{AB}}\right) c_i c_j \tag{2.6}$$

ΔH_{AB} : Enthalpy of mixing of the binary alloy AB (J mol^{-1})
4 : Factor to normalise the binary enthalpies of mixing

ΔH_{AB} is calculated using the relevant elements' electronegativity parameter (work function) and electron densities at the boundary of the Wigner-Seitz atomic cells. The theory behind these equations is described in [77–80] or more fully in [81]. The use of the Miedema model to assess binary mixing enthalpies is valid for disordered liquids, and solid binaries of metallic pairs, but the creators did not discuss the applicability of their model to more complex solutions. In addition, the values cited in [76] which are used in [71] to calculate Ω, are for 50/50 mixtures only, which means as solutions move away from this, a linear relationship between enthalpy and composition is assumed. The factor of 4 is included in order to normalise ΔH_{AB} for binaries; if ΔH_{ABC} was used for ternaries then a factor of 9 would be required [82]. It is also mathematically relevant to acknowledge that the equation of ΔH_{mix} does not include anything to avoid double counting, but this is required when implementing it e.g. in a five component alloy you must account for the binary between components two and four, but *not* between four and two.

Summing all relevant binaries is a short cut to quantifying the interactions between more complex systems, and so it does introduce inaccuracies. For example, if a system contains a binary whose value of ΔH_{mix} is highly positive, and another binary is highly negative, then these would sum to close to zero: Ω would imply single-phase HEA formation is likely. What may occur in the real alloy however, is the first binary pair would segregate away from one another, whilst the second

would either enter a solid solution or intermetallic phase. It should be noted that when initially proposed by Takeuchi and Inoue ΔH_{mix} was only intended for ternary systems to help predict the formation of BMGs, and it was Yang and Zhang that took this concept and applied it to more complex systems for HEA prediction. A key difference between these fields is that BMGs are by definition not thermodynamically stable, and so the ΔH_{mix} parameter is just used to show when a crystalline solid solution may be avoided by rapid solidification. HEAs on the other hand *are* meant to be stable, and so the thermodynamics between the disordered solid solution and competing phases are important, meaning that ΔH_{mix} and Ω should be accurate.

Of the three terms in Ω it is the ΔH_{mix} that is least accurate, but also the most variable. The melting point will almost always be between 1000 and 3000 K, whilst ΔS_{mix} is generally less than 20 J K^{-1} mol^{-1}. In contrast to this, ΔH_{mix} can vary from zero to 10^5 J mol^{-1}, and can scale Ω across ten orders of magnitude.

2.2.2.3 The meaning of Omega

Using the methodology described provides a high through-put method which easily produces a guiding parameter from a very basic set of input data (see [71] and [76]) which can be contained in a single spreadsheet. The obvious disadvantage is that by ignoring several entropy contributions, and only considering binary enthalpies of mixing, the accuracy of Ω is reduced.

There are several steps that could be taken to improve Ω, most of which focus on the least accurate parameter, ΔH_{mix}. For example, there are ways to expand the Miedema model for ternary system and beyond [83] which allows more complex interactions to be taken into account, but so far these have not been published.

The Ω parameter also only considers the disordered phase, and if the thermodynamic competition within HEAs is ever to be fully assessed, then any model must not only quantify the driving force for HEA formation, but also driving force for alternative phases. Without knowing the Gibbs free energy of formation for all possible phases (individual elements, solid solutions, intermetallics, etc.) there is no way to know which phase is truly thermodynamically stable: some predictive methods attempt to do this (such as the complex κ_1^{CR} parameters [84, 85]) but these rely on large resources of raw data and computational power that Ω is able to do without. The reason Ω has gained such wide use despite being such a blunt predictive tool, is its simplicity in both concept and implementation. It is a simple way of comparing alloy systems and compositions and trying to identify which are most likely to yield single-phased solid-solution microstructures, as is demonstrated in chapter 5.

2.2.2.4 The delta parameter

In addition to Ω, Yang and Zhang also defined δ [71] to quantify the lattice strain in the final alloy. This is mathematically achieved by comparing the atomic radii of each component to that of the average radii, and then taking a weighted average of this deviation, as shown in equation 2.7.

$$\delta = \sqrt{\sum_{i-1}^{N} c_i \left(1 - \frac{r_i}{\sum c_i r_i}\right)^2} \tag{2.7}$$

δ : The δ parameter
r_i : Atomic radius of element i (m)

The purpose of δ is to illustrate at what point the lattice strain induced by the disordered crystal structure will cause a breakdown in the single phase microstructure. An empirical upper limit for δ was set at 6.6%, based on experimental work previ-

ously done on BMGs. There are exceptions on both sides of 6.6% (see figure 2.3) but in general it is used to define the phase boundary between single-phase solid-solution microstructures, and BMGs or alloys that contain intermetallic precipitates. Attempts have also been made to consider the free energy cost of this misfit by Ye et al. [86, 87]; this has met with similar success as Ω, but requires a larger database of elemental information and is harder to implement, in addition to still having many of the same failings, such as using the same formalism to consider enthalpy.

2.2.2.5 Combining Omega and delta

Yang and Zhang [71] used the Ω and δ parameters discussed above to predict a window whereby single phased HEAs would form. This was empirically set at $\Omega \geq 1.1$ and $\delta \leq 6.6\%$: entropy must be dominant over enthalpy at the point of solidification, and the lattice strain in the alloy is not so high as to destabilise the structure of the solid solution. This region of parameter space is graphically represented in figure 2.3, along with data points representing experimental alloys from the literature, coloured according to their microstructure. The HEA window is in the top left corner, and indeed it mostly comprises solid solution microstructures of one or two phases. Tellingly however, there is a group of alloys on the borderline of the window labelled 'S+I'. These are solid solutions that contain intermetallic precipitates. After a close inspection of the supporting literature it is often unclear whether the reported microstructures are accurate, or whether microstructural examinations were simply not detailed enough to detect secondary phases, as in the references [40, 88], which closely examine ball-milled powder, but not a their sintered alloy. This is a running theme across the entire literature and it undermines all predictive models.

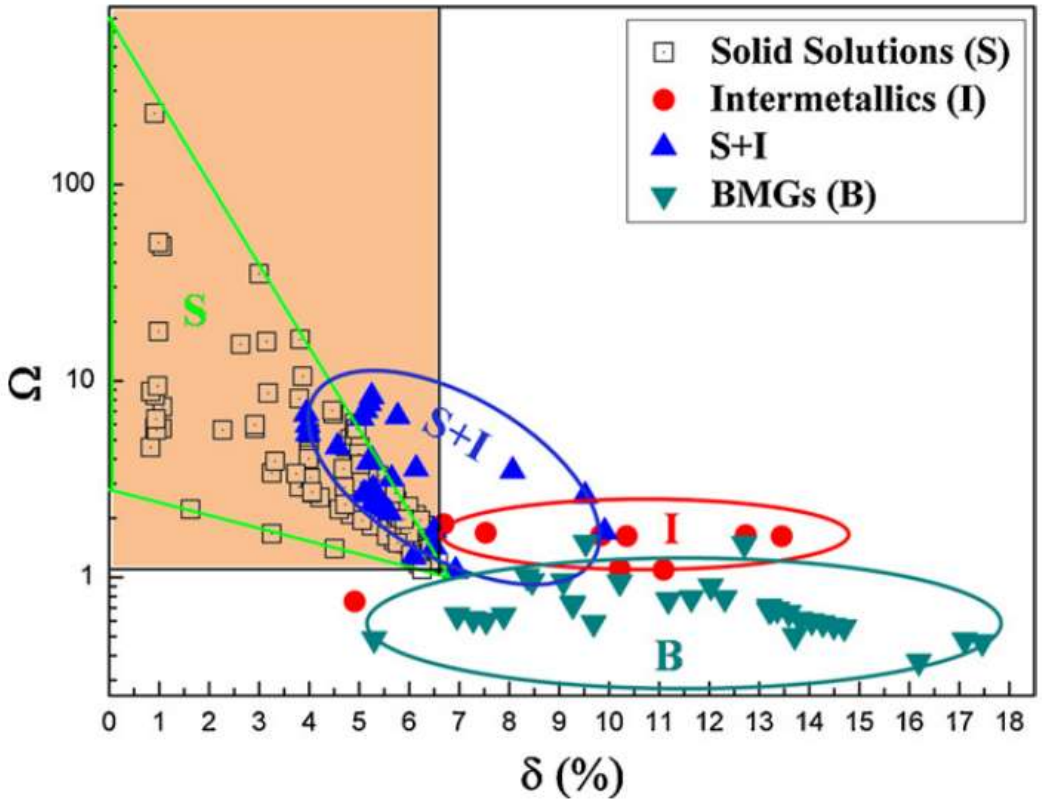

Figure 2.3: Graph plotting the Ω and δ parameters against one another. The points represent experimental evidence collected from the wider literature, and have been coloured so as to reflect their microstructure. Reproduced from reference [71].

2.2.3 Stability versus Metastability

In section 2.2.2 the origins of the Ω and δ parameters were explained, as were many of the assumptions that go along with them. At face value these assumptions seem justified, as the experimental evidence in the literature seems to support them (figure 2.3 shows a correlation between Ω and single-phase HEA formation). However, what is concerning is the lack of attention paid in the literature to the method of synthesising the alloys, and what effect this has on the observed microstructures.

2.2.3.1 Arc Melting

The vast majority of papers use arc melting, which involves striking an electric arc of high voltage and amperage which heats material within the crucible. These devices are capable of melting refractory metals such as W and Mo within a matter of seconds, and so in order to contain the heat loads generated by the arc the crucible is made of water cooled copper, and this acts as an efficient heat sync. In order to finish the casting the arc is turned off and the crucible extracts the heat. Solidification typically takes less than ten seconds and samples can be held in the hand in a matter of minutes. These high cooling rates are effectively a quench and so will lock in metastable microstructures that initially form on solidification. Yang and Zhang reference over forty papers as solid solutions in support of figure 2.3, out of these many authors never analyse their samples out of the as-cast state [25, 27–29, 33, 35, 36, 39, 52, 68, 69, 89–94] yet still parrot the hypothesis that HEAs are disordered lattices and are stabilised by a high mixing entropy, offering evidence to this in the form of an XRD trace and perhaps an Energy Dispersive X-ray (EDX) map acquired at low magnification. Some papers are are even more egregious in that they anneal their samples for the sake of testing hardness and melting behaviour, yet omit any information on microstructural changes that may or may not have occurred [16, 64, 95]. The reason for this either being strategic, as their findings would not have supported their initial hypothesis, or short sightedness, that they did not even consider looking. Only characterising samples in the as-cast state risks overlooking the importance of the cooling rate on the microstructure of the final material: the solution is to conduct several heat treatments on the samples, and analyse any microstructural evolution that may occur.

2.2.3.2 The effect of heat treatments

The fast cooling rates achieved in arc furnaces can make it difficult to distinguish between thermodynamically stable phases and metastable phases, and also the role they have in determining the final morphology of the microstructure; additionally the role of casting defects such as segregation and dendrite coring can be challenging to determine. Heat treatments such as a low temperature homogenisation will help separate out the effects of segregation from ordering as predicted by some models [96]. Long term anneals at temperatures high enough to allow diffusion are also essential in revealing what phases are thermodynamically stable. These kinds of studies have shown that some HEAs that were previously thought to be stable single-phase solid solutions actually decompose. The most studied HEA system, CrMnFeCoNi (otherwise known as the Cantor alloy) has now been shown to form CrMn precipitates after long anneals of 500 days at 700 °C [97]. Similar results have been found in other systems [47, 98–101].

2.2.4 Alternatives to arc-melting

There are alternative methods of HEA manufacture other than arc melting, including powder processing [40, 102–104], additive manufacturing [105, 106], levitation melting [107], and suction casting, which is sometimes used in conjunction with arc melting [108].

The main difference between these routes is the thermal history during the casting process. Powder processing does not require melting, and cooling rate can be actively controlled, contrast this with suction casting where the cooling rate is faster even than in standard arc melting, and there is no way to control the cooling rate. Lv et al. [109] attempted to quantify the effect of cooling rate differences on alloys

of Al_xCoCrFeNi prepared both by suction casting and traditional arc melting. Their results showed that the higher cooling rate in suction casting suppressed elemental segregation, phase separation, and lead to a marked refinement of the grain structure of the alloys. The effect of this was to reduce the density of observed deformation twins after compressive tests, but to increase the strength of the more rapidly cooled suction cast alloys.

Another interesting study which attempted to assess the effect of cooling rate on as-cast alloys was by Molnar et al. [110], who used spin casting to form droplets of CrFeCoNiGa, each of which contained a spectrum of microstructures, all of which had soidified under different cooling rates; an optical image of one of these droplets is shown in figure 2.4. In region A the cooling rate is estimated to be $1 \times 10^5\,\mathrm{K\,s^{-1}}$, while at the opposite end in region D it is estimated to be $1 \times 10^2\,\mathrm{K\,s^{-1}}$.

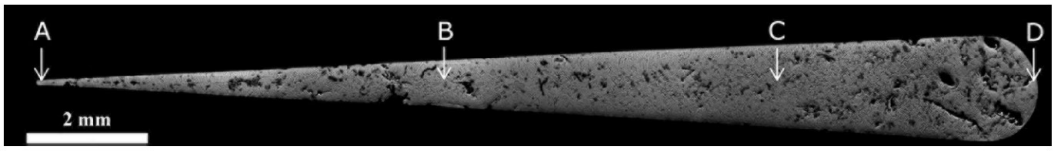

Figure 2.4: Optical image reproduced from reference [110] showing a droplet of CrFeCoNiGa formed by melt-spinning. The regions A, B, C, and D, have solidified progressively more slowly, although all have solidified rapidly.

They found that the alloy system phase separated at all cooling rates into a dendritic FCC phase and an interdendritic BCC phase. At higher cooling rates this separation was suppressed (40 vol% BCC phase at site A, and 45 vol% at site D), they also found that the chemical segregation between the two phases was suppressed by more rapid cooling, as shown in figure 2.5.

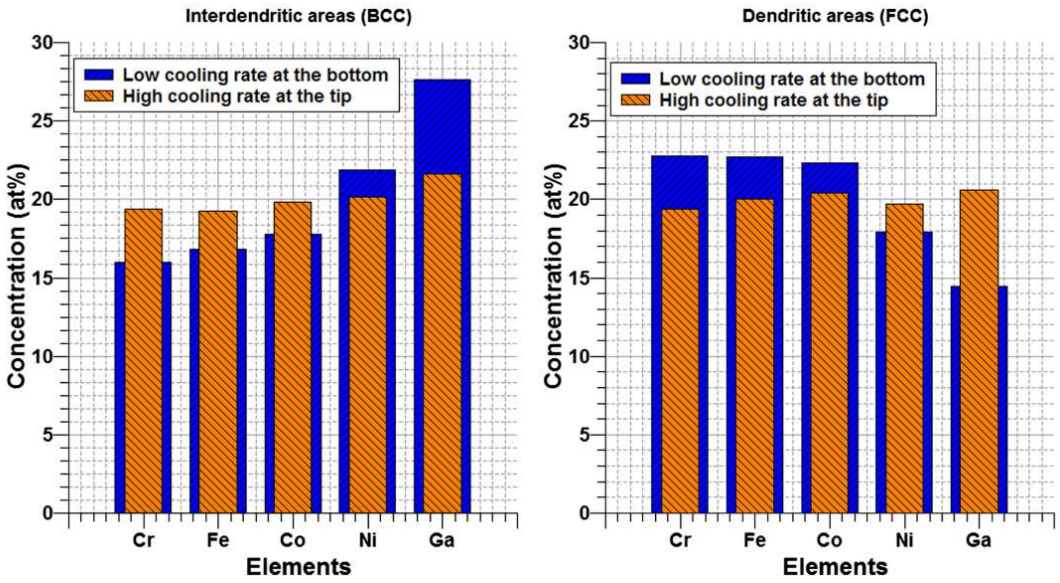

Figure 2.5: Bar chart reproduced from reference [110] showing a comparison of compositions in dendritic and interdendritic regions at different cooling rates in a sample of CrFeCoNiGa formed by melt-spinning. It can be seen that chemical segregation is more pronounced at slower cooling rates.

The results of Lv and Molnar show that cooling rate has a strong effect on the microstructures formed in as-cast HEAs, further highlighting the care that must be paid to understanding the solidification conditions of samples, and also the relevance of subsequent heat treatments to assessing the stability of their microstructures.

2.2.5 Alternative Microstructural Predictors

In the previous sections, the Ω parameter has been introduced, and the flaws in its formalisms have been highlighted, as well as the problems with its experimental validation. It is important to note that this flaw affects all models equally, not just Ω. This section discusses some of these other methodologies to try and predict HEAs.

2.2.5.1 Valence electron concentration

Several authors have correlated Valence Electron Concentration (VEC) with the properties of HEAs [48, 111, 112]. This can range from using it to determine the crystal structure of the alloy (which is shown in figure 2.6) to estimating the expected strength or hardness of HEAs.

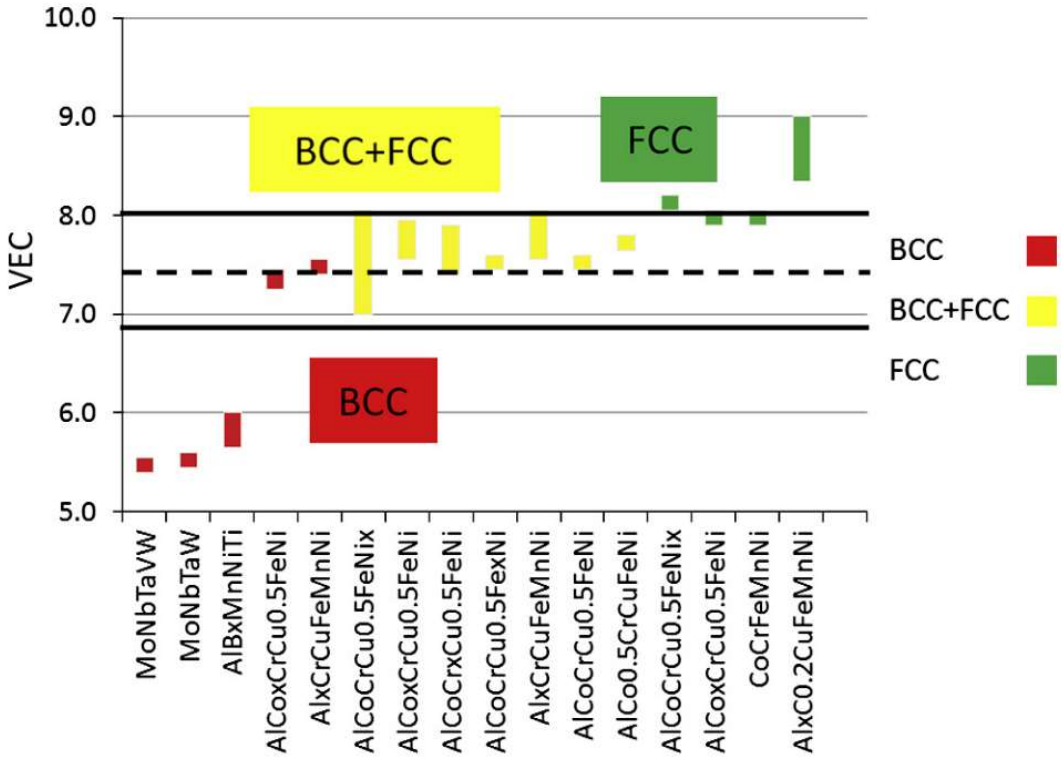

Figure 2.6: Graph plotting valence electron concentration for various alloy systems, with their observed crystal structures indicated. Reproduced from reference [62] using data from reference [111].

None of these papers offer any explanation as to why VEC would have a controlling influence on any of these properties, and it should be noted that the majority of supporting data is not only entirely based on as-cast microstructures, but also heavily based on the Al_xCrFeCoNiCu system, for which an increasing Al content causes a destabilisation of a soft FCC structure to the emergence of a hard and brittle BCC

one, along with a corresponding rise in VEC: this could be correlation being mistaken for causation, as there is no evidence offered that the Al additions stabilise the BCC structure through a change in the average valence electron concentration. In their review of the HEA field Miracle and Senkov found that "...no correlations are found between phases formed, and dχ or VEC, when a large number of alloys and a range of alloy families are considered" [19], where dχ represents the composition weighted average difference in electronegativity of all the components. In short, despite VEC often being mentioned as a possible predictive tool for HEAs, it has yet to be convincingly demonstrated.

2.2.5.2 The Oakridge method

The authors gave this method no name, and so the name "Oakridge method" is used within this review to distinguish it from others. Troparevsky et al. [113] use a DFT code to compare $T_{\mathrm{m}}\Delta S_{\mathrm{config}}$ for the disordered alloy with the enthalpy of formation for any intermetallic phase (ΔH_{IM}). In order to reduce the computational cost of these calculations only binary intermetallics are considered. This model improves on those previously described as it takes into account the free energy of competing phases as well as the disordered one. This requires a large number of calculations, as well as a list of all possible binary intermetallics. Each entry in figure 2.7 represents thousands of individual calculations.

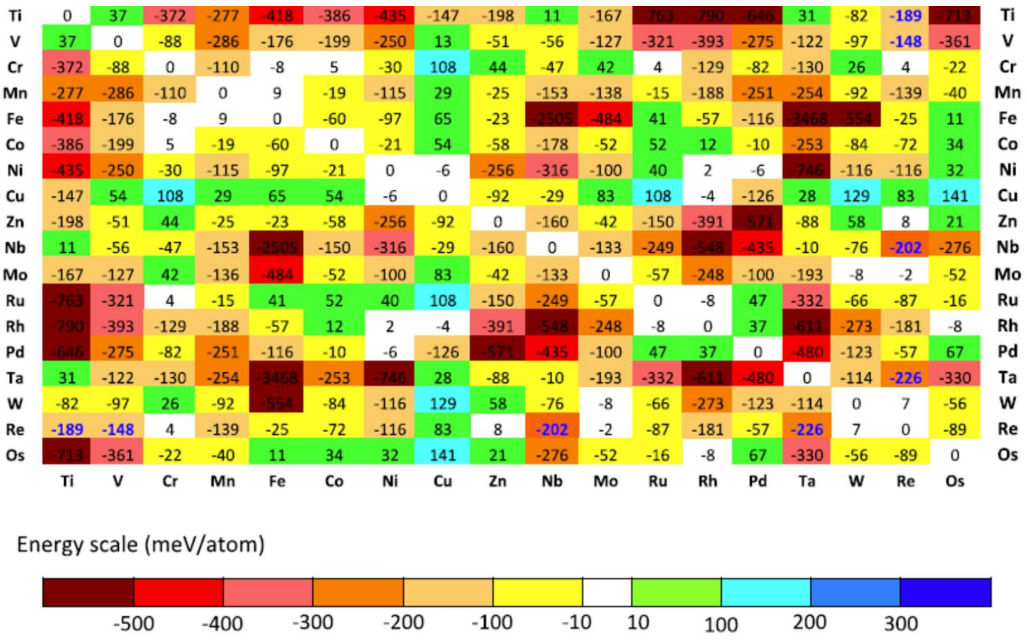

Figure 2.7: Table reproduced from reference [113] showing ΔH_{IM} for binary mixtures of elements. The extremes of the scale represent binaries that are more likely to destabilise single phase solid solutions.

The reasoning behind the Oakridge method is that if the enthalpies of formation for all binary compounds fall within the correct range (i.e. not too low so as to avoid precipitation, or too high to avoid immiscibility) then a single phase solid solution will form. This is a similar argument as presented for using the Miedema model to calculate ΔH_{mix}, but with a more fundamental approach taken during the calculations.

Although the Oakridge method is more complex than either ϕ or Ω, this does not reduce its usability, as the authors ran their calculations on tens of thousands of element palettes, and published their results in supplementary material for the entire community to use. This resource, although not fully verified experimentally, will be of great value to researchers to guide alloy selection.

2.2.5.3 CALPHAD

An alternative approach provided by Senkov et al. is to use CALPHAD (CALculated PHAse Diagram) techniques that are much used within other multicomponent fields, such as those for Ni superalloys [114]. CALPHAD is a technique that uses databases of thermodynamic information to interpolate, and sometimes extrapolate, to different or more complex systems. The thermodynamic information is often in the form of binary phase diagrams, as well as tables of specific values such as heat capacities, enthalpies, and melting temperatures. Better databases include more reliable and better verified data, as well as more complicated systems such as ternary phase diagrams. The key advantage of the CALPHAD technique is that it is already well understood and established, and allows a large number of potential systems to be analysed in a short space of time - for example in their 2015 paper Senkov et al. analysed 397,215 different element palettes, with between three and six components [115]. The disadvantage of CALPHAD models is that their predictive powers are entirely based on the quality and size of the databases used, and that their accuracy is both highly variable and hard to quantify. Two parameters of use in assessing accuracy are the fraction of assessed binaries (FAB) and fraction of assessed ternaries (FAT) [115].

$$\text{FAB} = \sum_i \frac{\kappa_i^B}{B_{\text{tot}}}$$
$$\text{FAT} = \sum_i \frac{\kappa_j^T}{T_{\text{tot}}} \tag{2.8}$$

κ_i^B : Level of assessment of an i[th] binary (or j[th] ternary). The level of assessment, or κ, equals 1 if a complete thermodynamic description is available, 0.1 if only partial information is available, and 0 if no information is available

B_{tot} : Total number of binaries (or ternaries) for a given alloy

Excluding alloys that have FAB = 0 and $T_{\text{m}} \leq 600\,^{\circ}\text{C}$ removes over 80% of the total alloys originally considered, showing that current databases are not ideal for HEA research.

For the case of Ni superalloys the huge amount of research over the last several decades has given a wealth of reliable and detailed data. This now means that CALPHAD is able to accurately predict the formation of γ' precipitates [116]. However, even with the extensive library of information CALPHAD still struggles in some areas, such as correctly predicting the presence Topologically Close-packed Phases (TCPs), which can be detrimental to mechanical properties. The proposed solution for superalloys is to better map the relevant ternary systems: improve the database's knowledge of multi-element interactions. It is therefore important to note that out of all the databases analysed for use with HEAs only 58 ternary systems have $\kappa_j^T = 1$ i.e. have full thermodynamic assessment, and no HEAs with more than 3 components had FAT = 1. Assessing all the ternaries of interest for HEA research is nearly as daunting a task as synthesising all possible HEAs.

Although CALPHAD is a more developed system, it is still predicting HEA microstructures using information from constituent binaries, and ignoring more complex interactions - in addition many high order alloys did not even have high FAB values, and were barely described by their binaries, as can be seen from figure 2.8, which shows the FAB and FAT values from Senkov's original paper [115].

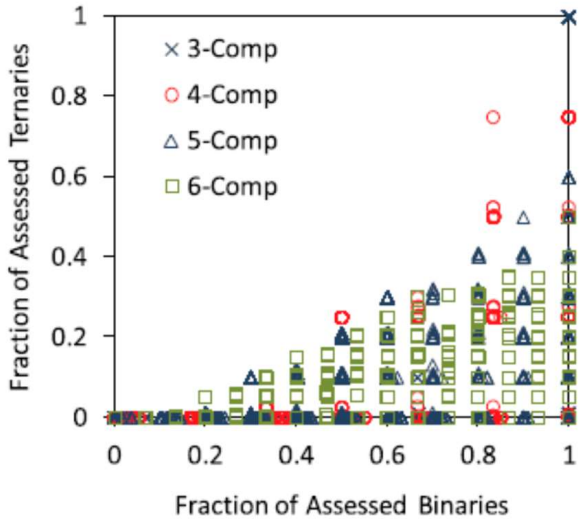

Figure 2.8: Graph showing the FAB and FAT values for 3 to 6 component alloys analysed by Senkov et al. Reproduced from reference [115].

Despite these disadvantages, several papers have already shown the applicability of CALPHAD to specific HEA systems. Ng et al. analysed the AlCrFeCoNiCu system at annealing temperatures up to the melting point of the alloy, and the observed microstructures agreed well with those predicted by Thermo-Calc, when modelling with the TTN18 database [117]. The microstructures in question were not simple but included multiple ordered and disordered BCC and FCC phases, as well as σ phases. Figure 2.9 shows the predicted and observed microstructures in the alloy.

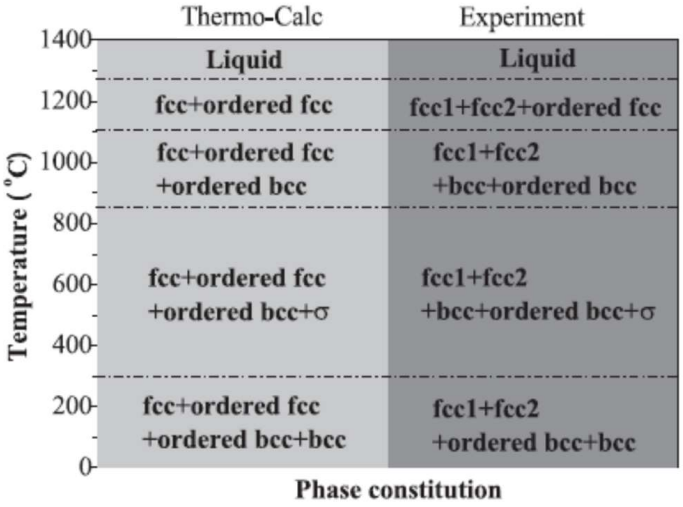

Figure 2.9: Table showing the experimentally observed, and ThermoCalc predicted, microstructures of an AlCrFeCoNiCu alloy on annealing at different temperatures. Reproduced from reference [117].

Manzoni et al. used a similar methodology to Ng to test AlCrFeCoNiCu alloys of different compositions, but with less success. Manzoni used a slightly different database (TTN17), and found good agreement with one alloy, but poor agreement with another [118].

In conclusion, CALPHAD is a well developed method of analysing a large number of candidate alloys very quickly, and although current databases are not ideal for providing details of microstructures of new alloys, CALPHAD can provide a first sweep to try and isolate groups of alloys that would be worth further modelling with more intensive techniques, such as the Oakridge method or the κ_1^{CR} proposed by Senkov [84].

2.2.6 Summary of predicting HEAs

To summarise this section, there are many approaches to modelling HEA microstructures, most of which rely on a parameter approximating the enthalpy interactions. The most common enthalpy approximation is to sum the binary values predicted using the Miedema model. This technique has been improved upon calculating the binary values more accurately using DFT calculations, and also in directly comparing the Gibbs free energy of the disordered phase to that of possible intermetallics. The biggest problem with the modelling of HEAs is unreliable validation data in the literature. The trend to analyse samples in the as-cast condition, rather than after satisfactory annealing, means that reported disordered microstructures may not be accurate. This has led to incorrect correlation between predictions and experimental work. Despite this, several techniques have been shown to be potentially useful in identifying alloys with useful microstructures, and as the literature expands to include more thoroughly annealed alloys, their accuracy can be better measured and improved upon.

2.3 Refractory and BCC HEAs

The work in this thesis focuses on BCC refractory HEAs, as these have the most advantageous properties for fusion applications, for example higher strength, hardness, and resistance to radiation induced swelling.

2.3.1 The TiVZrHfTa system

The primary alloy system investigated in this thesis is TiVZrHfTa, this alloy system has been previously investigated by Ayyagari et al. [95] in 2018, along with

a parallel investigation of TiVZrTaW. They used the DFT code ”Vienna Ab-Initio Simulation Package” (VASP) to estimate the propensity of elements to segregate in their alloys; the results of which were that W-Ta may segregate in TiVZrTaW, but that there should be good mixing in TiVZrHfTa. These predictions were borne out when the alloys were manufactured and analysed.

The researchers claimed to have melted 1.25kg billets of TiVZrHfTa and TiVZrTaW using arc melting. This is an incredibly large mass for a refractory arc melted billet, and although commercial arc melting units can produce billets of this size, it is rare to find them used in an academic setting, where masses of 10-100g are more common. As Ayyagari does not list the make nor model of the arc melter used, and gives no more information on the billet, it is possible that this claim of 1.25kg billets is a typo: it would not be the only one in the paper. The EDX data for these alloys is presented in figure 2.10 and shows that TiVZrTaW phase separates into a a TiZr phase, a TaW, and V is concentrated at the interfaces between the two. In contrast, TiVZrHfTa is shown to be chemically homogeneous, although the reader should be aware that the EDX map for Hf is mislabelled as W.

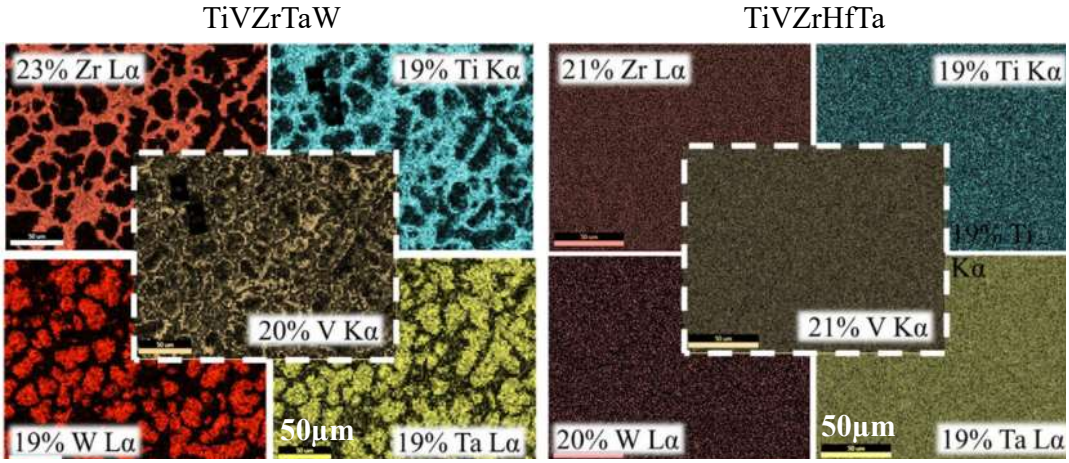

Figure 2.10: Elemental EDX maps of TiVZrTaW and TiVZrHfTa, reproduced from reference [95]. The W containing alloy has phase separated, while the Hf containing alloy is a chemically homogeneous and single phase. N.B. the EDX map for Hf is mislabelled as W.

The crystal structures of the two materials have been identified with XRD and using diffraction patterns in the TEM, the results for which are reproduced in figure 2.11. The results of this show that both alloys contain a BCC phase with a lattice parameters of $\sim$3.3 Å, and that surprisingly both phases in the TiVZrTaW alloy are BCC with similar enough lattice parameters that only a single structure is visible in XRD.

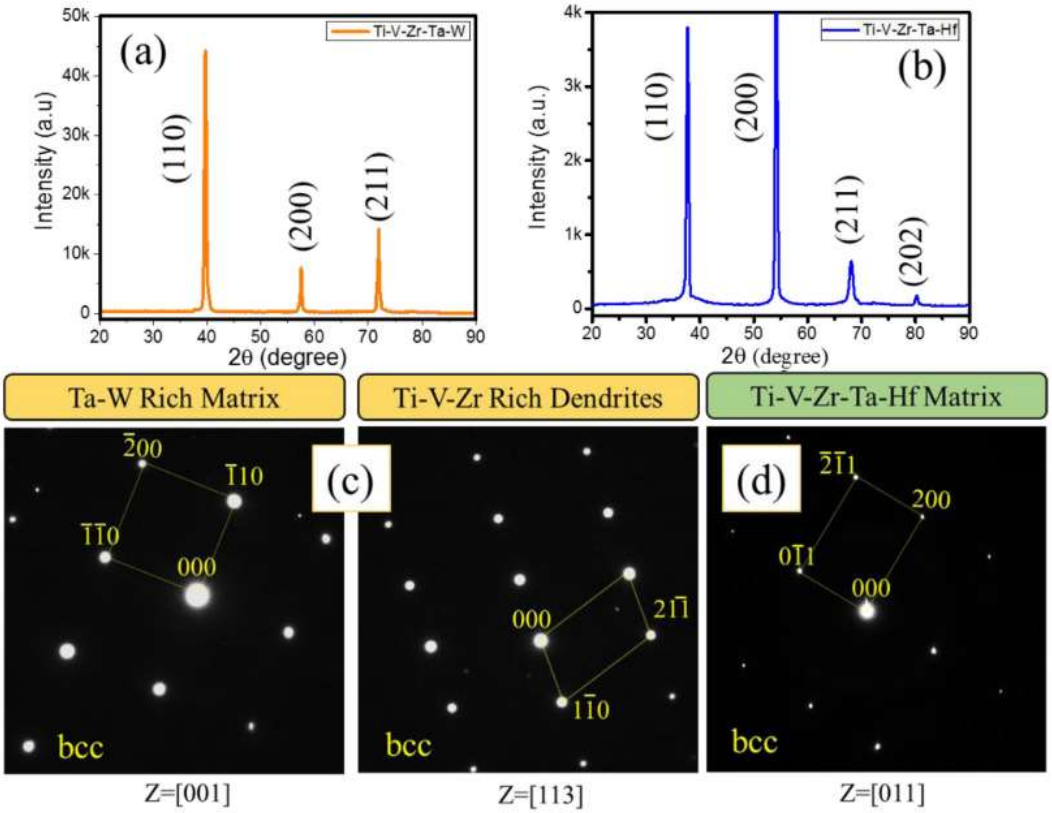

Figure 2.11: Collection of data showing XRD traces and TEM diffraction patterns reproduced from reference [95]. The data shows both TiVZrHfTa to be single phase BCC, and the two phases in TiVZrTaW to be BCC with the same lattice parameters, despite their different chemistries.

Ayyagari also used nanoindentation to highlight the high hardness of these alloys: 8GPa for the W alloy and 6.5GPa for Hf alloy. Indentation at elevated temperatures showed that these hardness measurements were relatively stable up to 575K, compared to 316 stainless steel, which showed a softening of 85% in the same tests. Although samples have been heated during that nanoindentation tests no microstructural analysis has been done on these annealed samples.

The results of Ayyagari et al. are not incredibly instructive for the purpose of this project, although they show that under the right conditions TiVZrHfTa can be synthesised in a chemically homogeneous single phase form, and that DFT modelling

predicted no elements were likely to segregate during solidification.

2.3.2 The ZrNbHfTa system

As stated previously a lot of HEA research is characterised by its brevity, an example being the paper by Feuerbacher et al. from 2018 [119] which boasted to have a homogeneous sample of TiVZrNbHf, which was manufactured using arc melting followed by a six hour anneal at 1500 °C. Other researchers have been more thorough however: Maiti et al [120] showed that although ZrNbHfTa is BCC when cast in an arc melter, if it is annealed for more than six days at 1800 °C a minor HCP phase also forms, which is visible in atom probe reconstructions of Zr and Hf, as shown in figure 2.12.

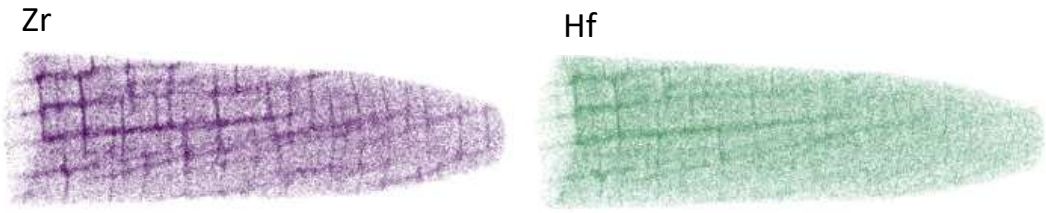

Figure 2.12: Atom Probe reconstructions reproduced from reference [120] showing the distribution of Zr and Hf in ZrNbHfTa after 8 days of annealing at 1800 °C. It can be seen that laths of a ZrHf-rich phase are forming.

2.3.3 The TiZrNbHfTa system

The most commonly investigated BCC HEA is TiZrNbHfTa, in which similar phase separation is observed as in ZrNbHfTa. Stepanov et al. [121] found that although homogenised arc melted samples of TiZrNbHfTa had a single phase BCC microstructure, annealing for more than ten hours at 600 °C resulted in the precipitation of an HCP phase throughout the alloy. This precipitation became more pronounced after longer or hotter anneals, as can be seen in figure 2.13.

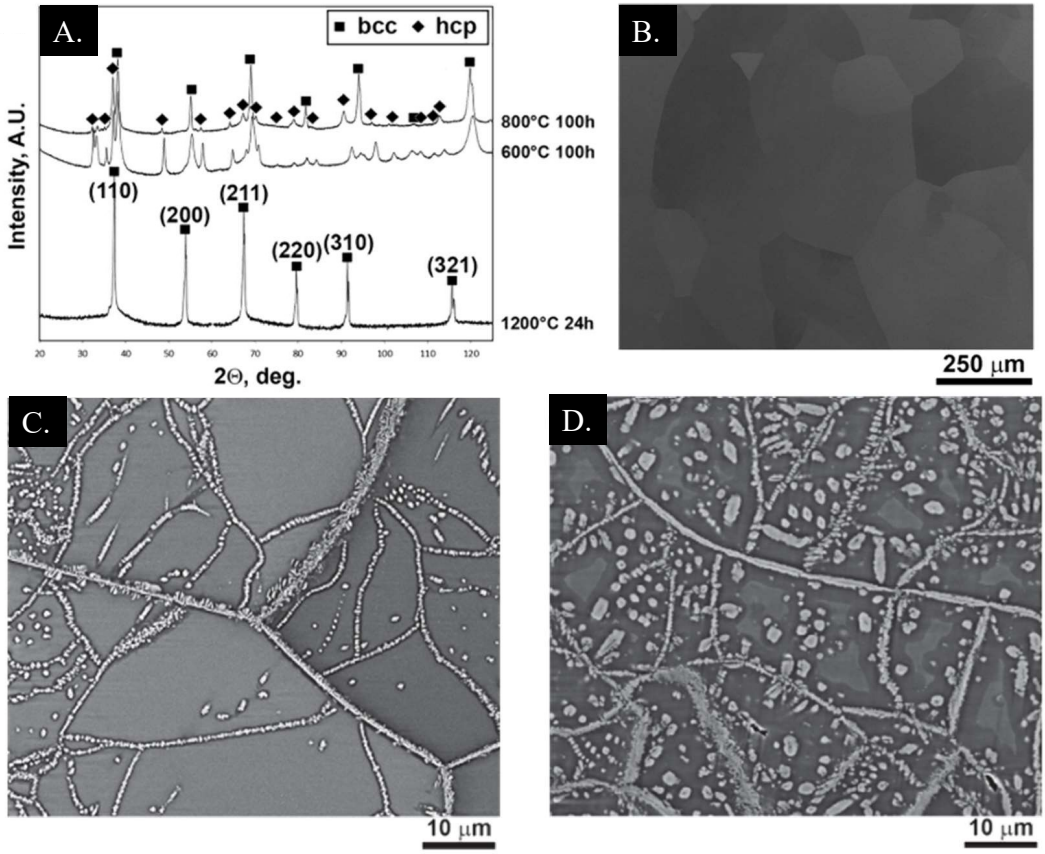

Figure 2.13: Data reproduced from reference [121] showing the phases present in different samples of TiZrNbHfTa. Graph A shows a comparison of XRD traces, while micrograph B through D respectively shows the microstructures of the homogenised alloy after additional annealing for 10 hours at 600 °C, 10 hours at 800 °C, and 100 hours at 800 °C respectively. The trend is that hotter and longer heat treatments result in more precipitation of an HCP phase.

These results are partially corroborated by Chen et al. [122] who did heat treatments at temperatures between 550 °C to 900 °C for between 2.5 and 96 hours. They also observed the precipitation of a HCP ZrHf phase and a secondary NbTa BCC phase in all heat treatments at 700 °C or above. The compositions of these phases were measured by TEM-EDX and with atom probe tomography; these were then compared to the compositions predicted by CALPHAD simulations, which were in agreement for the BCC precipitate but not the HCP ones. A comparison of the measured compositions are shown in figure 2.14 which is a table from Chen [122] sum-

marising the compositions measured in the alloy annealed at 700 °C for 96 hours.

Phase		Ta (at.%)	Nb (at.%)	Ti (at.%)	Zr (at.%)	Hf (at.%)
Ta-Nb-rich BCC	TEM-EDX	42.81	29.67	15.27	5.32	6.93
	APT	38.52	33.44	17.46	4.05	6.53
	CALPHAD	40.95	40.57	12.22	3.54	2.73
Hf-Zr-rich HCP	TEM-EDX	7.62	0.75	10.43	43.99	37.21
	APT	5.87	0.39	9.31	49.04	35.39
	CALPHAD	0.57	0.92	27.21	35.27	36.02
Matrix BCC	TEM-EDX	21.10	13.37	22.09	20.28	23.16
	APT	20.53	21.10	20.10	19.50	18.77

Note.
TEM-EDX: data was collected in the grain interior; APT: data was collected at the location close to the grain boundary.

Figure 2.14: A figure showing a table from Li [122] listing the compositions of the phases found in TiZrNbHfTa after being annealed at 700 °C for 96 hours. The composition of the BCC precipitate predicted by CALPHAD agrees with those measured by TEM-EDX and atom probe tomography, but the CALPHAD composition of the HCP precipitate is not similar to the one actually measured.

In addition to measuring the compositions of these phases, Li et al. also found an orientation relationship between the precipitates and the matrix. The BCC ones are aligned with the matrix except for a small distortion due to the lattice mismatch while the $\{0\,0\,0\,1\}$ plane of the HCP precipitates is aligned with $\{0\,\bar{1}\,1\}$ in the matrix phase. These results are in agreement with other researchers such as Schuh et al. [123], but in disagreement with Stepanov [121] who only found HCP precipitates.

More recently Yang et al. [124] found that after annealing at even higher temperatures the HCP precipitates dissolved and were replaced with a collection of FCC, HCP, and BCC precipitates, which varied considerably by annealing temperature. The breakdown of what phases form at which temperatures is shown in figure 2.15, which is the XRD traces of samples after being annealed at temperatures between 1000 and 1400 °C for either 24 or 168 hours.

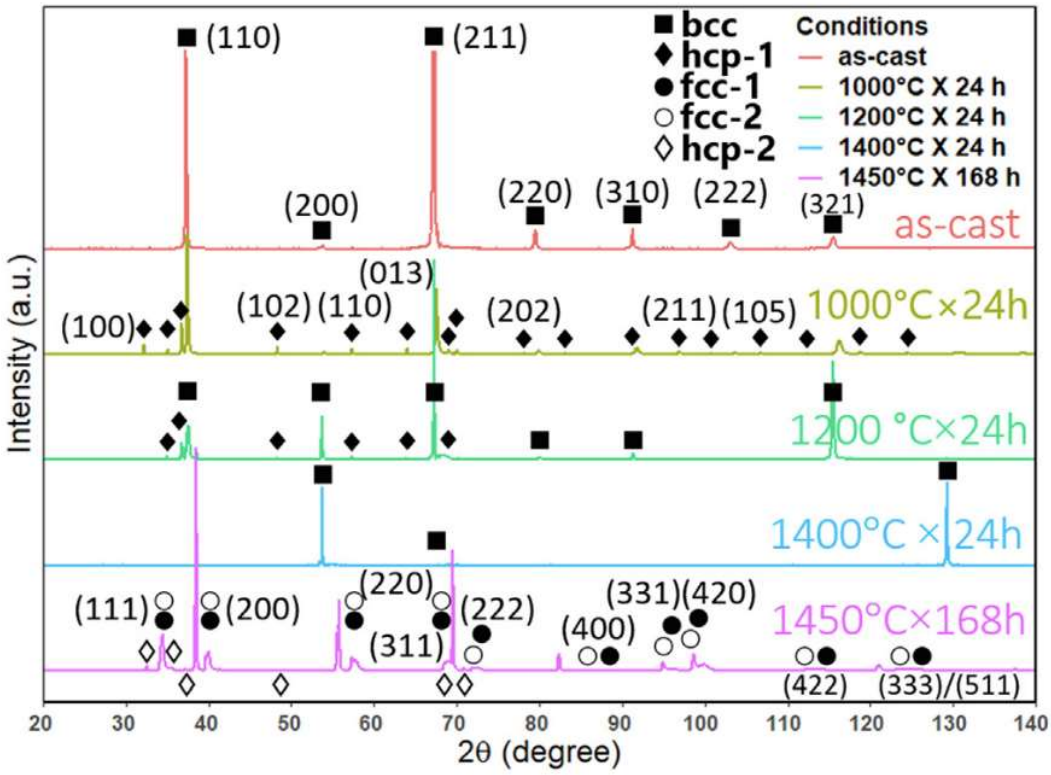

Figure 2.15: A collection of XRD traces reproduced from reference [124], showing the different phases found in samples of TiZrNbHfTa after being annealed between 1000 °C to 1450 °C for either 24 or 168 hours. It can be seen that a wide range of complicated microstructures form.

The FCC phases found in these alloys are enriched in Zr and Hf, and to a lesser extent Ti. When in the form of pure metals, these elements all form HCP and BCC structures, and they are not able to form FCC crystals. Although studies do exist that show FCC zirconium structures, this is only after intense plastic working in the form of high-energy room-temperature ball milling [125], and more recent work shows that group IV metals actually only form FCC structures as hydrides, rather than elemental metals [126]. It is quite likely that the FCC phases found by Yang et al. are actually stabilised by impurities and have been incorrectly identified. Similar occurances have been also found in other papers and are discussed further in the next section.

2.3.4 Summary of phase separation in BCC HEAs

In almost all of these papers the phase separation occurs between elements that are HCP at low temperatures (Ti, Zr, and Hf) and those that are BCC at low temperature (V, Nb, and Ta). The exception to this is Maiti et al. [120] who in their concluding remarks claim their HCP precipitates are enriched in Zr and Ta, although they present no evidence to support this claim.

2.4 High-Entropy Alloys and Ceramic Phases

A subset of HEAs highly relevant to this thesis are a group of High-Entropy materials which are, or contain, ionic phases such as carbides, oxides, or similar. These are sometimes referred to as High-Entropy Ceramics (HECs). Such materials have been reported as far back as 2008 by Shun [127], who used induction melting to cast $Al_{0.3}CoCrFeNiC_{0.1}$ and found the structure of the carbide formed varied depending on the ageing treatment. Since then several high profile papers have shown advantageous properties in various oxides [128–130], borides [131], and carbides [132, 133].

2.4.1 "High-Entropy" Ceramics

What is peculiar in these materials is that they are still considered "High-Entropy", despite existing as ordered crystals. It was noted in section 2.2.2 that the often cited equation 2.5, which is a formalism for configurational entropy is only truly applicable when applied to *liquid systems*, and that even small amounts of short range ordering are enough to dramatically reduce the configurational entropy within a material. In 2015 Rost et al. [128] addressed this directly by analysing the phase

transition within the ceramic material $MgCoNiCuZnO_5$. This material transitions from a dual phase rocksalt/tenorite structure to single-phase rocksalt structure at ~875 °C; and the researchers identify this latter structure as entropy stabilised due the the transition being both reversible and endothermic, data demonstrating this is reproduced in figure 2.16. Their evidence shows Differential Scanning Calorimetry (DSC) measurements identifying the transition from dual phase to single phase as endothermic, and XRD measurements after sequential annealing at 1000 °C, 700 °C showing the material repeatedly swapping between its dual-phase and single-phase microstructures.

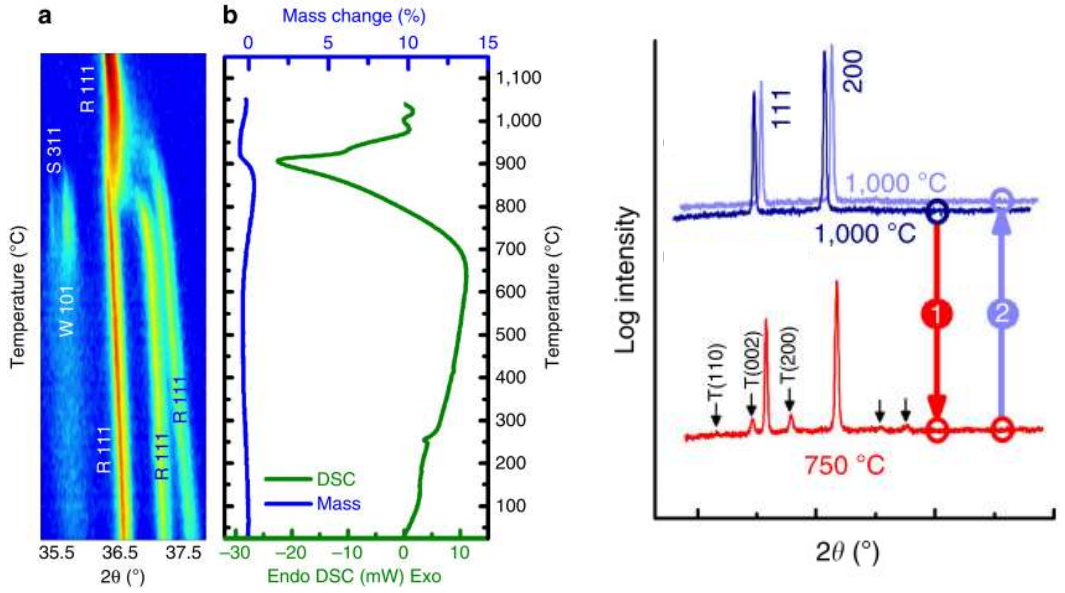

Figure 2.16: Data reproduced from reference [128] showing DSC results on the left demonstrating the endothermic nature of $MgCoNiCuZnO_5$ transition from dual phase to single phase, and XRD results on the right demonstrating this transition can be reversed.

Rost et al. demonstrate that entropy is capable of stabilising particular oxide structures over alternative ones. They also assess the enthalpic cost of the transition from the dual-phase to single-phase microstructure. What they do not do is satisfactorily demonstrate is whether the cation sublattice is truly disordered (as opposed to

simply homogeneous), or whether any ceramic material, of which the properties and structures are dominated by the anion-cation bond, draw any structural or functional properties from the amount of disorder on the cation sublattice.

2.4.2 Bulk HECs

Later work has also attempted to explore the possible advantageous properties of these materials, with Sarker et al. [132] showing increased hardness in high-entropy carbides, and Gild et al. showing improved corrosion resistance in high-entropy diborides [131].

The most interesting result so far was that made by Lei et al. [129] who have identified ordered oxygen complexes in a TiZrNbHf alloy, that have improved tensile strength by ∼50%, and ductility by ∼95%. They describe the ordered oxygen complexes as somewhere between dispersed interstitials and fully ordered oxide particles. This tensile data and an atom probe reconstruction showing the distribution of oxygen is reproduced in figure 2.17.

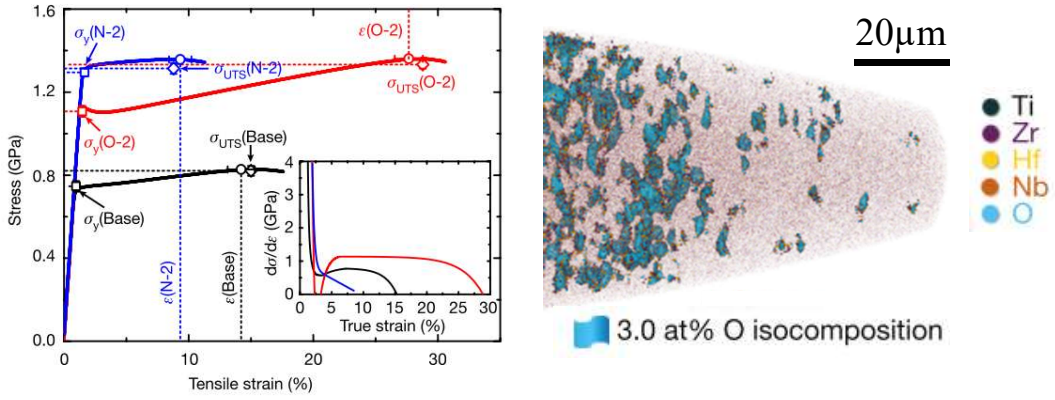

Figure 2.17: Data reproduced from reference [129] showing tensile data on the left from specimens of TiZrNbHf (black), $(TiZrNbHf)_{98}N_2$ (blue), and $(TiZrNbHf)_{98}O_2$ (red). It can be seen the oxygen containing sample has the best performance. On the right is an atom probe reconstruction of $(TiZrNbHf)_{98}O_2$, with surfaces showing a 3at% isocomposition, demonstrating the existence of oxygen complexes rather than oxide particles or isolated interstitials.

The increase in strength and ductility is attributed to a change in the dislocation shear mode from planar to wavy slip, enabling "an excellent balance between dislocation pinning, multiplication and substructure homogenization, and thereby leading (sic) to a high strain-hardening reserve and an increase in both strength and ductility". There is also a decrease in grain size visible in the oxygen containing alloys (shown in figure 2.18), although the author claims this is not responsible for the change in mechanical properties between the alloys.

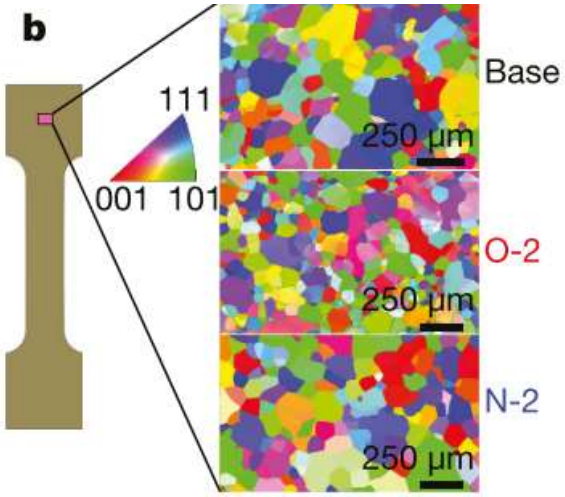

Figure 2.18: Data reproduced from reference [129], showing EBSD maps from the three alloys investigated: the base metal, the oxygen doped alloy, and the nitrogen doped alloy respectively. It can be seen that the oxygen containing alloy has the finest grain size.

High-entropy ceramics are an interesting subset of multicomponent alloys, although there are still important outstanding questions relating to them, such as: if by definition they are ordered crystals, can the entropy still be considered high? Even if the cation sublattice is disordered, does this actually convey any beneficial properties, and are these related to the properties of metallic HEAs? Finally, and perhaps most importantly, how do HEAs *containing* borides, carbides, nitrides, or

oxides behave, and do these precipitating phases convey beneficial or deleterious properties on the final alloy?

2.4.3 Ceramic inclusions due to impurities

Although Lei et al. [129] have found the addition of oxygen to be beneficial in their material, at 2at% it is at the typical level of an impurity, which normally act to embrittle materials either when in solution or precipitated as oxide particles [134, 135]; carbon, nitrogen, and boron can act in the exact same way. It is therefore unsurprising that occasionally HEA researches find impurity phases introduced during casting affect their alloys, for example it was previously mentioned that Yang [124] found FCC phases enriched in zirconium and hafnium when annealing TiZrNbHfTa alloys at temperatures higher than 1400 °C: as neither zirconium nor hafnium form FCC phases under these conditions, a more likely explanation of this phase is either carbon or nitrogen contamination causing the formation of a rocksalt structured-phase, which would indexes the same as an FCC phase by XRD.

In another example of possible contamination Poulia et al. [136] found phase separation to occur in their $Ti_{20}V_{10}Zr_{30}Nb_{15}Hf_{25}$ alloy, and identified the two phases formed as BCC and HCP, as shown in figure 2.19. Bizarrely, the XRD trace they gave did not show these crystal structures, as demonstrated by the *actual* trace for the hexagonal structure they describe displayed underneath their data.

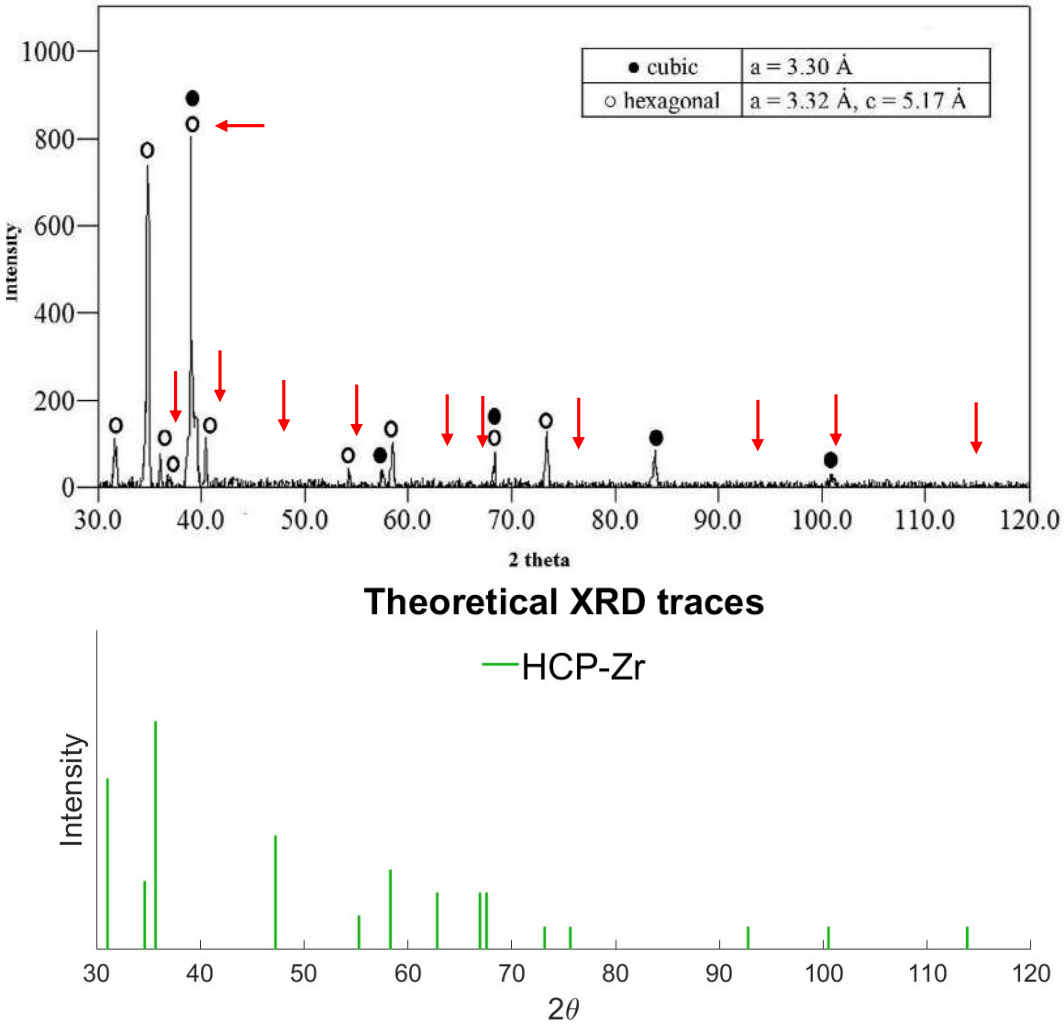

Figure 2.19: Comparison of the XRD results of Poulia et al. [136] on top, and a theoretical trace for a HCP Zr below. The red arrows have been added to Poulia's data in order to indicate the mislabelled and missing HCP peaks in Poulia's data.

A more accurate attempt at indexing Poulia's XRD data is shown in figure 2.20, although this is difficult to do without access to the original data. Their alloy seems to also contain an FCC or rocksalt structured phase with a lattice parameter of ∼4.5 Å. This phase most likely formed due to carbon or nitrogen contamination, as the cubic nitrides and carbides of all the elements in Poulia's alloy have this structure and the roughly the same lattice parameter (see table 4.2 and reference [137]).

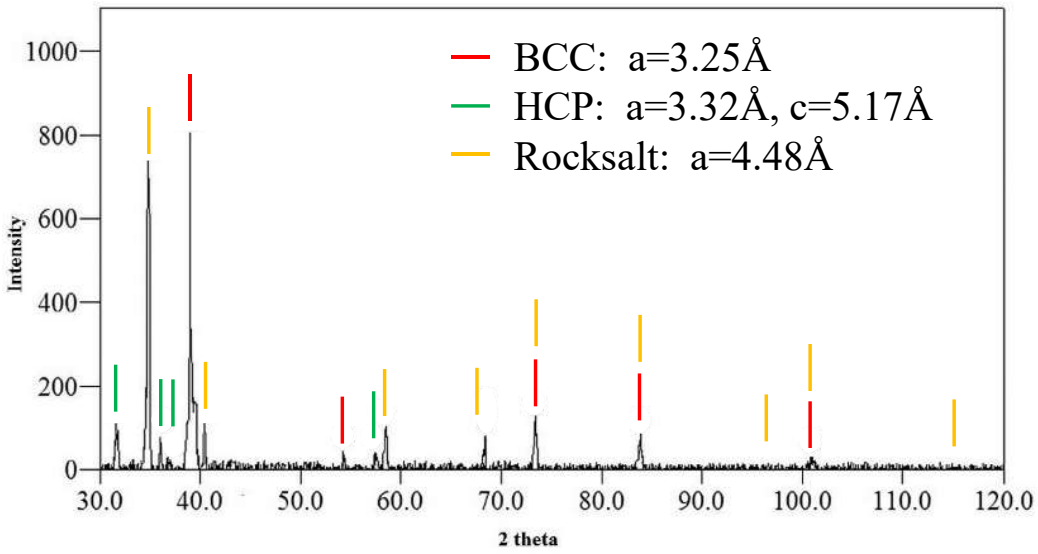

Figure 2.20: Re-indexed XRD data from the paper by Poulia et al. [136]. The diffraction pattern seems to be BCC, HCP, and potentially a rocksalt structured phase, although it is not possible to be certain of this without access to the original data

A final example of a potential ceramic phase that was misidentified as metallic was found in early work by Senkov et al. in 2011 [138]. They analysed the microstructure of Hot Isostatically Pressed (HIPped) $Ti_{20}Cr_{20}Zr_{20}Nb_{20}Mo_{10}Ta_{10}$ and identified BCC and FCC phases, as shown in their XRD and SEM results in figure 2.21. Although in some tables Senkov describes the FCC phase as "Laves", they do not explain how a phase primarily enriched in Cr and Zr can form an FCC phase, when their phase diagram contains only BCC, HCP, and C15 intermetallic phases in the temperature range of interest.

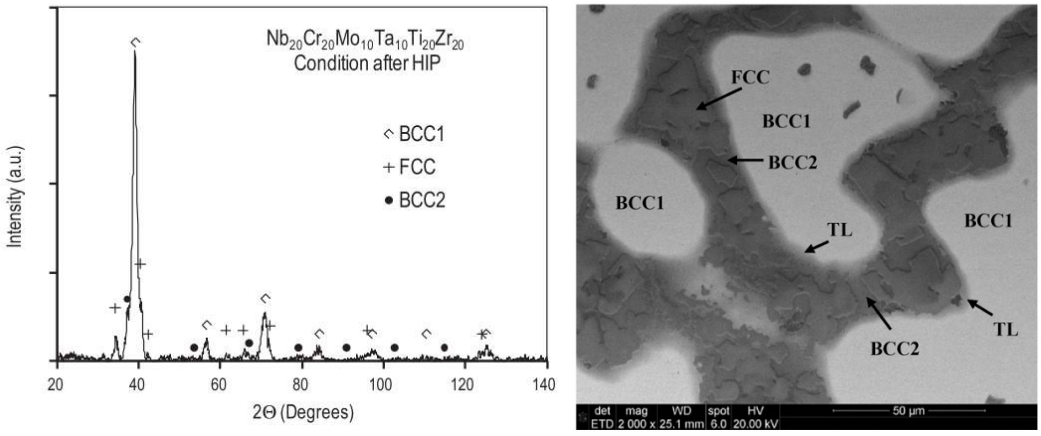

Figure 2.21: XRD data and secondary electron image of the phases formed in HIPped $Ti_{20}Cr_{20}Zr_{20}Nb_{20}Mo_{10}Ta_{10}$, showing two BCC phases and one FCC phase. reproduced from reference [138].

What is clear is that small amounts of impurities can lead to the formation of ceramic phases, regardless of the high configurational entropy of the metal phase. It is also clear that identifying these phases is not trivial, as compelling evidence has been found in at least three papers of misidentified phases actually being based on impurities.

2.5 Irradiation of HEAs

Any material that is intended to be used in a fusion application will have to be able to resist high radiation fluxes; one reason that HEAs are candidate materials for plasma facing components in fusion reactors is their resistance to such damage.

2.5.1 Swelling resistance in HEAs

An important consequence of material irradiation is swelling, defined as bulk shape changes due to the coalescence of voids and the diffusion of atoms to external sur-

faces: the resultant changes are particularly hazardous in critical components [9]. Multiple papers have demonstrated HEA to have a high resistance to radiation induced swelling both qualitatively [46, 139, 140] and quantitatively [14, 141] over a wide range of dpa. The study by Jin et al. [14] contained the most surprising results, finding that swelling in CrMnFeCoNi is 40 times less than in elemental Ni, after 53dpa of 3MeV Ni ions at 500 °C. The swelling measured in the CrMnFeCoNi was low enough that it was in line with the samples reported surface roughness of 3nm. The percentage of swelling for six equiatomic Ni based alloys is shown in 2.22.

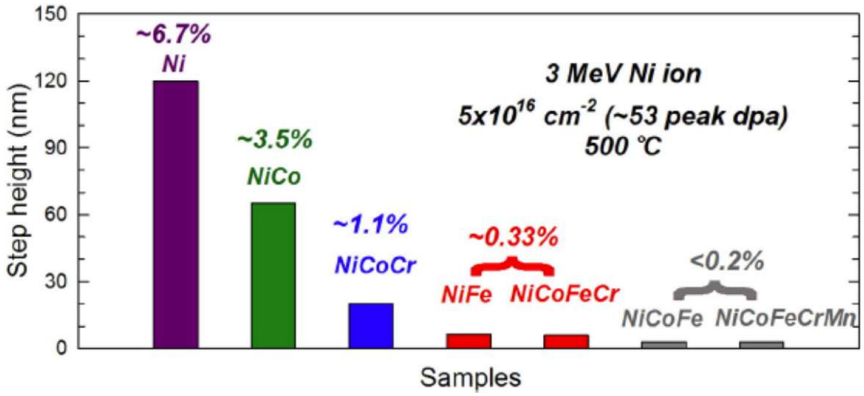

Figure 2.22: Measured swelling in six Ni based alloys after ion implantation of 53 dpa at 500 °C, measured by step height using optical profilometry. Reproduced from reference [14].

2.5.2 Defect clusters

Radiation damage has a deleterious effect on material properties by changing the nature and density of crystal defects within them. Another way that HEAs have been found to resist deleterious property changes is by how these crystal defects are stored. Dislocation analysis through TEM micrographs have shown that the loops in more compositionally complex alloys are smaller and more numerous than in single element materials they are compared to [46, 142, 143]. This is important as it is the largest dislocation loops that cause the most embrittlement in materials [9], and so

if more of the point defects are stored in smaller loops, this will cause less property degradation during service. An example of these loop measurements is shown in figure 2.23, where histograms of loop size in Ni and NiFe are compared. Clearly NiFe is not an HEA, but if the beneficial effects of alloying can be even be seen in binaries then this is encouraging for more complex multicomponent systems.

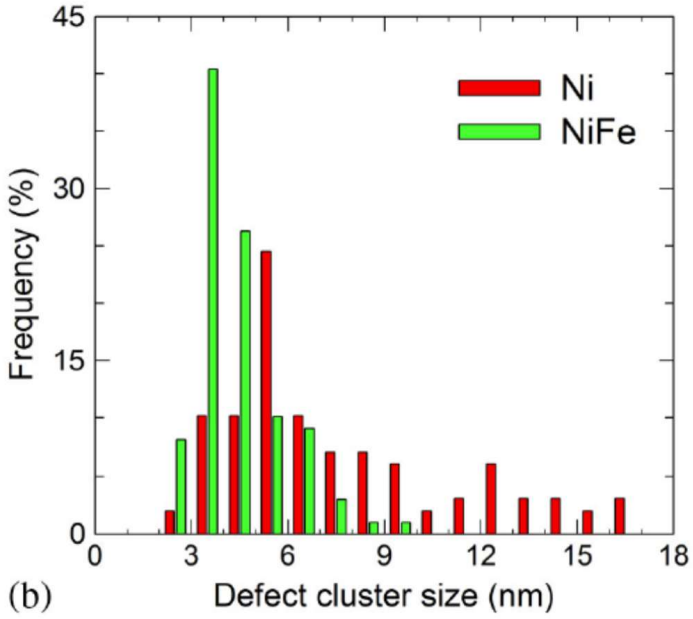

Figure 2.23: Statistical analysis on the size and number of dislocation loops in Ni and NiFe after 0.1 dpa of ion implantation. Reproduced from reference [143].

2.5.3 Radiation induced segregation

Radiation damage does not only alter the defect structures in materials, but can also alter their chemical and crystallographic structures [144, 145]. As there are still questions regarding the stability of the disordered structure of HEAs, a major concern is that radiation will induce chemical segregation (Radiation Induced Segregation or RIS), which could lead to phase separation and a degradation of the HEAs properties. The first HEA to show RIS was CrMnFeNi after 10 dpa of 3MeV Ni

ions at 500 °C. Kumar et al. [146] used STEM EDX to measure complete depletion of both Fe and Ni at the grain boundary, resulting in precipitation of CrMn, seemingly in line with that discussed in section 2.2.3.2 [97, 101]. However, in a subsequent paper by the same group [46] they found no segregation after 10 dpa at 700 °C. These two results have not been explained or rationalised, but it could have been due to the effect of temperature, some processing difference between samples, or poor selection of site for investigation.

More recently a paper was published focusing solely on the RIS within HEAs (which features at least one common author with the two papers discussed above [13]). This paper tested several Ni based HEAs (increasing in complexity from the FeNi binary to the CrMnFeCoNi quinary) with Electron Energy Loss Spectroscopy (EELS). Their results showed that the HEAs follow the trend of austenitic stainless steels in obeying the inverse Kirkendall mechanism (that there will be enrichment of fast diffusing species at sinks, such as grain boundaries or dislocation loops), though at a seemingly slower rate when compared to conventional steels. These observations were supported by Molecular Static (MS) simulations [13]. In 2019 A BCC alloy of VCrTaW was observed to phase separate slightly on implanting up to levels of 8dpa at 1073K. No dislocation loops were observed to form but there was a slight hardening measured with nanoindentation [147].

2.5.4 Mechanisms of radiation resistance in HEAs

It has been shown that certain HEAs possess some resistance to radiation damage, at least when compared to pure metals. A big challenge facing the community is explaining the mechanistic origin of this resistance, so that it can be applied to future alloy designs

2.5.4.1 Diffusion

One explanation of HEAs radiation resistance is one that focusses on the diffusion of interstitials. Lu et al. [140] used Molecular Dynamics (MD) to simulate the diffusive behaviour of defects, and found that in FCC metals self-interstitials diffused primarily along the $\langle 110 \rangle$ direction, i.e. diffusion is one dimensional (see figure 2.24, image a). However, as alloys become more complex (i.e. contain more principle components) the mean free path becomes shorter, meaning interstitials diffuse in a three dimensional manner (figure 2.24 images b and c).

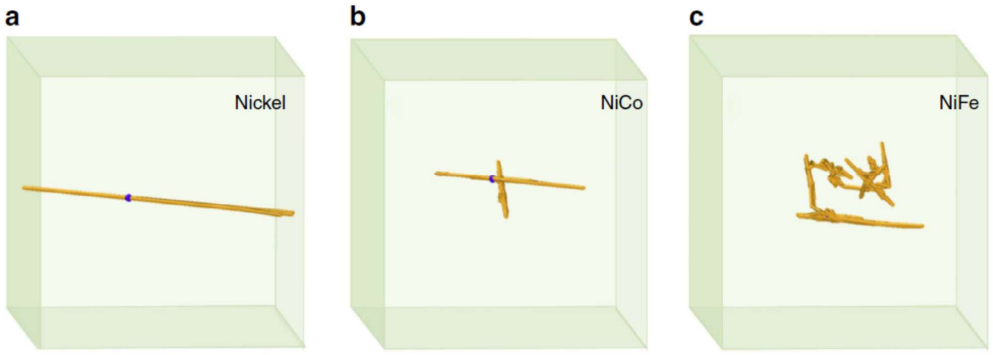

Figure 2.24: Results of MD simulations predicting the diffusion of a self-interstitial through various FCC alloys. In elemental Ni (a) and two equiatomic Ni binaries (b) and (c). Reproduced from reference [140].

In general interstitials diffuse more rapidly than vacancies, which over the relevant time scales are effectively static [148]. By reducing the mean free path of interstitials, the window at which a recombination event can occur is increased, and thus the effective rate of point defect injection is decreased. In ion-implantation this effect will be exaggerated, as the damage layer is so thin, and the bombardment so rapid, the slower diffusion will also give more opportunities for defects to be annealed out by subsequent cascades. Whether the diffusion of interstitials is slowed

sufficiently to impact the rate of damage accumulation during neutron irradiation is currently unknown.

2.5.4.2 Dislocation mobility

Another proposed mechanism, which in particular relates to the agglomeration of dislocation loops, is that the addition of more primary components acts to reduce the mobility of dislocations through the material. This would mean that their growth would be suppressed, explaining the observations of high densities of small dislocation loops in multicomponent materials. This mobility-based theory is supported by Molecular Dynamics carried out by Granberg [143]. It is not clear how this mechanism may relate to, or interact with, the diffusive one previously explained.

2.5.5 Radiation damage summary

To summarise, data collected so far shows that HEAs show a better resistance to radiation damage than their elemental counterparts, both in terms of void induced swelling and point defect clustering. They also show better phase stability than some nanostructured materials that have been previously been suggested as radiation resistant materials [149]. Current explanations of this resistance are based on the slow diffusion of point defects, leading to increased recombination events, and on the reduced mobility of dislocations, which inhibit the growth of dislocation loops. The majority of work done so far has focused on Ni based equiatomic alloys, and in particular the binaries and ternaries that are compositionally similar to austenitic steels, and so future work should focus on expanding from this region and testing whether the observations made up until now are applicable to other HEA systems with a greater numbers of components. A more up to date review on the properties of irradiated HEAs can be found in reference [150].

2.6 Research Aims for this work

In this review it has been shown that there are many hypothesis on HEAs, and that most lack thorough validation. It has also been shown that the method of alloy fabrication can have profound effects on the microstructures achieved. The purpose of this thesis is to develop a better understanding of the phase formation within refractory HEAs in order to develop one with potential application as a PFC in a fusion reactor. In order to accomplish this several research aims have been identified:

1. Determine what the controlling factors are in determining whether BCC, FCC, or HCP phases are found to form in refractory HEAs.

2. Assess whether the thermodynamics underpinning the Ω parameter are controlling the formation of single-phase alloys, and whether alloys with higher values of Ω have more stable solid-solution microstructures.

3. Building on the work by Molnar and Lv [109, 110] who investigated the effect of cooling rate on as-cast HEA microstructures, the variation in arc-melted billets will be examined. The nature of arc-melting means a variation in cooling rates are generated through individual billets, and the effect of this on microstructure will be looked at.

4. The suitability of any low-activation refractory HEAs for fusion will be investigated by measuring their response to ion-implantation. Research has shown FCC HEAs have good resistance to radiation damage, but as of yet there is not as much evidence collected for relevant BCC systems.

5. A new method of nanoindentation shall be tested on multiphase materials in order to determine their properties separately. Although bulk specimens of

multiphase materials have value, there is not yet a reliable method for understanding phases' individual properties.

These research aims will be investigated by fabricating alloys of various compositions and billet sizes, all within the TiVZrHfTa system. Their microstructures will be investigated before and after annealing with several characterisation techniques, and their mechanical properties shall be measured with nanoindentation after ion-implantation in order to test the effect of radiation on these HEAs. The full details of all these experimental methods are given in the next chapter.

Chapter 3

Experimental Methods

3.1 Arc Melting

The first step in any experimental analysis is fabricating samples. In this project all samples were manufactured by arc melting, a procedure which has dominated the research that was then possible. In this section the general method of arc melting is described, as well as many of the precautions taken so as to try and guarantee the best quality material.

3.1.1 Melting Procedure

Raw materials were purchased from Goodfellows as high purity lumps, with composition specified in table 3.1. Amounts were weighed out to the nearest 0.1g before being cleaned in acetone and then dried.

Element	Purity (wt%)
Ti	99.99
V	99.95
Zr	99.20
Hf	97.00
Ta	99.90

Table 3.1: Table listing the advertised purities of the metal feedstock used to manufacture alloys used in this thesis.

The raw materials were combined in the molten state using an Arcast 200 arc-melter. This machine, like any typical arc melter comprises a water-cooled copper crucible and a tungsten electrode which directs an electron plasma arc, all of which is contained within a vacuum chamber which can be flooded with argon, or a reducing gas such as hydrogen; a schematic of which is shown in figure 3.1. The raw materials are then placed in the crucible, and the arc is used to melt the material. Once the user is satisfied that all the raw material is molten and well mixed they turn the arc off and allow the melt to solidify. There are three important considerations that must be made when arc melting: the temperature and cooling rates through the melt, the mixing of the melt, and any sources of impurities that may contaminate the melt.

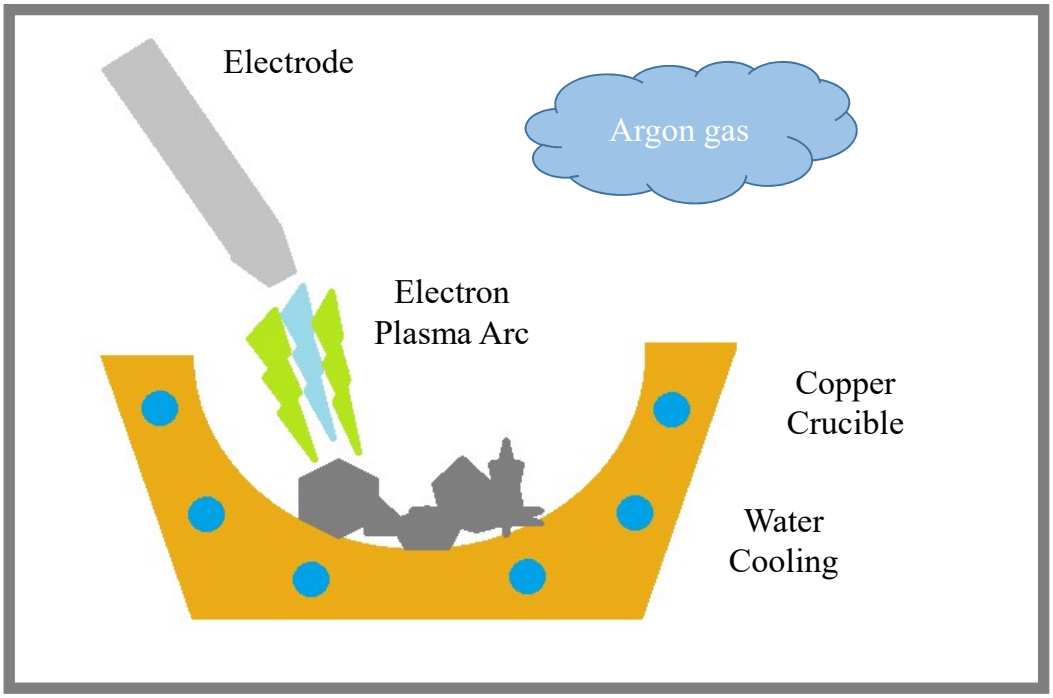

Figure 3.1: Schematic showing the primary components of an arc-melter, with the grey box representing the vacuum chamber.

3.1.2 Temperature considerations during arc melting

There is no way to measure the temperatures reached inside the arc melter, and the only control the user has is to change the intensity of the arc by using an attached foot pedal. This means there is a high amount of irreproducibility between melts in terms of what temperature is reached and how long the melt is molten for. The determining factor for melt time is how long it takes to liquefy the element with the highest melting point. If a melt contains refractory elements then insufficient melting can lead to inclusions of un-melted material, such as the tantalum inclusion shown in figure 3.2. This problem is harder to avoid in larger melts as un-melted solid is more difficult to find in deeper melt pools.

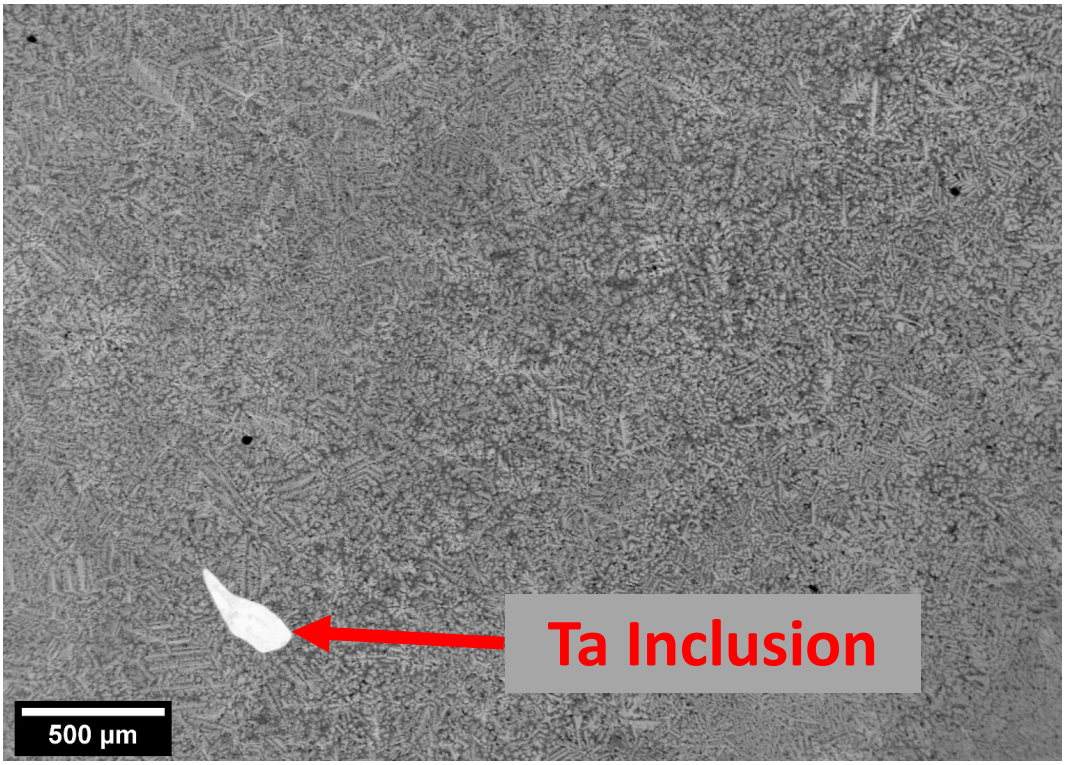

Figure 3.2: Back-scatter SEM image of a tantalum inclusion in a 10g billet of arc-melted equiatomic TiVZrHfTa. The inclusion is present as the melt did not maintain a high enough temperature for long enough to guarantee complete melting.

The cooling rate of the melt is also not controllable. Water from the mains is pressurised and pumped through the crucible and around the electrode at a flow rate of $\sim 80\,\mathrm{l\,min^{-1}}$; this is essential in order to prevent the heat generated from damaging the machine during operation. The temperature of the coolant will vary day to day (between 5 and 20 °C based on the season [151]), and the rate of heat extraction from different parts of the crucible also varies.

3.1.3 Liquid phase mixing during arc melting

A major concern in many publications that use arc melting is that the liquid material is well mixed. To this end it is common to remelt billets several times and flip them

in-between. All samples in this thesis were flipped and remelted at least once, but the primary method of mixing was the natural diffusion of the liquid metal, which is accelerated by the agitation caused by the arc, and also by using the electromagnetic stirring function built into the crucible. This is a coil which applies a small field to the melt and acts to stir it. Over the course of this project different regions of billets were analysed for composition with electron microscopy, and no macrosegregation was ever observed in the metallic elements.

3.1.4 Contamination considerations during arc melting

Contamination in the melt should be avoided, as it can introduce unwanted phases. This issue is made more challenging as neither X-ray diffraction nor scanning electron microscopy may not be able to reliably resolve or identify small carbides or oxides, particularly if these are concentrated in a region of the billet which is not being analysed. The main sources of impurities in the chamber are traditionally the material that is being melted; it is for this reason that high-purity raw material is used and why it is cleaned thoroughly prior to melting.

A secondary source of contamination is dirt or residual material stuck on the crucible walls; the solution for this is careful cleaning of the crucible after each melt, including the removal of any solvents used to clean the crucible. The third source of impurities is the quality of the vacuum, which was assessed by comparing as-received titanium metal to two arc-melted titanium billets which were melted under either a high or low-vacuum condition.

For the first melt the chamber was allowed to pump down to 3.40 Pa before being flooded with argon; this took approximately 30 minutes (referred to here as “quick vacuum”). For the second melt the chamber was left to back down overnight before

being flooded with argon (a "long vacuum"). The final chamber pressure after this was 2.40 Pa, which is the practical limit of the vacuum system. The samples were sent to AMG Superalloys for chemical analysis, in particular looking for hydrogen, carbon, nitrogen, and oxygen, and sulphur which are measured using the combustion infrared detection technique, the results of which are shown in table 3.1.4. AMG use a combination of LECO combustion analysis and X-ray Florescence, for more information see the AMG website [152]. Although these are the most accurate bulk measurements available, they are still not completely reliable. X-ray Florescence uses the same emission effect as discussed in section 3.4.1, while LECO combustion is not readily able to detect trace amounts of hydrogen, despite AMG reporting these concentrations.

Element	As-received	Quick Vacuum	Long vacuum
Ti	99.830	99.940	98.400
C	0.111	0.020	1.500
S	0.008	$\leq$0.001	0.009
N	0.008	0.001	0.038
O	0.049	0.032	0.054
H	17ppm	15ppm	27ppm

This test sufficiently demonstrated that the quality of the vacuum was high enough that it should not be the limiting factor on the cleanliness of the melt. The high carbon content in "Long Vacuum" sample is likely due to contamination in the feedstock metal, or unevaporated acetone that had been used to clean the crucible and feedstock metal.

3.1.5 Sample Preparation

All samples were sectioned using a Buehler IsoMet Low Speed Precision Cutter with a Diamond Blade, or by Electrical Discharge Machining in the Oxford University

Physics Workshop. Samples were then ground to remove any mechanical damage or oxide with 120-4000 grit grinding paper. They were then polished by hand with colloidal silica for at least 30 minutes.

3.2 Computational Modelling

3.2.1 Finite Element Analysis

Final Element Analysis (FEA) has been used to assess the thermal transport during arc-melting, the programme and package used was COMSOL v5.4 with the Thermal Transport module. For further information on the finite-element method see reference [153]. All material parameters were taken from COMSOL's built-in material library. Further details of the model are given in chapter 5 where the results are presented.

3.2.2 Matlab

Data processing was almost entirely conducted using Matlab [154]. In addition, Matlab was used to write an optimisation algorithm that made use of the in-built *fmincon* function. This is a non-linear optimisation code [155] run with a sequential quadratic programming method, which iteratively optimises constrained non-linear functions, such as the Ω parameter which is used to assess the thermodynamic stability of HEAs. The advantage of using the *fmincon* functions is that is ensures that the bounds and constraints are satisfied at each step, and is able to deal with *Nan* or *Inf* results, this gives the code a level of robustness, although it does not lend itself to being scaled up to larger problems [156]: luckily the optimisation algorithm does not require scaling. The matlab algorithm and associated functions are shown in

appendix B.

3.3 X-ray Diffraction

X-ray powder Diffraction (XRD) is a technique used to give crystallographic information about a sample, including crystal structures, lattice parameters, crystallite size, and elastic strain. It does this by by illuminating the sample with monochromatic X-rays, and then varying the angle of incidence between the emitter, sample, and detector through a geometric range which is typically referred to as 2θ. At certain angles diffraction occurs resulting in a peak in measured intensity. The position of the peaks are characteristic of the lattice structure, while relative peak intensities are related to chemistry and phase proportion, and peak broadening is related to elastic strain. For full details of this technique see Hammond [157].

3.3.1 XRD Data Analysis

Peak identification was achieved by comparing experimental data to simulated XRD traces using the CrystalDiffract software [158]. This allows multiple traces to be overlaid and their crystal structures and chemistries changed until a good fit can be found. Once the phases have been identified Highscore+ [159] can be used to to apply a Rietveld fit to the predicted phases, which can allow for extra information to be extracted, such as: volume fraction, crystallite size, and elastic strain.

3.3.1.1 Volume fractions

Volume fractions are calculated by comparing the relative areas under the curves for each phase, taking into account the predicted relative peak heights due to the chemistry of the phases being fitted. For this reason it was important to give the

best possible guesses for each phase, these initial guesses are listed in table 3.2. It should be noted that there are large yet unquantifiable errors when measuring parameters using this method: for example, in chapter 6 if the volume fraction of rocksalt phase is calculated for pure ZrC rather than the adjusted compositions determined with Atom Probe analysis, then the calculated volume fractions increase by approximately 5vol%. Throughout this thesis no errors are given with volume fraction values because they are difficult to quantify; however, a conservative estimate of error would be between 5-10%.

Parameter	BCC1	BCC2	HCP	Zr containing Rocksalt Phase	Non-Zr containing Rocksalt Phase
Lattice Parameter (Å)	3.24	3.35	a=3.20 c=5.12	4.5	4.5
Chemistry	Ta	Ta	Hf	taken from APT results (table 4.4)	TiC

Table 3.2: Table comparing lattice parameter and chemistry used for the intial guesses of phases when analysing XRD data.

3.3.1.2 Crystallite Size

Crystallite size and elastic strain (as caused by dislocations) can be extracted from the amount of peak broadening observed in each phase; this means that the quality of the fit achieved between the theoretical trace and the experimental data is even more important than when extracting volume fractions, as peak height and width both have to be matched closely. For this reason these values are less reliable than for those for volume fractions, although they are made best use when comparing samples as in chapter 6. Another important distinction is between *crystallite* size and *grain* size: the former being related to the average diffracting volume, which

is not necessarily the same as the latter, particularly for phases where grains are non-spherical or potentially contain sub-grains.

3.3.2 Errors and Assumptions

In order to use XRD and extract full quantitative data from it there are several underlying assumptions that must be understood. Those relevant to the data in this project are briefly outlined here.

This techniques full name is X-ray powder diffraction, and the word powder is important as diffraction depends on several variables and in order to simplify the experimental set-up fine grained powders are preferred. Using powders guarantees that at every point during the experiment at least one grain is being illuminated at every different orientation and that there are no effects of texture. If analysis is being carried out on bulk samples then it is important that the microstructure is suitably fine grained that this assumption can still be made; if the grains are too large then there may be absent peaks, or peaks may have lower intensities than would be expected based on the material. The larger the grains the worse the data. If a single crystal is analysed by this technique then the peaks visible will depend on the crystal's orientation relative to the equipment.

Another assumption is that the X-ray source only emits monochromatic light, however this is not strictly true as sometimes the source releases Kα and Kα1 radiation. Their energies are both quite similar and so this can be seen in the data as peak splitting, whereby the peak has two centres. This effect can be see in figure 3.3 where the effect has been circled. As this is a source effect it does not relate to the sample and can be ignored.

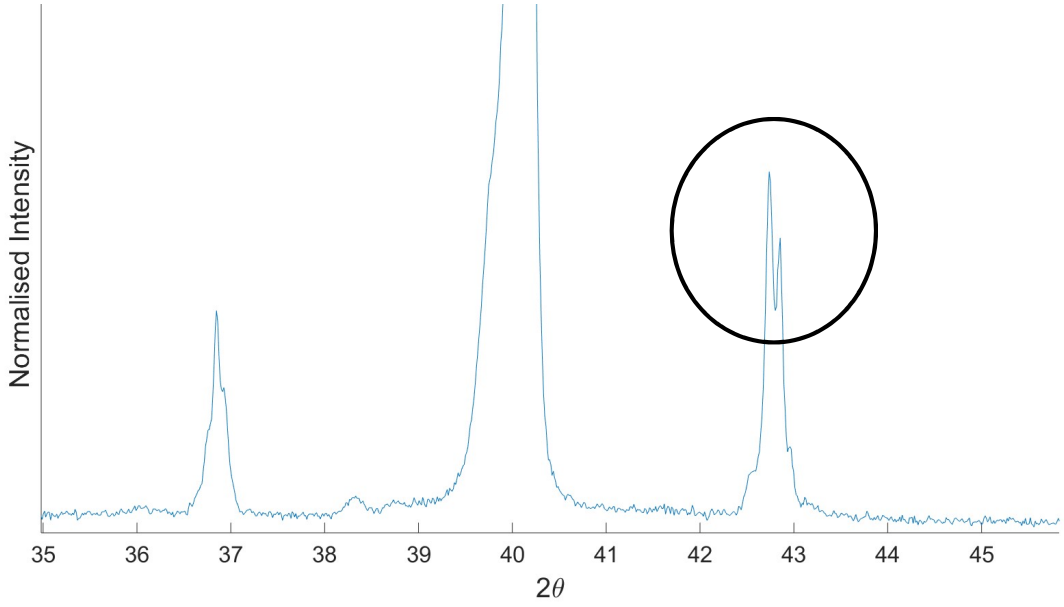

Figure 3.3: Clipped XRD data demonstrating the effect of peak splitting. The peak where this is most clearly visible has been circled.

A final source of error is due to the putty that is used to secure the sample in the holder. Occasionally the X-ray spot illuminates the putty and erroneous peaks are found in the data. An XRD trace of the putty on its own is shown in figure 3.4; it can be seen the largest peak occurs at 29°. When peaks relate to the putty instead of the sample they have been marked with a red X.

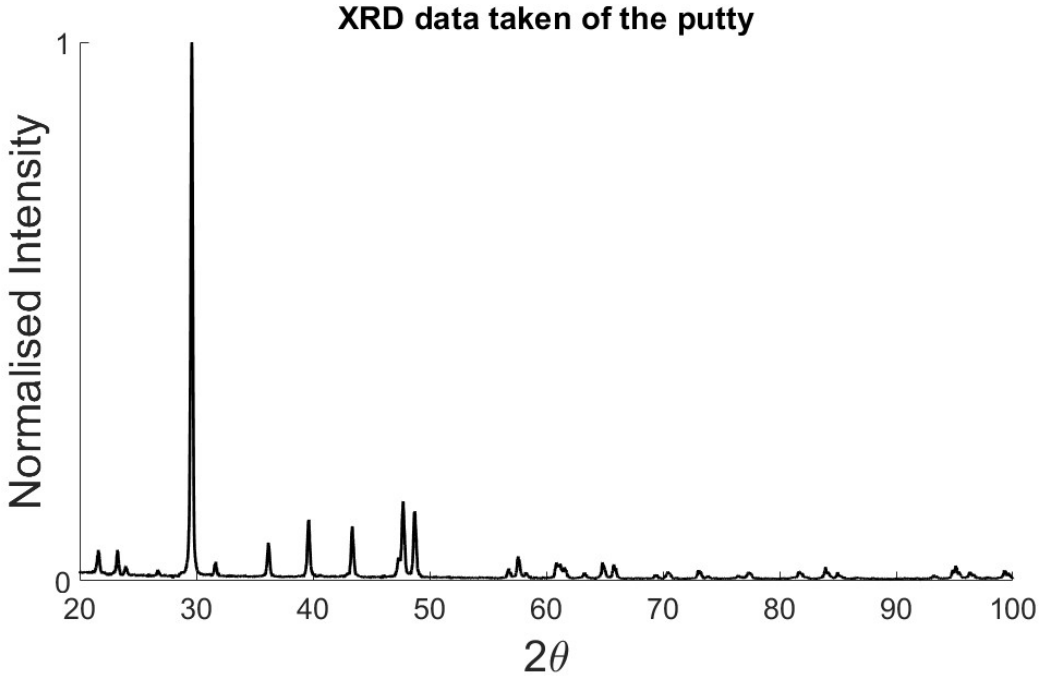

Figure 3.4: XRD data taken of the putty used to secure bulk samples. The largest peak at 29° is sometimes seen in actual data.

3.3.3 Machine Details

Two different XRD machines were used in this project. The first is a Rigaku Miniflex, using a copper Kα source at 40kV and 15mA. The second is a Panalytic Empyrean, also using a copper Kα source but at 40kV and 40mA. The latter machine was operated by Guillaume Matthews. The Empyrean is a superior machine with higher current and improved detector efficiency, leading to a higher signal-to-noise ratio than for the Miniflex.

3.4 Scanning Electron Microscopy

Scanning electron microscopy (SEM) is used to analyse and image microstructural features in polished materials. They are comprised of an electron source, accelerator,

and focussing lenses that allow the beam to be condensed into a spot on the sample and then scanned across it. Detectors inside the vacuum chamber are set up so as to record different signals from each point and thus build an image of the scanned area. The types of signals relevant to this thesis are: secondary electrons, back-scattered electrons, and electron induced X-ray emission.

Each of these signals is generated by a different interaction of the beam with the sample, and so each signal has a characteristic interaction volume and thus a characteristic resolution. Secondary electrons are inelastically scattered from the sample atoms by the beam; their emission is sensitive to the angle between the beam and the surface and so show good topographic contrast. Back-scattered electrons originate due to elastic scattering by nuclei in the material, this means their intensity provides compositional contrast. In addition, due to the effect of channelling (whereby certain crystallographic directions have a different penetration depth than others) orientation or channelling contrast is also possible under the correct conditions. Back-scattered electrons can also be used to determine grain size and crystal structure, which is discussed further in section 3.4.3.

The final form of scattering relates to X-ray emission: some beam electrons give enough energy to core electrons that they are emitted, leaving behind a hole. An outer shell electron then falls back into this lower energy state resulting in the emission of an X-ray, the energy of which will be the difference between the two electron states. As the various shell energies are sensitive to atomic number, each element has a unique fingerprint of X-ray energies it will emit, allowing composition to be identified by measuring the energy of the emitted X-rays using either and Energy Dispersive (EDX) or Wave Dispersive (WDX) detector.

3.4.1 Energy Dispersive X-ray spectroscopy

Energy Dispersive X-ray spectroscopy (EDX) is a relatively quick, easy, but less accurate method of quantifying composition in different phases. The detector works by measuring the conductivity of a Si chip, which changes based on the number of electron-hole pairs that are created by interactions with X-rays. Higher energy X-rays mean more charge carriers and thus a higher measured conductivity. A window is placed between the detector and the sample to reduce the noise in the detector, however this has the effect of blocking low energy X-rays such as those characteristic of lighter elements such as C, N, and O.

All EDX analysis was done using Oxford Instruments AZtec software, which has several operating modes: Point&ID for quantitative spectra analysis at a point or over an area, Linescans for quantitative analysis along a specified line, which can also be broken down into a row of Point&ID measurements, and finally mapping for qualitative information over an area. Each of these techniques collects an energy spectra (measured in keV against counts per second per eV) and then calculates concentration from the relative peak intensities. When analysing lines and maps there are three methods built into AZtec - line/map takes the spectrum at each pixel and segments it according to which elements it is analysing for: this is acceptable when there is good peak separation, but when there are peak overlaps, as there are between Hf and Ta, the user should select a TruLine or TruMap method. These are algorithms which predict the peak shape of each element and thus deconvolutes overlapping peaks from one another and also from the background signal. A final analysis type is QuantLine and QuantMap, whereby the spectra at each point is deconvoluted, and peak heights are analysed so as to give concentrations in either weight or atomic percent. There are several peak overlaps pertinent to this thesis: C

and Ta, N and Ti, O and V, and Hf and Ta: for this reason TruMap and QuantLine methods have been used throughout. For more information, see the relevant the Oxford Instruments web page and user manual [160].

3.4.2 Wave Dispersive X-ray Spectroscopy

Wave Dispersive X-ray spectroscopy (WDX) is a slower and more complicated method of collecting the same information as EDX, but with an improvement in energy resolution and range that allows for more accurate compositional information of all elements, including lighter ones. It works by using a crystal to diffract X-rays of a specific wavelength onto a static detector; this crystal is then rotated across an angular range in order to diffract X-rays of different wavelengths onto the detector; a schematic of this is shown in figure 3.5 which is reproduced from [161].

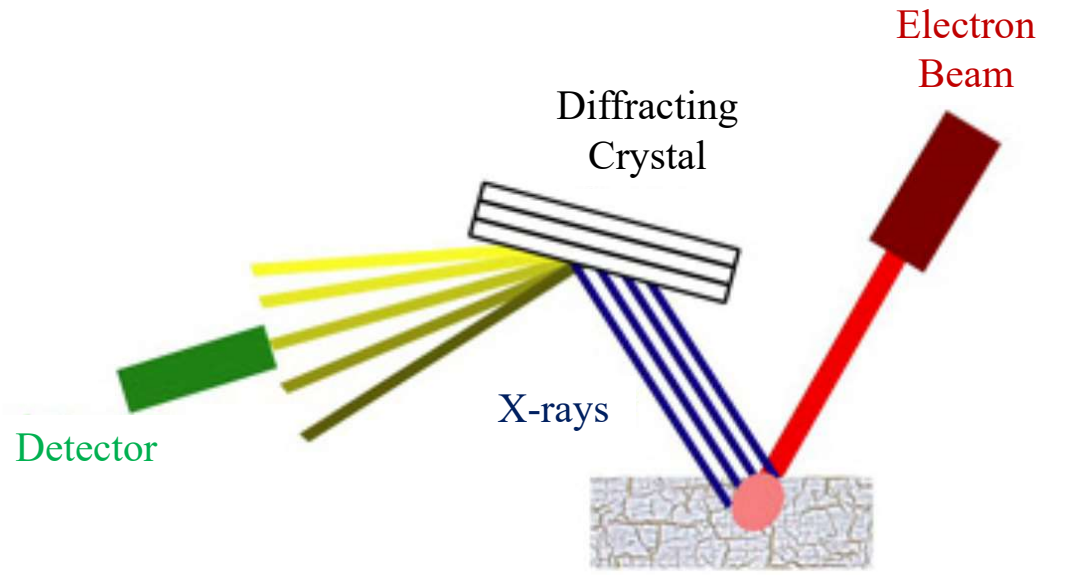

Figure 3.5: Schematic of a WDX spectrometry unit reproduced from [161].

The difficult in using WDX is that the peak positions are not fixed, and are susceptible to movements in angular space due to imprecisions in the detector motion.

For this reason it is important that peak positions and widths are measured on a set of standards prior to each session in order to ensure that when quantitative analysis is undertaken, the peak and background intensities are correctly measured. This workflow means that WDX is not a useful technique if the user is unsure what elements are present in their sample.

3.4.3 Electron Back-Scatter Diffraction

Electron Backscatter Diffraction (EBSD) is an SEM technique capable of identify grain orientations and crystal structures. As back-scattered electrons leave the sample some leave at the Bragg angle and undergo diffraction. This results in a Kikuchi pattern forming which is comprised of bands related to the system geometry, the crystal structure, and the underlying orientation of the crystal. In order to maximise the backscattered signal the sample is highly tilted, typically to 70°. A detector with a phosphor screen is then used to collect the Kikuchi pattern. Each pixel on the sample has its own Kikuchi pattern and is separately analysed in order to build a map of orientation and phase. A weakness of EBSD is the relative insensitivity to lattice parameter compared to XRD. This means EBSD is only useful for distinguishing between dramatically different phases: two BCC phases that have lattice parameters within 20% cannot be distinguished. The EBSD detector also uses diodes placed around the phosphor screen to pick up fore-scattered electrons which can provide unquantified crystallographic resolution in what is known as an "Argus image". These are used occasionally in this thesis as an alternative to secondary or back-scatter signal images.

3.4.4 Machine Details

All EDX, EBSD, and EM images were collected on a Zeiss Merlin SEM at operating voltages of 5, 10, or 20 kV. An Oxford Instruments EDS attachement and a Bruker EBSD detector was used to collect the relevant data. Images of porosity in chapter 6 were collected on a Zeiss Crossbeam 540. The WDX analysis was conducted by Dr. Phil Gopon on a Cameca SX-FE EPMA (Electron Probe MicroAnalysis) machine with five WDS spectrometers and Bruker EDS unit.

3.5 Atom Probe Tomography

Atom Probe Tomography (APT) is a method of characterisation which provides high spatial and chemical resolution, superior to that of any electron microscopy technique. It is used to provide 3D reconstructions with an XY spatial resolutions of up to 0.2nm [162], a Z resolution of up to 0.06nm [163], and can detect elements of any mass with a sensitivity of up to 100 atomic parts per million [162].

3.5.1 Basic Principles

Atom Probe Tomography uses highly controlled field evaporation to deconstruct a sharp needle-shaped specimen atom by atom. This is done by applying a static electric field, and then pulsing either an additional field or a laser (all APT data shown in this thesis was collected in laser mode). As the oscillating signal reaches its peak a single atom is ionised and removed from the tip. These ion are then accelerated towards a detector which records the time of flight and and impact position. Time-of-flight is used to calculate the mass-to-charge ratio and therefore chemistry of each ion, while the impact position is used to calculate the ion's starting position

on the needle [164]. A schematic of an APT machine is shown in figure 3.6 which is reproduced from [165].

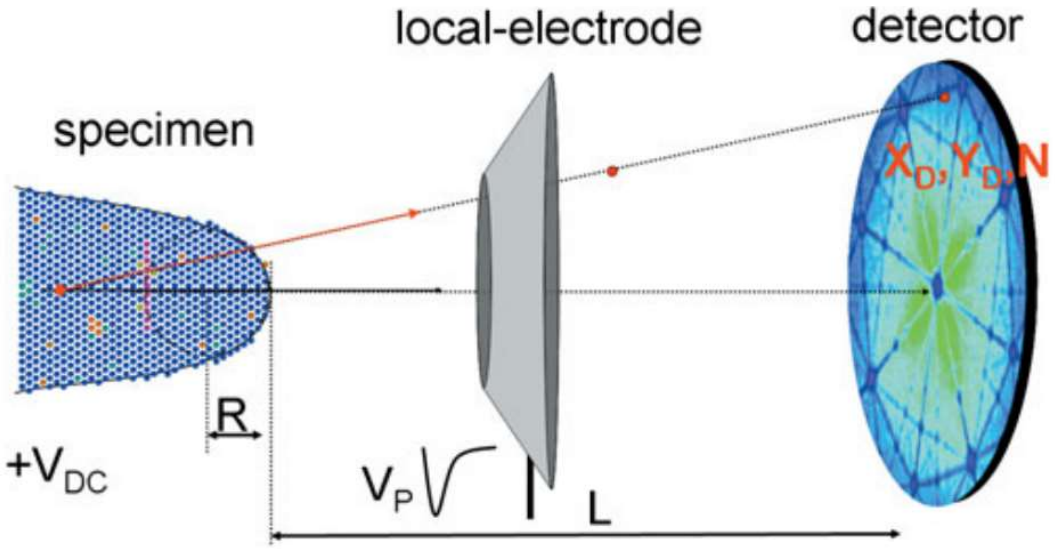

Figure 3.6: Schematic of an Atom Probe Tomograph showing left to right: a sharp needle-like sample, an accelerating electrode, and a position sensitive detector. Reproduced from [165]

3.5.2 Sample preparation

Atom probe needles can be prepared either by electropolishing, or in the case of this work, Focused-Ion-Beam (FIB) milling. This technique uses an ion beam to either remove material with Ga ions, or deposit other elements such as Tungsten, in order to prepare samples of precise shapes at the micro-scale. The work flow of FIB preparation is shown in figure 3.7 and is to: select the region or phase of interest (A.); deposit a protective layer of Tungsten and mill out trenches so as to isolate a free cantilever of material (B.); remove the cantilever from the sample using a micromanipulator (C.); progressively attach and section segments of this cantilever onto sample posts (D.); finally use a low energy Ga beam to sharpen and polish the segments into needle shapes (E.). The protective layer of Tungsten, and the low

energy Ga ions at the polishing stage, are used so as to limit the number of implanted Ga ions in the needle.

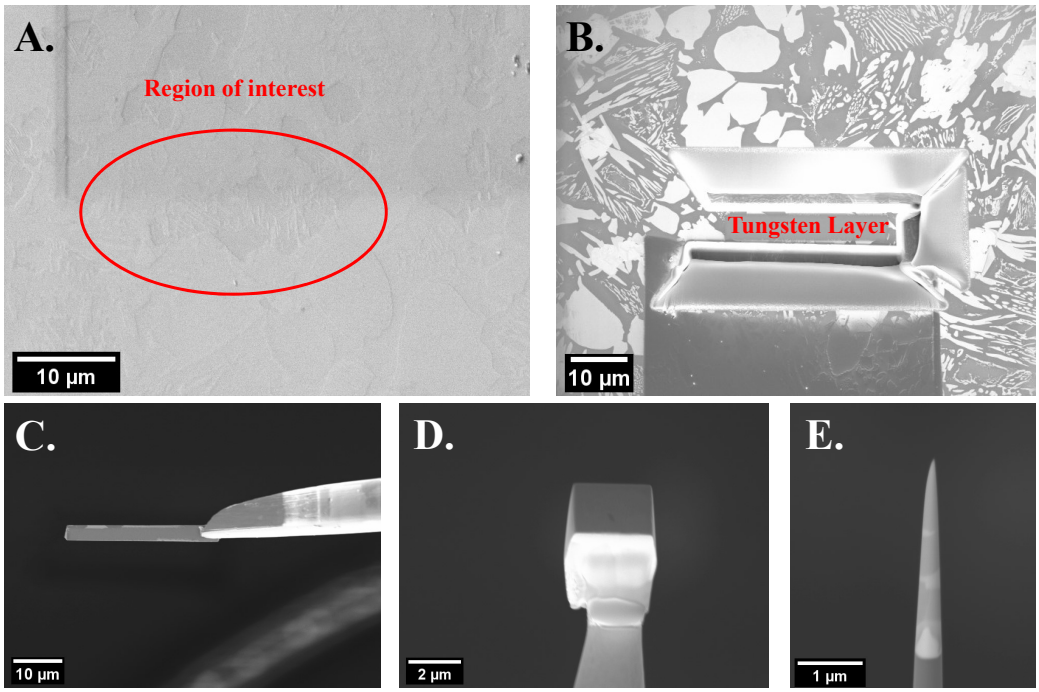

Figure 3.7: Electron microscope images showing the preparation of the Atom Probe Needles analysed in this project.

3.5.3 APT Data Analysis

As previously stated the time-of-flight data is used to generate a mas-to-charge ratio for each ion. This data is then represented in a mass spectra, which the user must range in order to identify which peaks relate to which ions; difficulties occur when different species have very similar mass-to-charge ratio, for example Zr^{++}= 45.6Da, while Hf^{++++}= 44.6Da, and these problems are compounded when it is considered that all these atoms have lighter and heavier isotopes that will also overlap. The solution is take the natural abundancies of the isotopes into account and to deconvolute the the peaks in the mass spectra: allowing bulk compositions to be more accurate.

For this work the algorithm AtomProbeLab v0.1.4 has been, which is based on the methods proposed in [166] and [167].

3.5.4 Machine Details

The FIB and APT in this thesis was conducted by Dr. Benjamin Jenkins on a Zeiss N-Vision 40 and a LEAP 5000XR, operated at 50K with a Laser energy of 50pJ oscillating at 200kHz.

3.6 Indentation

Indentation is the easiest method of extracting mechanical properties from materials. It requires no sample fabrication other than a polished surface, and can be used to give information such as hardness and modulus dependent on the method used.

3.6.1 Microindentation

Vickers indentation has been used to calculate hardness for some samples. This is done by using a square-based pyramidal tip to apply a known force on a material. Measurements of the size of Vickers indent can then be used to calculate hardness according to equation 3.1. In this equation the factor of 0.189 is related to the area of a Vickers indent.

$$H = \frac{0.189 * P}{d^2} \tag{3.1}$$

H : Hardness (MPa)
P : Applied load (N)
d : Measured Diagonal of the indent (mm)

Microindentation was carried out on a Matsuzawa Seiki MHT-1 Micro Hardness Tester, while measurements of indent size were conducted on a Leica DM2700M optical microscope. The hardness values reported are averaged from indents placed in the centre of each sample, and are each the average of 15 total indents, three each made at 100, 200, 300, 500, and 1000gf. The errors given are the standard deviation of this data. The value of hardness calculated at each force was always self-consistent, demonstrating that the plastic zone of each indent was capturing a large enough volume to be immune from size effects.

3.6.2 Nanoindentation

Nanoindentation allows for mechanical properties such as hardness and elastic modulus to be extracted from a material as a function of depth. This is achieved by pressing into the surface with a diamond tip, sharpened into the shape of a triangular based pyramid, commonly called a Berkovich tip. If the precise shape of the tip is known then the load and displacement data can be converted into mechanical data for the material. The most commonly used methodology for nanoindentation is called the Continuous Stiffness Measurement (CSM), whereby an oscillating load is applied on top of the static load which allows for a measurement of elastic modulus to made as a function of depth: the methodology of CSM indentation is fully described in the paper by Oliver and Pharr [168]. The two most important equations for CSM indentation are those that calculate the values of hardness and modulus as functions of depth, which are shown in equation 3.2 and 3.3.

$$H = P_{max}/A \tag{3.2}$$

$$S_{unload} = \beta \frac{2}{\sqrt{\pi}} E_{\text{meas}} \sqrt{A} \qquad \text{where} \qquad \frac{1}{E_{meas}} = \frac{1-\nu^2}{E_{real}} + \frac{1-\nu^2}{E_{\text{i}}} \tag{3.3}$$

H	:	Hardness (Pa)
P	:	Load (N)
S_{unload}	:	Elastic Unloading Stiffness (Pa)
β	:	Numerical factor, usually taken as close to unity
E	:	Young's modulus, either the measured value (E_{meas}), the material's real value (E_{real}), or the modulus of the indenter (E_i) (Pa)
A	:	Area function (m^2)
ν	:	Poisson's ratio

The machine used in this project is an Agilent Technologies Nanoindenter G200, with an XP indenter head. The indenter tip was regularly recalibrated onto a sample of fused Silica with a known modulus of 72 GPa. Two methods have been used, the first is the CSM method, sometimes referred to as conventional indentation. The frequency of the sinusoidally oscillating load used is 45 Hz and the amplitude is 2 nm. The second nanoindentation method used is the Express method, which is explained in the next section.

3.6.3 Nanomechanical Mapping and Express Indentation

The Express method allows for large arrays of thousands of shallow indents to be made, which can be combined in order to create a map of mechanical properties. A single CSM indent requires several minutes to complete, whereas an express indent requires only seconds. This acceleration is achieved by no longer measuring mechanical properties as a function of depth, but simply indenting to a predetermined load or depth and making a single measurement. Further details of this technique are given in chapter 7.

3.7 Ion Implantation

As HEAs are being proposed as nuclear materials, it is important to understand how they may react to irradiation. In order to test this samples have been exposed to ion implantation before being analysed for their chemical and mechanical properties.

3.7.1 General Theory

Ion implantation is a method of simulating high-energy neutron damage in materials. The ion does not represent the neutron, but instead represents a primary knock on atom (PKA) that the neutron creates. The advantage of this technique is that ion implantation equipment is dramatically cheaper and more available than neutron sources, and that higher amounts of damage can be generated in shorter time frames in environments. The other key advantage is that the environments in ion-implantation units are easier to control than in neutron sources, such as fission reactors, where temperature, atmosphere, and neutron flux can vary based on position. It also allows for higher damage simulations to be run in a reasonable time frame

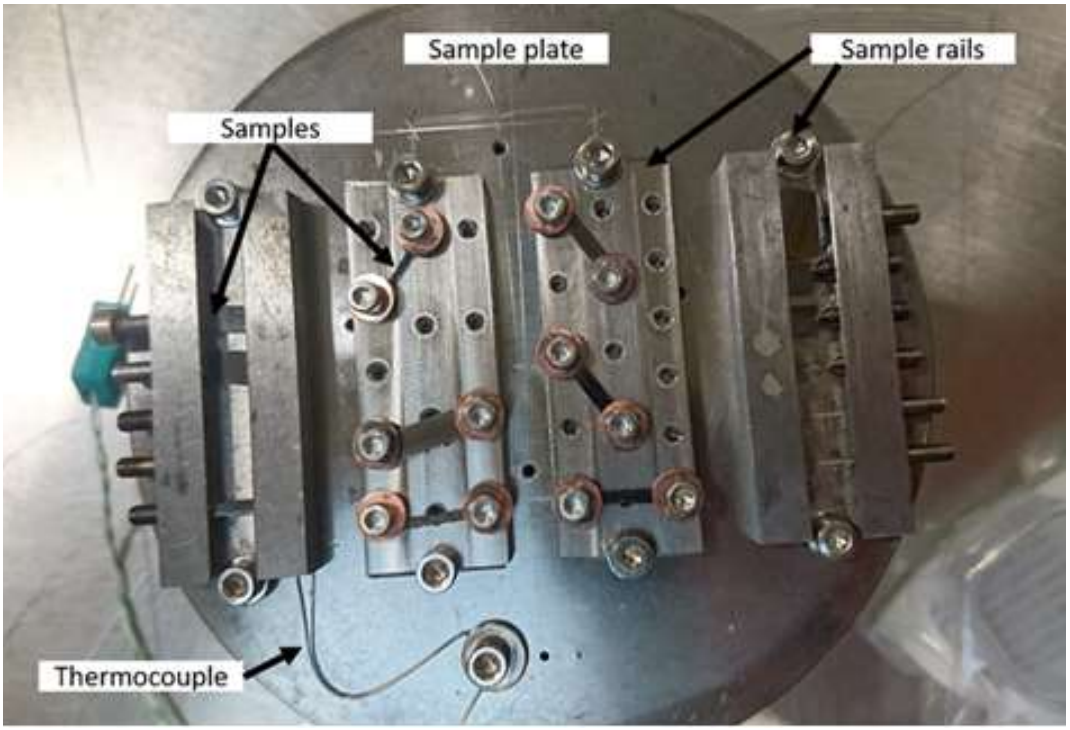

Figure 3.8: Photograph of the set of mounted samples at Surrey Ion Beam Centre, courtesy of Alex Leide.

(days rather than years), and at much lower cost.

3.7.2 Machine Details

All ion implantation discussed in this thesis was carried out at the University of Surrey at the National Ion-Beam Centre with the help of Dr Nianhua Peng. Samples are mechanically mounted on rails which are in turn bolted onto a temperature controlled stage. The rails come in different forms so as to be able to secure samples with different geometries in ways that do not apply too much stress through them. As the samples are mechanically secured it means that the covered areas act as a control: these two regions are referred to as "implanted" and "unimplanted". A photograph of a set of mounted samples on the rails and stage is shown in figure 3.8.

The Surrey Ion Beam Centre uses a 2MV Van de Graff implanter and the beam

is scanned over a 75mm diameter area. Implantation is undertaken at a vacuum of approximately 1×10^{-6} mbar. Thermocouples attached to a sample rail and also the back of the stage are used to monitor the temperature. The temperature for all irradiations discussed in this thesis was 500 ± 20 °C.

In order to determine the dpa implanted into the materials simulations were run using Stopping Range of Ions in Matter (SRIM) [169]. The methodology used was "Quick Calculations", which were run for 20,000 ions using threshold displacement energies of 30eV for Ti [170], 32eV for V [171], 35.5eV for Zr [172], and 43eV for Ta [173]. There was no threshold displacement energy available for Hf and so it was given a value of 35.125eV, an average of the values for the other elements. Standard densities were used for the dpa calculations in the pure materials, and a density of 8.9 g/cm^3 was used for TiVZrHfTa: which was determined using the Archimedes density method.

Chapter 4

Phase formation in the TiVZrHfTa systems

4.1 Alloy Introduction

This chapter discusses the microstructures of several of the alloys that are pertinent to this project. They have been analysed primarily by XRD and SEM, which has shown how cast microstructures evolve and phase separate both on initial cooling, and after heat treatments. Throughout this chapter samples are referred to by their sample codes for both the writer and reader's convenience. These codes work by taking the number of elements in the system (5, 4, or 3), whether the composition is equiatomic (eq) or optimised (opt), and in the as-cast (C) or annealed (A) states. Unless otherwise stated the heat treatment used is to be annealed for 24 hours at 1400 °C and then cooled to room temperature in the furnace. Examples of these codes are: a piece of optimised TiVZrTa in the as-cast state will be 4optC. A piece of equiatomic TiVZrHfTa in the annealed state is 5eqA. A matrix of samples and their codes is given in table 4.1 to be used as a reference.

	Equiatomic As-cast	Equiatomic Annealed	Optimised As-cast	Optimised Annealed
TiVZrHfTa	5eqC	5eqA	5optC	5optA
TiVZrTa	4eqC	4eqA	4optC	4optA
TiVTa	3eqC	3eqA	3optC	3optA

Table 4.1: Matrix of alloy codes discussed in this and other chapters.

The optimisation of alloy compositions is discussed in much more detail in chapter 5, but for this section it is sufficient to say that the optimised compositions are specific non-equiatomic compositions which have a higher value of Ω than their equiatomic counterparts. The target compositions of each alloy are given in the relevant sections for each alloy. All samples discussed in this chapter were cast by arc melting as 50g billets, which is the largest billet size discussed in this thesis.

4.2 The Rocksalt Phase

4.2.1 Introduction

For the majority of the project it was thought that the material manufactured by arc-melting matched the target composition, and did not contain any impurities. The reason for this was that optically billets appeared metallic, containing BCC and HCP phases, and previous experience with oxygen contaminated TiVZrHfTa was that when contaminated it was extremely brittle and could not be sectioned using equipment such as slow-saws. Despite this, in the final year of the project analysis showed that the assumed cleanliness of the samples was incorrect, and many of the manufactured samples contained impurities such as carbon, nitrogen and oxygen. The first sign of these impurities was from XRD data taken on the Empyrean machine, which has superior resolution compared to the Rigaku Miniflex which had

been used up until this point. The data produced by the Empyrean was higher resolution and so more peaks could be resolved and a new phase identified, a comparison of the data from the two machines is shown in figure 4.1.

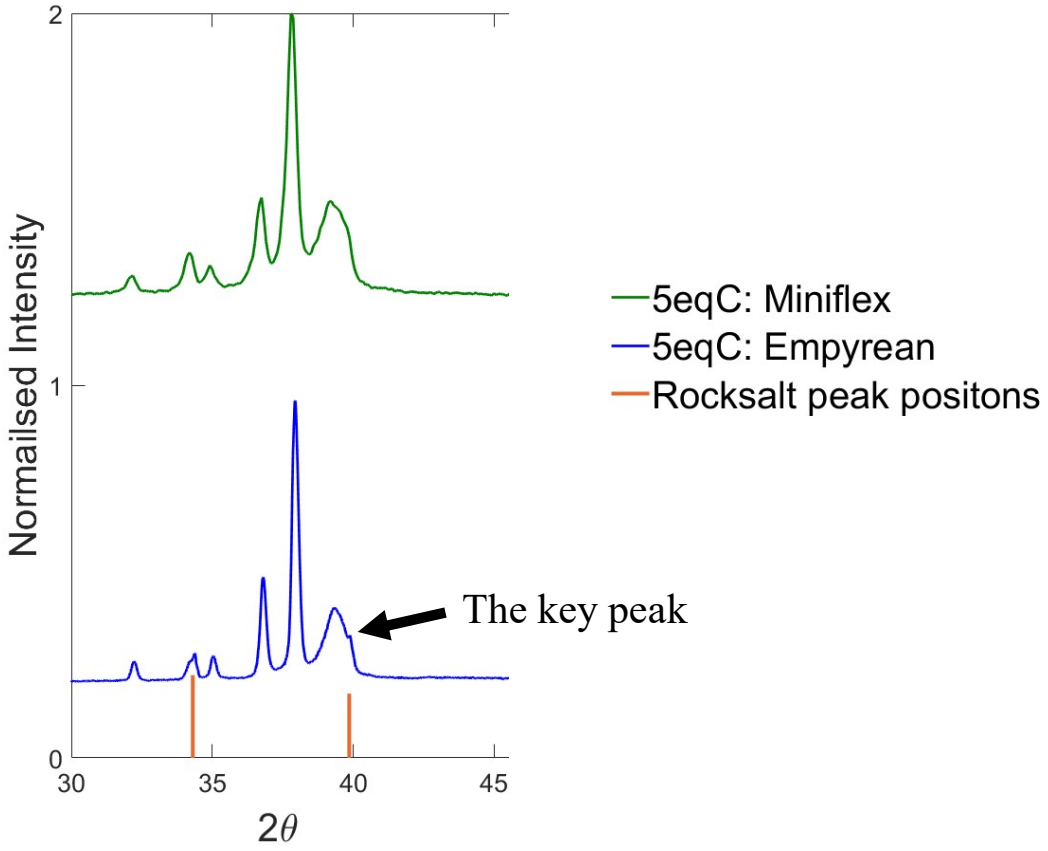

Figure 4.1: XRD traces of 5eqC taken in the Rigaku Miniflex (green) and also the Empyrean (blue). The latter data has superior resolution, and allowed the rocksalt phase peaks to be resolved and indexed.

The newly identified phase had the rocksalt crystal structure with a lattice parameter of ∼4.5 Å. This new phase was then verified with EBSD: figure 4.2 shows an EBSD phase map of 5eqA, on the left indexed for Ta-BCC and Hf-HCP only, and on the right indexed for these phases and also ZrC-Rocksalt. It can be seen that the matrix is consistently indexed as BCC, but that the precipitates are incorrectly indexed as HCP, unless the rocksalt crystal structure is offered. The reason for this

is that the Kikuchi patterns for HCP and FCC type structures are very similar due to the effect of pseudosymmetry [174, 175], and unless the correct phases are suggested then the software is unable to recognise that the HCP is incorrect. On this evidence alone it is not clear whether the precipitates are HCP or rocksalt, however the latter is corroborated by compositional information discussed in section 4.3.1.1.

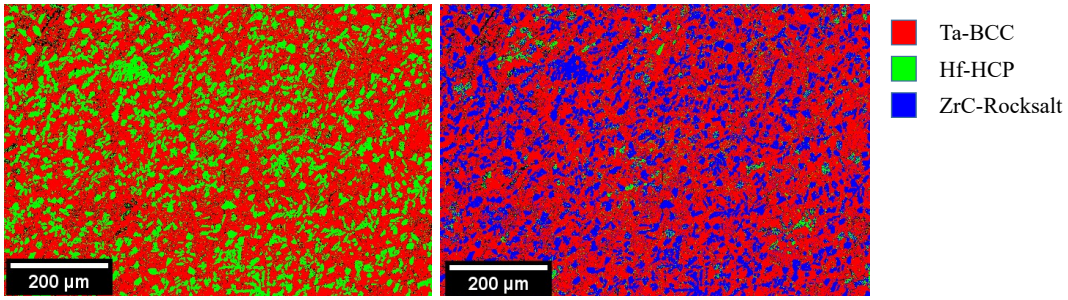

Figure 4.2: EBSD phase maps of 5eqA. The left-hand image is indexed for Ta-BCC and Hf-HCP only, the right hand image is for Ta-BCC, Hf-HCP, and ZrC-Rocksalt.

The rocksalt structure does not match any known intermetallic in the binaries of the TiVZrHfTa system, but does match the ionic crystals formed with carbon and nitrogen (with the exception of TaN, which forms a tetragonal phase). A comparison of these lattice parameters is shown in table 4.2. The oxides of Ti, V, Zr, Hf, and Ta are not know to form cubic crystals in bulk, but instead form monoclinic and tetragonal phases [176].

Element	Cubic Carbide (Å)	Cubic Nitride (Å)
Ti	4.33 [177]	4.24 [178]
V	4.18 [179]	4.17 [178]
Zr	4.70 [180]	4.57 [181]
Hf	4.65 [182]	4.52 [183]
Ta	4.43 [184]	- [178]

Table 4.2: Table comparing the lattice parameters of the cubic carbides and nitrides of Ti, V, Zr, Hf, and Ta. All these lattice paramters are within 0.35 Å of the rocksalt phase identified by XRD in 5eqC.

4.2.2 Complete chemical analysis: the actual composition

In order to ascertain accurate and complete compositions for the alloys in this project chemical analysis was conducted by AMG superalloys. They used X-ray Fluorescence (XRF) for the metallic elements, and a combination of infrared absorption and thermal conductivity to determining concentrations of C, N and O, full details are available on their website [152]. A wide variety of elements were tested for, but if they were reported as being at trace concentrations, then it was assumed they were not present and have not been included. The bulk compositions for each billet found in this thesis can be found in table 4.3.

The % Error value given is the average deviation away from the target composition when all impurities are ignored, it is useful for assessing how far away from the target composition the final alloy is after melting. These values show that the compositional error in this sense is an average of 0.56at%, and the metallic elements are, at the very least, melted in the correct ratios.

Element	5eq Billet (at%)	5opt Billet (at%)	4eq Billet (at%)	4opt Billet (at%)
Ti	**17.92**	**32.38**	**22.40**	**30.27**
V	**18.07**	**14.70**	**22.45**	**14.14**
Zr	**17.95**	**14.58**	**22.15**	**13.24**
Hf	**17.04**	**16.48**	0.02	0.03
Ta	**17.94**	**20.05**	**21.27**	**27.90**
C	1.00	0.69	2.07	1.04
N	7.68	0.30	7.00	10.46
O	2.30	0.71	2.54	2.68
W	0.03	0.03	0.02	0.17
Cu	0.08	0.08	0.07	0.07
% Error	0.33	0.28	0.45	0.47

Element	3eq Billet (at%)	3opt Billet (at%)	Sectioned Billet (at%)
Ti	**28.46**	**30.60**	**16.55**
V	**26.69**	**13.23**	**17.41**
Zr	0.05	0.06	**16.59**
Hf	0.02	0.03	**15.79**
Ta	**27.57**	**44.08**	**16.72**
C	0.34	0.17	0.40
N	11.58	8.67	8.83
O	4.94	2.99	3.44
W	0.13	0.08	0.08
Cu	0.22	0.08	0.21
Fe	-	-	3.98
% Error	0.82	1.16	0.44

Table 4.3: Table summarising the results of chemical analysis conducted by AMG Superalloys. The % Error is the error between the target concentrations of the primary elements, and the concentration actually achieved, if the impurities are ignored. W and Cu are included in these statistics as the W electrode and Cu crucible can be a source of impurity in arc-melted samples. Primary elements for each sample are shown in **bold**. The Sectioned Billet is discussed in chapter 6

4.2.3 Identification of the Rocksalt Phase

As the primary techniques available during this project (XRD and EDX) were unable to reliably identify the precise compositions of the rocksalt-structured phase, Atom Probe Tomography (APT) has been used. As machine time was valuable a single sample was selected for study: 5eqA. This microstructure is discussed further in section 4.3, but here it is sufficient to say it contains a BCC phase, an HCP phase, and the rocksalt-structured phase. The distribution of these phases is shown in figure 4.2; back-scatter images such as in figure 4.3, show that the darker contrast precipitates also contain laths of a lighter contrast. This morphology seems to share an orientation relationship, the angle between them being 70°, suggesting a crystallographic relationship between the phases. Sadly, the phases proved to small, and too prone to drift to be analysed reliably with EBSD. However, using 4.2 the rocksalt-structured phase was identified and atom probe needles were prepared using FIB, and analysed in order to identify the compositions of the various phases.

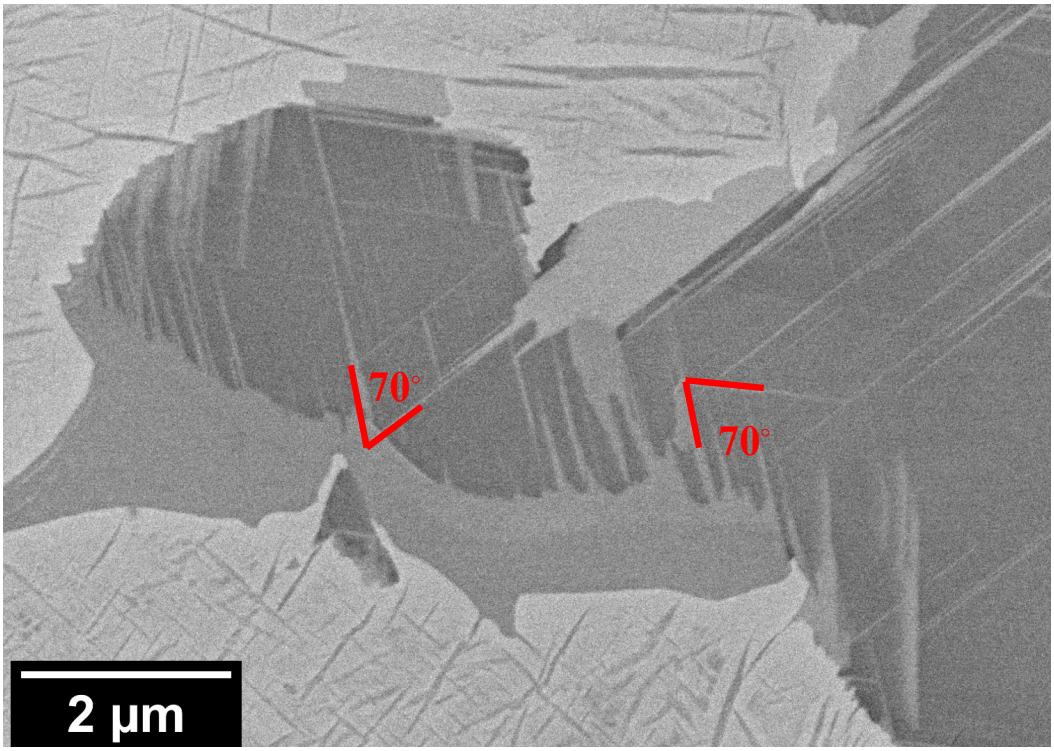

Figure 4.3: Back-scatter SEM image of 5eqA, demonstrating that the rocksalt-structured precipitates identified by EBSD often contain lighter contrast laths.

4.2.4 Atom Probe Analysis

Samples were prepared for APT using Focused-Ion-Beam milling (FIB) and subsequently run and analysed by Dr. Benjamin Jenkins (see chapter 3 for details); of the four needles analysed two were metallic and enriched in Ti, V, and Ta: a composition approximately matching the matrix phase. Another needle was also metallic but enriched in Zr and Hf, while the fourth needle contained a phase boundary between the ZrHf phase and what has been identified as a carbonitride. Reconstructions of carbon, nitrogen, and oxygen across this boundary are shown in figure 4.4. The boundary is defined as the 6.5at% C isosurface. It can be seen that the carbon is concentrated in the right-hand phase, while the oxygen is concentrated in the left-hand phase. The nitrogen is more evenly distributed, but has a higher concentration

in the right-hand phase also.

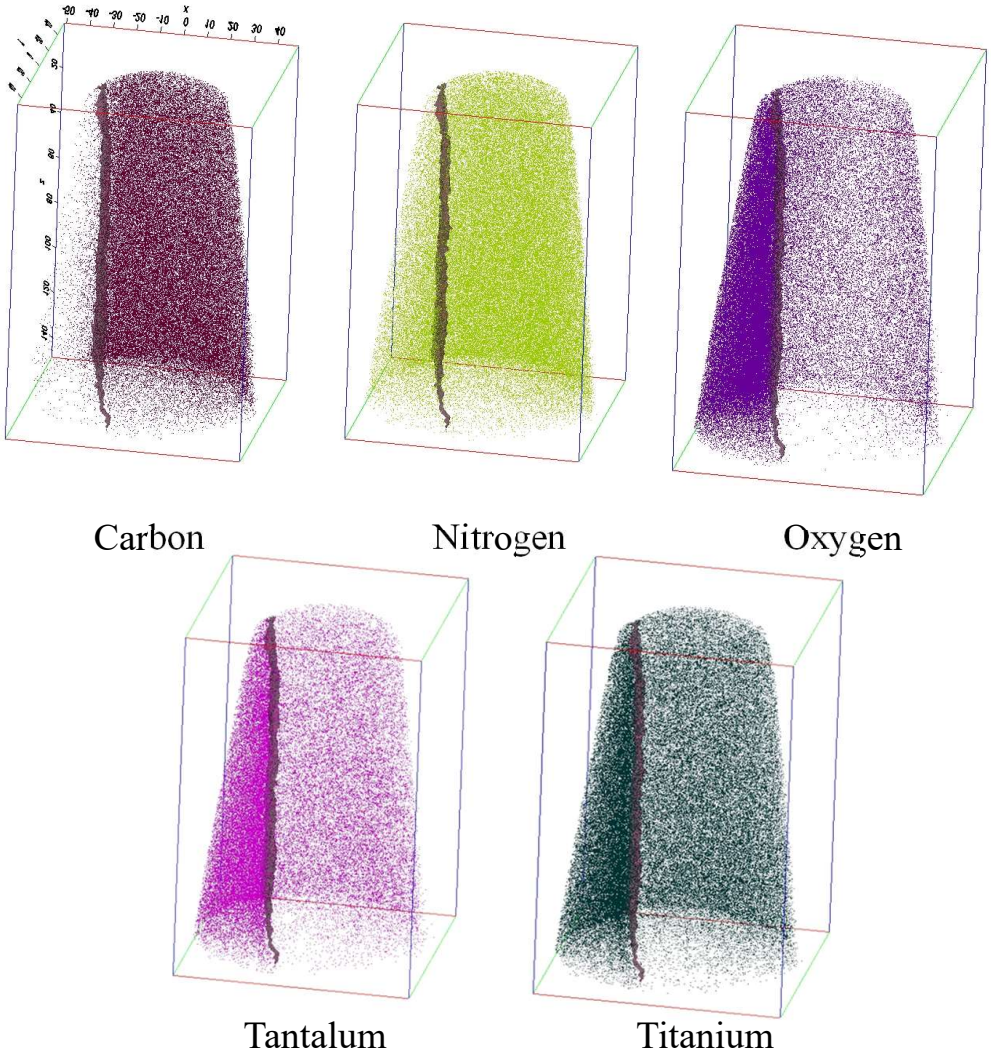

Figure 4.4: Atom probe reconstructions of carbon, nitrogen, oxygen, tantalum, and titanium across the phase boundary, which is a 6.5at% C isosurface.

It is easier to see the distribution of elements across the phase boundary in figure 4.5 where they are shown as line profiles. The left hand phase is enriched in the metallic elements, with Zr, Hf and Ti being the primary components. The right-hand phase is comparatively enriched in C and N. The two phases shown in figure 4.4 and 4.5 are therefore identified as the HCP phase, and a carbonitride with the rocksalt structure.

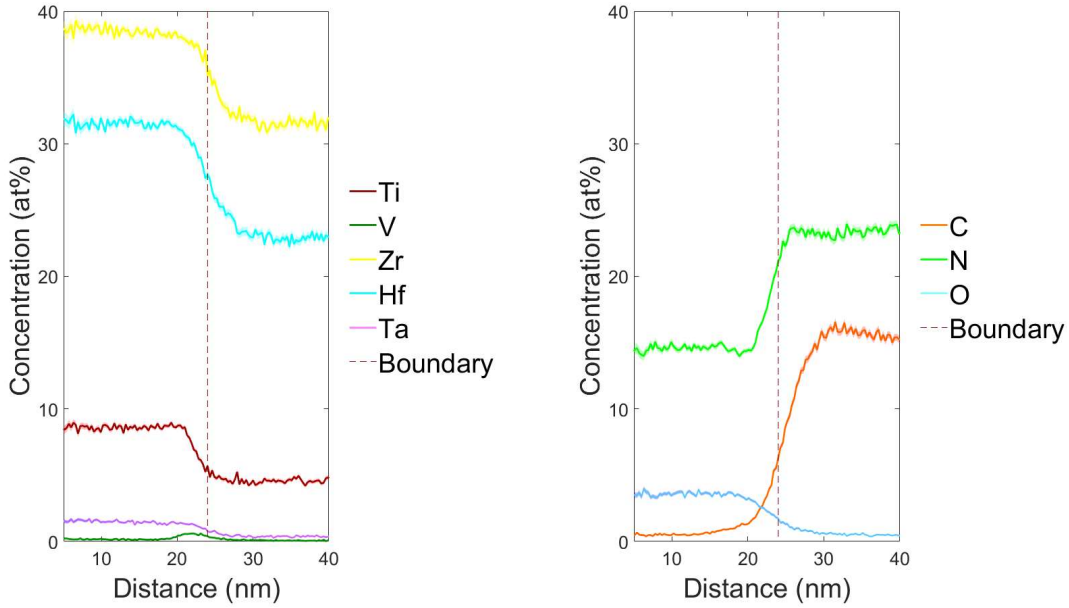

Figure 4.5: Line profiles showing concentration across the phase boundary shown in figure 4.4

The composition of the three identified phases: the TiVTa phase (thought to be the matrix), the ZrHf phase (thought to be the HCP phase), and the carbonitride phase, have been calculated from the APT needles and are shown in table 4.4. These compositions are generated using AtomProbeLab v0.1.4 which deconvolutes peak overlaps in the mass spectra, thus improving the compositional accuracy.

Element	TiVTa Phase Composition (at%)	ZrHf Phase Composition (at%)	Carbonitride Composition (at%)
Ti	23.48 ± 0.04	9.09 ± 0.06	4.40 ± 0.03
V	37.35 ± 0.04	0.15 ± 0.01	0.05 ± 0.00
Zr	2.99 ± 0.06	40.25 ± 0.11	31.49 ± 0.07
Hf	4.28 ± 0.02	29.61 ± 0.10	22.12 ± 0.05
Ta	31.63 ± 0.04	1.20 ± 0.03	0.33 ± 0.01
C	0.01 ± 0.01	0.54 ± 0.02	16.02 ± 0.05
N	0.22 ± 0.01	14.01 ± 0.08	25.09 ± 0.05
O	0.10 ± 0.01	5.15 ± 0.07	0.50 ± 0.02

Table 4.4: Table comparing the compositions of the phases identified using APT. In order to get accurate compositions the data has been analysed with AtomProbeLab v0.1.4

The APT analysis shows that the rocksalt phase in 5eqA is a carbonitride of primarily Zr and Hf, with small amounts of Ti (<5at%): these elements are known to be stable in the rocksalt structure [183]. Rocksalt has a 1:1 cation to anion ratio, and so this composition requires there to be an excess of vacancies on the anion sub-lattice. If the cation sub-lattice is assumed to have no vacancies, then the site occupation on the anion sub-lattice should be 41.66at% nitrogen, 26.54at% carbon, and 31.80at% vacant sites. This depletion on the anion sub-lattice is known to be stable, with reports of vacancy concentrations as high as 60% [182].

4.2.4.1 The Phase boundary

The final interesting result of the APT is the distribution of V across the phase boundary (marked as the 6.5at% C isosurface), where it has been segregated to dislocation cores. Three different orientations of the V reconstruction are shown in figure 4.6.

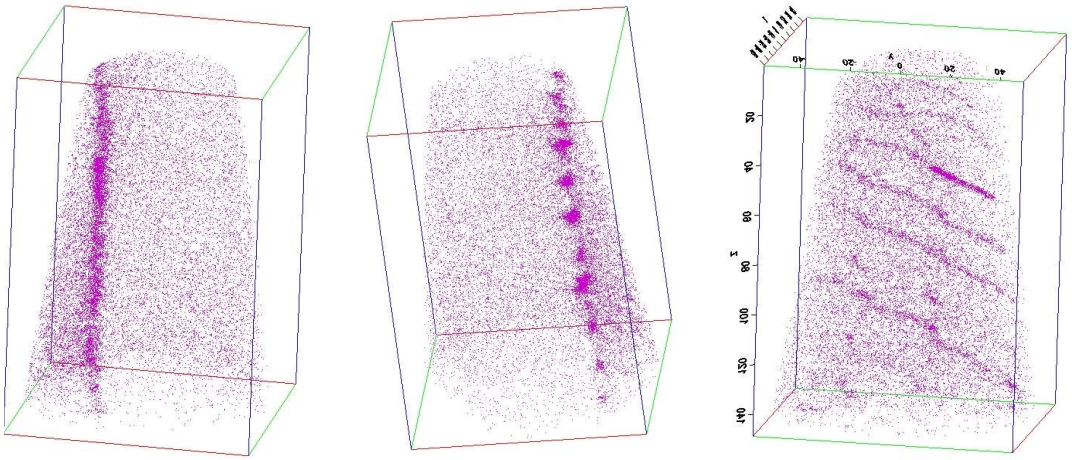

V – Orientation 1 V – Orientation 2 V – Orientation 3

Figure 4.6: Three orientations of the atom probe reconstructions of V, showing dislocation decoration at the phase boundary, which is a 6.5at% C isosurface. Orientation 1 is the same as shown in figure 4.4

Vanadium has a low solubility in HCP crystal structures, as seen in the binary phase diagrams in appendix A, and so it being segregated to the phase boundary is not surprising, however, the presence of dislocations at this boundary suggests that it is either low angle, or coherent with dislocations present to take up the misfit strain. This observation reaffirms the hypothesis that there is a crystallographic relationship between the rocksalt and HCP phases.

4.2.5 X-ray Analysis

The chemical analysis provided by AMG combined with the APT has given accurate bulk concentrations and the compositions of specific phases, despite quicker methods of compositional analysis such as EDX and WDX proving unable to do this; the purpose of this section is to discuss the underlying reasons why.

4.2.5.1 Energy Dispersive Spectrometry

The compositions reported by AMG do not agree with the compositions measured with EDX analysis. Table 4.5 shows the composition of 5eqC using an EDX Point&ID area scan, compared to the results for the 5eq billet from AMG. It can be seen that EDX has overestimated the carbon concentration by a factor of nearly 27, the oxygen concentration by a factor of nearly 4, yet underestimated everything else, including the nitrogen concentration, by a factor of 2.

Element	5eqC By EDX (at%)	5eqC By AGM (at%)	Error in EDX (at%)
Ti	11.52	17.92	-6.4
V	10.21	18.07	-7.86
Zr	13.19	17.95	-4.76
Hf	13.62	17.04	-3.42
Ta	11.90	17.94	-6.04
C	26.69	1.00	+25.69
N	3.87	7.68	-3.81
O	8.98	2.30	+6.68
W	0.00	0.03	-0.03
Cu	0.01	0.08	-0.07

Table 4.5: Table comparing the compositions of the 5eq billet by EDX and AMG's analysis. Of particular note is EDX's overestimation of carbon and oxygen, and underestimation of nitrogen concentration.

The energy peaks for carbon, nitrogen, and oxygen are at 0.277, 0.392, and 0.525keV. There are energy peaks for Ta, Ti, and V at 0.210, 0.452, and 0.518keV, which all overlap strongly with the impurities' peaks. The metallic elements have higher order peaks that make quantitative analysis easier, and the ratios of the metallic elements is consistent between both EDX and AMG's analysis. In contrast, the lower energy peaks can not be analysed accurately: figure 4.7 shows an EDX spectrum of the 5eqC sample along with a theoretical trace generated by the AZtec software as it calculates the composition given in table 4.5. The Ti Kα peak is fitted well, and is used to generate the (relatively accurate) concentration, however the Ti Lα/N Kα peak is poorly fitted, with the theoretical spectra *overestimating* the peak at this energy. This would suggest that the AZtec software is overestimating the composition of nitrogen, despite the fact that is has actually *underestimated* it. In contrast, the 0.3keV carbon peak and the 0.5keV oxygen peak are better fitted, yet AZtec has overestimated the carbon and oxygen concentrations.

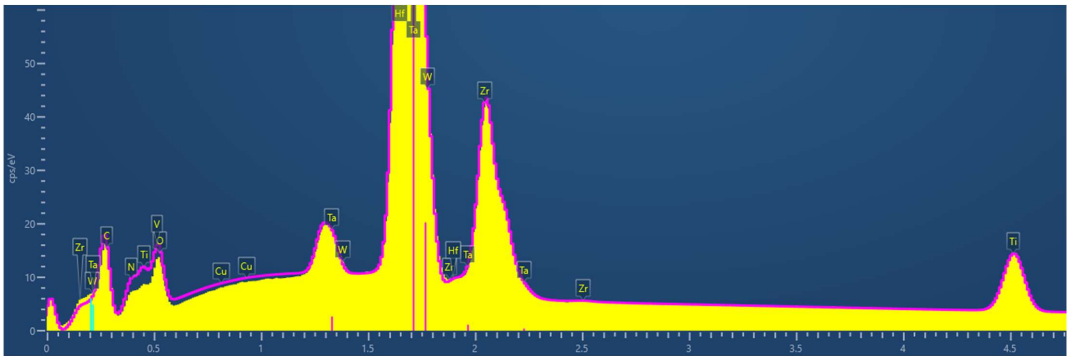

Figure 4.7: EDX spectrum (yellow) of 5eqC. The line trace (pink) is the theoretical spectrum for the composition shown in 4.5.

In summary, the AZtec software can approximately give the ratio of metallic elements, but it cannot be used to measure the concentration of the impurities; this is either due to surface contamination of elements such as carbon and oxygen, or due to the spectral interference which is common at lower energies [185], or most likely a combination of both.

4.2.5.2 Wave Dispersive Spectroscopy

As the energy resolution of EDX is insufficient to separate out the metallic and impurity signals, an alternative is the wave dispersive technique, WDX. This is slower and more difficult, but can give improved peak resolution, particularly at lower energies. Figure 4.8 shows three wave scans across the Ti/N peak range, one for BN, one for metallic Ti, and one for the carbonitride phase identified by APT. It can be seen that the centre of the peak in the carbonitride wave scan is closest to the nitrogen peak, although they are not perfectly aligned. The phase in question contains both N and Ti, and so the peak is potentially a combination of both signals, which would have shifted the centre betwixt the two.

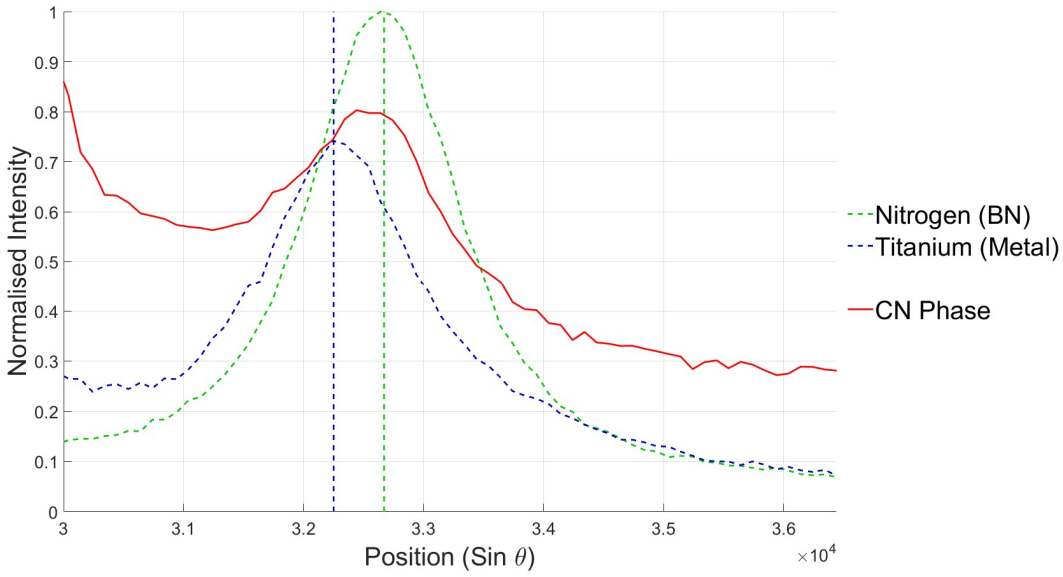

Figure 4.8: Wavescans taken across the angular range containing the Ti/N peak overlap. Three separate wave scans are shown: one for BN, one for Ti metal, and one for the carbonitride phase.

The peak overlap between nitrogen and titanium is problematic but can be resolved and accounted for, but this does have one caveat: the user must have a reasonable idea of what elements are present beforehand, and roughly what ratio they are in. The APT has already shown that the carbonitride phase contains ∼5wt% Ti, and so the WDX can be calibrated against a material or mineral with a similar Ti concentration. Figure 4.9 shows wave scans across the same angular range as in figure 4.8, but taken for several minerals and standards containing varying concentrations of titanium. It can be seen that in Ilmenite, which contains 27.4wt% Ti, the Ti peak visible, but for KK1 and Andradite which contain <5wt% Ti, there is no measurable peak.

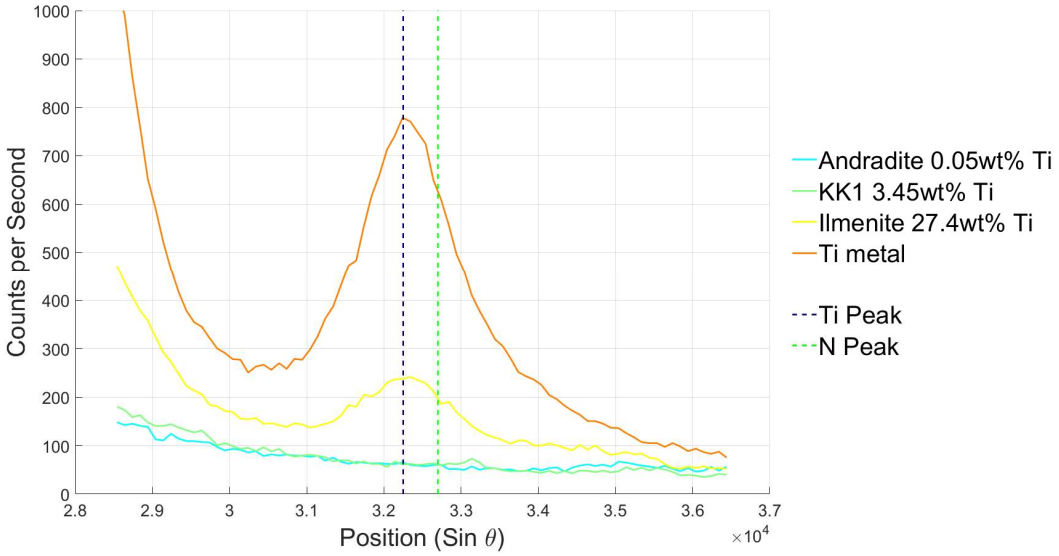

Figure 4.9: Wave scans taken across the angular range of the N/Ti peak overlap, for several minerals and standards with varying concentrations of titanium

Pre-armed with the compositions from APT it is clear that the peak in the carbonitride phase is entirely due to the nitrogen: without the APT data the only way to be sure of this is to use a higher order Ti peak to deconvolute the two signals. Spectrometers are not able to rotate through large angular ranges without recalibration, and so two separate spectrometers would be required to quantify a single element, which is particularly costly in a five component alloy with multiple impurity atoms which also require quantification.

In summary, WDX *is* able to resolve and deconvolute the peak overlaps that EDX cannot. However, this is a difficult and time intensive process that requires a skilled operator *and* a reasonable idea of the compositions in order to calibrate the spectrometers before any reliable quantitative analysis can be done. This technique is not able to identify and measure impurities on its own.

4.2.6 Impurity Source

An important question is where these impurities came from. It was shown in chapter 3 that the furnace itself does not, as a rule, introduce high fractions of impurities; it was also shown that the Ti feedstock material was clean, containing only 0.176at% of impurities (see table 3.1.4). Consequently, AMG were asked to chemically analyse the Zr and Hf feedstock material, as well as 50/50 binary alloys that had been melted using the Ti, V, and Ta feedstock material; unfortunately by the time the contamination issue was fully realised all of the Ti, V, and Ta had been melted, and none was left for further examination. The results of AMG's analysis is shown in table 4.6.

Element	Zr Raw (at%)	Hf Raw (at%)	TiV Billet (at%)	TiTa Billet (at%)	VTa Billet (at%)
Ti	0.09	0.18	**48.84**	**49.52**	0.12
V	0.08	0.17	**48.18**	0.11	**47.18**
Zr	**90.75**	3.31	0.03	0.06	0.06
Hf	0.02	**92.76**	0.01	0.03	0.03
Ta	0.02	0.05	0.01	**48.04**	**47.59**
C	5.87	2.54	0.52	0.37	0.08
N	2.82	0.79	0.49	1.27	3.64
O	0.26	0.02	1.86	0.49	1.18
W	0.02	0.05	0.01	0.03	0.03
Cu	0.07	0.13	0.04	0.09	0.09

Table 4.6: Table summarising the results of chemical analysis conducted by AMG Superalloys. Primary elements for each sample are shown in **bold**.

These results show that the Hf and Zr are contaminated with carbon (2.54 and 5.87at% respectively): this is likely the source of the carbon contamination in the melted alloys, as the carbon content in the non-ZrHf containing alloys is lower than those that do. The oxygen and nitrogen concentrations do not correlate with any particular element, and the 5opt billet which contains all five elements is the cleanest

sample of all. After discussions with the arc melter's manufacturer, the primary diagnosis is a faulty door seal. Problems were encountered with this component several times over the course of the project, however it was never thought to be impairing sample fabrication, as fixes were always quickly installed and no change in as-cast alloy microstructures were witnessed. The most convincing evidence of an air leak being the source of the contamination is that there is always between 3 or 4 times as much nitrogen as oxygen, which is roughly the same as their relative concentrations in air.

4.2.7 Carbonitride Conclusions

During the later stages of this project a rocksalt-structured phase was identified, and after extensive analysis it was discovered that this was in fact a carbonitride formed primarily with zirconium and hafnium. Correctly identifying the impurity species was made difficult because the contamination was not consistent between all billets, and because of strong peak overlaps in the X-ray spectra between the metallic and non-metallic elements. It was observed in chapter 2 that some authors had identified zirconium-rich phases as having FCC crystal structures [124, 136]. It is possible that these observations are also due to issues with contamination, as zirconium is only found as a metallic FCC phase in very specific conditions [125]. Cleanliness during arc-melting is of paramount importance, but it is also difficult to ensure or to investigate without advanced chemical testing such as that conducted by AMG. If an analytical service such as AMG cannot be used to test every single billet, then an alternative is to verify observed phases using database-based predictive techniques (e.g. CALPHAD); if a discrepancy is found between the two then further investigation is more likely to be warranted.

4.3 TiVZrHfTa

The five component alloy TiVZrHfTa is the alloy of primary interest in this project. It is this alloy system that chapters 6 and 7 are based on. The target compositions of the equiatomic and optimised alloys are shown in table 4.7.

Element	Equiatomic Compostion (at%)	Optimised Composition (at%)
Ti	20	35.1
V	20	13.7
Zr	20	13.1
Hf	20	19.4
Ta	20	18.6

Table 4.7: Table comparing the target compositions of equiatomic and optimised TiVZrHfTa.

4.3.1 As cast Equiatomic TiVZrHfTa

The microstructure of as-cast equiatomic TiVZrHfTa (5eqC) has been analysed by XRD and indexed in figure 4.10. The trace shows the alloy is multiphase with two BCC phases, an HCP phase, and a rocksalt-structured phase. The lattice parameters and volume fractions of each phase are shown in table 4.13.

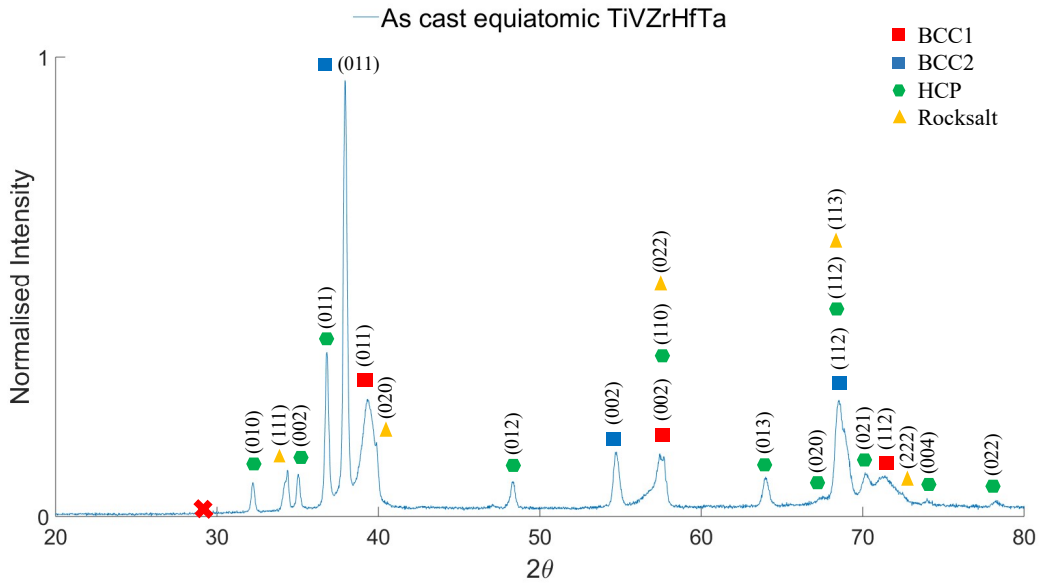

Figure 4.10: XRD trace of as-cast equiatomic TiVZrHfTa. Four phases have been identified: two BCC phases, an HCP, and a rocksalt-structured phase.

5eqC Phases	Lattice Parameter (Å)	Volume Fraction (vol%)
BCC1 (red)	a=3.24	58.8
BCC2 (blue)	a=3.36	21.2
HCP (green)	a=3.20, c=5.12	12.1
Rocksalt (yellow)	a=4.53	8.0

Table 4.8: Table comparing the lattice paramters and volume fractions determined by XRD in 5eqC.

Identifying which phase is which in SEM is not trivial. Figure 4.11 shows a back-scatter SEM image of 5eqC. A typical cast microstructure is visible, with dendrites, dendritic segregation (which has resulted in interdendritic phases), and precipitation.

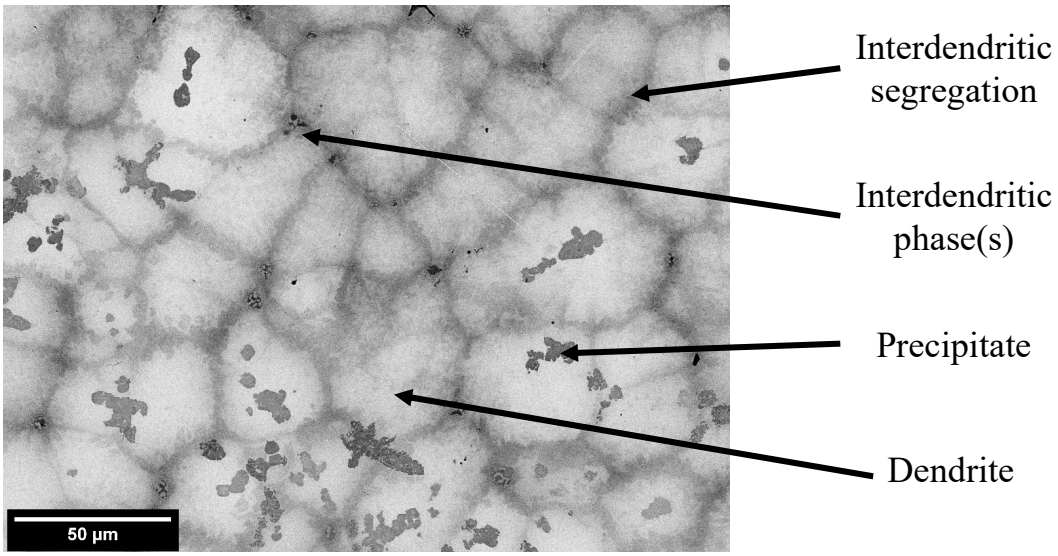

Figure 4.11: Back-scatter SEM image of 5eqC, showing dendrites, interdendritic segregation, interdendritic phases, and precipitates.

Figure 4.12 shows a secondary electron image with an EBSD phase map overlaid. It can be seen that the matrix is BCC, the large precipitates are rocksalt, and the interdendritic regions are a combination of BCC, HCP, and rocksalt-structured phase. There is also a clear eutectic or eutectoid microstructure visible, further demonstrating the complexity of this microstructure

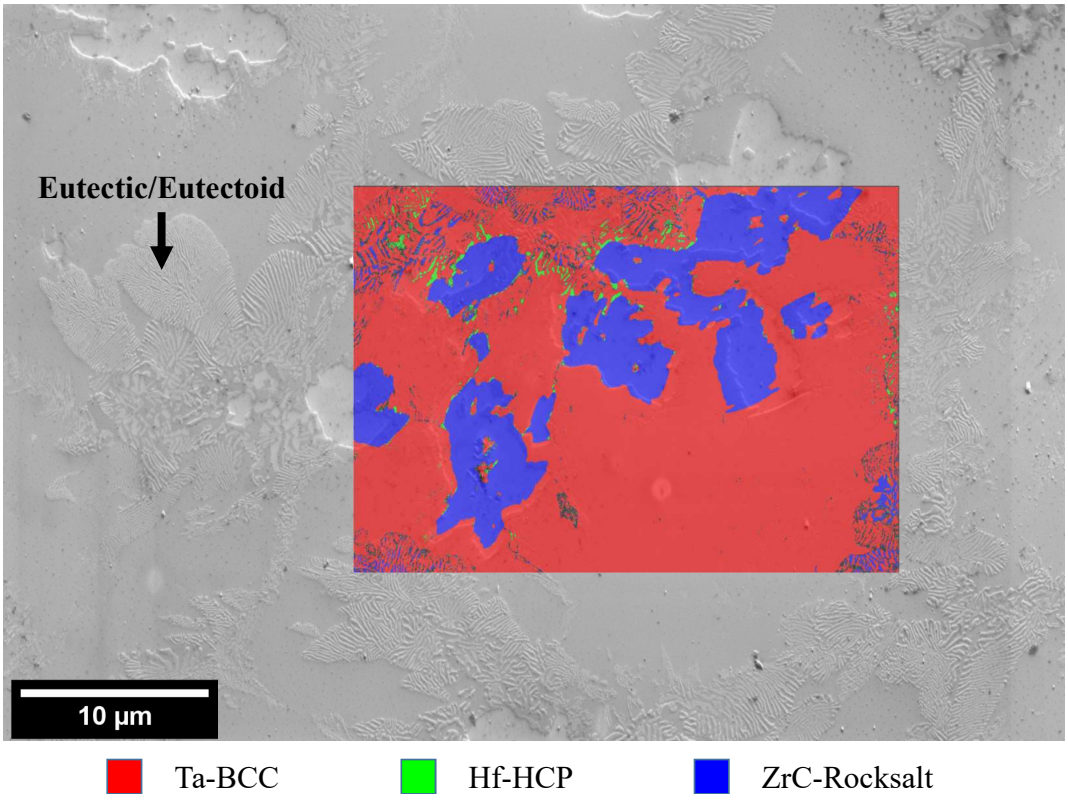

Figure 4.12: Secondary electron image of 5eqC with an EBSD phase map overlaid. Phase map indexed for Ta-BCC, Hf-HCP, and ZrC-Rocksalt.

4.3.1.1 Precipitates

It was previously stated that the large precipitates in 5eqC are rocksalt structure. Back-scatter electron images show that the precipitates are darker contrast than the dendrites, suggesting that they have a lower average Z number. However, table 4.9 compares their EDX compositions and average Z numbers, and finds that the precipitate composition (which is mostly Zr and Hf) has a *higher average Z number* despite appearing darker than the dendrites in the back-scatter signal. As the EDX composition of the precipitates overestimates the average Z number, these precipitates must be where a large proportion of the light element impurities are grouped and it is for this reason that the precipitates can, with confidence, be identified as the

rocksalt-structured carbonitride.

Element	Dendrite composition (at%)	Precipitate composition (at%)
Ti	20.07 ± 0.8	13.94 ± 1.0
V	18.45 ± 0.8	0.35 ± 0.3
Zr	17.63 ± 1.4	39.12 ± 1.3
Hf	19.46 ± 0.6	42.72 ± 0.8
Ta	24.41 ± 1.8	4.09 ± 0.6
Z_{ave}	45.0	52.5

Table 4.9: Table comparing the compositions and aveage Z numbers of 5eqC dendrites (lightest contrast phase) with the large precipitates. Data was collected using EDX Point&ID analysis. The data is averaged from 10 individual spectra and the error is the standard deviation of this data.

The carbonitride precipitates have formed throughout the 5eqC billets. In some instances they appear to have formed in the dendrite cores and mirror the dendrite geometry, for example in figure 4.13, at other times this is less obvious, as in figure 4.11. If they were found in the dendrite cores then it could be assumed that these solidified first (the melting point of carbonitrides is well above 3500K), however due to the seemingly random positions of the precipitates it is not possible to be certain when they formed during the solidification process.

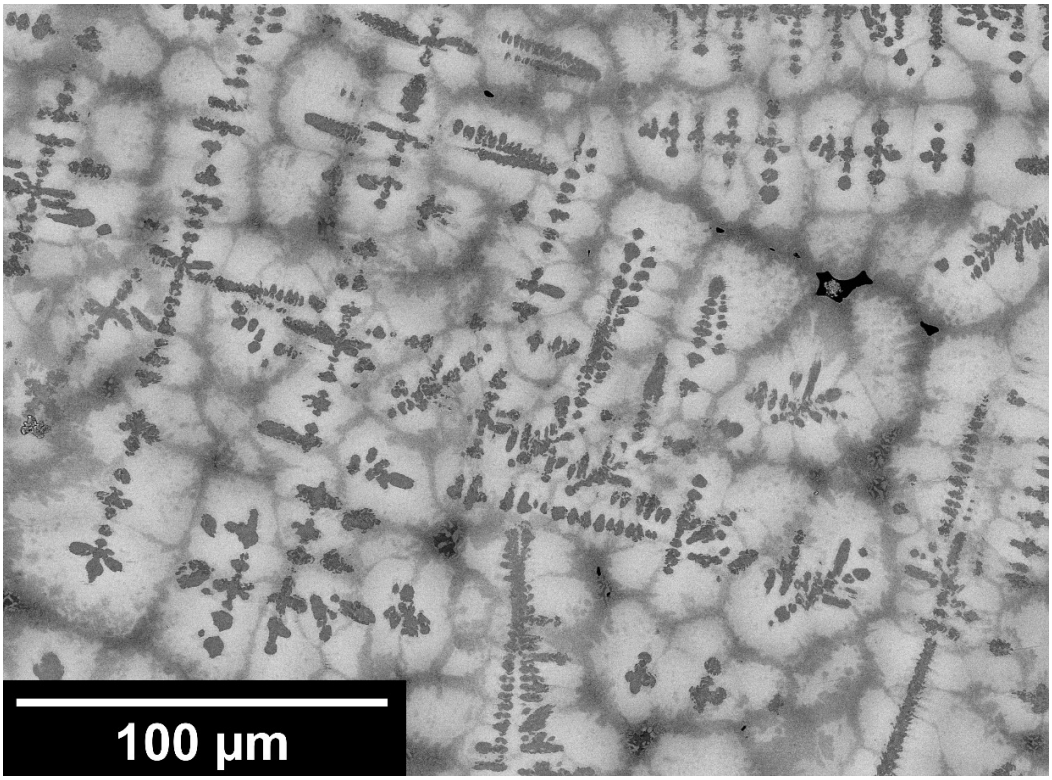

Figure 4.13: Back-scatter SEM image of 5eqC, showing precipitation that has occurred, mirroring the underlying dendritic structure.

4.3.1.2 Segregation

The dendritic segregation is primarily in the Ta; which is enriched in the dendrites, and V and Zr; which are enriched in the interdendritic regions. This can be seen in figure 4.14 which shows an EDX Linescan across two interdendritic regions. Additionally, table 4.10 shows the average composition by EDX of the metallic elements in the dendrites and the interdendritic regions from a total of 10 Point&ID scans in each region. The compositions of Ti and Hf are within the margin of error: there does not appear to be any dendritic segregation occurring in these two elements. The average Z number from the EDX composition correlates with the back-scatter contrast, and so no conclusions can be drawn on the distribution of impurities.

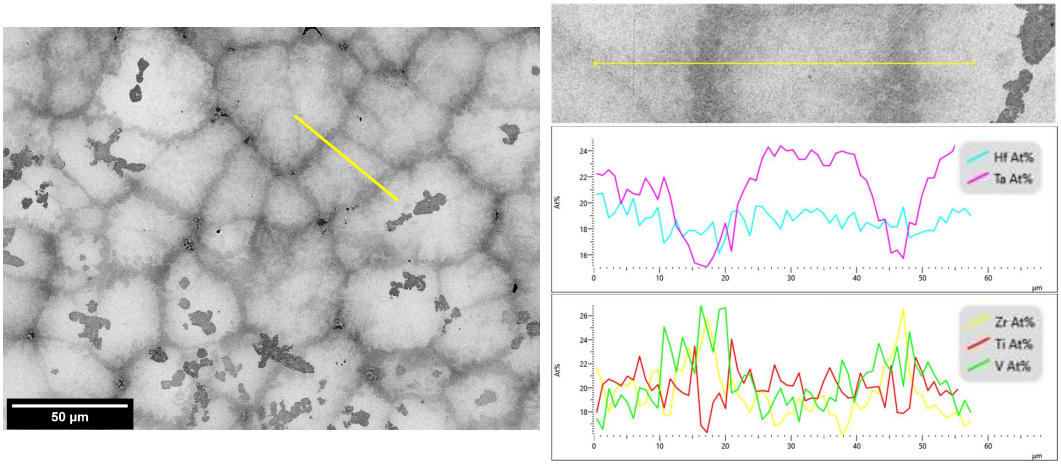

Figure 4.14: Back-scatter electron image of 5eqC including an EDX Linescan showing the change in composition due to dendritic segregation. The line taken is highlighted in yellow, and goes over two interdendritic regions.

Element	Dendrite composition (at%)	Interdendritic composition (at%)
Ti	20.07 ± 0.8	18.68 ± 0.9
V	18.45 ± 0.8	$\mathbf{21.97} \pm 2.3$
Zr	17.63 ± 1.4	$\mathbf{24.04} \pm 2.3$
Hf	19.46 ± 0.6	19.02 ± 1.5
Ta	$\mathbf{24.41} \pm 1.8$	16.30 ± 1.2
Z_{ave}	44.96	39.97

Table 4.10: Table comparing the compositions and aveage Z numbers of 5eqC in dendritic and interdendritic regions. Data was collected using EDX Point&ID analysis. The data is averaged from 10 individual spectra, and the compositions in **bold** are higher than their counterpart by more than the margin of error, which is the standard deviation of the data.

4.3.1.3 Interdendritic Phases

At some interdendritic regions there is phase separation visible at high magnification. A back-scatter SEM image of this is shown in figure 4.15. The EDX data shows that one phase is enriched in Zr and Hf, while the other is enriched in Ti, V, and Ta. Combining this with the EBSD from figure 4.12 it is logical that the ZrHf phase is HCP, while the TiVTa is BCC. The average Z number by EDX correlates with the

back-scatter contrast and so no conclusions can be drawn on the concentration of impurities across these phases.

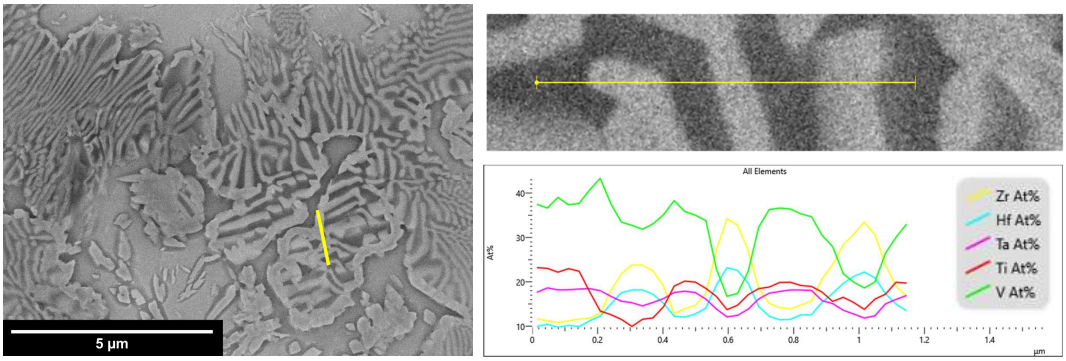

Figure 4.15: Back-scatter SEM image of 5eqC. Includes an EDX Linescan showing the change in composition across the fine phase separation that occurs in some interdendritic regions.

Element	ZrHf segregated composition (at%)	TiVTa segregated composition (at%)
Ti	13.76 ± 2.3	20.57 ± 1.4
V	21.59 ± 5.9	35.51 ± 1.4
Zr	30.32 ± 4.0	14.15 ± 1.6
Hf	21.13 ± 2.1	12.18 ± 1.3
Ta	13.19 ± 1.2	17.60 ± 0.3
Z_{ave}	44.96	39.97

Table 4.11: Table comparing the compositions and average Z number of two fine scale phases that form in some interdendritic regions in 5eqC. Data was collected using EDX Point&ID analysis and is averaged from 5 individual spectra. The error values given are the standard deviation of this data

At junctions of the interdendritic regions several new phases form. These are highlighted in figure 4.11 and shown at greater magnification in figure 4.16, along with EDX maps of the metallic elements. This shows that the interdendritic phases are complex, containing several phases. The EDX maps shows that separation has occurred between a ZrHf phase and a TiVTa phase: the compositions of these phases are shown in table 4.12.

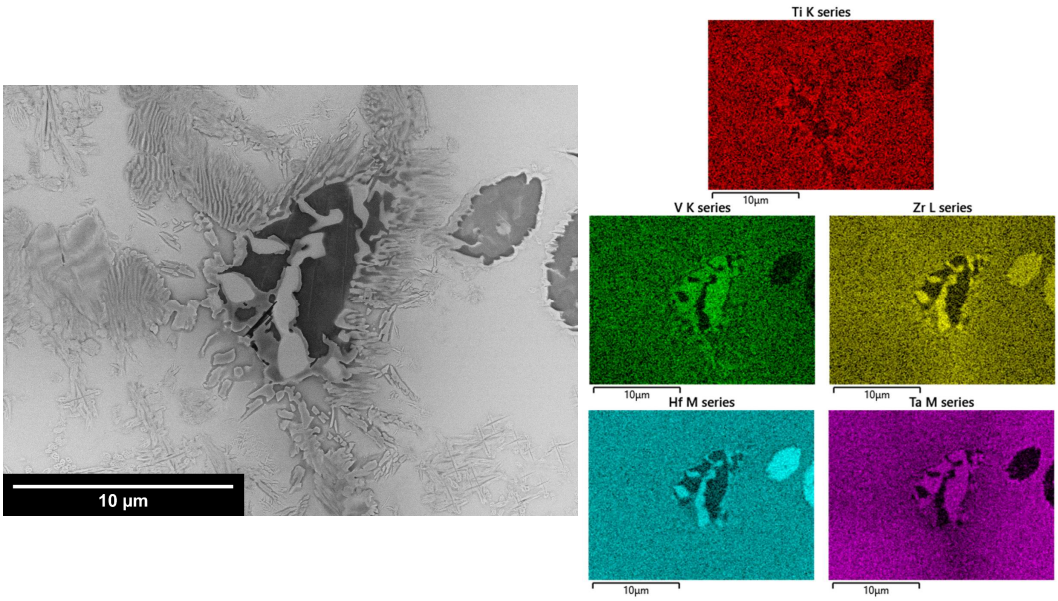

Figure 4.16: Back-scatter SEM image of 5eqc; also includes EDX maps for the metallic elements, showing phase separation between a VTa-rich and a ZrHf-rich phase.

Element	ZrHf Interdendritic Phase (at%)	TiVTa Interdendritic Phase (at%)
Ti	8.49 ± 1.0	19.56±1.0
V	3.18 ± 2.1	49.59±1.7
Zr	54.68± 2.2	6.42 ±1.5
Hf	30.98± 1.5	6.35 ±0.9
Ta	2.70 ± 0.9	18.09±0.7
Z_{ave}	48.75	36.05

Table 4.12: Table comparing the compositions and average Z number of the two primary phases found in the interdendritic region of 5eqC. Data was collected using EDX Point&ID analysis and is averaged from 10 individual spectra at different points. The error values given are the standard deviation of this data.

These two interdendritic phases are widespread throughout 5eqC, however occasionally there are small quantities of additional phases alongside them. Figure 4.17 shows EDX maps of 5eqC where, in the circled region, there are: the ZrHf and TiVTa phases shown previously, and also a Ti rich phase. This phase is highlighted in figure 4.18, along with its composition. It has the highest Ti composition of any

phase analysed in this material, and is also enriched in both Zr and Hf compared to its surroundings.

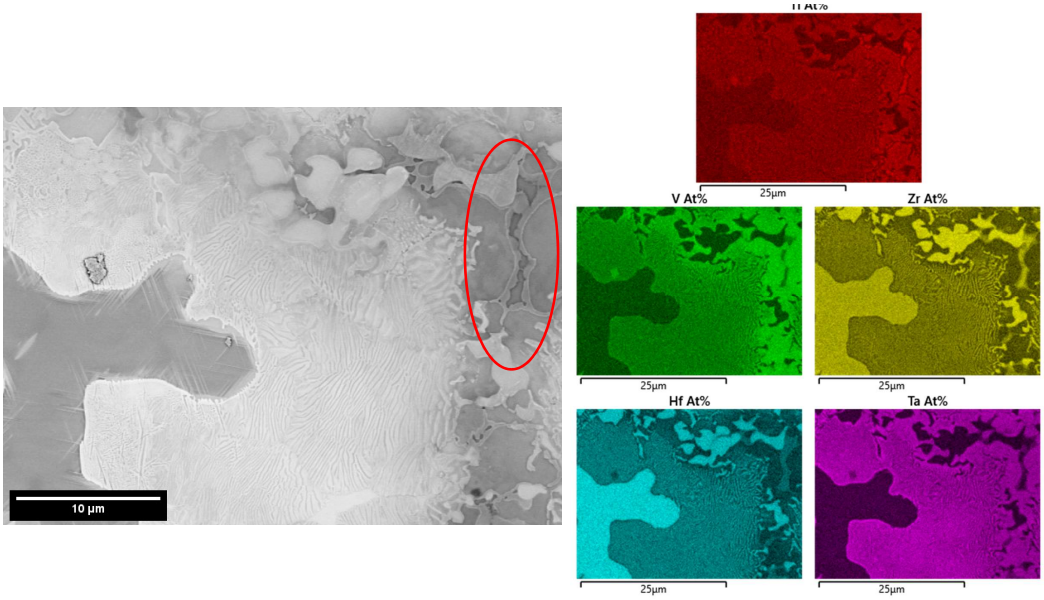

Figure 4.17: Back-scatter SEM image of 5eqC. It includes EDX maps for each element, showing the phase separation that occurs in the interdendritic region. The red circle highlights a Ti rich phase that is distinct from the ZrHf and TiVTa phases discussed previously.

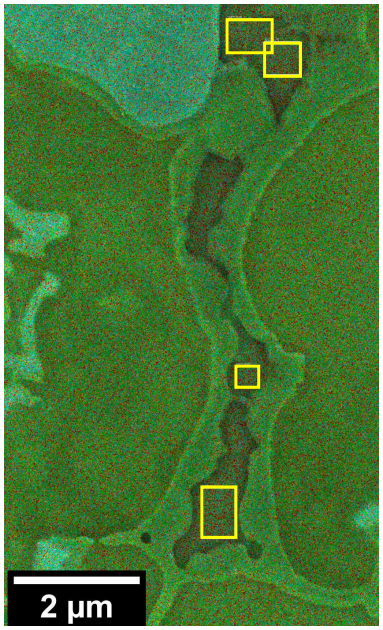

Element	Ti-rich phase composition (at%)
Ti	36.75±2.8
V	10.36±2.5
Zr	31.43±1.4
Hf	15.17±0.4
Ta	6.30±0.6

Figure 4.18: Layered EDX image of the back-scatter image and the elemental maps for Ti, V, and Hf. The yellow boxes show the regions where Point&ID analysis was conducted for the compositions shown in the adjacent table. The error values given are the standard deviation of this data.

In addition to this Ti-rich phase, a Cu-rich phase has also been found. Figure 4.19 shows a region of interdendritic phases where a Cu rich phase was identified using EDX Point&ID scans in the sectioned billet. This phase is very small and only contains ∼5at% Cu. The source of the Cu is most likely from the crucible of the arc melter during casting. The sample in question was found by AMG to contain 0.21at% Cu, one of the highest fractions observed in any billet.

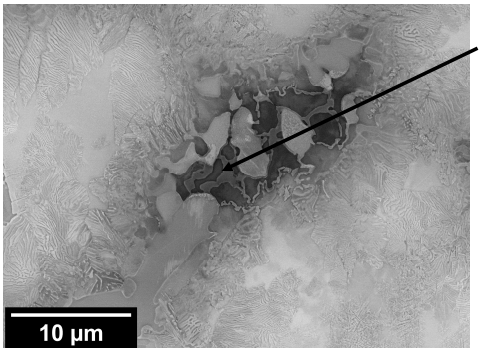

Element	Phase Composition (at%)
Ti	12.39 ± 1.7
V	41.95 ± 2.1
Cu	5.20 ± 0.9
Zr	17.03 ± 2.8
Hf	11.42 ± 1.8
Ta	12.01 ± 1.7

Figure 4.19: Back-scatter SEM image of 5eqC. The arrow indicates which phase appears to contain Cu, and the table gives its composition. The composition is determined from three EDX Point&ID spectra, with the error being the standard deviation of this data.

Both the Ti-rich and Cu-rich phases are uncommon throughout the billets, and it is unlikely that they would be shown by XRD. The observation of these phases in the interdendritic region demonstrates the variability of these areas. The reason these complex regions form is that during casting they are the last areas to solidify. The composition of this liquid is determined by the phases formed locally and the microsegregation that has occurred. It is unsurprising therefore that these regions do not form a stable single phase, but instead break down; and also that there are variations in what phases form, as each liquid pocket will vary locally.

4.3.2 Annealed equiatomic TiVZrHfTa

The XRD trace for annealed equiatomic TiVZrHfTa (5eqA) is indexed in figure 4.20. As with the as-cast alloy it is a complex mixture of phases, including a BCC phase, an HCP phase and a rocksalt phase. The small peak at 29° is a signal from the sample holder. The lattice parameters of these phases are shown in table 4.13.

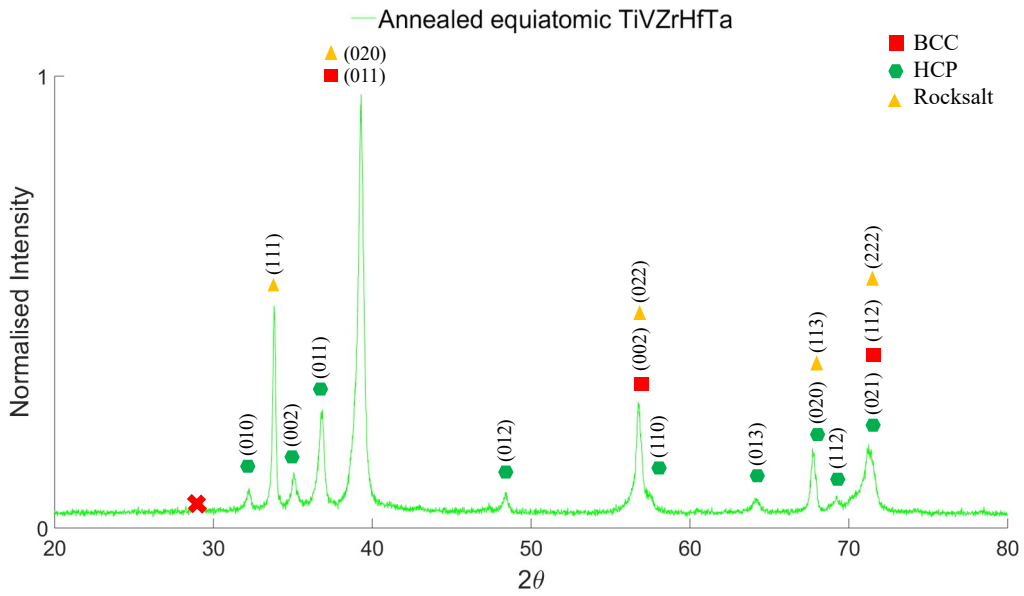

Figure 4.20: XRD trace of 5eqA. Three phases have been identified: a BCC phases, an HCP, and phase with the rocksalt structure.

5eqA Phases	Lattice parameters Å	Volume Fraction (vol%)
BCC1 (red)	a=3.24	56.1
HCP (green)	a=3.20, c=5.11	13.9
Rocksalt (yellow)	a=4.59	30.0

Table 4.13: Table comparing the lattice parameters and volume fractions determined by XRD in 5eqA

The morphology of the phases varies from sample to sample, presumably because of differences in their starting morphologies caused by the arc melting process (discussed further in chapter 6). Figure 4.21 shows three samples of 5eqA, all cut from the same billet and annealed in the same conditions. Each shows different distributions of phases, despite the composition of each being roughly the same, as shown in table 4.14.

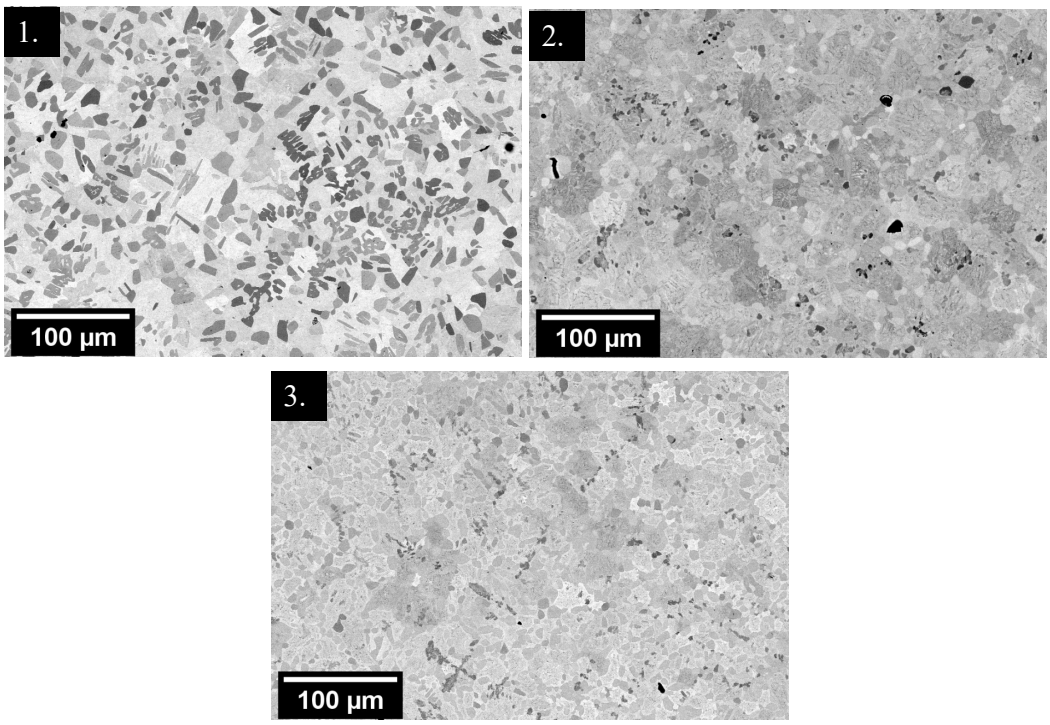

Figure 4.21: Back-scatter SEM images of three different samples of 5eqA. All were cut from the same billet and annealed in the same way. It can be seen that the precipitates are distributed differently, and are of different sizes.

Element	Adjusted AMG Composition (at%)	Sample 1 (at%)	Sample 2 (at%)	Sample3 (at%)
Ti	20.15	18.33 ± 0.7	19.32 ± 0.3	19.00 ± 0.2
V	20.32	20.87 ± 0.5	19.49 ± 0.5	18.94 ± 0.4
Zr	20.19	19.63 ± 0.3	20.87 ± 0.2	21.08 ± 0.3
Hf	19.17	19.22 ± 0.1	20.50 ± 0.2	20.67 ± 0.3
Ta	20.18	21.96 ± 0.3	19.82 ± 0.2	20.31 ± 0.1
δ_{ave}	-	0.95	0.81	1.01

Table 4.14: Table comparing the bulk compositions by EDX of the three 5eqA samples shown in figure 4.21 to each other, and also the composition given by AMG, once adjusted to only consier the metallic elements. The δ_{ave} is the average deviation from this composition. It can be seen that although the microstructure changes, the composition is roughly consistent amongst all the samples.

Which phase has which crystal structure has been determined with EBSD. Figure 4.22 shows an EBSD phase map indexed for Ta-BCC, Hf-HCP, and ZrC-rocksalt; these are distributed in a similar way to 5eqC, whereby the matrix is BCC, the precipitates are rocksalt, and the HCP forms a complimentary phase where there has been phase separation.

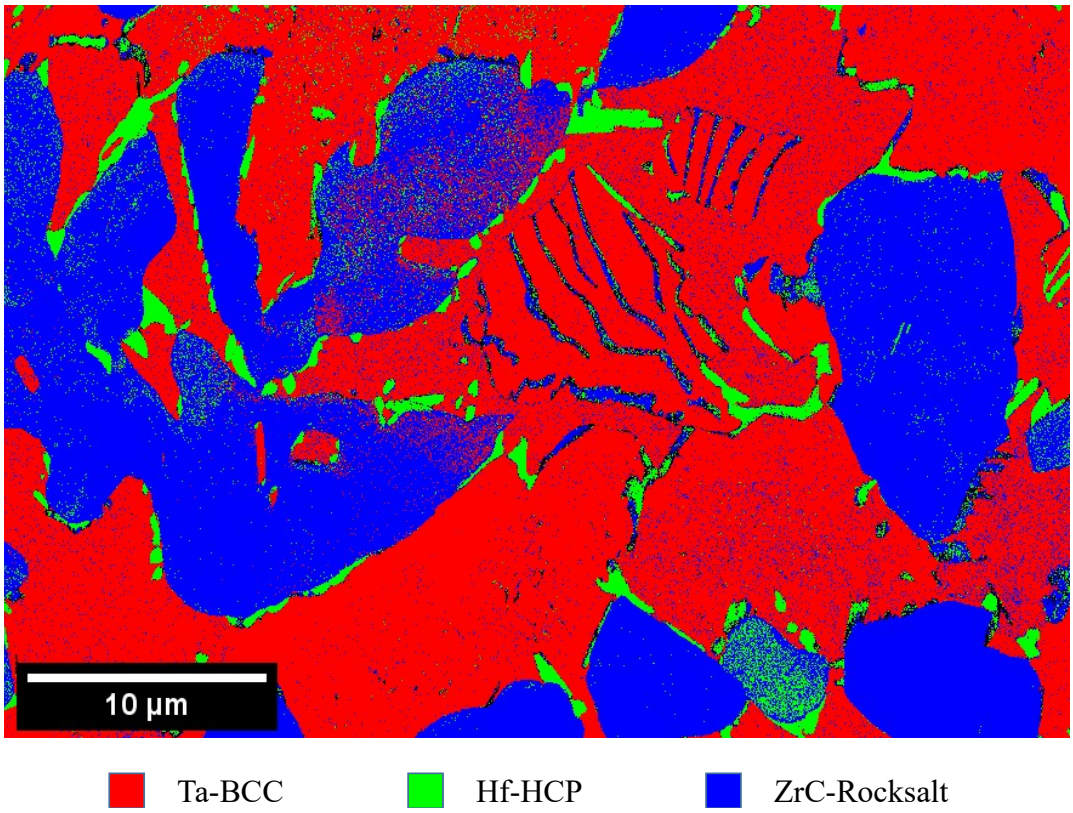

Figure 4.22: EBSD phase map of 5eqA, indexed for Ta-BCC, Hf-HCP, and ZrC-Rocksalt.

Back-scatter images show at least two types of precipitates: dark-contrast ones, presumably with high impurity concentrations, and lighter-contrast ones with lower impurity concentrations. Figure 4.23 shows an example of this.

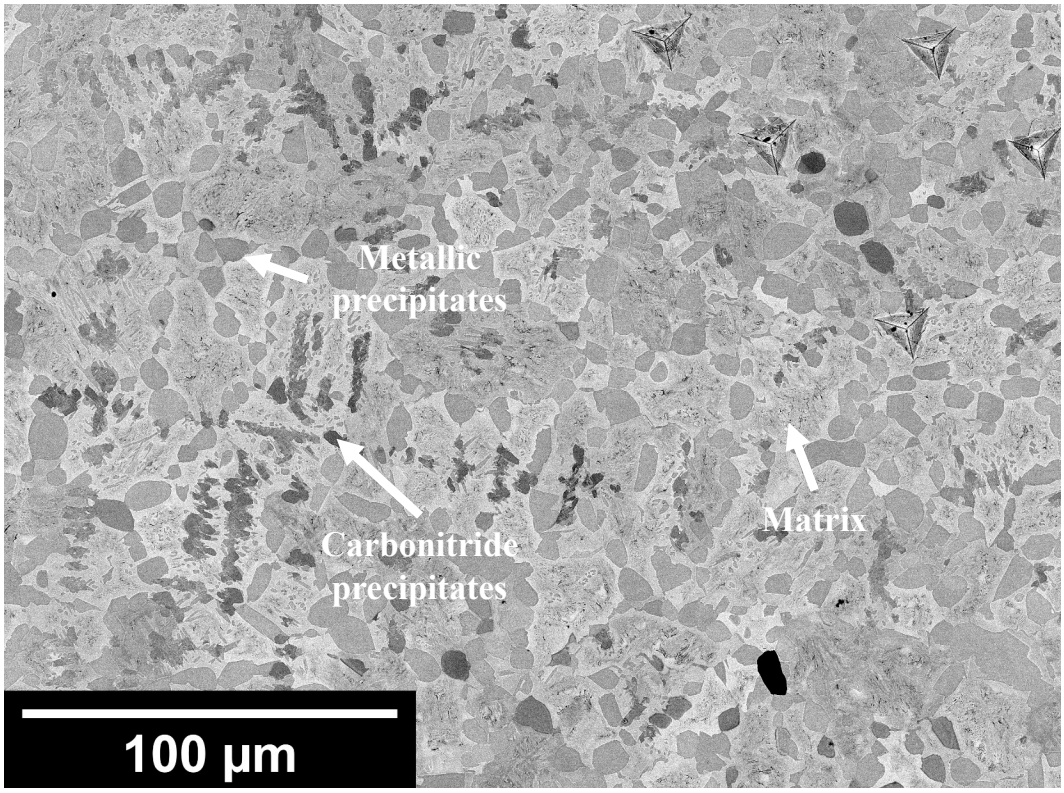

Figure 4.23: Back-scatter SEM image of a 5eqA sample, showing that the precipitates have a variety of contrasts, most likely due to differences in impurity concentrations leading to differences in average Z number.

4.3.3 Optimised TiVZrHfTa

The composition of optimised TiVZrHfTa (5optC) is given in table 4.7, and the microstructure has been analysed by XRD and indexed in figure 4.24. It shows that 5optC is much closer to being single phase than the equiatomic variant of TiVZrHfTa, possibly due to the lower impurity concentrations. The alloy is primarily BCC but contains a small fraction of the rocksalt phase; which could not be found with SEM analysis. The volume fractions and lattice parameters of these two phases calculated by XRD are shown in table 4.15.

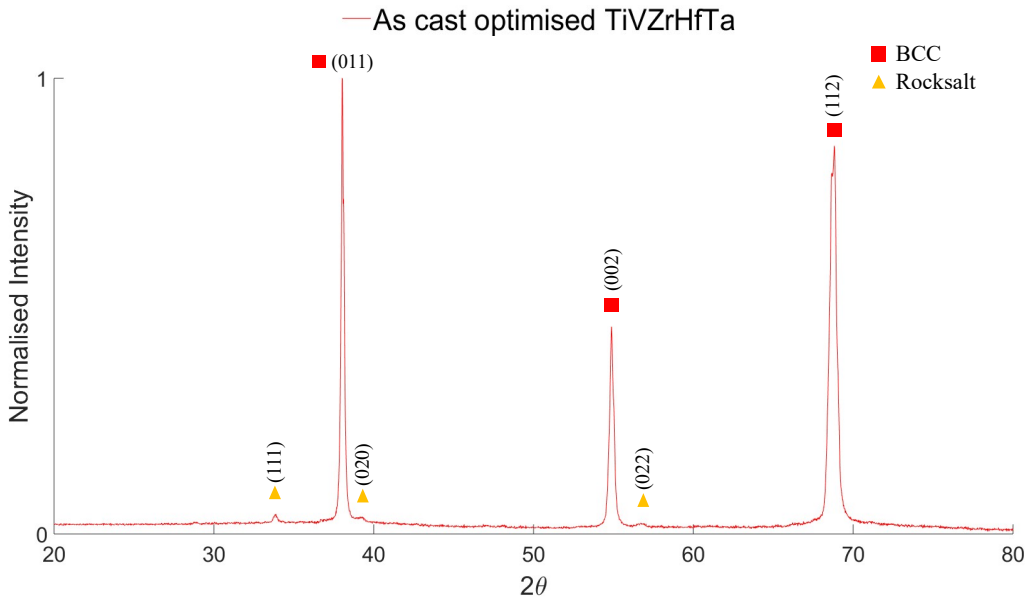

Figure 4.24: XRD trace of as-cast optimised TiVZrHfTa. Two phases have been identified: a BCC phase and a rocksalt-structured phase.

5optC Phases	Lattice parameters Å	Volume Fraction (vol%)
BCC1 (red)	a=3.35	92.4
Rocksalt (yellow)	a=4.59	7.6

Table 4.15: Table comparing the lattice parameters and volume fractions determined by XRD in 5optC

4.3.3.1 Low temperature annealing

During the two ion-implantation studies samples discussed in chapter 7, the samples were held at 500 °C for different periods of time. It was initially thought that this had caused no change in microstructure, however, changes in hardness and modulus were observed when comparing nanoindentation from the unimplanted region of each sample: this is shown in figure 4.25. Table 4.16 shows the composition by EDX of each sample. The spectra were taken of an area in the centre of each sample at minimum possible magnification. It can be seen that the three compositions are

very similar: any differences in microstructure or mechanical properties are not due to compositional variations.

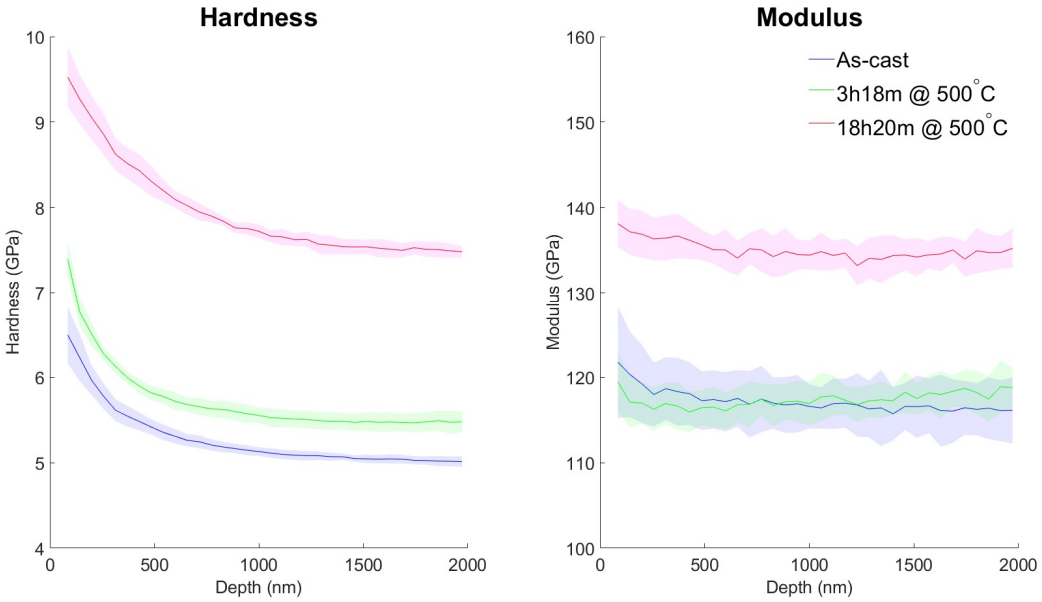

Figure 4.25: Nanoindentation data from three samples of 5optc which either in the as-cast state or after being held at 500 °C 3h and 18m or 18h and 20m. The shaded regions are the standard deviation of the data.

Element	Adjusted AMG (at%)	As cast Sample (at%)	500 °C for 3h18m (at%)	500 °C for 18h20m (at%)
Ti	32.98	32.55	32.03	32.44
V	14.97	14.49	15.21	14.26
Zr	14.85	13.90	13.91	14.23
Hf	16.78	17.65	17.70	17.98
Ta	20.42	21.40	21.15	21.10
δ_{ave}	0.0	0.74	0.75	0.75

Table 4.16: Table comparing the compositions of 5optC in the as-cast condition, as well as after annealing at different times at 500 °C to the composition provided by AMG, adjusted to only consider the metallic elements. The δ_{ave} is the average deviation from this composition. Data is from a single EDX Point&ID scan taken at minimum magnification. There is no standard deviation given as there is only one scan per sample.

Higher magnification images show that in the samples that have been held at 500 °C there has been some precipitation. Figures 4.26 and 4.27 show EDX line scans of these precipitates; which are enriched in Zr and Hf and depleted in Ti. In the sample that has been annealed for the longer time the precipitates are more pronounced and the chemical segregation is more extreme, which could explain the variation in mechanical properties shown in figure 4.25. As previously stated no precipitates can be found in the as-cast sample, indicating that the heat treatment has caused the microstructural evolution.

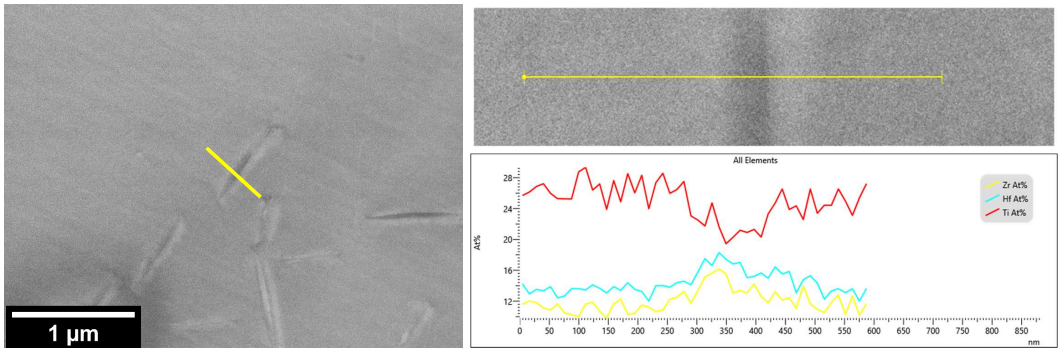

Figure 4.26: Back-scatter SEM image of optimised TiVZrHfTa after annealing at 500 °C for 3h18m. Includes EDX Linescans of the Ti, Zr, and Hf signals across a precipitate.

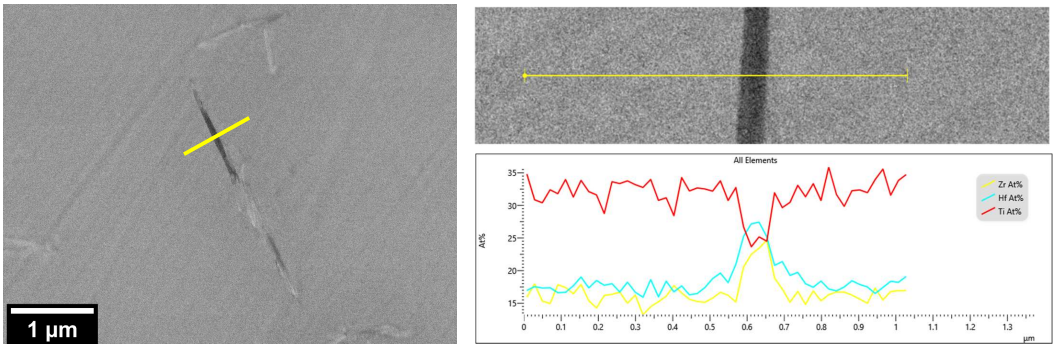

Figure 4.27: Back-scatter SEM image of optimised TiVZrHfTa after annealing at 500 °C for 18h20m. Includes EDX line scans of the Ti, Zr, and Hf signals across a precipitate.

This lack of thermal stability makes this alloy already undesirable for application in any fusion environments. It also demonstrates that despite the matrix of this alloy being a solid solution phase similar to the ideal microstructure of an HEA, it has not been prevented from phase separating either by any thermodynamic stability or sluggish diffusion.

4.3.4 Annealed optimised TiVZrHfTa

After the standard annealing treatment of 24 hours at 1400 °C followed by furnace cooling, the as-cast structure breaks down further and the fraction of rocksalt phase increases. The XRD trace for the annealed sample (5optA) is more difficult to analyse as there was substantial grain growth during the annealing process; the average grain area by EBSD is 35 000 μm^2. This grain growth resulted in the relative peak intensities being skewed and so were unreliable for quantitative analysis, see section 3.3 for details. Despite this the peak locations in 2θ can still be analysed and the trace is indexed in figure 4.28.

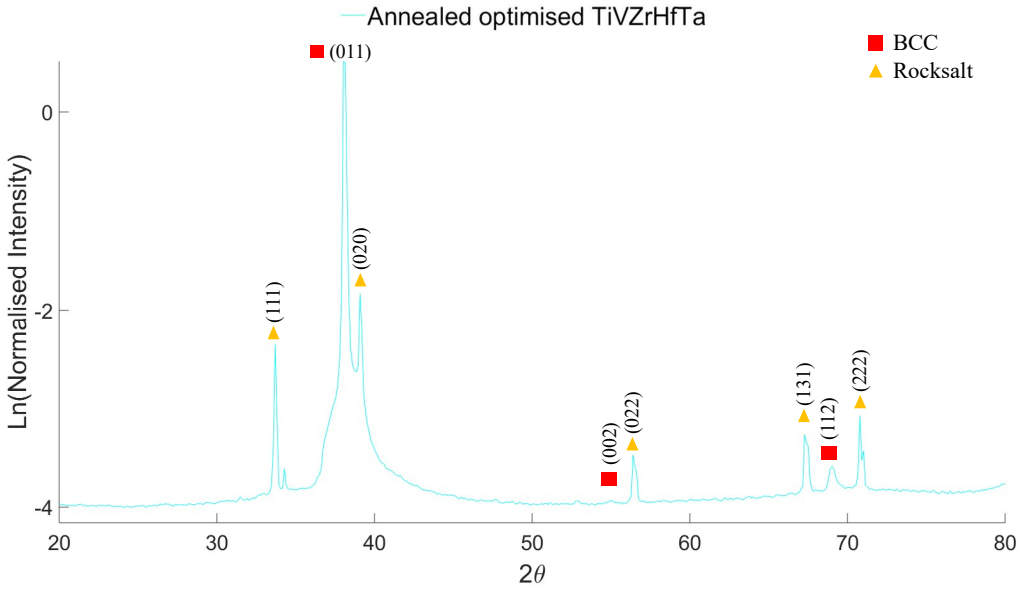

Figure 4.28: XRD trace of annealed optimised TiVZrHfTa. Two phases have been identified: a BCC phases and a phase with the rocksalt structure.

The XRD data shows 5optA has a BCC matrix with rocksalt-structured precipitates. Figure 4.29 shows a secondary electron image with an EBSD phase map overlaid, indexed for Ta-BCC and ZrC-rocksalt. This is corroborated by the EDX: table 4.17 shows a comparison of composition and average Z number between the matrix and precipitate phase in 5optA. The precipitates' average Z number is much higher than for the matrix, yet still the majority of precipitates are darker in back-scatter electron images, meaning they must contain a majority of the impurities, which are all have a low Z number.

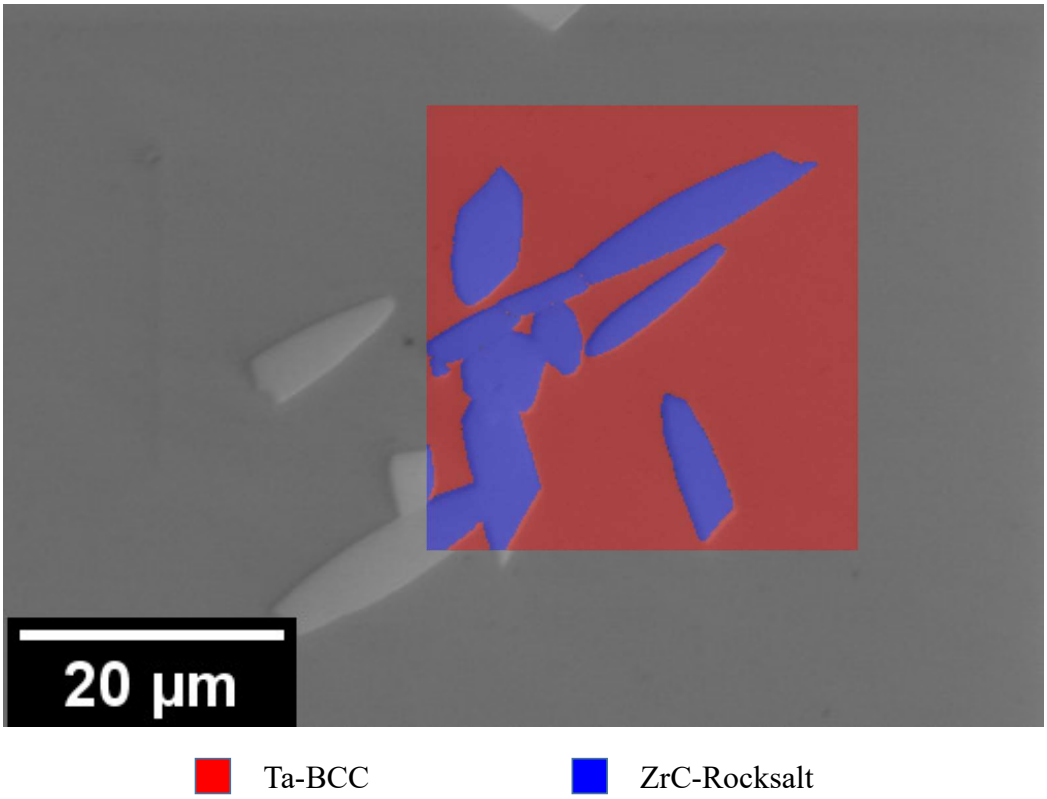

Figure 4.29: Secondary electron image of 5optA with an EBSD phase map overlaid, indexed for Ta-BCC and ZrC-Rocksalt.

Element	Matrix Composition (at%)	Precipitate Composition (at%)
Ti	34.86 ± 0.4	5.17 ± 0.5
V	15.63 ± 0.4	0.27 ± 0.3
Zr	13.08 ± 0.3	37.28 ± 1.4
Hf	14.73 ± 0.1	54.60 ± 1.5
Ta	21.69 ± 0.2	2.69 ± 0.4
Z_{ave}	42.9	57.4

Table 4.17: Table comparing the composition and average Z number of the matrix and precipitates in 5eqA. The composition of the matrix is reproduced from table 4.18 and the composition of the precipitates is an average of 15 EDX spectra. The error values are the standard deviation of this data.

It is worth noting that there is a large variation in contrast between some of the precipitates, as shown in figure 4.30. The EDX spectra used in table 4.17 are taken from these however, and the composition of the metallic elements across all of them is consistent. The contrast could be due to variations in impurity concentration, although this is unlikely due to how large the differences in contrast is. The differences in contrast are most likely due to a combination of impurity concentration and a channelling effect, whereby the penetration depth of electrons (and so the measured signal) varies depending on crystal orientation.

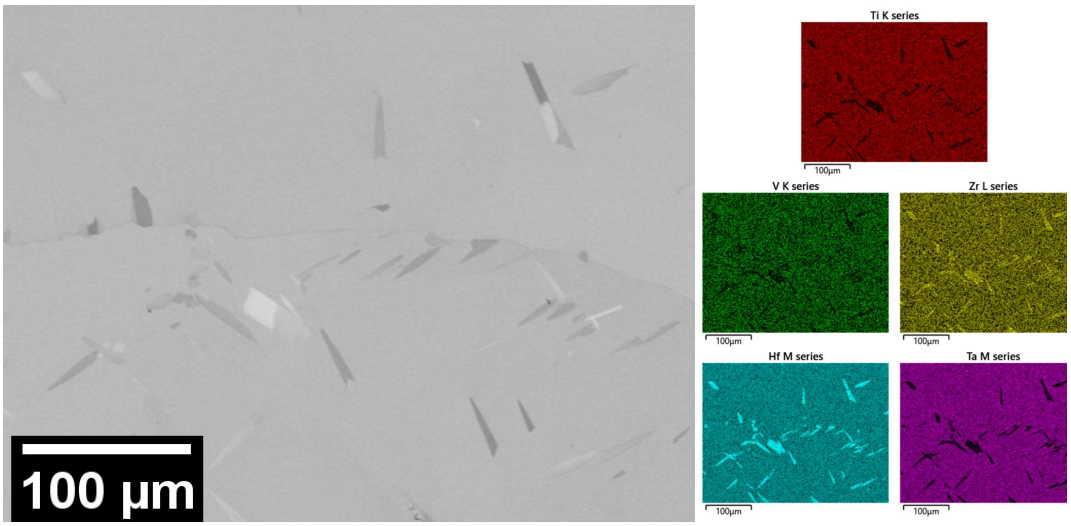

Figure 4.30: Back-scatter SEM image of optimised TiVZrHfTa in the annealed state at high magnification. It includes EDX maps for each element, showing the precipitation that has occurred.

It is remarkable that even though the 5opt billet contains the lowest amount of impurities, it has still been sufficient to cause the formation of of a rocksalt-structured phase. The tolerance of this alloy to contamination is very low, and the fact that there is sufficient diffusion occurring at 500 °C for precipitation to occur suggests that diffusion is not sluggish in TiVZrHfTa alloys.

4.3.5 As cast and Annealed comparison

The composition of 5optC and the matrix of 5optA are shown in table 4.18, along with the target composition. Although not completely accurate, it can be seen that there has been only a limited change in composition due to melting and due to annealing. It is of note that this sample has the lowest concentrations of impurities (see table 4.3), and also the lowest amount of phase separation. It is not possible to know whether the relative thermodynamic stability of the matrix composition is due to "the high-entropy effect" or whether it is simply due to a lower amount of impurities encouraging the phases to separate.

Element	Target Composition (at%)	5optC Composition (at%)	5optA Matrix Composition (at%)
Ti	35.1	31.92 ± 0.4	34.86 ± 0.4
V	13.7	14.96 ± 0.2	15.63 ± 0.4
Zr	13.1	14.74 ± 0.5	13.08 ± 0.3
Hf	19.4	17.69 ± 0.1	14.73 ± 0.1
Ta	18.6	20.70 ± 0.1	21.69 ± 0.2

Table 4.18: Table comparing the compositions of bulk 5optC and the matrix of 5optA. Data for the fomer was taken as an EDX Point&ID area scan at the lowest possible magnification from three different areas. The compostion of the matrix of 5optA is averaged from five sepate EDX Point&ID spectra. The error values given are the standard deviation of this data.

4.4 TiVZrTa

The four component alloy TiVZrTa is the second alloy system described here. The target compositions of the equiatomic and optimised alloys are shown in table 4.19.

Element	Equiatomic Compostion (at%)	Optimised Composition (at%)
Ti	25	35.7
V	25	16.1
Zr	25	16.1
Ta	25	32.1

Table 4.19: Table comparing the target compositions of equiatomic and optimised TiVZrTa.

4.4.1 As cast Equiatomic TiVZrTa

The microstructure of as-cast equiatomic TiVZrTa (4eqC) has been analysed by XRD and indexed in figure 4.31. It shows there are three BCC phases with lattice parameters of 3.48, 3.27, and 3.21 Å and a rocksalt-structured phase with a lattice parameter of 4.58 Å.

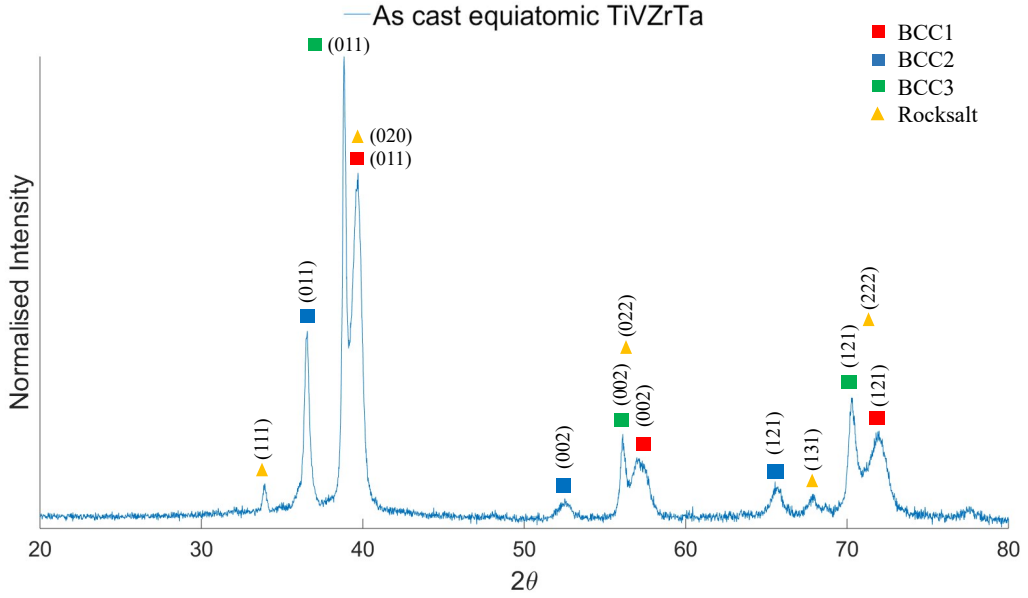

Figure 4.31: XRD trace of as-cast equiatomic TiVZrTa. Four phases have been identified: three BCC phases and phase with the rocksalt structure.

4eqC Phases	Lattice parameters Å	Volume Fraction (vol%)
BCC1 (red)	a=3.28	48.7
BCC2 (blue)	a=3.48	15.8
BCC3 (green)	a=3.22	32.1
Rocksalt (yellow)	a=4.58	3.4

Table 4.20: Table comparing the lattice parameters and volume fractions determined by XRD in 5optC

A back-scatter image of 4eqC is shown in figure 4.32 along with EDX Maps showing the distribution of metallic elements. It can be seen that the dendrites are in enriched in Ta (and to a lesser extent V), while the interdendritic region are enriched in Zr. There are also at least two precipitate phases in the interdendritic region: one enriched in V, one enriched in Zr. There is also fine scale phase separation occurring in the dendrites and interdendritic regions, which are highlighted in blue and red respectively. Although these are visible in the back-scatter signal, they could not

be resolved by EDX or EBSD. Figure 4.33 shows an Argus image of 4eqC with an EBSD phase map overlaid, which has been indexed for Ta-BCC and ZrC-Rocksalt. The Zr-rich precipitates are identified as the rocksalt phase, while the remainder of the sample is indexed as Ta-BCC. If the data is indexed for the three BCC phases taken from figure 4.31, then the software is unable to distinguish between them and picks only one; this is due to the lattice parameter resolution of EBSD being quite coarse ($\sim$10%). Based on this the single BCC phase shown in figure 4.33 is most likely a combination of all three BCC phases identified with XRD.

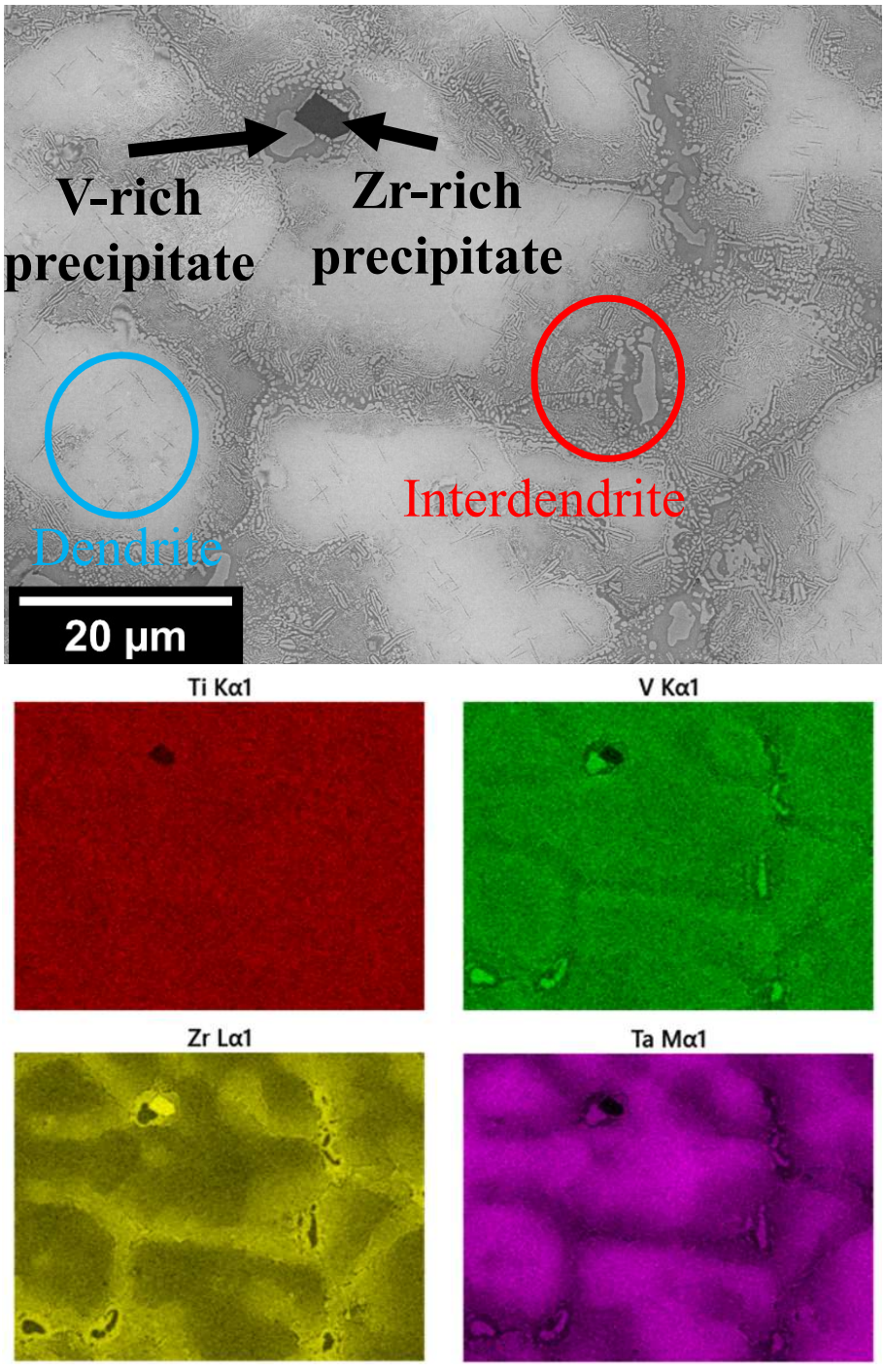

Figure 4.32: Back-scatter SEM image of 4eqC, along with EDX maps showing the distribution of the metallic elements in the alloy.

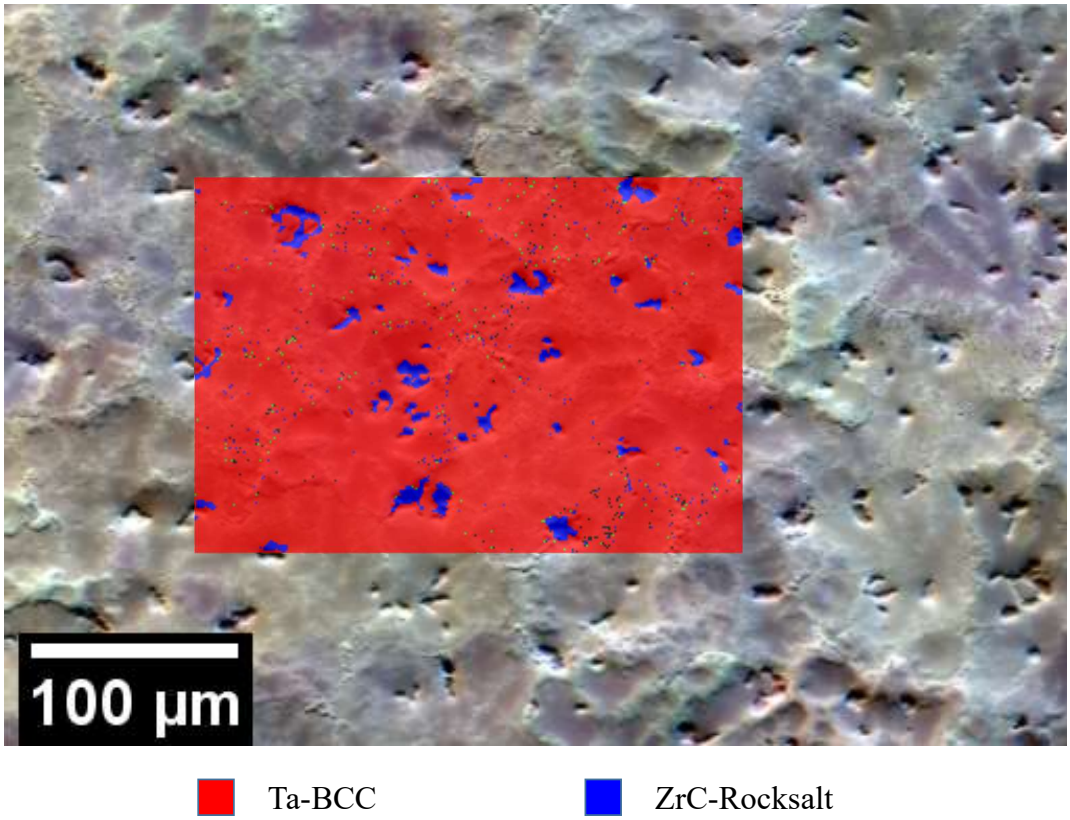

Figure 4.33: Argus image of 4eqC with an EBSD phase map overlaid, indexed for Ta-BCC and ZrC-Rocksalt.

The compositions and average Z number of the dendritic and interdendritic regions has been analysed by averaging five EDX Point&ID area scans in table 4.21. The compositions and average Z number of the two large precipitate phases has similarly been averaged from three area scans in table 4.22.

Element	Dendrite Composition (at%)	Interdendritic Composition (at%)
Ti	24.36 ± 0.3	24.84 ± 0.5
V	26.18 ± 1.8	21.22 ± 1.2
Zr	18.31 ± 0.6	40.23 ± 0.8
Ta	31.15 ± 1.8	13.70 ± 0.6
Z_{ave}	41.4	36.4

Table 4.21: Table comparing the composition and average Z numbers of the dendrites and interdendritic regions of 4eqC. These are calculated from five EDX Point&ID area scans, and the errors are the standard deviation of this data.

Element	Zr-rich Phase (at%)	V-rich Phase (at%)
Ti	6.57 ± 1.5	22.43 ± 0.1
V	0.06 ± 0.1	45.82 ± 0.1
Zr	92.33 ± 1.4	9.46 ± 0.2
Ta	1.05 ± 0.2	22.29 ± 0.2
Z_{ave}	39.2	35.53

Table 4.22: Table comparing the composition and average Z numbers of the Zr-rich and V-rich precipitates in 4eqC. These are from three EDX Point&ID area scans, and the errors are the standard deviation of this data.

The EDX compositions are used to calculate the average Z numbers, which do not correlate with the contrast in the back-scatter SEM image. The dendrite phase correctly appears brighter than the interdendritic region, however the Zr-rich precipitate should appear brighter than the surrounding material, yet they are the darkest phase. Similarly, the V-rich precipitate has a very low average Z number suggesting it should appear dark in back-scatter, despite the grey-scale value being indistinguishable from the interdendritic region as a whole. Thus, the low Z impurities are concentrated in the Zr-rich regions of 4eqC.

4.4.2 Annealed Equiatomic TiVZrTa

The microstructure of annealed equiatomic TiVZrTa (4eqA) has been analysed by XRD and is indexed in figure 4.34. It shows that the microstructure has evolved to show two BCC phases, an HCP phase, and a rocksalt-structured phase. The lattice parameters and volume fractions as calculated by XRD are shown in table 4.23.

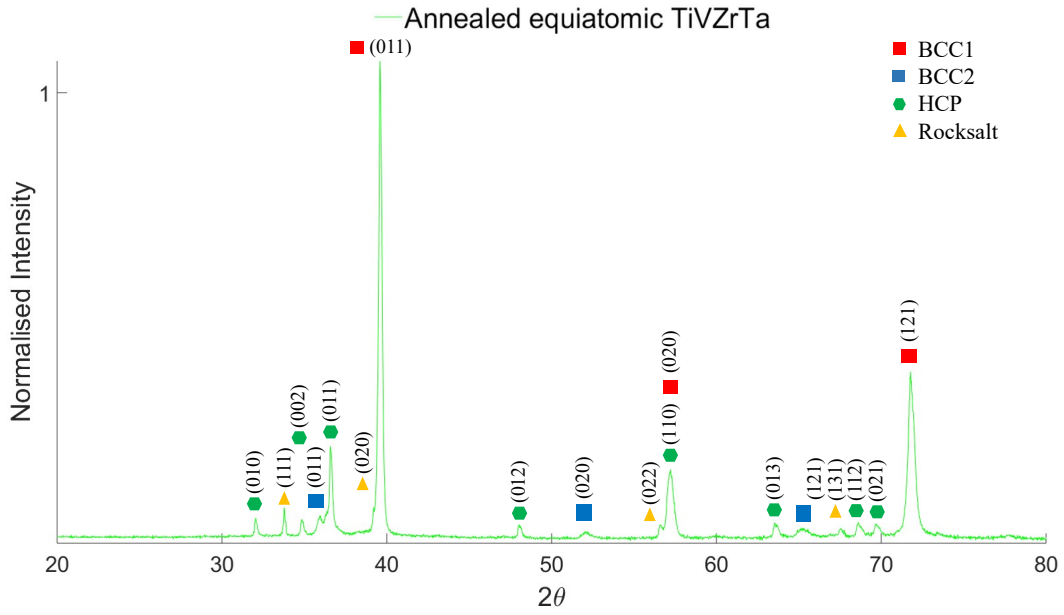

Figure 4.34: XRD trace of annealed equiatomic TiVZrTa. Four phases have been identified: two BCC phases, an HCP, and phase with the rocksalt structure.

4eqA Phases	Lattice parameters Å	Volume Fraction (vol%)
BCC1 (red)	a=3.22	69.2
BCC2 (blue)	a=3.51	10.1
HCP (green)	a=3.42, c=5.14	17.4
Rocksalt (yellow)	a=4.59	3.3

Table 4.23: Table comparing the lattice parameters and volume fractions determined by XRD in 4eqA

The microstructure of 4eqA varies dramatically across the sample according to the grain size; in order to demonstrate this two back-scatter images from the same sample are shown in figure 4.35. The left-hand image shows a collection of grain boundaries, all of which have formed a thick dark phase; similar phases have also formed in the centre of grains. The right-hand image shows a different region where the thicker phase has precipitated at some grain boundaries, but internally each grain has phase separated into a layered structure, this is also shown at greater magnification in figure 4.36

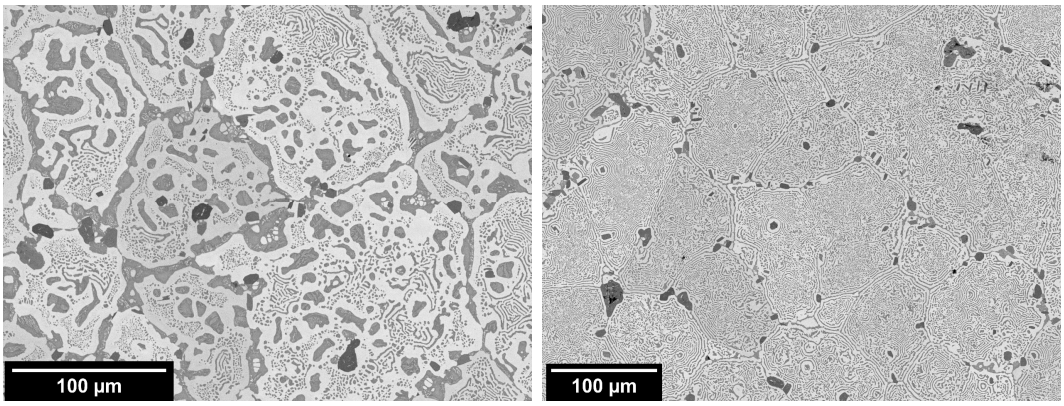

Figure 4.35: Back-scatter images of 4eqA. The left-hand images shows that the grains have phase separated into two fine scale layers, while the grain boundaries have formed a thicker separate phase.

Identifying the crystal structures of these phases with EBSD is difficult. Figure 4.36 shows two secondary electron images with EBSD phase maps overlaid. The light contrast matrix phase is consistently indexed as BCC, but the darker contrast phase varies between rocksalt and HCP. As stated previously these two structures share vary similar Kikuchi diffraction patterns thus making differentiating them difficult.

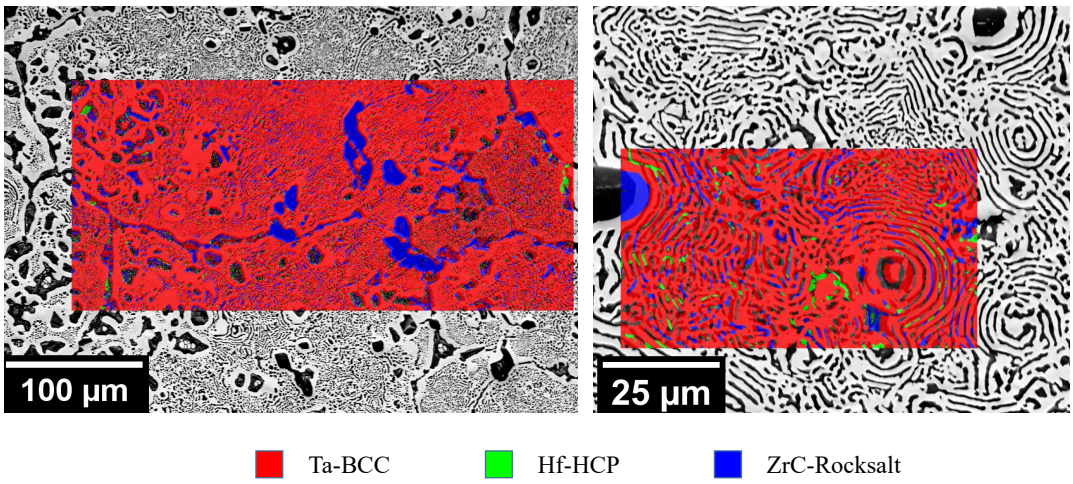

Figure 4.36: Secondary electron image of two regions of 4eqA with EBSD phase maps overlaid, indexed for Ta-BCC, Zr-HCP, and ZrC-Rocksalt.

The structure of the phases in 4eqA appears visually similar to pearlite and other eutectoid alloys, suggesting that these phases have formed cooperatively. Figure 4.37 shows an EBSD phase map and IPF-Z map; it can be seen that within a BCC grain many of the rocksalt/HCP phases have the same crystal orientation. In a eutectoid microstructure this can happen as when the alternative phase nucleates on the boundary of the previous phase there is a low energy crystallographic configuration which is repeated at each boundary: this leads to separate layers having the same orientation [186].

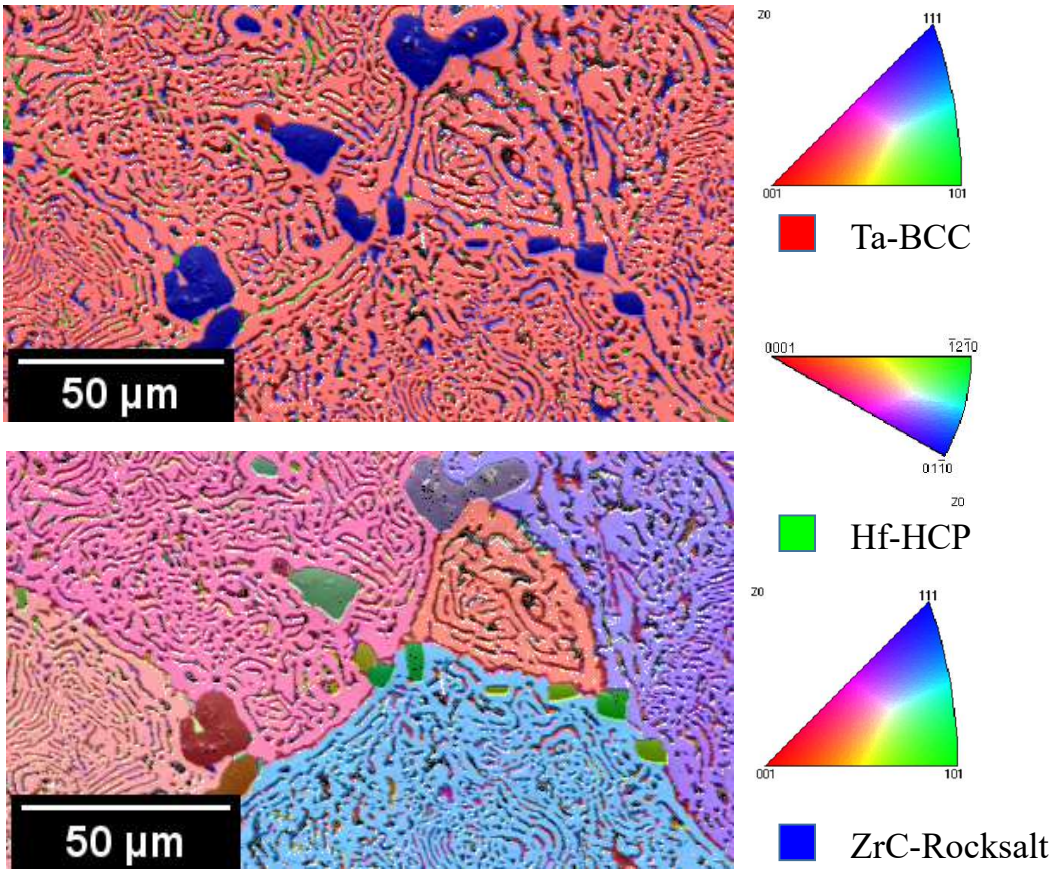

Figure 4.37: Secondary electron image of 4eqA, the top map is overlaid with the EBSD phase map and the bottom with the IPF-Z map. The inverse pole figures relating to the orientation of each phase are shown to the right.

In order to better assess the orientation relationships between the phases in 4eqA, pole figures for Ta-BCC and ZrC-Rocksalt are compared in figure 4.38. This has been done for the two bottom grains shown in figure 4.37. These pole figures show an alignment relationship between the $\{1\,1\,1\}$ and $\{1\,1\,0\}$ planes, which is reciprocated in both materials. This orientation relationship is to be expected as both plane types are close packed, adding evidence that that this microstructure forms cooperatively.

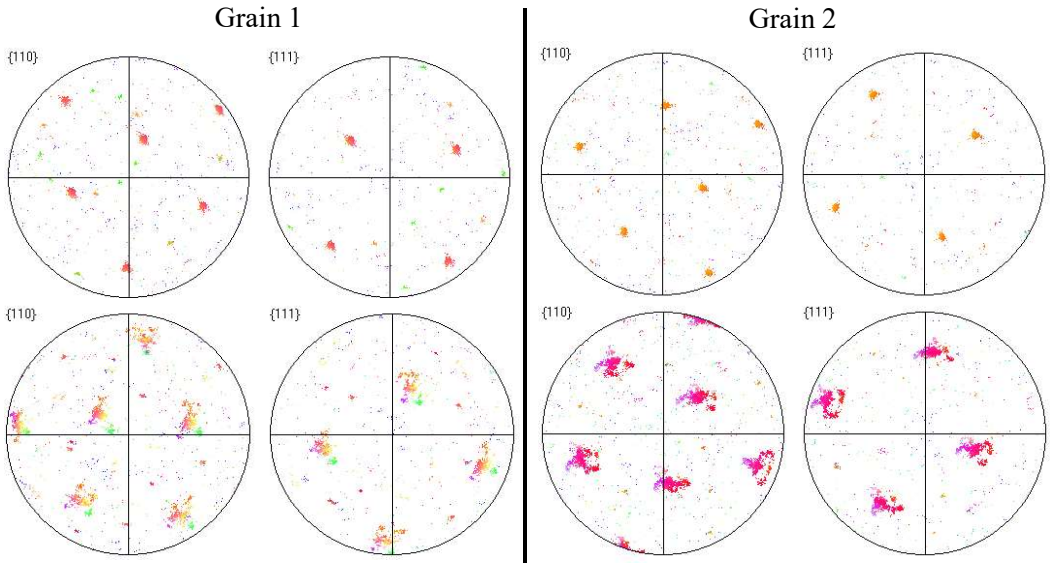

Figure 4.38: Pole Figures showing the grain orientations of the Ta-BCC phase (top), and the ZrC-Rocksalt phase (bottom) in the bottom two grains shown in figure 4.37. It can be seen that there is alignment between the $\{1\,1\,1\}$ planes and four of the $\{1\,1\,0\}$ planes in both phases.

Extracting the compositions of each distinct phase with EDX is difficult in this alloy as many of the phases are not clearly distinct from one another in back-scatter or secondary imaging. Figure 4.39 shows a back-scatter image of one region of 4eqA, along with EDX maps showing the distribution of metallic elements. There is a matrix phase, and then two sub-phases: one broken up into small bits reminiscent of the shape of coral, and the other in bigger blocks. This region was then analysed with EDX Point&ID analysis in order to extract the compositions and average Z numbers shown in table 4.24.

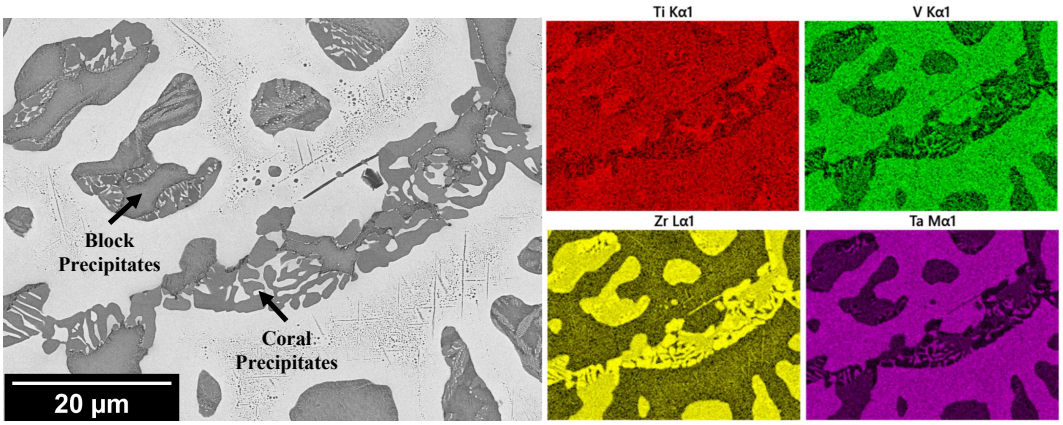

Figure 4.39: Back-scatter SEM image of 4eqA along with EDX Maps showing the distribution of metallic elements.

Element	Matrix Phase (at%)	Coral precipitates (at%)	Block Precipiates (at%)
Ti	24.84 ± 0.7	11.30 ± 0.1	33.44 ± 1.4
V	32.17 ± 0.9	0.62 ± 0.2	5.98 ± 0.4
Zr	11.24 ± 1.6	87.40 ± 0.1	55.17 ± 1.1
Ta	31.76 ± 0.2	0.68 ± 0.1	5.41 ± 0.5
Z_{ave}	40.5	38.1	39.4

Table 4.24: Table comparing the composition and average Z number of some of the phases identified in 4eqA. Data was collected using EDX Point&ID sacns and has been averaged from three separate spectra. The errors given are the standard deviation of this data.

These compositions and average Z numbers correlate with the back-scatter contrast, and it is difficult to learn much from it that is not apparent in the EBSD data: the impurities have moved to the grain boundaries where rocksalt and HCP phases have formed.

4.4.3 As cast Optimised TiVZrTa

The microstructure of as-cast optimised TiVZrTa (4optC) has been analysed by XRD. The trace is indexed in figure 4.40 and shows a BCC phase and a rocksalt

phase; their lattice parameters and volume fractions calculated by XRD are shown in table 4.25.

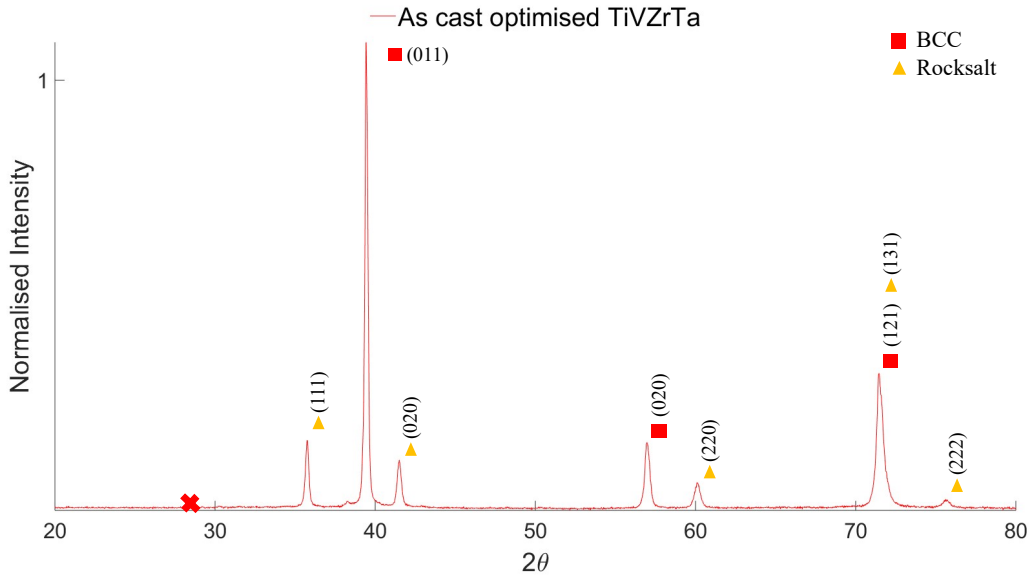

Figure 4.40: XRD trace of as-cast optimised TiVZrTa. Two phases have been identified: a BCC phase and a rocksalt-structured phase.

4eqC Phases	Lattice parameters Å	Volume Fraction (vol%)
BCC1 (red)	a=3.23	77.3
Rocksalt (yellow)	a=4.36	22.7

Table 4.25: Table comparing the lattice parameters and volume fractions determined by XRD in 4optC

Two back-scatter SEM images of 4optC are shown in figure 4.41 along with a secondary electron image with an EBSD phase map overlaid in figure 4.42. There are two larger phases: a BCC matrix and rocksalt-structured precipitates, and then inside each of these there are also a set of sub-precipitates of the opposing crystal structure.

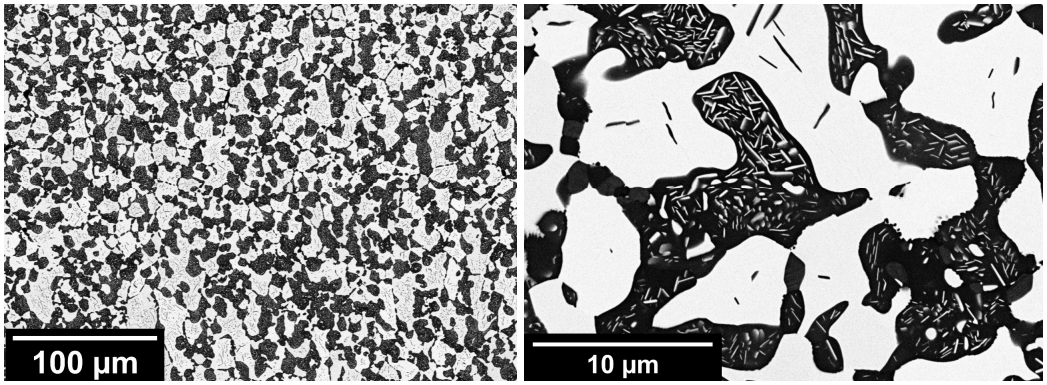

Figure 4.41: Back-scatter SEM image of 4optC, showing two large scale phases each containing sub-precipitates.

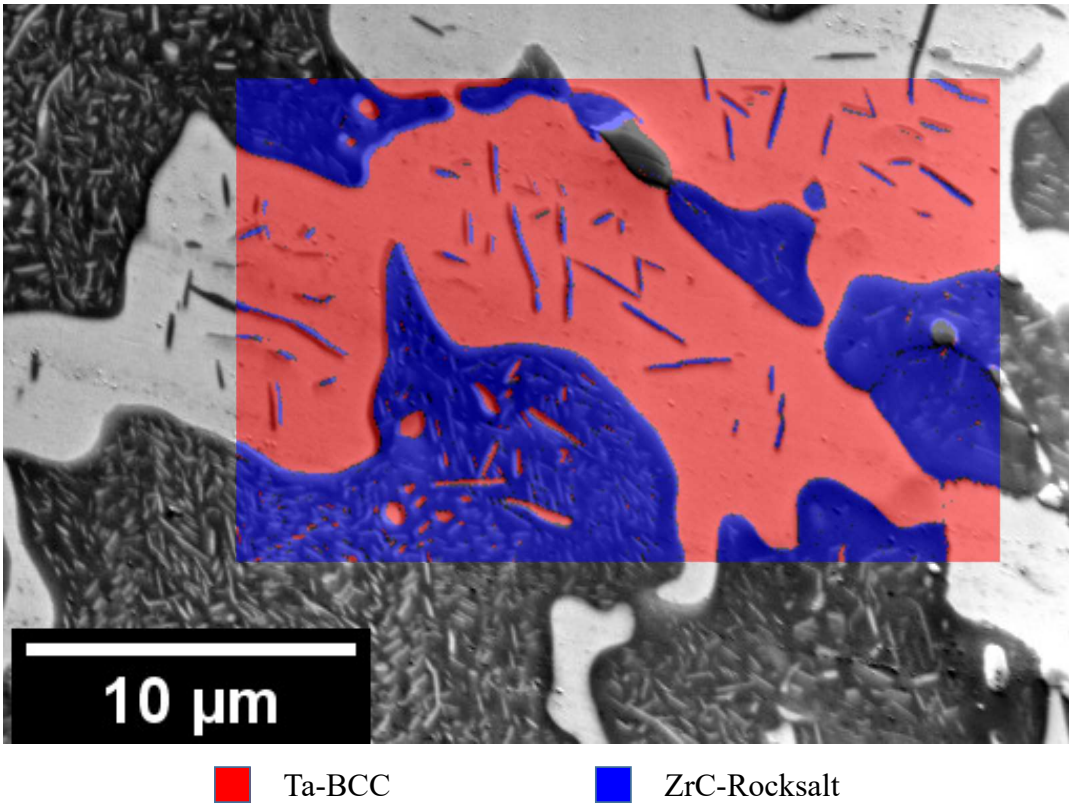

Figure 4.42: Secondary electron image of two regions of 4optC with an EBSD phase map overlaid, indexed for Ta-BCC and ZrC-Rocksalt.

The composition and average Z number of these phases has been analysed by EDX and is shown in table 4.26. It shows that the BCC phases are enriched in Ta (and to a lesser extent V). The rocksalt phases are enriched in Ti and Zr. The compositions of the sub-precipitates are more difficult to quantify than most phases as they are so small: the EDX spot likely encompasses some of the surrounding phase, and is likely why the standard deviations on these concentrations are higher than the larger phases.

	Light contrast Phase (at%)	Sub-precipitates (at%)	Dark contrast Precipitates (at%)	Sub-Precipiates (at%)
Ti	14.24 ± 0.7	41.55 ± 0.7	59.49 ± 1.2	16.19 ± 1.5
V	25.37 ± 0.5	10.04 ± 1.1	1.73 ± 0.1	23.98 ± 1.1
Zr	1.89 ± 0.1	22.55 ± 1.0	35.92 ± 1.0	4.72 ± 2.4
Ta	58.50 ± 0.1	26.70 ± 1.8	2.86 ± 0.8	54.84 ± 2.8
Z_{ave}	52.4	40.0	29.94	51.06

Table 4.26: Table comparing the composition and average Z number of the phases in 4optC. Data was collected using EDX Point&ID scans and has been averaged from three separate spectra. The errors given are the standard deviation of this data.

The contrast in the back-scatter images is consistent with the average Z numbers calculated from the EDX compositions. However, it is highly likely that the compositions of the rocksalt phases are incorrect, as there must be a high fraction of impurities in these phases.

4.4.4 Annealed Optimised TiVZrTa

The microstructure of annealed optimised TiVZrTa (4optA) has been analysed by XRD, and has been indexed in figure 4.43. It shows that the phases are thermally stable, having not changed structure or lattice parameter after being heat treated (shown in table 4.27); this is in sharp contrast to the alloys previously discussed

which have all phase separated or evolved after heat treatments.

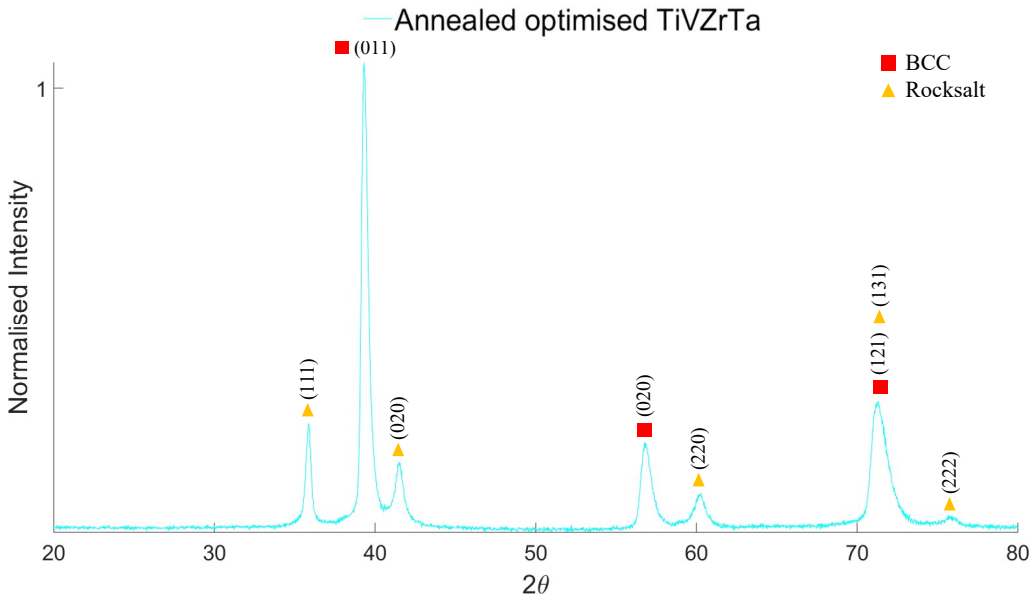

Figure 4.43: XRD trace of annealed optimised TiVZrTa. Two phases have been identified: a BCC phase and a rocksalt-structured phase.

4eqC Phases	Lattice parameters Å	Volume Fraction (vol%)
BCC1 (red)	a=3.24	73.9
Rocksalt (yellow)	a=4.35	26.1

Table 4.27: Table comparing the lattice parameters and volume fractions determined by XRD in 4optA

Back-scatter and EBSD micrographs of 4optA in figure 4.44 and 4.45 show that, similar to the as-cast state, there are two large scale phases each containing sub-precipitates of the opposite phase.

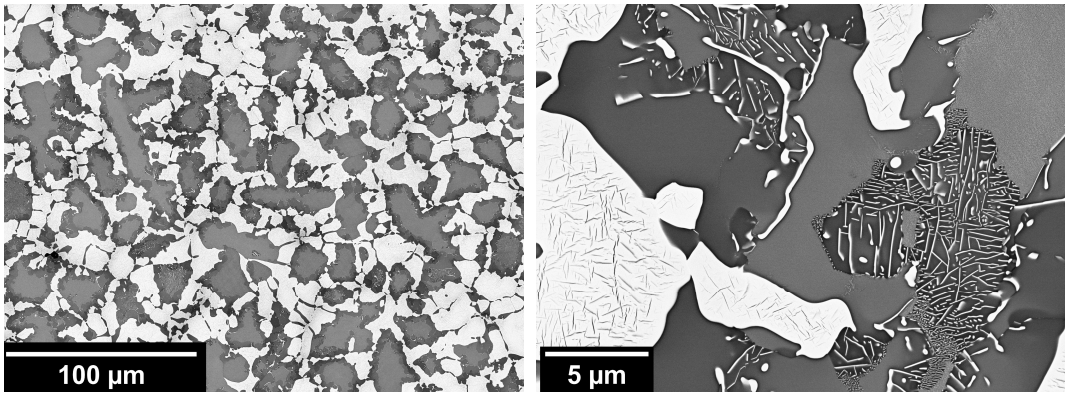

Figure 4.44: Back-scatter SEM images of 4optA, showing two large scale phases each containing sub-precipitates.

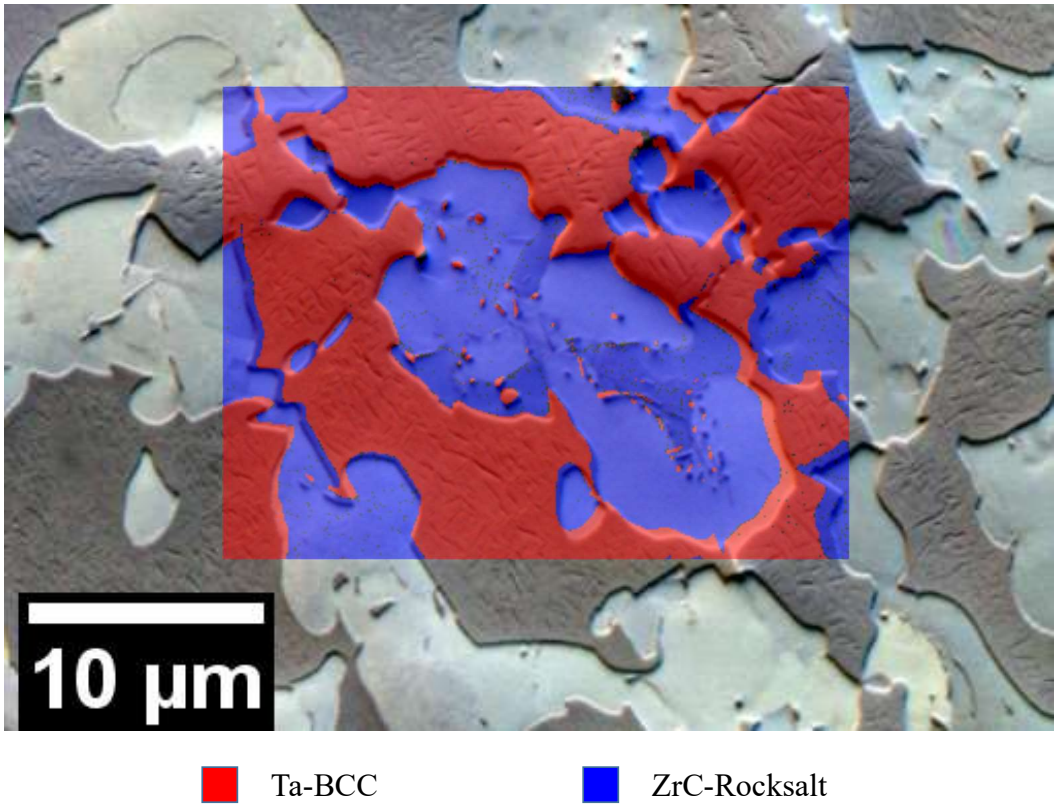

Figure 4.45: An Argus image of two regions of 4optA with an EBSD phase map overlaid, indexed for Ta-BCC and ZrC-Rocksalt.

The composition of the phases has been analysed by EDX and is shown in table 4.28. The light contrast phase is enriched in Ta (and to a lesser extent V); its sub-precipitates are enriched in Ti and Zr. The dark contrast phase is enriched in Ti (and to a lesser extent Zr); its sub-precipitates are comparatively enriched in Ta, but still have a high concentration of Ti and Zr.

Element	Light-contrast Phase (at%)	Sub-precipitates (at%)	Dark-contrast Phase (at%)	Sub-Precipiates (at%)
Ti	18.41 ± 1.3	29.00 ± 1.6	55.07 ± 1.3	43.22 ± 2.6
V	21.45 ± 1.6	12.49 ± 1.6	3.30 ± 1.2	7.34 ± 0.9
Zr	5.00 ± 0.9	16.60 ± 2.2	27.51 ± 0.9	23.94 ± 1.2
Ta	55.14 ± 1.0	41.90 ± 2.3	14.12 ± 1.6	25.49 ± 2.7
Z_{ave}	51.2	46.5	34.2	39.4

Table 4.28: Table comparing the composition and average Z number of the large phases and sub-precipitates in 4optA. Data is extracted from EDX Linescans as individual spectra at points of minimum or maximum Ti-concentration. The data shown is an average of seven separate spectra each, and the error is the standard deviation of this data.

The average Z numbers from these EDX compositions correlate to the contrast observed in the back-scatter images. However, based on the EBSD data shown in figure 4.45 it is clear that the impurities are grouped in the dark contrast TiZr rich phases in this alloy.

4.5 TiVTa

The three component alloy TiVZrTa is the third and final alloy system described here. The target compositions of the equiatomic and optimised alloys are shown in table 4.29.

Element	Equiatomic Compostion (at%)	Optimised Composition (at%)
Ti	33.3	36.5
V	33.3	14.6
Ta	33.3	48.8

Table 4.29: Table comparing the target compositions of equiatomic and optimised TiVTa.

4.5.1 As cast Equiatomic TiVTa

The microstructure of equiatomic TiVTa in the as-cast state (3eqC) has been analysed by XRD in figure 4.46. Two phases have been indexed, a BCC phase and a rocksalt phase; their lattice parameters and volume fractions calculated by XRD are shown in table 4.30

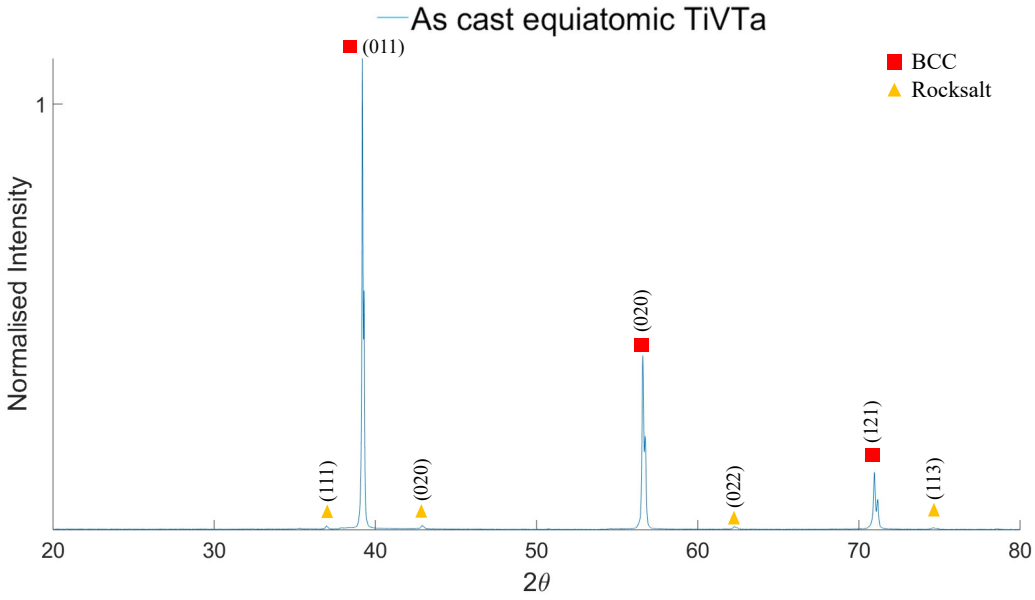

Figure 4.46: XRD trace of as-cast equiatomic TiVTa. Two phases have been identified: a BCC phase and a phase with the rocksalt structure.

3eqC Phases	Lattice parameters Å	Volume Fraction (vol%)
BCC1 (red)	a=3.25	90.9
Rocksalt (yellow)	a=4.21	9.1

Table 4.30: Table comparing the lattice parameters and volume fractions determined by XRD in 3eqC

There are three phases visible in 3eqC when analysed by SEM. A matrix enriched in Ta and V, and two sets of precipitates. Figure 4.48 shows EBSD analysis of this alloy showing that both the large and small precipitates have the rocksalt structure, while the matrix is BCC.

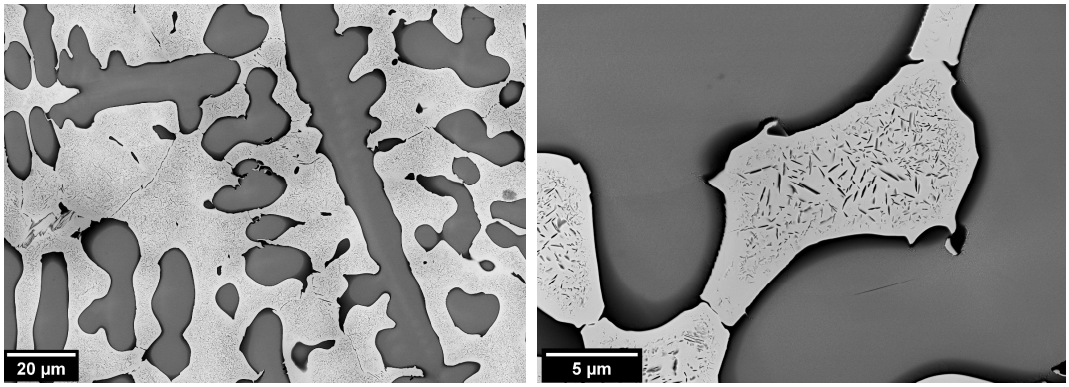

Figure 4.47: Back-scatter SEM image of the microstructure of 3eqC, showing the large precipitates, and the matrix containing the sub-precipitates.

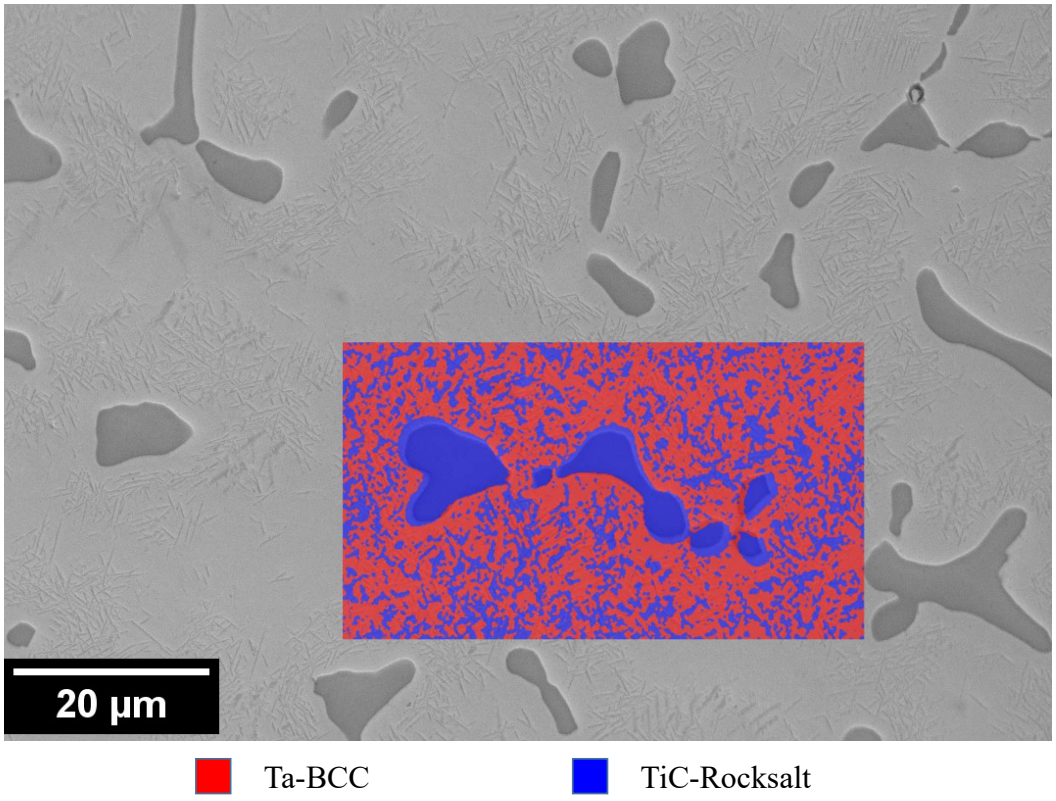

Figure 4.48: Secondary electron image of 3eqC with EBSD phase map overlaid, indexed for Ta-BCC and TiC-Rocksalt.

The compositions and average Z number of these phases has been analysed by EDX and is shown in table 4.31; these are calculated from five EDX Point&ID spectra have been used to find the composition of the matrix and Ti-rich precipitates, the error being the standard deviation of this data. As the smaller precipitates are much finer, averaging a width of only ∼50nm, their composition is more difficult to assess. The numbers given are the average of three EDX Linescans, with the composition taken at the point of maximum Ti concentration.

Element	Matrix Phase (at%)	Sub-Percipitates (at%)	Large Precipitates (at%)
Ti	19.29 ± 9.5	41.09 ± 2.2	67.04 ± 0.4
V	37.59 ± 5.1	28.78 ± 2.4	12.50 ± 0.3
Ta	43.12 ± 4.5	30.13 ± 1.3	20.48 ± 0.2
Z_{ave}	44.4	37.7	35.6

Table 4.31: Table comparing the compositions and average Z numbers of the phases identified in 3eqC. The compositions of the Ta-rich matrix and Ti-rich precipitates are an average of five EDX Point&ID spectra. The composition of the plate like precipitate are the average composition of three EDX linescan converted to Point&ID scans in the peak of Ti concentration. The errors are the standard deviations of this data.

The average Z numbers calculated from the EDX compositions roughly correlate with the back-scatter contrast. The Z values of the precipitates mean that they should be darker than the matrix. As the EBSD also shows these precipitates have the rocksalt structure this is clearly where the impurities are concentrated.

4.5.2 Annealed Equiatomic TiVTa

The microstructure of annealed equiatomic TiVTa (3eqA) has been analysed by XRD and has been indexed in figure 4.49. The annealed variant contains a BCC phase and a rocksalt-structured phase. The lattice parameters of these phase has been calculated by XRD and is shown in table 4.32; the fitting procedure was un-

able to reliably identify the volume fractions of these phases, most likely due to the high number of peaks from the putty used to secure the sample.

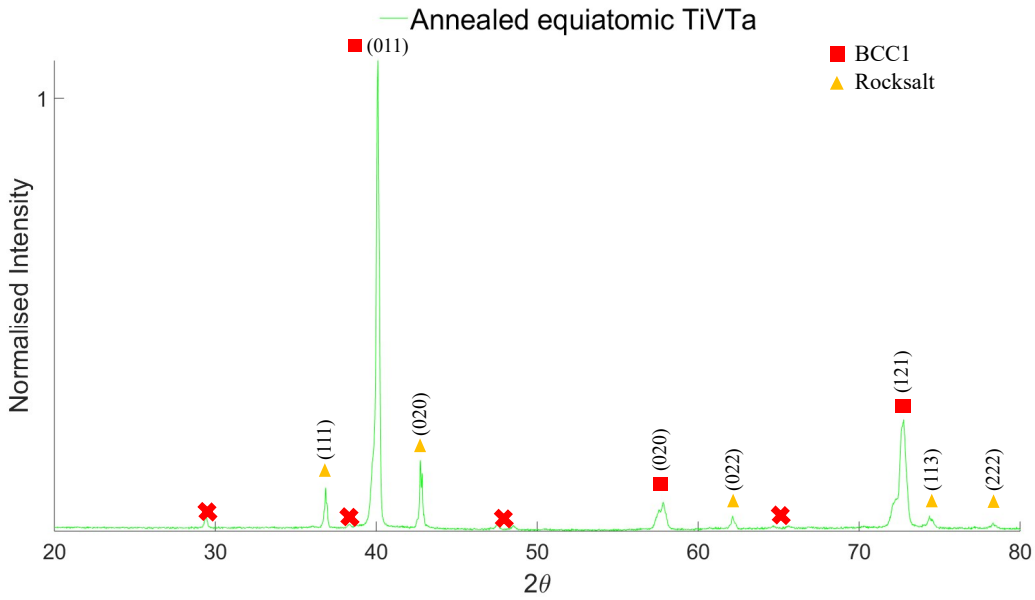

Figure 4.49: XRD trace of annealed equiatomic TiVTa. Three phases have been identified: a BCC phase, a rocksalt-structured phase, and an intermetallic with the C14 structure.

3eqA Phases	Lattice parameters Å	Volume Fraction (vol%)
BCC1 (red)	a=3.19	-
Rocksalt (yellow)	a=4.23	-

Table 4.32: Table comparing the lattice parameters and volume fractions determined by XRD in 3eqA

The microstructure of 3eqA is visibly similar to 3eqC, but a new set of sub-precipitates have formed within the larger rocksalt-structured precipitates. Back-scatter SEM images of this microstructure are shown in figure 4.50 along with a secondary electron image with an EBSD phase map overlaid in figure 4.51, and this shows the light contrast matrix phase is BCC, the large dark contrast precipitates are rocksalt, while the sub-precipitates have the opposing crystal structure.

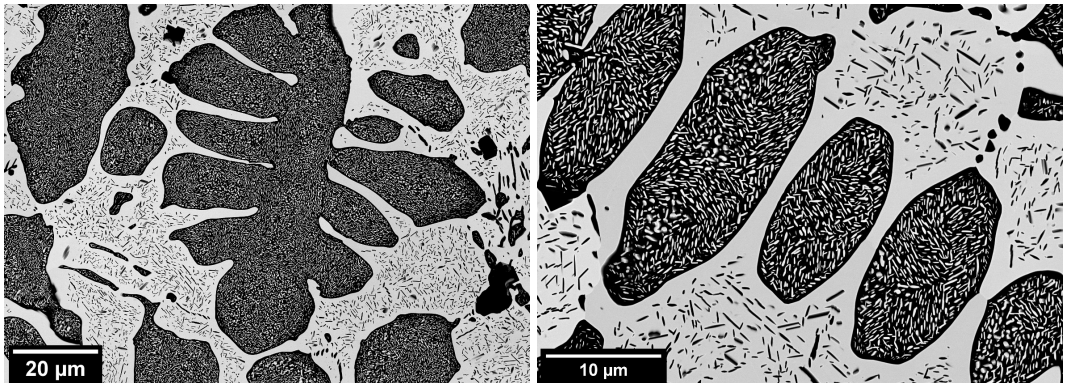

Figure 4.50: Back-scatter SEM images of the microstructure in 3eqA. It can be seen that annealing has caused light-contrast precipitates to form in the Ti-rich phase.

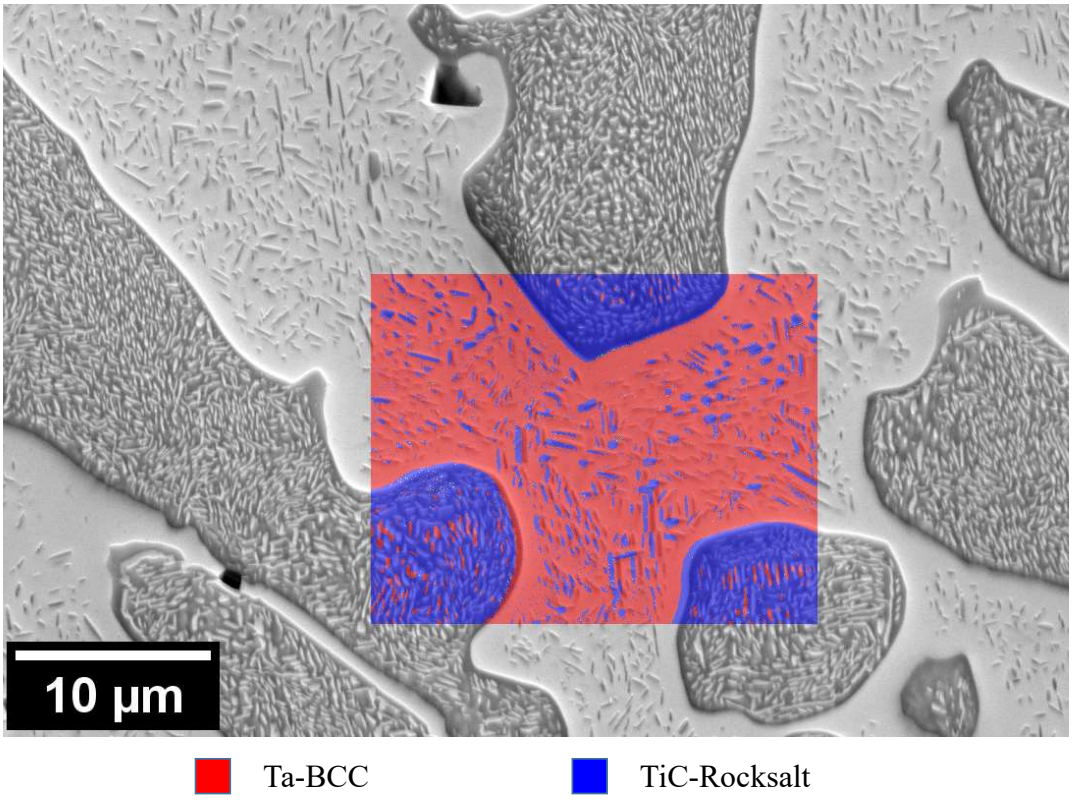

Figure 4.51: Secondary electron image of 3eqA with EBSD phase map overlaid, indexed for Ta-BCC and TiC-Rocksalt.

The composition of these phases has been determined by averaging three EDX Point&ID analyses in table 4.33. The error given is the standard deviation of this data.

Element	Matrix Phase (at%)	Sub-Precipitates (at%)	Large Precipitates (at%)	Sub-Precipitates (at%)
Ti	6.68 ± 0.4	80.72 ± 1.1	92.19 ± 0.3	23.99 ± 1.0
V	46.69 ± 0.8	8.33 ± 1.0	3.41 ± 0.2	31.78 ± 1.1
Ta	46.63 ± 0.4	10.95 ± 0.7	4.40 ± 0.2	44.23 ± 0.5
Z_{ave}	46.2	27.7	24.3	44.9

Table 4.33: Table comparing the compositions and average Z number of the phases identified in 3eqA. The composition of each primary phase is the average of three EDX Point&ID spectra taken in different locations. The composition of the secondary precipitates are Point&ID spectra extraced from Linescans in the region of minimum or maximum Ti concentration. The errors given are the standard deviation of this data.

Once again the EDX on these phases is unreliable, as the average Z number predicted by EDX does not correlate with the contrast in the back-scatter images: the matrix phase has the highest average Z number, but the BCC precipitates have the brightest contrast. What is likely happening is the Ta in the large precipitate is being rejected, thus precipitating out. The composition by EDX may be wrong as these precipitates are so small it is likely the EDX spot is too large to analyse them accurately, thus causing a large error in the calculated composition.

4.5.3 As cast Optimised TiVTa

The microstructure of as-cast optimised TiVTa (3optC) has been analysed by XRD and indexed in figure 4.52. The XRD shows a BCC phase and a rocksalt-structured phase; their lattice parameters and volume fractions are shown in table 4.34.

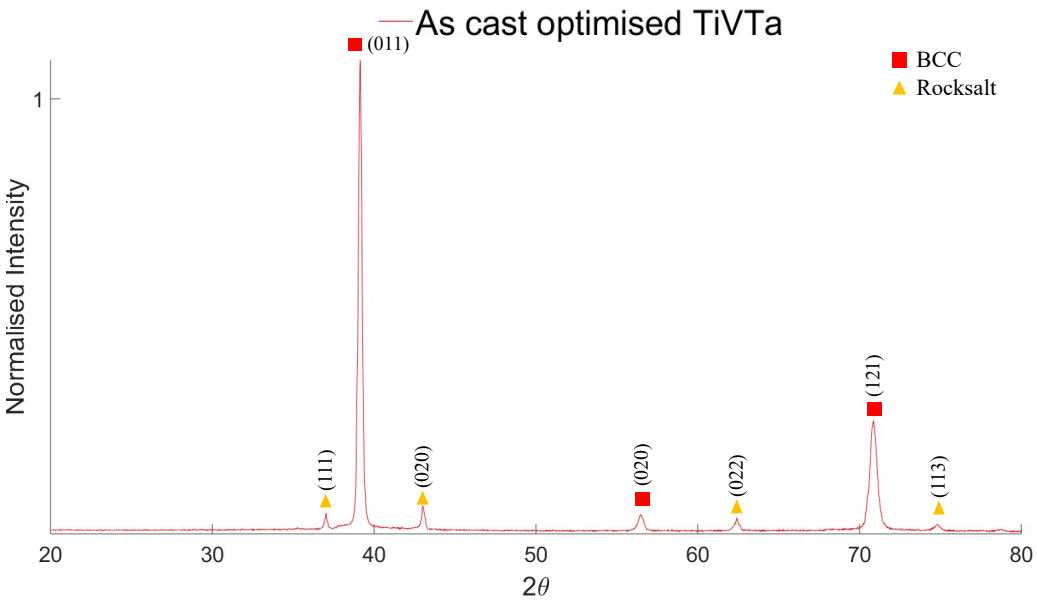

Figure 4.52: XRD trace of as-cast optimised TiVTa. Two phases have been identified: a BCC phase and a rocksalt-structured phase.

3optC Phases	Lattice parameters Å	Volume Fraction (vol%)
BCC1 (red)	a=3.25	75.1
Rocksalt (yellow)	a=4.20	24.9

Table 4.34: Table comparing the lattice parameters and volume fractions determined by XRD in 3optC

The as-cast microstructure of 3optC is shown in figure 4.53. It is similar in appearance to 3eqC in that there is a Ta-rich matrix containing two length scales of Ti-rich precipitates. Also similar to the equiatomic case the matrix is BCC with both sets of precipitates indexing as rocksalt, as shown in figure 4.54

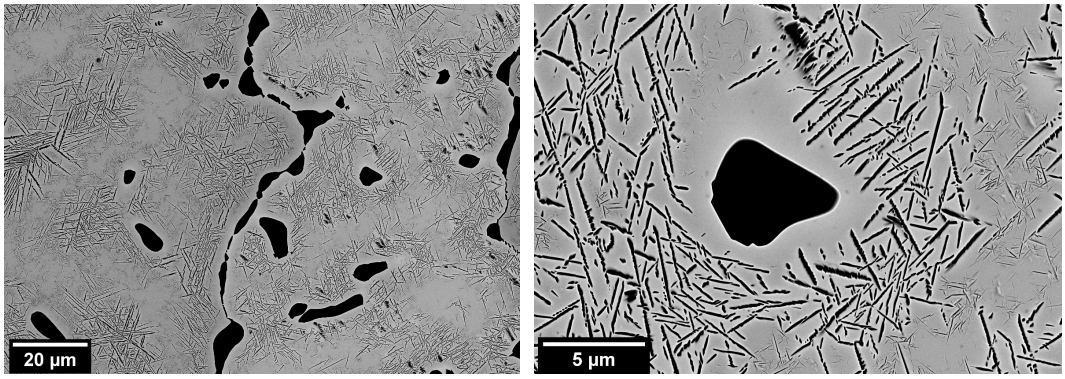

Figure 4.53: Back-scatter SEM images of the microstructure in 3optC. There are two types of Ti-rich precipitates: one large and one small and needle-like.

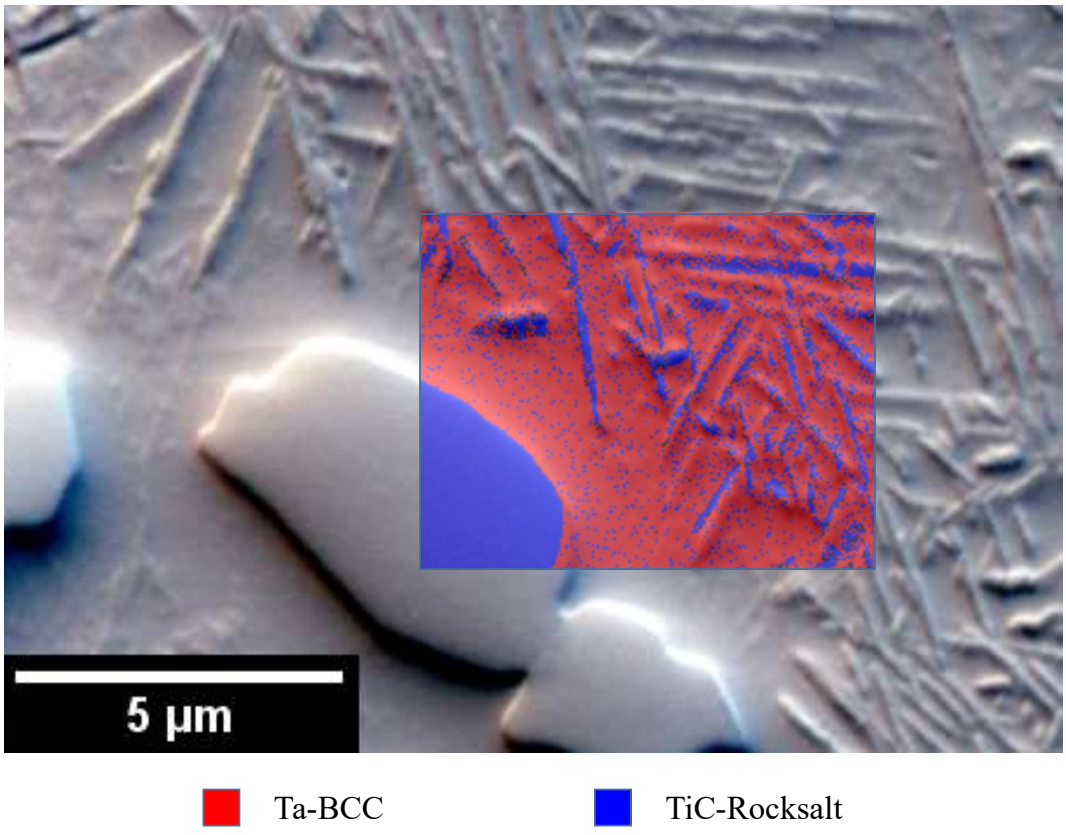

Figure 4.54: Argus image of 3optC with EBSD phase map overlaid, indexed for Ta-BCC and TiC-Rocksalt.

The compositions and average Z number of the three phases is shown in table 4.35; five EDX Point&ID spectra have been used for the two larger phases, with the error being the standard deviation of the data. The composition of the needle-like precipitates is calculated by taking the composition from an EDX Linescan at the point of highest Ti concentration.

Element	Matrix Phase (at%)	Sub-Precipitates (at%)	Large Precipitates (at%)
Ti	27.98 ± 2.2	67.80 ± 2.5	77.37 ± 0.9
V	16.55 ± 0.2	6.13 ± 1.0	6.03 ± 0.1
Ta	55.46 ± 1.9	25.89 ± 1.8	16.61 ± 0.7
Z_{ave}	50.4	35.2	30.5

Table 4.35: Table comparing the compositions and average Z number of the phases identified in 3optC. The compositions of the Ta-rich matrix and Ti-rich precipitates are an average of five EDX Point&ID spectra. The errors are the standard deviations of these spectra. The composition of the plate like precipitate are the average composition of three EDX Linescan, taken at the point of maximum Ti concentration.

4.5.4 Annealed Optimised TiVTa

The microstructure of annealed optimised TiVTa (3optA) has been analysed by XRD and is indexed in figure 4.55. Similar to the as-cast state there is a BCC and a rocksalt-structured phase, with their lattice parameters and volume fractions shown in table 4.36

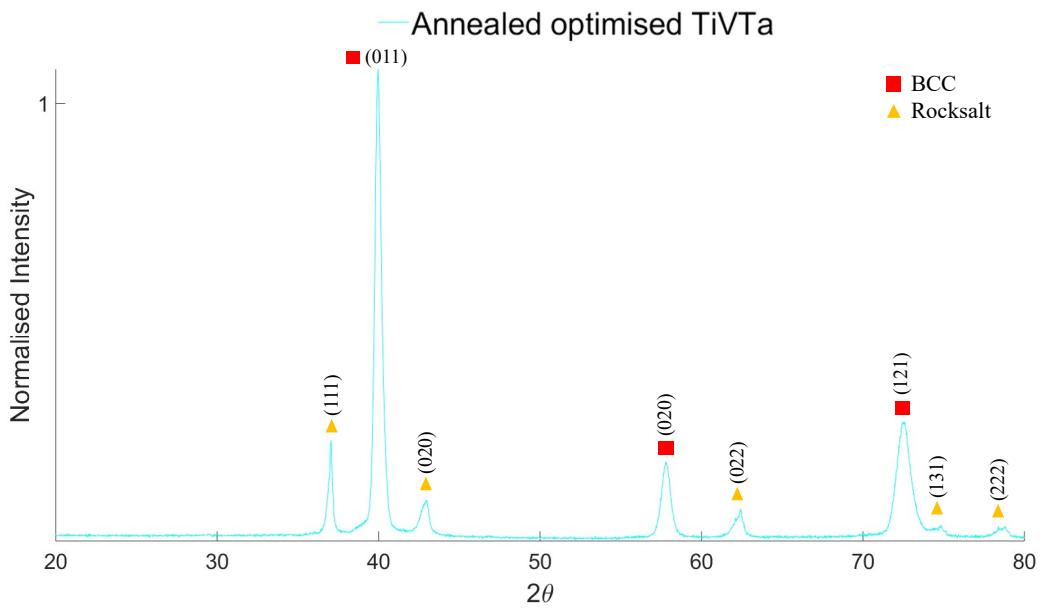

Figure 4.55: XRD trace of annealed optimised TiVTa. Two phases have been identified: a BCC phase and a rocksalt-structured phase.

3optA Phases	Lattice parameters Å	Volume Fraction (vol%)
BCC1 (red)	a=3.19	59.7
Rocksalt (yellow)	a=4.21	40.3

Table 4.36: Table comparing the lattice parameters and volume fractions determined by XRD in 3optA

Further SEM analysis of 3optA shows that the microstructure has evolved in a similar way to the equiatomic alloy, with a new set of precipitates forming within the Ti-rich phase which also index as BCC (see figure 4.57). The main difference between 3eqA and 3optA is that the fraction of the large rocksalt-structured precipitates has decreased, which is to be expected as Ti is the primary component of this phase and is at a lower concentration in this alloy.

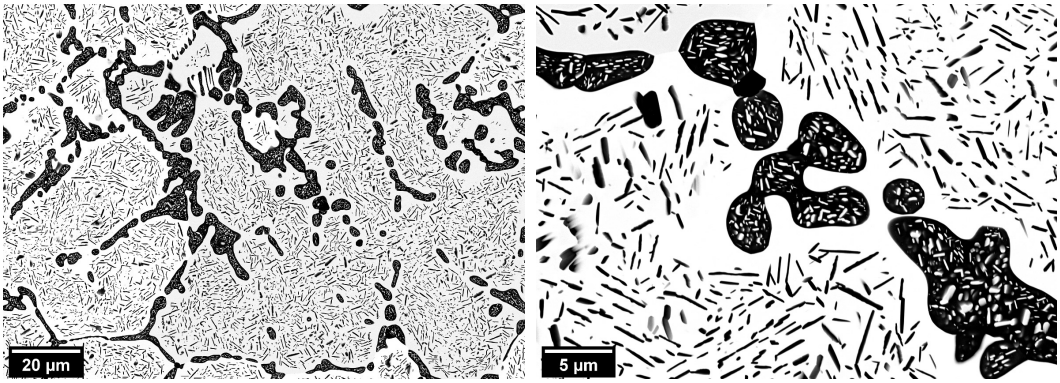

Figure 4.56: Back-scatter SEM images of the microstructure in 3optA. It can be seen the microstructure is very similar to that found in 3eqA.

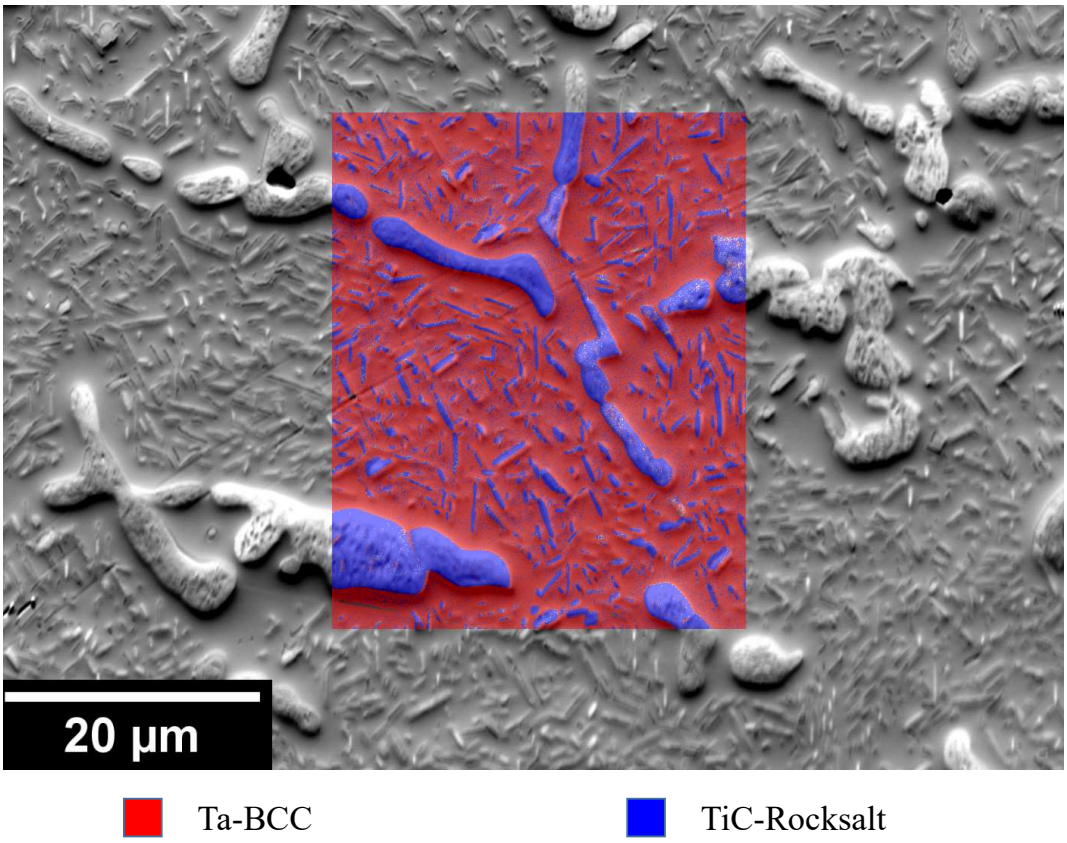

Figure 4.57: Argus image of 3optA with an EBSD phase map overlaid, indexed for Ta-BCC and TiC-Rocksalt.

The composition of all the phases identified using EDX in 3optA are shown in table 4.37, and were found by averaging three EDX Point&ID spectra, with the errors given being the standard deviation of this data.

Element	Ta-rich Phase (at%)	Sub-Precipitates (at%)	Ti-rich Phase (at%)	Sub-Precipitate (at%)
Ti	18.99 ± 0.2	84.33 ± 2.3	93.12 ± 1.3	40.35 ± 6.0
V	18.62 ± 0.3	4.44 ± 0.7	2.35 ± 0.3	17.16 ± 1.2
Ta	62.38 ± 0.4	11.23 ± 1.7	4.44 ± 1.0	42.49 ± 4.8
Z_{ave}	54.0	27.8	24.3	43.8

Table 4.37: Table comparing the compositions and average Z numbers of the phases identified in 3optA. The composition of each phase is the average of three EDX Point&ID spectra taken in different locations. The errors given are the standard deviation of this data.

The EDX analysis once again shows the rocksalt-structured phases to be enriched in Ti, while the BCC phases are enriched in V and Ta. The contrast in the back-scatter image is consistent with the EDX composition, with the BCC phases appearing white and the rocksalt ones appearing black: this is consistent with the average Z number from the EDX, and also the impurities being concentrated in the Ti-rich rocksalt-structured phase.

4.6 Discussion

4.6.1 The carbonitride in TiVZrHfTa

For the quinary alloys the impurities (C, N, O) have primarily segregated with zirconium and hafnium; and to a lesser extent, titanium. This correlates with the heat of formation of the metal nitrides, shown in table 4.38 [187]. The most stable cubic nitrides are of zirconium, followed by hafnium and then titanium. The observed segregation trends do not correlate as strongly with the heat of formations for the

cubic carbides, for which TaC is more negative than TiC. This is either due to the lack of stability of cubic TaN causing Ta to be rejected from the phase, or because the nitrogen is dominating the phase formation.

Element	Carbide ΔH_f (kJ mol^{-1})	Nitride ΔH_f (kJ mol^{-1})
Ti	-56	-168
V	-38	-93
Zr	-92	-202
Hf	-85	-184
Ta	-71	-128

Table 4.38: Table comparing the Heat's of formation of the rocksalt-structured carbides and nitrides. Values are taken from reference [187]

The rocksalt-structured phase in 5eqA has been identified by APT as being a ZrHf carbonitride, with a lesser but non-negligible amount of titanium alloyed on the cation sub-lattice. This composition is consistent with the SEM based EDX measurement on the other quinary alloys. For the anion sub-lattice the only measurement of composition is given by APT, as shown in table 4.4. A method of assessing whether these compositions are representative is to scale them according to the volume fractions of each phase as calculated by XRD, and then comparing this to the bulk compositions provided by AMG. This has been done for 5eqA in table 4.39, also taking into account the calculated vacancy concentration. The results are in reasonable agreement for most elements except for carbon (which is overestimated by a factor of four) and hafnium (which is underestimated by nearly 5at%), demonstrating the possibility of variations in phase composition throughout the sample.

Element	AMG Composition (at%)	Predicted Composition (at%)	Difference
Ti	17.92	15.58	2.34
V	18.07	20.97	-2.90
Zr	17.95	15.37	2.58
Hf	17.04	12.22	4.82
Ta	17.94	17.91	0.03
C	1.00	4.06	-3.06
N	7.68	8.32	-0.64
O	2.30	0.77	1.53

Table 4.39: Table comparing the composition of the 5eq billet as provided by AMG, with the calculated composition based off of the APT and XRD results presented in chapter 4.

The thermodynamic driving force for the formation of the carbonitride is most likely provided by the carbon being rejected from the HCP phase. Evidence for this is provided in appendix A where the Zr-C, Zr-N, and Zr-O phase diagrams show the solubility limits in HCP zirconium to be 0, $\sim$23, and $\sim$29at% respectively. This explains why the APT data demonstrates such a sharp boundary between the HCP and rocksalt-structured phase in the carbon concentration, but not in the nitrogen, which is soluble in both phases. The oxygen concentration drops to zero in the rocksalt-structured phase as there are no stable cubic oxides formed with any of the elements in this alloy [176].

4.6.2 The carbonitride behaviour in TiVZrTa and TiVTa

The rocksalt-structured phase in equiatomic TiVZrTa has a similar concentration of Ti to the same phase in the quinary alloys, while the rest of the cation sub-lattice is Zr, according to the EDX measurements, it is therefore identified as a Zr carbonitride in the equiatomic alloy. In contrast, the rocksalt-structured phase in the optimised TiVZrTa alloys contains much more Ti than Zr (see table 4.26). The reason for this is that the bulk concentrations of Ti is much higher than for Zr (30.27 and 13.24at%

respectively from AMG's analysis), this means that there is not enough Zr to consume all of the carbon and nitrogen, and so the Ti reacts with the remainder. This is confirmed by the concentration of Zr in the metallic-matrix phase being $\leq$2at%: it's all in the carbonitride. In the optimised TiVZrTa the rocksalt-structured phase is therefore identified as a TiZr carbonitride. In the TiVTa alloys there is obviously no zirconium or hafnium, and so the rocksalt-structured phase is a Ti carbonitride (Ti concentration is $\geq$90at% on the cation sub-lattice according to EDX). It is of note that the best way to identify which phase is rocksalt structured would be to use TEM diffraction spot to illuminate each phase in turn. From here the crystal structure of each phase can be reliably determined; this could not be done in this project due to time and equipment limitations, and so a combination of EDX and XRD was used instead.

In some of the samples presented here the carbonitride phase contains sub-precipitates after annealing; the composition of these is very variable, sometimes being highly enriched in vanadium (in 4optC for example they contain 12x more vanadium than the surrounding carbonitride), but sometimes also highly enriched in titanium or zirconium, as in 4optA. The reason for this is that the sub-precipitates formation is highly sensitive to its localised environment, any atoms that have not reacted with an impurity are being rejected; they either form a sub-precipitate or are rejected into the matrix, leading to the denuded zones that have been observed.

4.6.3 Refractory HEAs with FCC phases

In chapter 2 several papers were identified which had fabricated refractory HEAs out of elements which stabilised only BCC and HCP crystals; despite this, their results suggested that their alloys contained some FCC phases [124, 136, 138]. Based

on the results presented here, it is highly likely that the alloys they fabricated were contaminated by a light element that has stabilised a rocksalt-structured phase. All their materials contain zirconium, found here to be a strong nitride and carbide former. Phase separation in HEAs based on group IV and V metals is complicated, and made far more so by their intolerance to contamination. Researchers must be careful to conduct full chemical analysis on their billets, and based on the experience of this project it is best to do this directly after fabrication, rather than after characterisation and analysis has been concluded.

4.7 Conclusions

The alloys described in this chapter all phase separate when annealed. At first it was thought that this phase separation was due to the elements that are HCP at low-temperatures (Zr and Hf) segregating away from the low-temperature BCC elements (V and Ta), as similar occurrences have been reported in the literature [120–124]. However, in the later stages of the project it was realised that the fabricated alloys were contaminated, and that they contained enough carbon and nitrogen to nucleate a rocksalt-structured phase, now known to be a carbonitride. Based on the behaviour of these alloys, it is clear the impurities dominate phase formation, and it cannot be stated whether these alloys would or would not phase separate when uncontaminated.

Chapter 5

Achieving Single-phase microstructures in HEAs

5.1 Introduction

Many of the advantageous properties of HEAs are thought to come from the solid solution microstructure, and so a primary aim of many researchers is to identify systems or compositions that have a single phase solid solution microstructures. Initial work done in this project focussed on finding ways to optimise the thermodynamics of the alloy to generate this desired microstructure, however later work showed that single phase alloys could most easily be generated by manipulating the kinetics during the casting process.

5.2 Optimisation of Ω

The Ω parameter [71] is referred to repeatedly in this chapter, and so is recapped here. A full discussion of it can be found in section 2.2.2. Omega is a parameter

which depends on composition according to:

$$\Omega = \frac{T_{\mathrm{m}} \Delta S_{\mathrm{mix}}}{|\Delta H_{\mathrm{mix}}|} \tag{5.1}$$

where:

$$\Delta S_{\mathrm{mix}} = -R \sum_{i=1}^{N} c_i \ln c_i \tag{5.2}$$

and:

$$\Delta H_{\mathrm{mix}} = \sum_{i=1, j \neq 1}^{N} \left(4 \Delta H_{\mathrm{AB}}\right) c_i c_j \tag{5.3}$$

Ω	:	The Ω parameter
T_{m}	:	Melting temperature (K)
ΔS_{mix}	:	The configurational entropy of mixing (J K^{-1} mol^{-1})
ΔH_{mix}	:	Enthalpy of mixing (J mol^{-1})
c_i	:	Composition of component i (at%)
ΔH_{AB}	:	Enthalpy of mixing of the binary alloy AB (J mol^{-1})
4	:	Normalises the binary enthalpy of mixing

Its function is to assess the competition between entropy and enthalpy *at the point of solidification*. Its main assumptions are that the melting point is the weighted average of the components, that the primary contributor to entropy is the configurational entropy and is equivalent to the entropy in the fully mixed liquid phase. The final set of assumption is that the enthalpy of mixing can be calculated by adding the binary enthalpies, and that positive and negative binaries will cancel one another out.

5.2.1 Preliminary work on phase separation

Initial studies of this alloy showed that although as-cast samples of TiVZrHfTa could be single phase, this microstructure separated into multiple phases after being heat

treated at 1400 °C for 24 hours and then furnace cooled. Figure 5.1 shows a back-scatter SEM image of the microstructure of this alloy. The composition of the phases visible are shown in table 5.1 along with the associated values of configurational entropy, enthalpy of mixing, and Ω. It can be seen that both phases have a higher value of Ω than the equiatomic phase, but that the Ω of the matrix phase has nearly doubled. The resultant hypothesis was that Ω was correctly capturing thermodynamic effects, and that the observed matrix phase is more stable than the equiatomic composition: thus when the sample is annealed precipitation occurs so that the composition shifts to this more stable value.

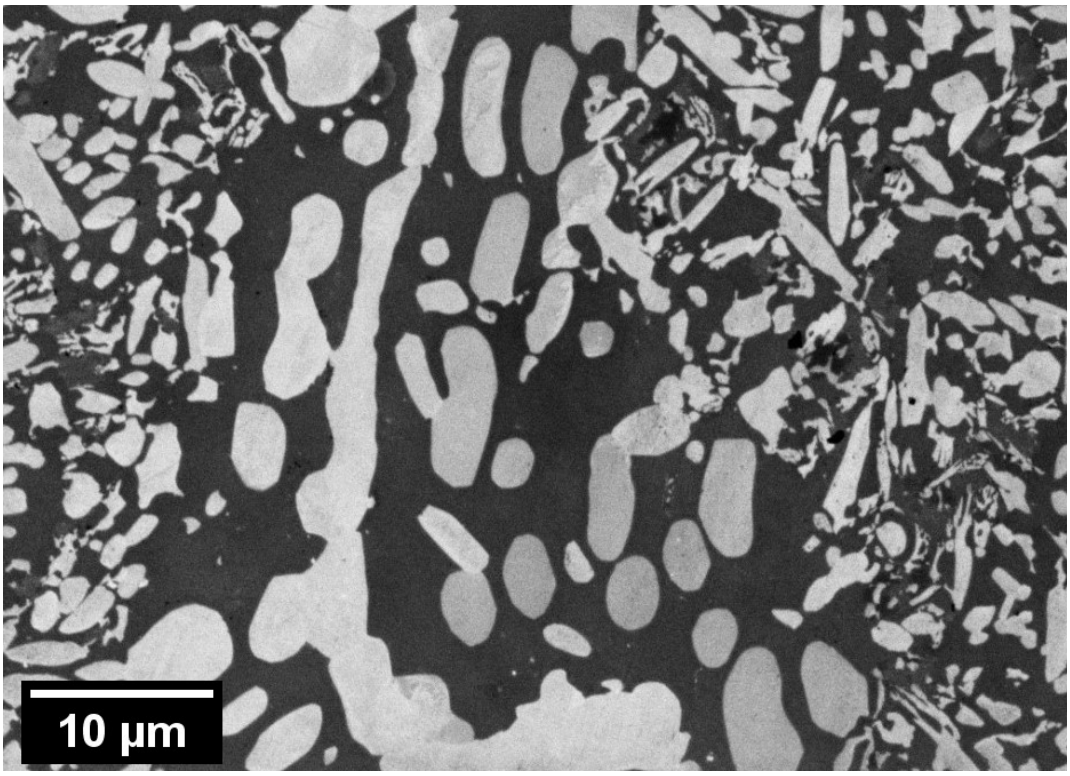

Figure 5.1: Back-scatter SEM image of equiatomic TiVZrHfTa annealed at 1400°C for 24 hours and then furnace cooled. This is a separate sample from those discussed in chapter 4, and was melted in 2015.

Element	Equiatomic Composition (at%)	Dark Contrast Phase (at%)	Light Contrast Phase (at%)
Ti	20	35	8
V	20	12	2
Zr	20	14	46
Hf	20	20	40
Ta	20	19	4
ΔS_{config}	13.4	12.8	9.4
ΔH_{mix}	6.5	153.2	198.4
Ω	100.6	196.9	109.7

Table 5.1: Table comparing the composition, configurational entropies, enthalpies of mixing, and Ω values of equiatoimc TiVZrHfTa to the two phases found after it has been annealed, which are shown in figure 5.1. Composition was determined using EDX Point&ID analysis, conducted by Prof. S. Speller.

Equiatomic alloys were of primary interest in the literature as this maximises configurational entropy, however the above results suggested that the most stable single phase solid solution composition may not be equiatomic. In order to explore how Ω varied in composition space an algorithm was written to optimise composition in order to maximise Ω. Different alloy systems have then be melted and compared in the equiatomic and optimised compositions in order to test the initial hypothesis.

5.2.2 The Optimisation Algorithm

The optimisation algorithm was written in Matlab and uses the fmincon function in order to tailor composition in order to maximise Ω; fmincon is discussed further in chapter 3). Two constraints were placed on the algorithm, that all concentrations must sum to 100%, and that the average lattice mismatch (δ) must never exceed 6.6%. Additionally, upper and lower bounds were set on possible concentrations so that the composition always stayed in the "high-entropy" regime. The algorithm and associated functions are listed in appendix B. After optimising many different sets

of elements there are four observations about Ω and how it varies with composition.

1. The Ω of equiatomic compositions can always be increased by optimising, and the increase is normally several orders of magnitude.

2. Optimised composition can be near-equiatomic or they can result in an element being dropped from the set of elements entirely, moving the composition outside of the commonly accepted definition of HEAs.

3. Peaks in composition space are sharp.

4. The Ω surface is not smooth in composition space. There are always many local maxima in composition space.

5.2.3 Equiatomic alloys can always be optimised

The Ω value of an equiatomic alloy can always be increased by optimisation. For example, the Ω value of TiCrMnNbMo and VMnNiSnW both increase by six orders of magnitude on optimising from equiatomic compositions. This is shown in table 5.2 and 5.3.

Element	Equiatomic Alloy (at%)	Optimised Alloy (at%)
Ti	20	2.61
Cr	20	15.71
Mn	20	30.41
Nb	20	12.10
Mo	20	39.18
Ω	6.99	4.46×10^6

Table 5.2: Table comparing the composition and Ω values of equiatomic and optimised TiCrMnNbMo

Element	Equiatomic Alloy (at%)	Optimised Alloy (at%)
V	20	15.72
Mn	20	15.79
Ni	20	16.09
Sn	20	4.92
W	20	47.48
Ω	16.09	1.53×10^7

Table 5.3: Table comparing the composition and Ω values of equiatomic and optimised VMnNiSnW.

Simply from a statistical standpoint it is highly unlikely that the equiatomic composition will be directly in a local maxima of Ω. What is particularly striking however, is the dramatic increases in Ω that are possible. When just comparing alloys in the literature the highest value of Ω that Yang and Zhang found [71] was 233.88 for $Mn_2Cr_2Fe_2Ni_2Cu$ (which on optimising can be increased to 3.85×10^8 as shown in table 5.6). Mathematically these peaks are due to the value of ΔH_{mix} reducing to a value close to 0, as negative ΔH_{AB} cancel almost perfectly with positive ΔH_{AB}.

5.2.4 Near-equiatomic optimisation, and non-equiatomic optimisation

The peaks in Ω occur at different points in composition space. Sometimes these peaks are "near-equiatomic", that is to say that the ratios of concentration in the optimised alloys are close to 1. The alternative is that during optimisation, the concentration of one or more elements is reduced to nearly zero, or as close to zero as the boundary conditions will permit. An example of this is CrMnFeCoNi (the Cantor alloy); when optimised Ω increases from 5.79 to 2.61×10^7, but only by reducing the Co and Ni content so low that Mn is 49.2 times more concentrated. In contrast, when CrMnFeMo is optimised Ω increases from 24.21 to 1.38×10^9 and the highest ratio of concentration is 2.1 - the composition is still (relatively) close to equiatomic. The data for these alloys is shown in tables 5.4 and 5.5.

Element	Equiatomic Alloy (at%)	Optimised Alloy (at%)
Cr	20	14.1
Mn	20	49.2
Fe	20	34.7
Co	20	1.0
Ni	20	1.0
Ω	5.79	2.61×10^7

Table 5.4: Table comparing the composition and Ω values of equiatomic and optimised CrMnFeCoNi

Element	Equiatomic Alloy (at%)	Optimised Alloy (at%)
Cr	25	26.5
Mn	25	16.8
Fe	25	38.5
Mo	25	18.1
Ω	24.21	1.38×10^9

Table 5.5: Table comparing the composition and Ω values of equiatomic and optimised CrMnFeMo.

5.2.5 Sharp peaks in Ω

The peaks in Ω do not encompass a wide range of concentrations; changing composition by small amounts can lead to increases or decreases in Ω of several orders of magnitude. An example is the $Cr_2Mn_2Fe_2Ni_2Cu$ previously mentioned and shown in table 5.6. When optimised no elemental concentration is altered by more than 1.2%, and yet Ω increases by 6 orders of magnitude. This is particularly important, as when alloys are being formed precise control of composition is impossible: in an arc melter it is difficult to ensure all the concentrations are within 2at% of the target, let alone 0.02at%. A demonstration of this is when comparing the precisely optimised composition of CrMnCoNiMo to the approximate value (rounded to the nearest whole number, and more likely achievable in reality). The value of Ω has decreased from 2.31×10^6 to 741.69 as shown in table 5.7.

Element	Starting Alloy (at%)	Optimised Alloy (at%)
Cr	22.22	21.68
Mn	22.22	21.93
Fe	22.22	21.61
Ni	22.22	23.43
Cu	11.11	11.35
Ω	233.88	3.85×10^8

Table 5.6: Table comparing the composition and Ω values of $Cr_2Mn_2Fe_2Ni_2Cu$ before and after being optimised.

Element	Optimised Alloy (at%)	Rounded Alloy (at%)
Cr	23.797	24.0
Mn	27.221	27.0
Co	9.434	9.0
Ni	3.6301	4.0
Mo	35.918	36.0
Ω	2.31×10^6	741.69

Table 5.7: Table demonstrating how much Ω decreases when the optimised composition of CrMnCoNiMo is rounded from three decimal places to none.

5.2.6 Local maximum in Ω

The peaks in Ω are not only high, but also many. The optimisation algorithm scans around a starting point, until it finds a maxima; this maxima is only local however, and others may and do exist. As the maxima found depends on the starting point there are still questions with respect to finding which maxima in Ω will be the most stable. For example, when equiatomic TiVZrHfTa is optimised it results in the composition shown in table 5.8, which is very close to equiatomic. However, as shown in table 5.9, a different peak in Ω is found when optimising the matrix phase of annealed TiVZrHfTa (shown at the beginning of this discussion in figure 5.1). This demonstrates that "the most stable composition" found experimentally may not relate to the Ω peak closest to the starting composition, although the composition identified by EDX is clearly situated within a peak in Ω, as optimisation has only led to small changes in composition ($<$1at%).

Element	Equiatomic Alloy (at%)	Optimised Alloy (at%)
Ti	20	19.64
V	20	18.05
Zr	20	18.51
Hf	20	20.25
Ta	20	23.56
Ω	100.71	2.12×10^7

Table 5.8: Table comparing the composition and Ω values of equiatomic and optimised TiVZrHfTa

Element	Starting Alloy (at%)	Optimised Alloy (at%)
Ti	35	35.08
V	12	13.71
Zr	14	13.16
Hf	20	19.47
Ta	19	18.59
Ω	196.90	1.24×10^7

Table 5.9: Table comparing the composition and Ω values of the matrix phase of annealed TiVZrHfTa before and after optimisation.

5.2.7 Further work on Ω optimisation

If the process of optimising Ω were to be taken further the next step would be to adjust the algorithm so that it found as many local maxima as possible, and then compared them. Experimental studies could then attempt to compare what kind of Ω peak gives the most ideal microstructure for a High-Entropy Alloy.

5.3 Experimental Verification

The hypothesis that higher values of Ω relate to more thermodynamically stable single phase microstructures in multicomponent alloys can be most easily tested by comparing different alloy compositions. The first comparison to be made was between equiatomic TiVZrHfTa and the composition found when optimising the matrix phase of the alloy discussed in section 5.2.1. This comparison was made prior to the work on optimising Ω but is the source of the material discussed in chapter 4. All other comparisons are made between equiatomic alloys, and the optimised composition found from them. These alloys are all discussed at length in chapter 4, but the key points are reiterated again here.

5.3.1 TiVZrHfTa

The two compositions of the TiVZrHfTa alloys are repeated in table 5.10, and SEM images of their microstructures are shown in figure 5.2. It can be seen that equiatomic alloy is multiphase when cast as a 50g billet and that when annealed the phases identified remained, although the microstructure does visually change when examined in SEM. In contrast the optimised alloy is cast as single phase, and on annealing there is only a small amount of precipitation. As shown in tables 5.8 and 5.9 the change in composition between the two billets corresponds to a large increase in the value of Ω. The main conclusion from examining these four alloys was that impurities such as nitrogen and carbon drive the precipitation of a rocksalt structure, and that Zr and Hf segregated away from V and Ta to form a HCP phase. The increase in Ω has also led to a more "idealised" microstructure, but even though the optimised alloy has a low impurity concentration it has still phase separated.

Element	Equiatomic Compostion (at%)	Optimised Composition (at%)
Ti	20.0	35.1
V	20.0	13.7
Zr	20.0	13.2
Hf	20.0	19.5
Ta	20.0	18.6
Ω	100.71	1.24×10^7
δ	6.54 %	5.69 %

Table 5.10: Table comparing the compositions of equiatomic and optimised TiVZrHfTa, as well as the associated Ω and δ values.

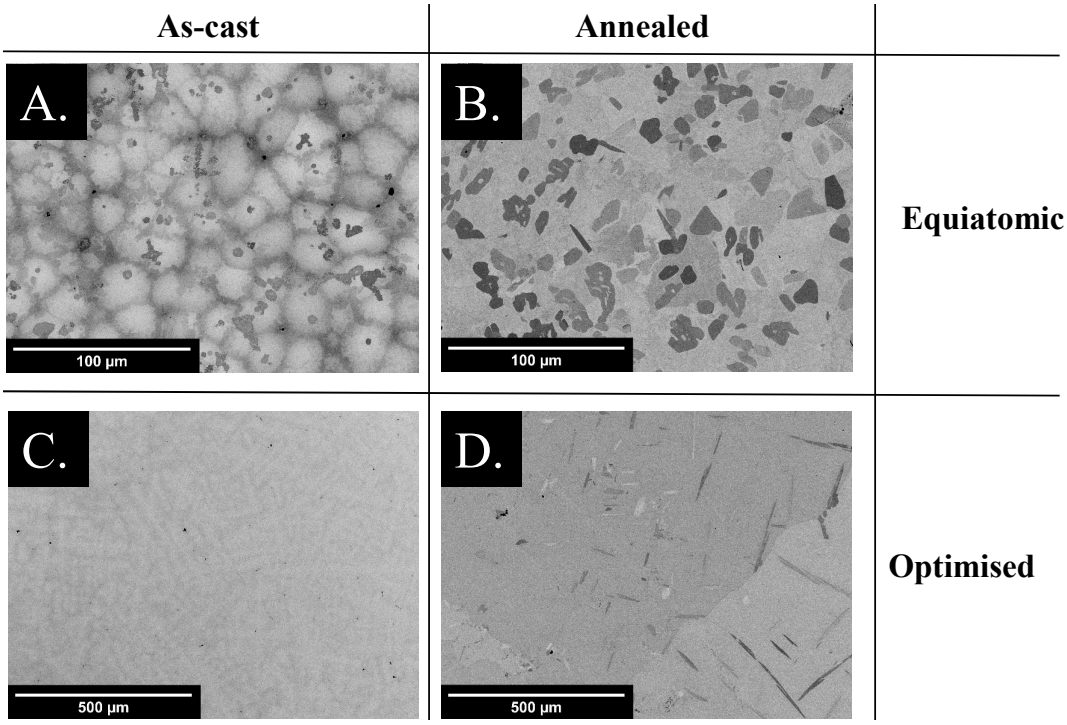

Figure 5.2: Back-scatter SEM images of the four variants of TiVZrHfTa discussed in chapter 4. From A to D they are 5eqC, 5eqA, 5optC, and 5optA. It can be seen that the equiatomic alloys are more microstructurally complex than the optimised one, although even the latter has phase separated on annealing.

5.3.2 TiVZrTa

Following on from the quinary alloy the quaternary alloy TiVZrTa was studied. The two compositions of which are repeated in table 5.11, and SEM images of their microstructures are shown in figure 5.3. The as-cast equiatomic alloy has three BCC phases and a rocksalt phase, which is precipitated again due to Carbon and Nitrogen impurities. On annealing this evolves into two BCC phases, a rocksalt phase, and an HCP structure. As can be seen in chapter 4 these microstructures are strikingly different when examined in SEM.

Element	Equiatomic Compostion (at%)	Optimised Composition (at%)
Ti	25.0	24.5
V	25.0	18.6
Zr	25.0	21.1
Ta	25.0	35.8
Ω	36.64	1.35×10^7
δ	6.47 %	5.85 %

Table 5.11: Table comparing the compositions of equiatomic and optimised TiVZrTa, as well as the associated Ω and δ values.

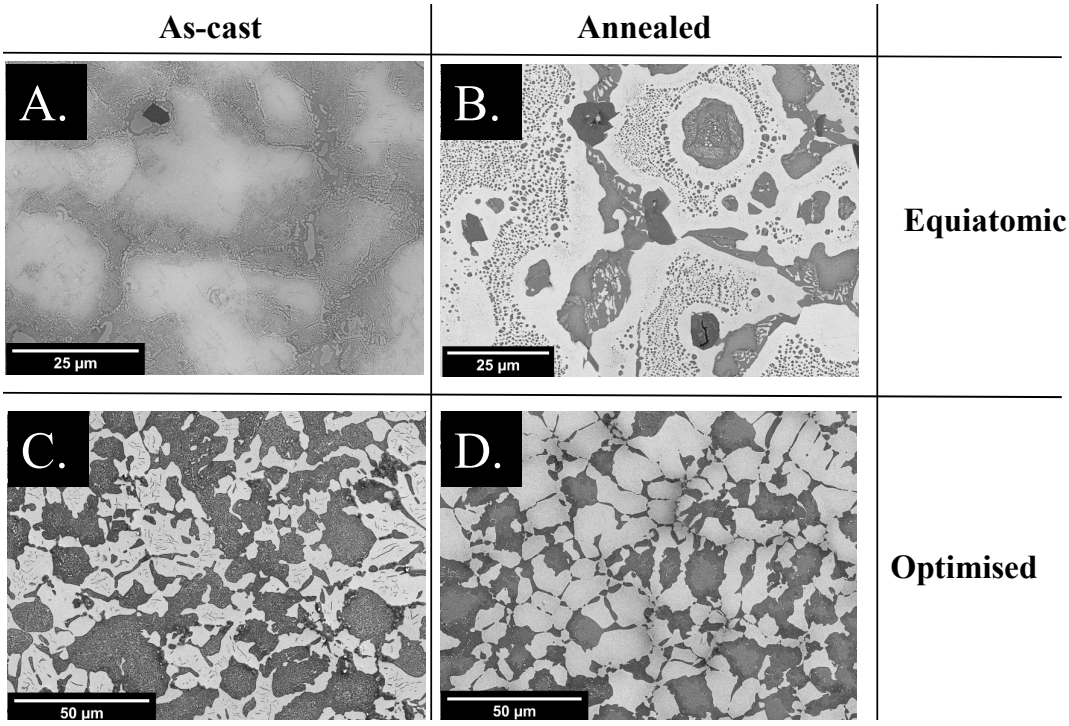

Figure 5.3: Back-scatter SEM images of the four variants of TiVZrTa discussed in chapter 4. From A to D they are 4eqC, 4eqA, 4optC, and 4optA. It can be seen that the equiatomic alloys are contain several phases and annealing has dramatically changed the microstructure. The optimised alloys have phase separated, but annealing has not led to any dramatic changes in microstructure.

The optimised TiVZrTa is more thermally stable than the equiatomic variant. Both the as-cast and annealed material contains BCC and rocksalt phase, however it is not possible to attribute its thermal stability to the efficacy of the optimisation

process. Table 5.12 and 5.13 shows the compositions of the two phases in the as-cast and annealed alloys. Although the bulk composition is close to a peak in Ω both of these two phases are dramatically different from this, due to the segregation that has occurred between the TiZr phase and the VTa phase. The value of Ω for the TiZr phase is still high but it is practically a binary alloy, rather than a high-entropy one: the optimisation has not succeeded.

As cast	Dark Phase (at%)	Light Phase (at%)
Ti	59.5	14.2
V	1.7	25.4
Zr	35.9	1.9
Ta	2.9	58.5
Ω	1904.5	47.7
δ	4.8%	3.6%

Table 5.12: Table showing composition and Ω for the two major phases in the optimised, as-cast TiVZrTa (4optC).

Heat Treated	Dark Phase (at%)	Light Phase (at%)
Ti	54.4	29.1
V	4.3	11.9
Zr	27.2	6.5
Ta	14.1	55.9
Ω	54.0	215.8
δ	4.9%	5.0%

Table 5.13: Table showing composition and Ω for the two major phases in the optimised TiVZrTa after being annealed at 1400 °C for 24 hours and furnace cooled (4optA).

5.3.3 TiVTa

The two compositions of the TiVTa alloys are repeated in table 5.14, and SEM images of their microstructures are shown in figure 5.2. The equiatomic variant contains a BCC structure and a small amount of rocksalt phase according to XRD, although SEM analysis shows the phase separation to have gone a lot further, particularly in segregation between Ti and Ta. On annealing this general structure persists, a Ti rich phase and a Ta rich phase, as well as precipitation occurring throughout all the larger phases. The optimised variant of this alloy is similar to the equiatomic. XRD shows a BCC and rocksalt phase, and SEM demonstrates continued segregation between the Ti and Ta. On annealing a similar structure emerges as with

the equiatomic case: two primary phases with internal precipitation. The three component alloy is different from the four and five component alloys, in that the change in composition from optimisation has *not* resulted in a dramatic change in microstructure. The most likely explanation for this is that although the composition has changed, the increase in Ta and decrease in V concentrations have not moved the composition of the alloy into a different phase field, thus microstructurally the alloys appear similar, albeit with different fractions of each phase.

Element	Equiatomic Compostion (at%)	Optimised Composition (at%)
Ti	33.3	36.2
V	33.3	14.6
Ta	33.3	49.2
Ω	25.39	9.44×10^6
δ	3.65 %	2.75 %

Table 5.14: Table comparing the compositions of equiatomic and optimised TiVTa, as well as the associated Ω and δ values.

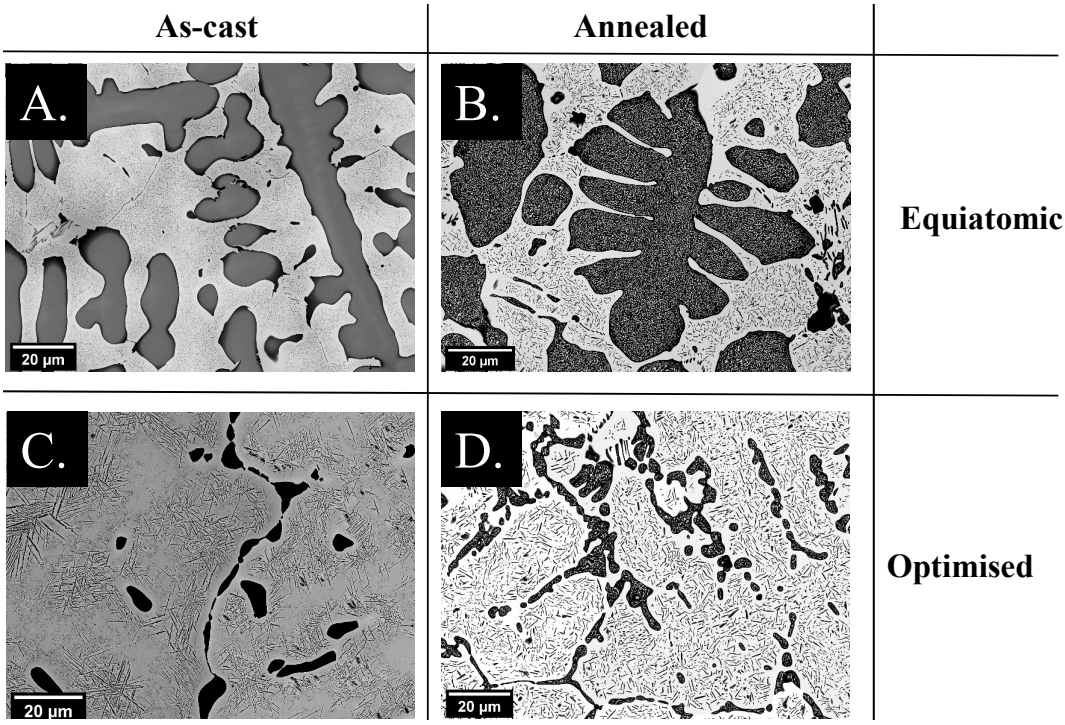

Figure 5.4: Back-scatter SEM images of the four variants of TiVZrHfTa discussed in chapter 4. From A to D they are 3eqC, 3eqA, 3optC, and 3optA. It can be seen that the microstructures of both cast alloys are similar, as are the annealed alloys; this is despite the compositions being different.

5.3.4 Discussion on Ω optimisation

Due to the contamination discussed in chapter 4 it is difficult to draw solid conclusions based on these results. Initially, it was thought that the phase separation observed was due to the same effects as captured by the Hume-Rothery Rules; and that as HEAs supposedly contradict these rules that these observations undermined the high-entropy hypothesis as a whole. This guided the rest of the work conducted during this thesis.

With a better understanding of the effect of the impurities in the fabricated alloys this conclusion is less reliable, but still has some validity when in the context of the wider literature, where there are very few single-phase HEAs which are known to

be thermally stable. There have been numerous attempts to quantify the thermodynamics that underpin the high-entropy hypothesis; none have been particularly successful unless compared to carefully pruned data sets (see section 2.2.3.1). One method that has had success is using CALPHAD modelling, but this is built on databases which reaffirm traditional metallurgy, such as the Hume-Rothery Rules; offering evidence against the high-entropy effect rather than for it.

The one result which does reaffirm both the Ω parameter and the high-entropy effect is that of 5opt. The composition has the highest Ω value (1.24×10^7), and also the most stable solid-solution microstructure, where the only affect of annealing was to cause the precipitation of carbides. A good starting point for future work would be to re-melt these optimised alloys in a reliable arc-melter and to re-examine their microstructures in order to see whether the results of 5opt are repeated.

5.3.5 Alternatives to Thermodynamic Optimisation

At the beginning of this section a hypothesis was suggested that the Ω parameter is successfully capturing the thermodynamics which underpins the formation of single phase solid solution microstructures in multicomponent alloys, and that by finding compositions with the highest values of Ω, single phase alloys with greater thermal stability could be found. After the work discussed here, a new hypothesis was formed: that the thermodynamics within the alloy are not the only factor to determine the microstructure of as-cast samples, but kinetics during the casting process are also a key component. As the majority of the literature focusses on as-cast arc-melted samples, there may be something particular about this process that is generating the sought-after single-phase solid-solution microstructures.

5.4 Single Phase through kinetic manipulation

It is common practise in alloy systems such as Al-Mg to solution treat at high temperature, and then quench the material so as to lock in a metastable amount of solid solution strengthening. If the quenched alloys are subsequently annealed then solute comes out of solution as precipitates. The reformed hypothesis is that a similar effect is happening in as-cast high-entropy alloys, and in particular arc-melted samples where material is melted and then solidified and cooled to room temperature within seconds. In this section FEA simulations are used to compare the cooling behaviour of small and large billets, and then the effect of this on alloy microstructure is examined by comparing 10 and 50g billets of the equiatomic alloys discussed in chapter 4.

5.4.1 Simulations modelling of casting in an arc melter

Finite Element Analysis (FEA) simulations of the casting process inside an arc melter have been undertaken using COMSOL. These simulations do not demonstrate anything surprising: small samples cool quicker and Cu is a better extractor of heat than gas; however, they do demonstrate the variation in thermal condition of different sized metal billets as they cool from thousands of degrees to room temperature in an actively cooled environment.

5.4.1.1 Materials and Geometry

As multicomponent materials are compositionally complex, and modelling the interactions and solidification behaviour were beyond the scope of these simulations, a more simple system was studied: solid structural steel. This means that despite temperatures in the simulations exceeding the melting point of steel, it was never treated

as a liquid; thus solidification effects such as solid/liquid interfaces and latent heat were ignored. The Cu crucible was modelled as solid Cu and the low pressure Ar atmosphere was modelled as air at a pressure of 10×10^5 Pa. All material parameters required by the simulations were taken from COMSOL's inbuilt material library, these parameters include the relevant specific heat capacities and thermal transport coefficients.

The geometry of the sample is modelled as a half-ellipse in axisymmetric geometry. The equation for an ellipse is given in equation 5.4, with the dimensions for each domain taken from real 10 and 50g billets of TiVZrHfTa. The geometry of the environment is modelled as a larger ellipse, with the bottom half being Cu, and the top half air. The parameters and dimensions of these shapes is given in table 5.15 and diagrams and pictures of the billets are shown in figure 5.5.

$$\frac{x^2}{a^2} + \frac{y^2}{b^2} = 1 \tag{5.4}$$

a : Semi-major axis
b : Semi-minor axis

Parameter	Small Billet	Large Billet	Crucible & Air
a	0.009	0.015	0.0225
b	0.003	0.0075	0.015
Radius	0.9cm	1.5cm	2.25cm
Height	0.3cm	0.75cm	1.5cm
Volume	0.9cm^3	7.1cm^3	31.8cm^3

Table 5.15: Table comparing the geometry of the three ellipses used to build the COMSOL simulations. The volume is that of the axisymmetric sample

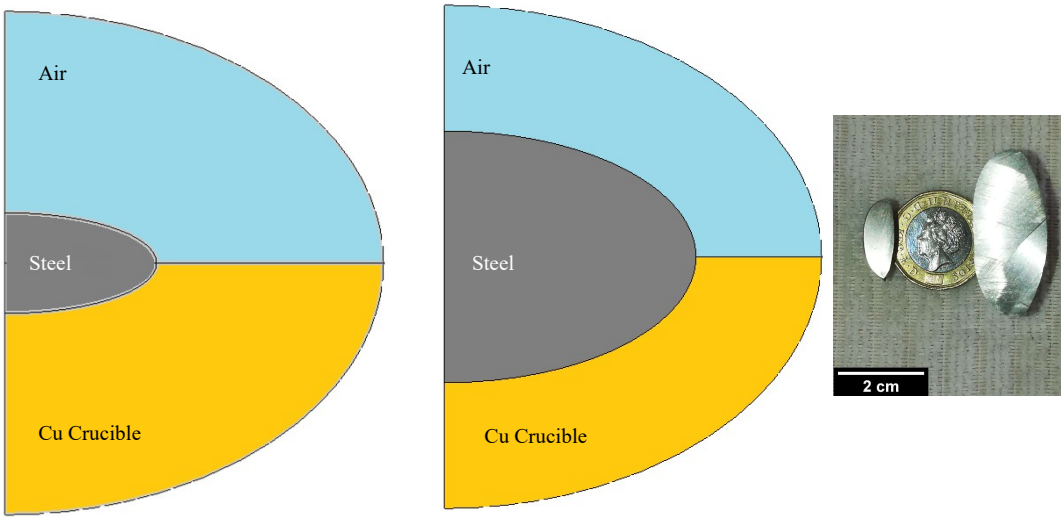

Figure 5.5: Schematic of the two COMSOL simulations, along with a picture of cross-sections of a 10 and 50g billet.

5.4.1.2 Simulation conditions

A boundary condition was applied to the outer arc of the Cu and air domains: that T=293.15K. This represents an assumption that the water cooling is effective in extracting the heat out of the surrounding environment. Initial conditions were applied to the domains so that the starting temperature of the Cu and air was 293.15K, and that the starting temperature of the steel was 3500K. This gives a discontinuity at the steel surface, but after a short number of time steps the system is able to equilibrate, so that it is physical within the temperature range of interest (3000K down to room temperature). The data shown here does not show the equilibration periods, but begins instead when T_{max}=3350K. The simulations are time-dependent studies run for 5s, with a step size of 0.01 seconds. The mesh is auto-generated within COMSOL, with the finest mesh possible given within the steel, and a "normal" mesh within the crucible and air.

5.4.1.3 The cooling behaviour of small and large billets

The main result of these simulations is that the entirety of the small billet reaches solidification temperatures 4x faster than the large billet. Figure 5.6 shows how long different regions of the billet took to reach 2000K after initialisation; this is used as an approximate melting temperature for refractory alloys that may be formed in an arc melter. The small billet takes 0.6s to entirely cool to below 2000K whereas the large billet takes 2.43s.

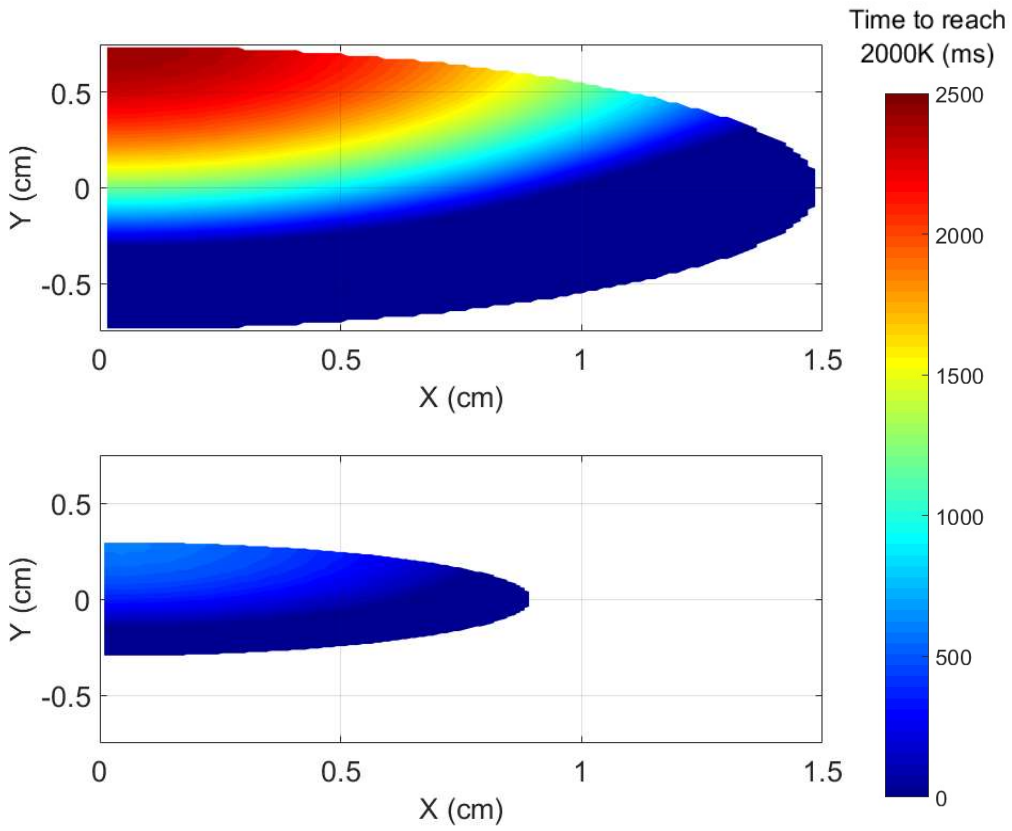

Figure 5.6: Plots showing how long each simulated node within the sample took to cool to less than 2000K.

In both billets the region closest to the Cu is already cooler than 2000K after initialisation. This is representative of the melt pool in an arc melter never being fully liquefied; on the crucible surface there is constant solidification and remelting occurring, however hot the user is able to take the melt.

Another observation is that the cooling behaviour is completely dominated by the Cu, rather than a combination of the Cu and the atmosphere. The final material to cool below 2000K is the region furthest from the Cu, even though it it is directly exposed to the atmosphere, thus the cooling direction is perpendicular to the Cu.

The cooling of the billet will not only affect its solidification behaviour, but also the microstructure formed after this. Figure 5.7 shows the fraction of each sample that is below different temperatures at each time step. It can be seen that for the small billet it has cooled entirely below 500K after 2.18 seconds. At this point diffusion will have stopped and the opportunity for precipitation has passed. In contrast, only 18% of the big sample has cooled to below 500K by the end of the simulation, and only 64% has cooled to below 1000K. This means that there is enough time during cooling for diffusion and for precipitation to occur.

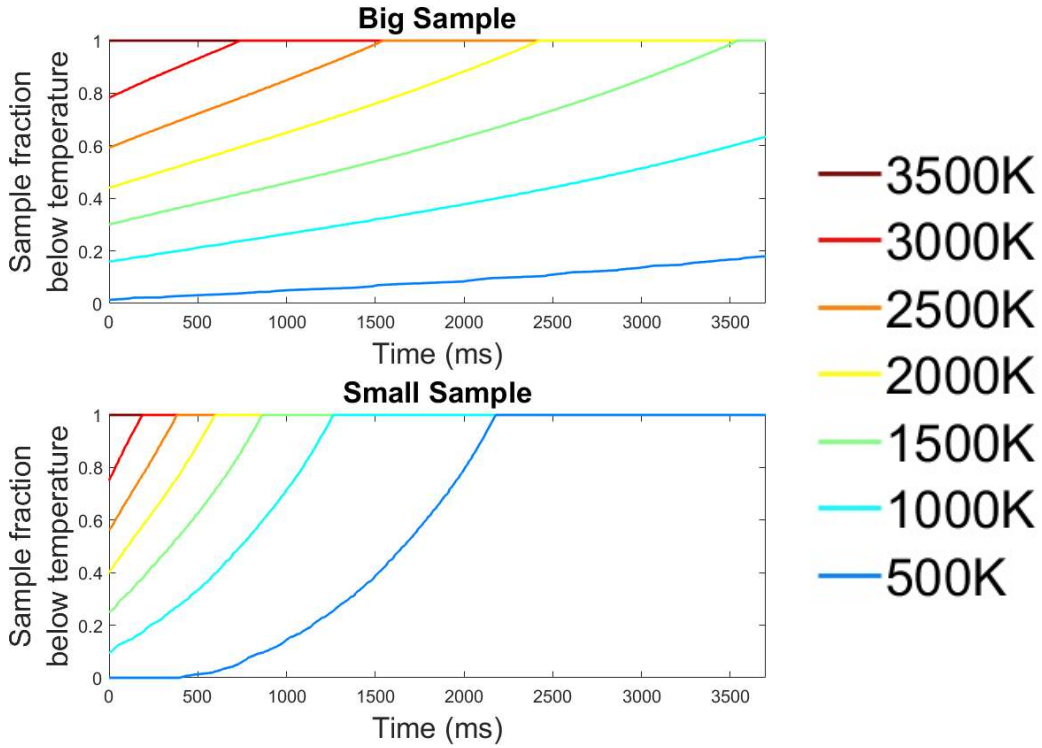

Figure 5.7: Graph showing the fraction of sample nodes that are below certain temperatures at each time step.

The next stage is to fabricate 10g billets of equiatomic TiVZrHfTa, TiVZrTa, and TiVTa, and compare them to the as-cast 50g billets that were analysed in the previous chapter.

5.4.2 Microstructural Comparison

Each section details the comparison of 10 and 50g billets of as-cast material. The phases are analysed using XRD, while back-scatter SEM images show the morphologies of phases and compare the grain structures found throughout samples.

5.4.2.1 TiVZrHfTa

Figure 5.8 shows XRD of a 10g piece of equiatomic TiVZrHfTa on the left, compared to the 50g piece on the right, volume fractions of the identified phases are given in table 5.16. It can be seen that the 10g billet is much more dominated by a primary phase, which comprises more than 85vol% of the whole. In contrast the primary phase in the 50g billet is only 58.8vol%, with the remainder being made up of 3 different phases.

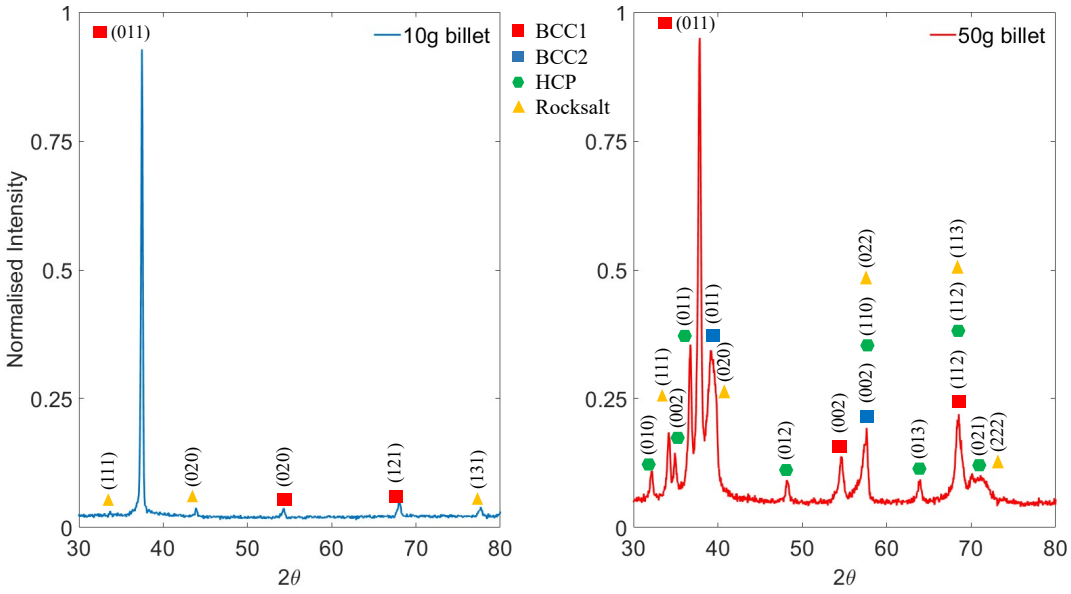

Figure 5.8: XRD traces of two billets of equiatomic TiVZrHfTa. On the left is a 10g billet which is primarily BCC with small amount of a rocksalt phase, and on the right is a 50g billet which was discussed in chapter 4

Phase	Lattice Parameter (Å)	10g Billet Volume Fractions (vol%)	50g Billet Volume Fractions (vol%)
BCC1 (red)	3.24	85.4	58.8
BCC2 (blue)	3.22	-	21.2
HCP (green)	a=3.20, c=5.11	-	12.1
Rocksalt	4.58	14.6	8.0

Table 5.16: Table comparing the lattice parameters and volume fractions for a 10 and 50g billet of equiatomic TiVZrHfTa.

The observations of suppressed phase separation are supported under SEM examination. The microstructure of the 10g billet is shown in figure 5.9, with back-scatter SEM images of the billet centre on the right, and the billet edge closest to the crucible face on the left. On the crucible face the grains are columnar, having grown in line with the cooling direction. In the centre of the billet there has been dendritic solidification, with a small amount of interdendritic segregation being visible in the back-scatter signal. Importantly, there is no obvious formation of a second phase; which is in stark contrast to the 50g billet where a multitude of different phases and precipitates were identified.

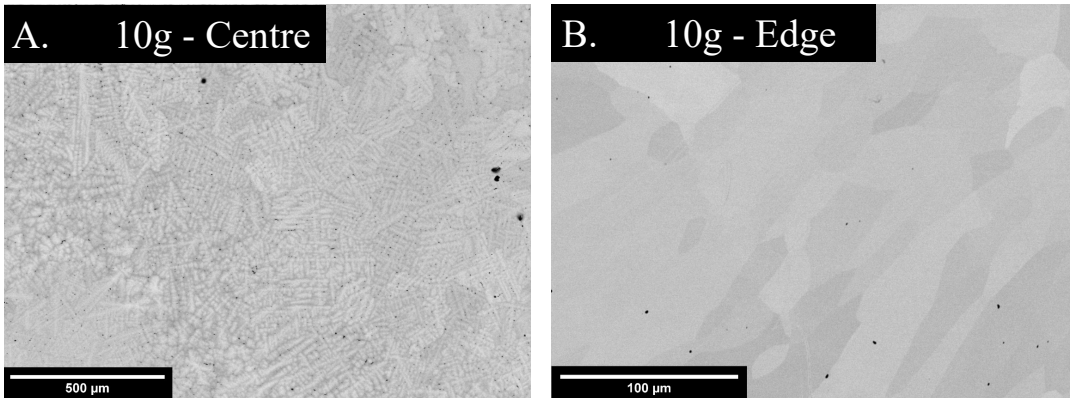

Figure 5.9: Back-scatter SEM images of a 10g billet of equiatomic TiVZrHfTa. The left-hand image is taken in the centre of the billet. The right-hand image is taken at the edge closest to the crucible.

5.4.2.2 TiVZrTa

A similar comparison is made of two billets of TiVZrTa; in figure 5.10 the XRD trace from a 10g billet is shown on the left, and a 50g billet on the right, while the volume fractions of each phase are given in table 5.17. Both samples contain the same sets of peaks relating to three different BCC phases and a rocksalt-structured phase, but in the 10g billet, the peaks relating to the primary BCC phase are far more dominant. The XRD data shows that although the volume fraction of the rocksalt-

structured phase has increased, so has the volume fractions of the primary phase, demonstrating the suppression of phase separation.

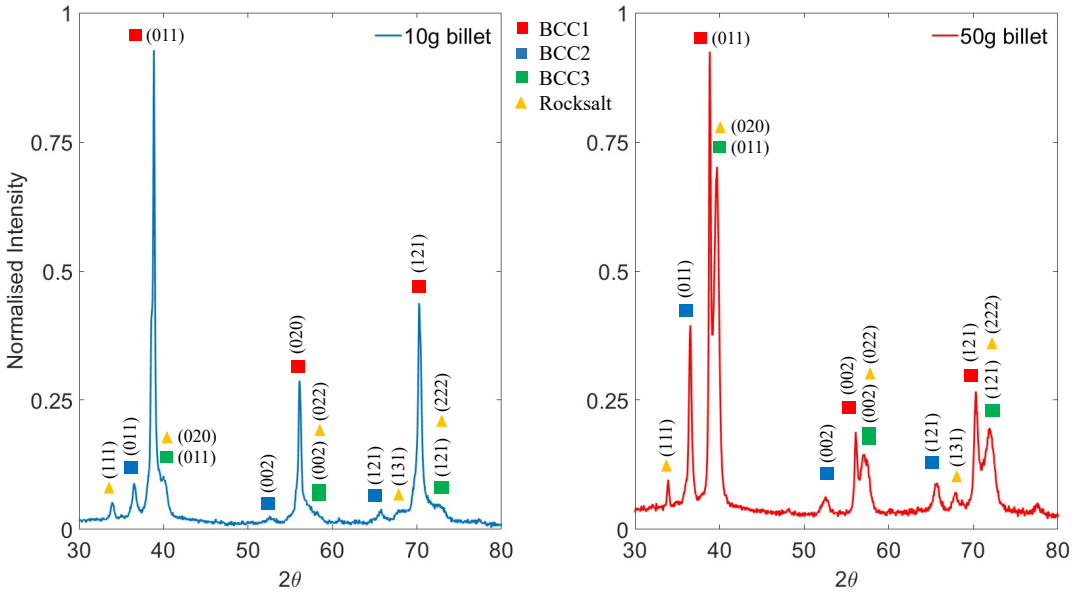

Figure 5.10: XRD traces of two billets of equiatomic TiVZrTa. On the left is a 10g billet which is BCC and a rocksalt phase, and on the right is a 50g billet which was discussed in chapter 4

Phase	Lattice Parameter (Å)	10g Billet Volume Fractions (vol%)	50g Billet Volume Fractions (vol%)
BCC1 (red)	3.28	73.9	48.7
BCC2 (blue)	3.48	10.7	15.8
BCC3 (green)	3.22	5.6	42.1
Rocksalt	4.58	9.8	3.4

Table 5.17: Table comparing the lattice parameters and volume fractions for a 10 and 50g billet of equiatomic TiVZrTa.

This is corroborated in the SEM; images A and B in figure 5.11 shows two micrographs of the 10g billet of TiVZrTa, image A is the centre of the billet where a dendritic microstructure with small dark-contrast precipitates can be seen, and image is B is taken at the edge of the billet closest to the crucible face, where a columnar grain structure can be seen but with no precipitation visible. Image C is of

the centre of the 50g billet, and acts as a comparison to image A, demonstrating that the microstructure is finer, and the precipitates are smaller in the 10g billet, which explains the change in relative peak height of the different phases in the XRD data.

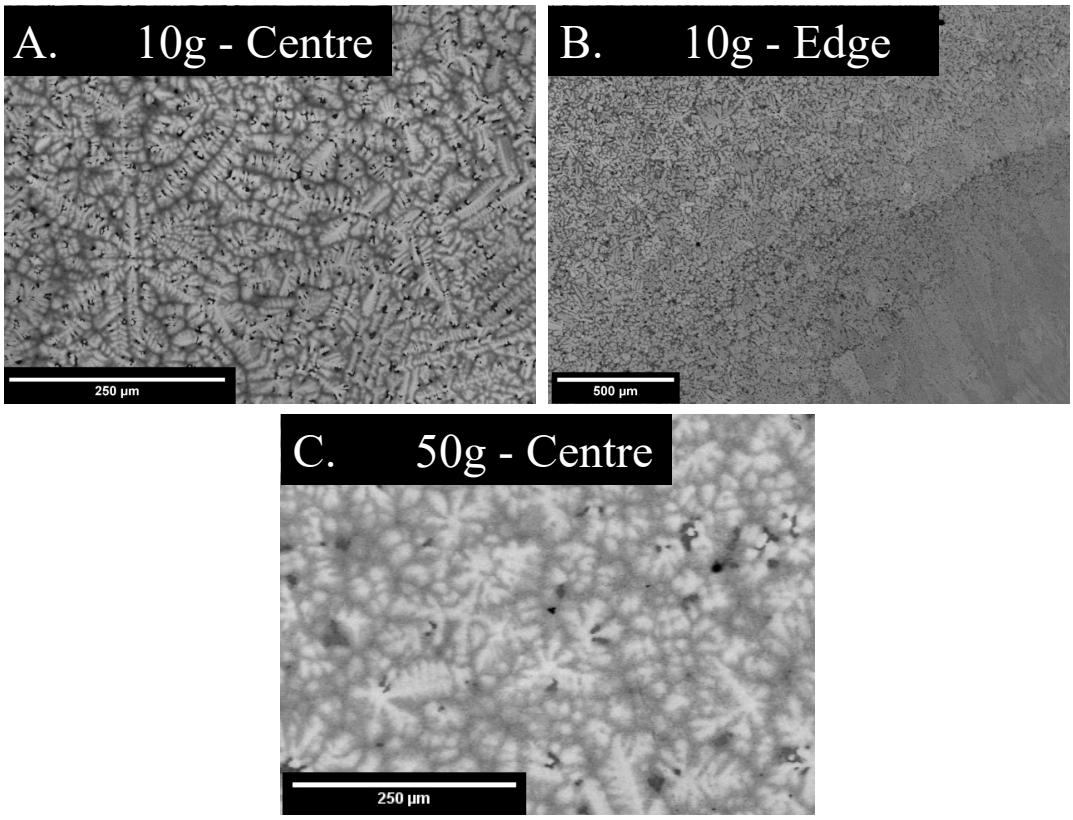

Figure 5.11: Back-scatter SEM images of equiatomic TiVZrTa. Images A and B are taken of the 10g billet, in the centre and the crucible edge respectively. Image C is taken from the centre of the 50g billet. It should be noted that the brightness-contrast levels and resolution are different for image C.

5.4.2.3 TiVTa

The final alloy where billets of 10 and 50g are compared is TiVTa. Figure 5.12 shows the XRD comparison, and it can be seen that both billets contain primarily a BCC phase, but also contain a small amount of a rocksalt-structured phase. It is not possible to draw distinctions between the microstructures based on the XRD data alone, as the data could not be fit sufficiently well to extract reliable volume

fractions for each phase.

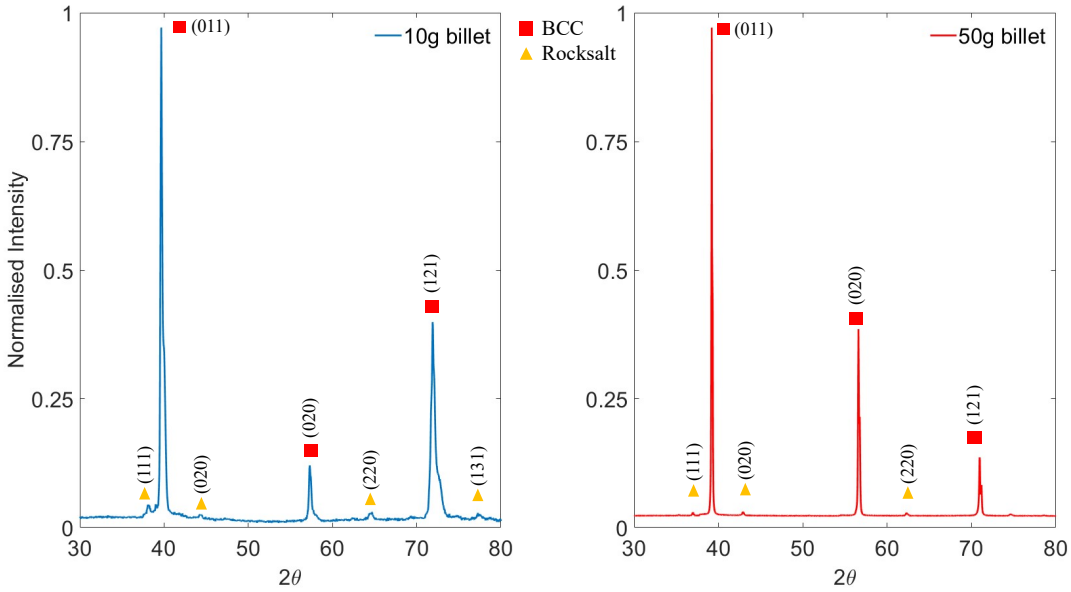

Figure 5.12: XRD traces of two billets of equiatomic TiVTa. On the left is a 10g billet which is BCC and a rocksalt phase, and on the right is a 50g billet which was discussed in chapter 4

Back-scatter SEM images of the 10g billet are shown in figure 5.13, with the left hand image taken in the centre of the billet, and the right hand image taken at the edge closet to the crucible. As in the five and four component alloys the centre of the billet has a dendritic microstructure, with interdendritic segregation and precipitation of a dark-contrast phase visible. At the edge of the billet the grain structure is columnar, and there is no visible precipitation.

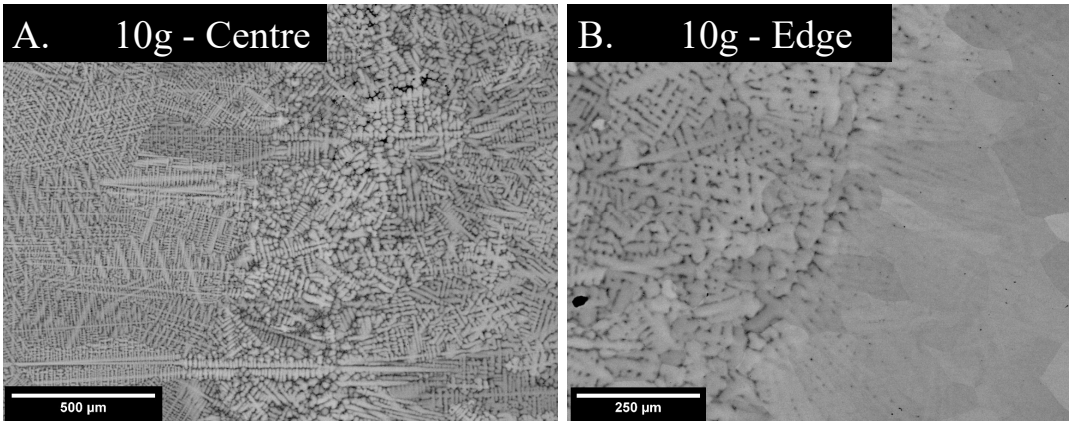

Figure 5.13: Back-scatter SEM images of a 10g billet of equiatomic TiVTa. The left-hand image is taken in the centre of the billet. The right-hand image is taken at the edge closest to the crucible.

It useful to contrast the microstructures of the 10 and 50g billets of TiVTa. Figure 5.14 shows two EBSD phase maps of the 10g billet on the left and the 50g billet on the right. In the 10g billet the rocksalt structure takes the form of lath like precipitates in the interdendritic regions of the sample. In the 50g billet the laths still appear, but there are also much larger rocksalt-structured precipitates that are more spheroidal in shape.

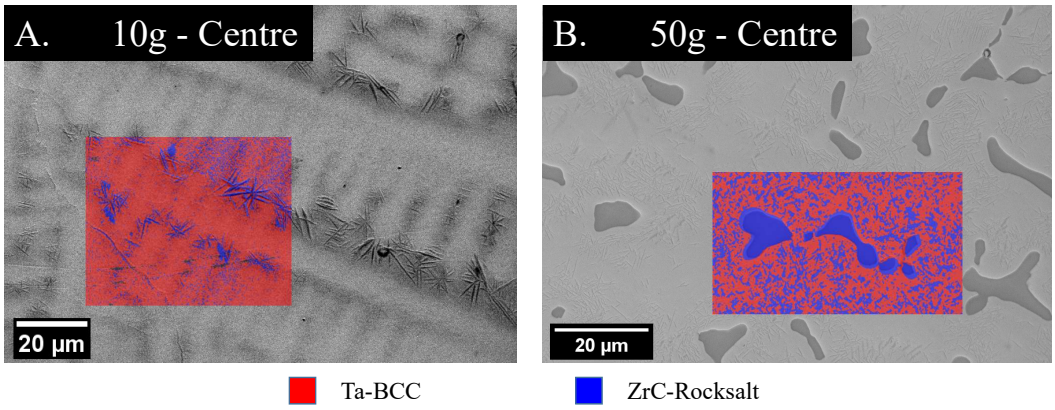

Figure 5.14: Two EBSD micrographs of TiVTa. On the right is the 10g billet, containing rocksalt-structured laths in the interdendritic region. On the right is the 50g billet which contains laths, but also much larger and more spheroidal rocksalt-structured precipitates.

5.4.3 Discussion on the effect of Billet size

In all three 10g billets the microstructures are more simple than in the 50g counterparts. This is not due to differences in composition which have been measured by EDX and found to be very simialr, as shown in tables 5.18 to 5.20.

Element	10g Billet composition (at%)	50g Billet Composition (at%)
Ti	21.16 ± 0.6	19.00 ± 0.1
V	19.61 ± 0.4	18.94 ± 0.3
Zr	20.65 ± 0.2	21.08 ± 0.4
Hf	19.61 ± 0.3	20.67 ± 0.2
Ta	18.97 ± 0.3	20.31 ± 0.4

Table 5.18: Table comparing the compositions of the 10g and 50g billets of equiatomic TiVZrHfTa. The data is an average of three EDX Point&ID scans taken at minimum magnification across different regions of the sample. The error is the standard deviation of this data.

Element	10g Billet composition (at%)	50g Billet Composition (at%)
Ti	25.52 ± 0.3	23.87 ± 0.2
V	24.59 ± 0.7	24.22 ± 0.2
Zr	28.12 ± 0.3	29.34 ± 0.2
Ta	21.75 ± 1.2	22.57 ± 0.4

Table 5.19: Table comparing the compositions of the 10g and 50g billets of equiatomic TiVZrTa. The data is an average of three EDX Point&ID scans taken at minimum magnification across different regions of the sample. The error is the standard deviation of this data.

Element	10g Billet composition (at%)	50g Billet Composition (at%)
Ti	33.98 ± 0.2	43.09 ± 0.4
V	33.39 ± 0.2	28.06 ± 0.4
Ta	33.63 ± 0.1	28.84 ± 0.1

Table 5.20: Table comparing the compositions of the 10g and 50g billets of equiatomic TiVTa. The data is an average of three EDX Point&ID scans taken at minimum magnification across different regions of the sample. The error is the standard deviation of this data.

The explanation for the differences in microstructure is that in the smaller billets, the faster cooling rate predicted by FEA has resulted in less diffusion and so less precipitate growth. The observation of *no* precipitation close to the crucible face demonstrates that the very fast cooling achieved here is enough to generate a completely different microstructure, even to the rest of a 10g billet. This is in agreement with the results of Molnar and Lv [109, 110] who found secondary phase formation decreased when using casting techniques that involve faster cooling.

What is new in these results is demonstrating that changing the arc-melting conditions is sufficient to dramatically reduce the amount of precipitation achieved, even in alloys containing impurities which are prone to phase separation. Researchers only rarely give information on the size of their arc-melted billets, however based on the evidence collected here, this potentially has more effect on the as-cast microstructure than the composition does. Arc-melted billet mass *must* be included in experimental details if the effect of sample fabrication is to be understood.

5.5 Conclusions on single-phase microstructures in HEAs

Throughout the literature there are many attempts to quantify the thermodynamics underpinning HEA formation. These have met with mixed success, as has the new method proposed here of optimising composition in order to maximise the Ω parameter. Although the alloys studied in this project have issues with contamination, it has been clearly demonstrated that reducing billet size and thus increasing cooling rate is a more successful route to manufacturing single phase high-entropy alloys than altering composition. This implies that single-phase HEAs are more akin to metastable alloys such as Al-Mg than their name, which is routed in thermodynamics, would suggest. Many authors have proposed new names for high-entropy

alloys which tie in better to their way of thinking, for example Multicomponent Alloys (MCAs) or Complex Concentrated Solutions (CCSs). Each of these names has problems: MCAs also include BMGs and intermetallics, while for CCSs it is arguable that HEAs are neither comositionally complex *or* concentrated. This author also has his own new name: Non-Traditional Solution Alloys (NTSAs), as this implies that their compositional novelty, as well as stating the microstructure that is thought to confer the best properties. Most importantly, it does not mislead new researchers into the field and puts clear distance between new work, and old work which was underpinned by now defunct hypotheses, such as the cocktail effect.

Chapter 6

Microstructural variations throughout an arc-melted billet

6.1 Introduction

In the previous chapters it was shown that the alloys melted for this project are contaminated by carbon, nitrogen, and oxygen impurities. These alloys contain several phases, as well as microsegregation which has led to further phase separation. It has also been demonstrated that the phase separation can be suppressed in as-cast arc melted samples by reducing sample size and thus increasing cooling rate. This chapter continues to examine the microstructural variation that occurs in arc melted billets, by exploring how chemistry, crystal structures, and porosity vary through a 50g billet.

6.2 Experimental details

The data presented here is taken from a 50g billet of as-cast equiatomic TiVZrHfTa, which has been sectioned along its long axis (i.e. perpendicular to the geometries shown in section 5.4.1). This is the sample previously referred to as the "Sectioned Billet" and the bulk composition provided by AMG have been reproduced in table 6.1.

Element	Target Composition (at%)	AMG Compostion (at%)
Ti	20.00	16.55
V	20.00	17.41
Zr	20.00	16.59
Hf	20.00	15.79
Ta	20.00	16.72
C	-	0.40
N	-	8.83
O	-	3.44
W	-	0.08
Cu	-	0.21
Fe	-	3.98

Table 6.1: Table comparing the target composition of the Sectioned Billet to the one provided by AMG that was actually achieved.

All other samples in this thesis have been sectioned along the small axis, meaning the material analysed has a variety of thermal histories, including material that solidified almost instantly; and material that took several seconds to solidify, and tens of seconds to reach room temperature. In contrast the individual slices sectioned along the long axis all have different thermal histories, and although this varies from the edge to the centre of individual samples, it allows a more direct comparison between material close to the crucible face, which has solidified instantly, and the

material which is closer to the Ar atmosphere of the chamber, which has solidified more slowly. Schematics of these sample geometries are shown in figure 6.1 and the results of the FEA simulations in chapter 5 are reproduced for the ∼50g sample in figure 6.2, showing the variation in approximate solidification time along the short-axis.

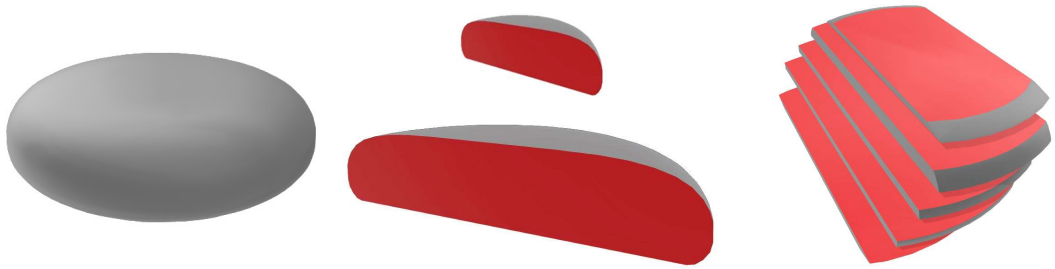

Billet - unsectioned | Sectioned along the short axis | Sectioned along the long axis

Figure 6.1: Schematics left-to-right showing the shape of an as-cast billet, a billet sectioned along the short axis, as is standard, and a billet sectioned along the long axis, as is done for the samples in this chapter.

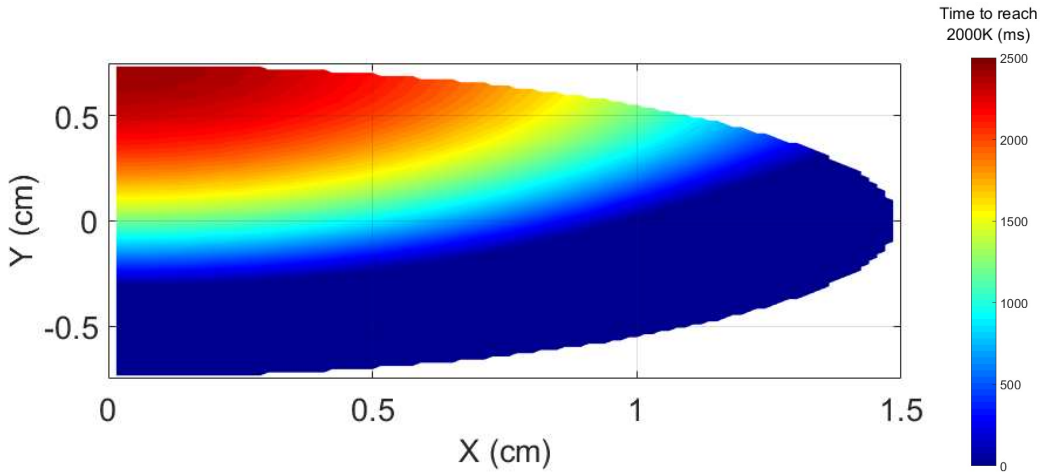

Figure 6.2: Plot showing the time each node took to reach 2000K in the COMSOL simulation of an ∼50g sample, reproduced from section 5.4.1

6.2.1 Sample Identification

The billet was sectioned into 5 slices, and both sides of each slice were polished to give a total of 10 samples. Sample 1 and sample 10 were on the two edges of the billet, and were ground back so as to give a flat surface for analysis. Sample 1 is the part of the billet closet to the Cu crucible. Sample 10 is the part of the billet directly exposed to the Ar atmosphere. During this chapter "samples" will relate to a specific polished surface, while "slice" will relate to a specific piece of metal. The billet was sectioned using a slow-saw for some cuts, and also a spark cutter for others. The approximate thickness of these is 0.5mm, while the polishing process is estimated to remove 200 µm per sample. The measured thickness of each slice after being polished is shown in table 6.2, while the calculated distance along the z axis of the centre of each sample is shown in table 6.3.

Slice	Post-polishing Thickness (mm)
Slice A	1.75
Slice B	1.15
Slice C	0.75
Slice D	1.35
Slice E	1.75

Table 6.2: Table comparing the thicknesses of each slice of the Sectioned Billet.

Sample Number	Distance from Crucible (mm)
1	0.55
2	2.30
3	3.20
4	4.35
5	5.25
6	6.00
7	6.90
8	8.25
9	9.15
10	10.9

Table 6.3: Table comparing the calculated distance from the centre of each sample to the very bottom of the crucible bowl (i.e. the distance along the z axis)

The original billet thickness was measured as 12.1mm thick, while the sum of the slice thicknesses and the material removed is 11.5mm; a difference of approximately 5%, which is a reasonable margin of error.

6.3 Compositional changes

The first variability to be examined is compositional: has there been any macrosegregation throughout the billet, or has the electromagnetic stirring and billet-flipping ensured compositional homogeneity? As discussed in chapter 4 assessing composition of impurities with EDX is difficult, but the ratio of metallic elements is consistent with the analysis provided by AMG. Figure 6.3 shows the composition of the metallic elements on each slice of the sample, with data being taken at minimum magnification. The metallic composition is consistently equiatomic from end to end, demonstrating that bulk composition of the metallic elements does not vary. To further demonstrate this figure 6.4 shows the normalised EDX spectra for the data presented in figure 6.3. Relative peak heights are all consistent, except for carbon, where the relative intensity nearly doubles on samples 3 and 4. This measurement could be due to surface contamination rather than bulk composition, but it does demonstrate that there may be some variation in the impurities through the billet. If the relative peak heights in EDX are proportional to carbon concentration, and AMG's bulk carbon concentration of 0.4at% is accurate, then this implies that sample 3 contains 0.72at%, sample 4 contains 0.46at%, while the other four samples contain 0.31at%; which means the standard deviation on the carbon concentration of the slices is only 0.15at%. Despite the relative peak intensity for carbon varying, it does not translate into big errors in concentration.

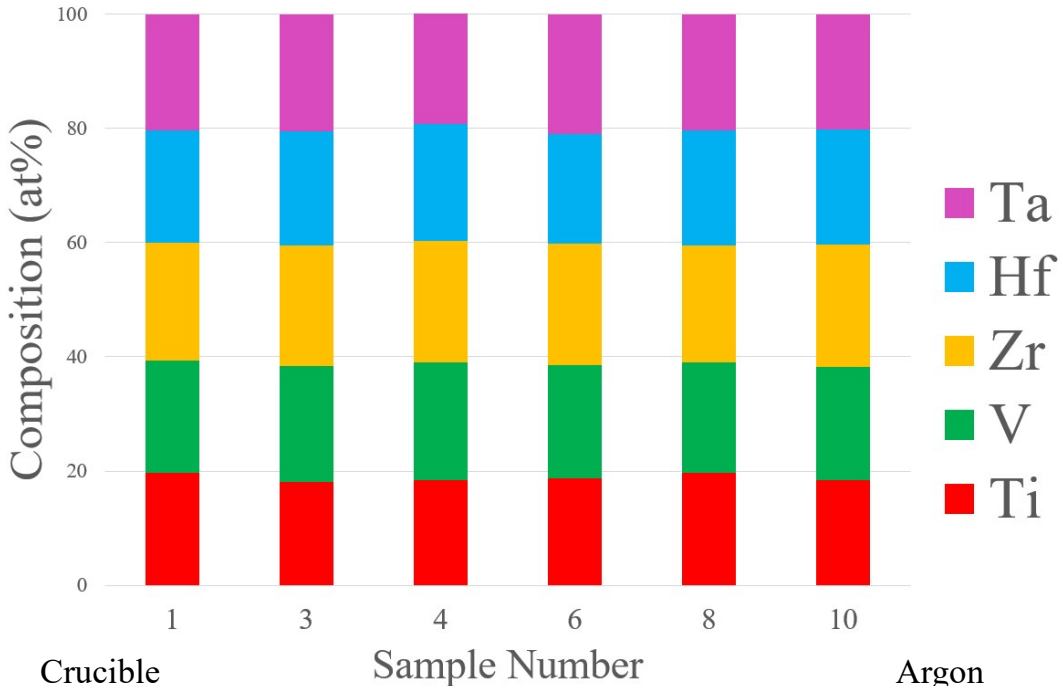

Figure 6.3: Chart showing the variation in composition from the base of the billet (closest to the crucible) to the top (exposed to the Ar atmosphere). Data has been collected as area scans near the centre of each sample at low magnification.

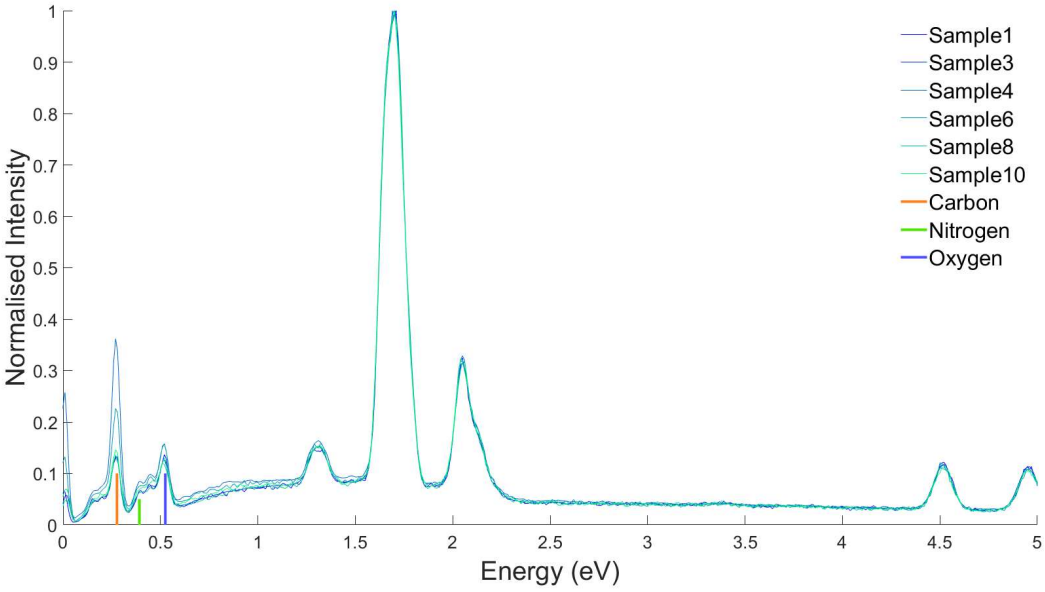

Figure 6.4: Graph comparing the normalised intensities of EDX spectra taken from some of the samples throughout the billet. The thick lines are the theoretical positions of the Carbon, Nitrogen, and Oxygen signals.

6.4 Crystallography changes

The second variability to be examined is crystallographic: what phases are present in each sample, and in what proportions? The XRD traces for all ten samples are shown in figure 6.5; it is difficult to analyse data in this form, but it can already be seen that the height of several peaks is increasing dramatically from sample 1 to sample 10, these are indicated by red arrows. The same four phases have been identified as for 5eqC, as indexed in figure 4.10: two BCC phases, an HCP phase, and a rocksalt-structured phase. It is worth noting that the analysed region is in the centre of the sample, selected with a 1cm diameter aperture.

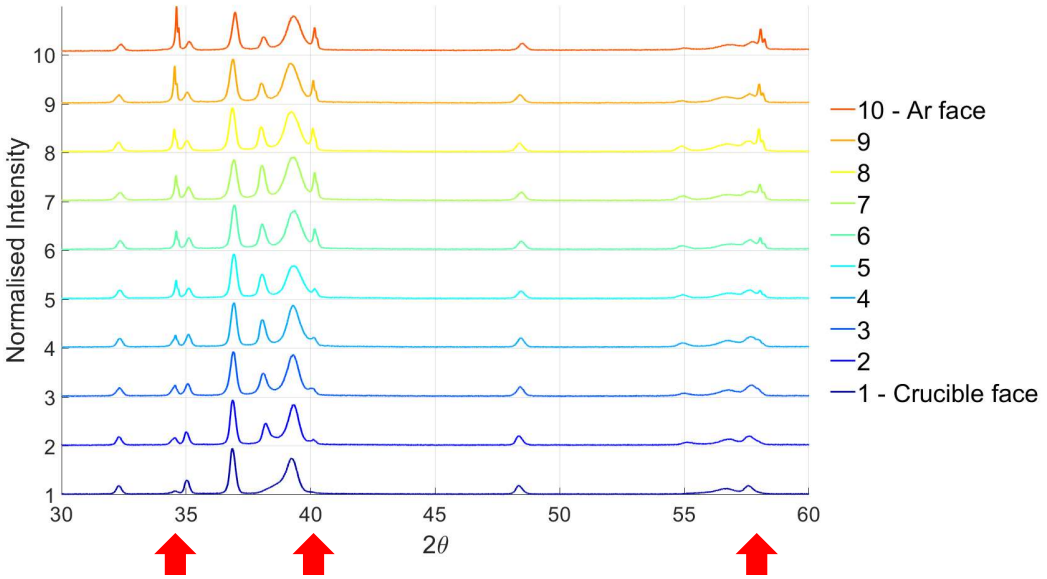

Figure 6.5: Chart showing the XRD traces for each sample from the sectioned billet. The red arrows indicate the peaks whose heights are changing the most between samples

The XRD traces for sample 1 and 2 are from the opposite sides of the same slice, and show the most dramatic variability between adjacent samples. This is shown in figure 6.6 along with the peak positions for the indexed phases. Sample 1 is closet to the crucible face and therefore has the fastest cooling rate; sample 2 is on the opposite side of the same slice (which is 1.75mm thick) and so, except for at the edges, sees a slower cooling rate. This reduction in cooling rate has allowed a greater volume fraction of the rocksalt phase and the second BCC phase to form.

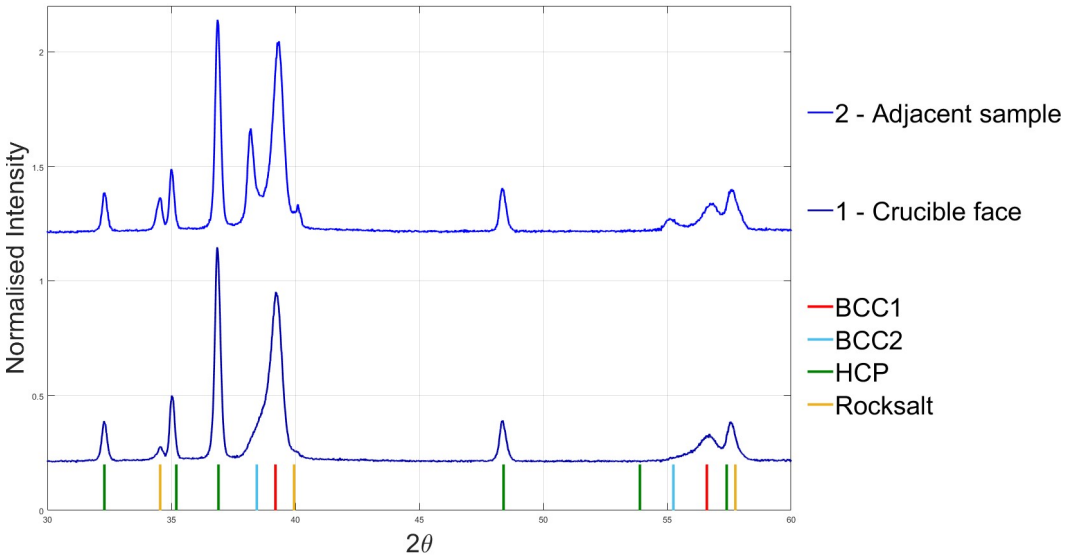

Figure 6.6: Chart comparing the XRD traces for sample 1 (on the crucible face) and sample 2 (on the reverse side of that slice), along with peak positions for the four identified phases. Sample 2 has much larger peaks relating to the rocksalt-structured phase and to the second BCC phase.

6.4.1 Phase Volume Fraction

Each trace has been fitted for the four indexed phases, this allows properties to be extracted such as volume fraction, crystallite size, and elastic strain. The methods and difficulties of extracting this information from XRD data is given in chapter 3, but an important point to reiterate is that although there are unquantifiable errors on the absolute numbers given here, they are much more valuable as comparisons between samples; each XRD traces was fitted for the same initial guesses and so relative changes are expected to be accurate.

The change in volume fraction from sample to sample is shown in figure 6.7. It can be seen that BCC1 is consistently the primary phase, remaining between 70 and 75 vol% consistently. The secondary BCC phase is always of a low volume fraction, suggesting it is most likely one of the phases forming in the interdendritic

regions of the sample. The fraction of HCP phase decreases from 20 to 15 vol% from the crucible face to the Ar face, while the volume fraction of the rocksalt phase increases from 0 to 10 vol%. The HCP and rocksalt phases seem to be linked: while the former decreases the latter increases in its volume fraction.

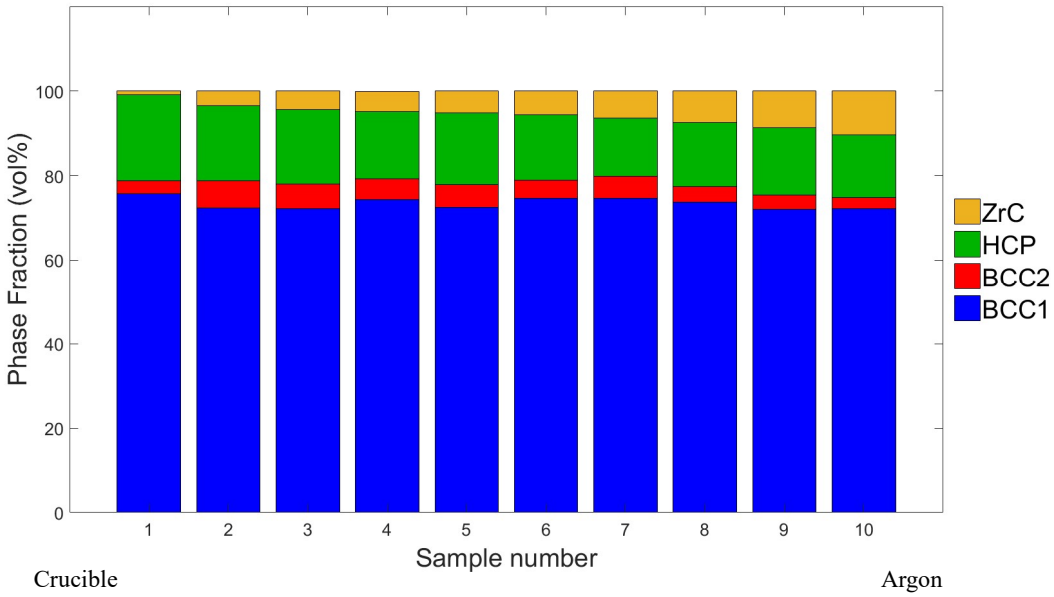

Figure 6.7: Chart showing the variation in phase fraction through the crucible. Data is collected by analysing XRD traces for each sample using rietveld refinement.

6.4.2 Crystallite size

The calculated crystallite sizes for each phase in each sample is shown in figure 6.8. The BCC2 phase has no data shown, as values of crystallite size and strain could not be reliably extracted; this was due to a problem in the software used rather than an intrinsic issue with the data. Values could be extracted for the other phases, and these show that the BCC1 has a relatively consistent crystallite size and elastic strain; this is expected if it is the primary phase and its formation conditions are not impinged by any surrounding material. The crystallite size of the HCP phase decreases slightly, while the rocksalt-structured phase increases. This reaffirms what was observed in

their volume fractions: the rocksalt phase is forming at the expense of the HCP phase.

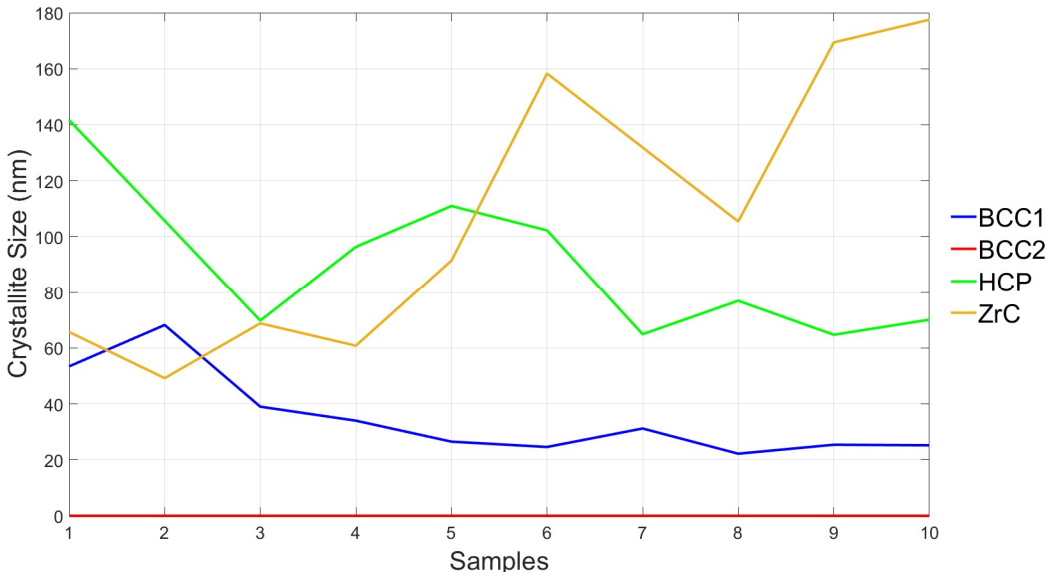

Figure 6.8: Graph showing the change in crystallite size of the four indexed phases throughout the Sectioned Billet as measured by XRD. The values for BCC2 are set to zero as no measurements could be taken of this phase.

6.5 Mechanical Properties by microindentation

It has been shown that composition is consistent throughout the billet, but that microstructure evolves to have a higher fraction (∼10vol%) of rocksalt phase in sample 10 than in sample 1. In order to assess whether this also changes the properties of the material, microindentation has been used on each slice to measure the mechanical response. The data shown in figure 6.9 and is plotted alongside the change in volume fraction of the rocksalt-structured phase, as measured by XRD. The results show that measured hardness increases from 6.44 at the base of the billet, to 7.21GPa at the top. This demonstrates that the changes in microstructure generated by the variation in cooling rate can have tangible effects on the measured properties of the alloy, not just it's microstructural morphologies.

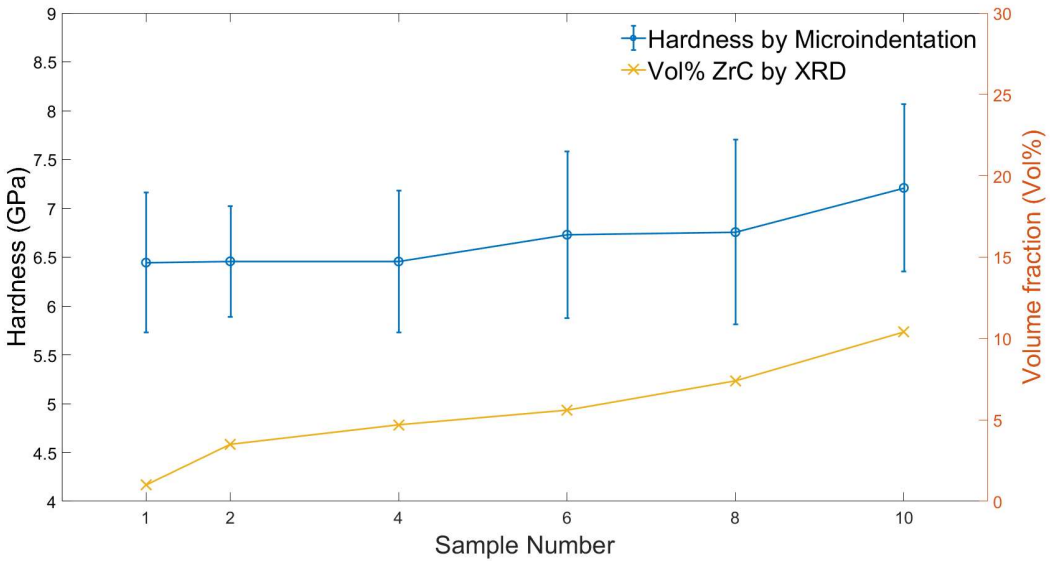

Figure 6.9: Graph comparing the microhardness of the sectioned billet to the volume fraction of the rocksalt phase by XRD in each sample.

6.6 Edge of Billet versus middle

SEM images taken throughout the billet also demonstrate how billets can vary from the centre of the billet to an edge. Figure 6.10 shows low magnification SEM images of the edge and centre of sample 3. It can be seen that there is much reduced precipitation of the rocksalt phase. The reason for this is that due to the geometry of the crucible, the cooling rate does not decrease evenly from slice A, to E: the edges of slices A, B and C were all in contact with the crucible, and share roughly the same thermal history, it is only in the centre of the billet that the cooling rates slow down dramatically. It is worth noting that the XRD conducted on the Sectioned Billet was targeted at the centre of each sample, using a 1cm diameter aperture. Figure 6.11 shows similar SEM images of sample 1, but at a higher magnification. This shows that even in the sample closet to the crucible face, the differing solidification environment has led to very different phase morphologies.

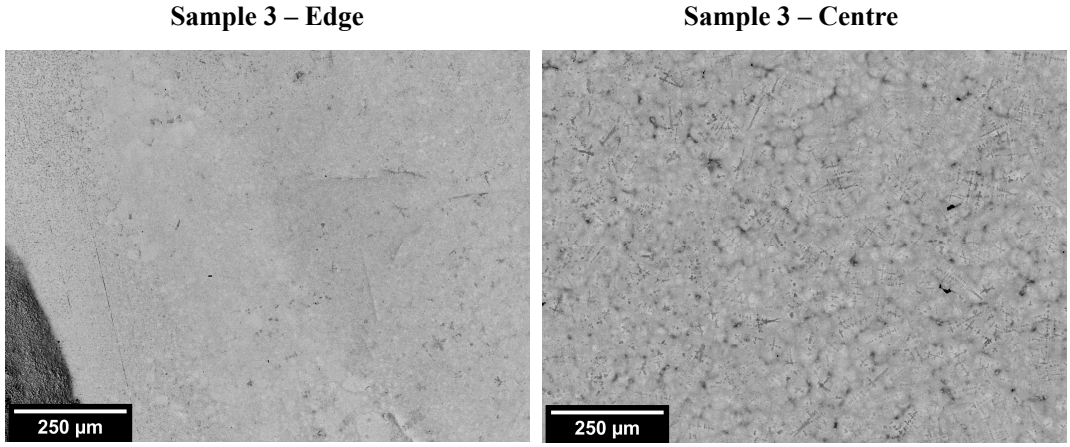

Figure 6.10: Back-scatter images of sample 3 showing the edge and centre of the billet. It can be seen that there is increased precipitation of the HCP phase in the centre of the billet. The dark grey region on the edge image is physical side of the billet, which is angled downwards.

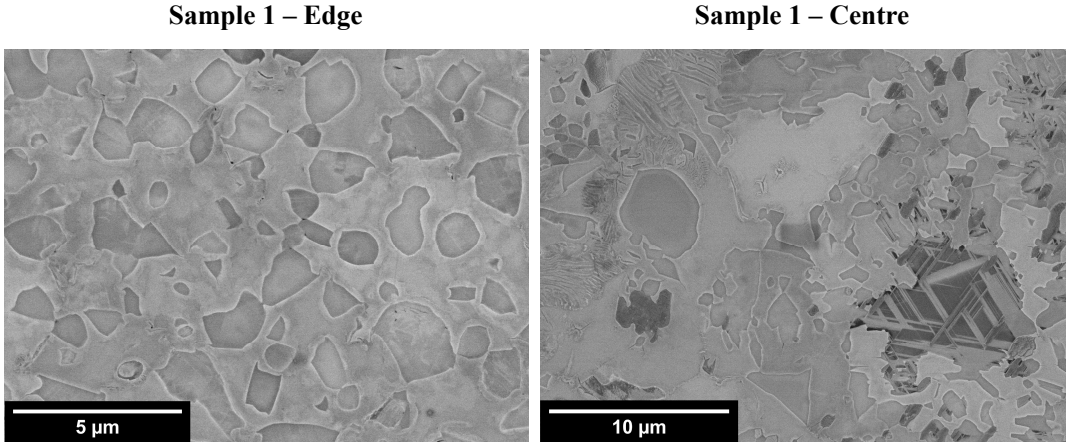

Figure 6.11: Back-scatter images of sample 3 showing the edge and centre of the billet. It can be seen that there is increased precipitation of the HCP phase in the centre of the billet. The dark grey region on the edge image is physical side of the billet, which is angled downwards.

6.7 Porosity through the billet

The amount of porosity through a billet is dependent on the chemistry of the melt, the geometry of the crucible, and the local cooling/solidification rate achieved. In order to measure porosity effectively throughout the billet, each slice was examined using an SEM algorithm that imaged each area of the sample sequentially; using FIJI (ImageJ) these micrographs could be stitched together to form one large image, or analysed one by one in order to extract statistics.

Using this latter approach the micrographs could be analysed for porosity by using the in-built Fiji functions for thresholding and "Analyze Particles" which counts pixels in order to extract information such as the number of pores and their size. Figures 6.12 and 6.13 show a progression of this analysis from a raw to analysed image.

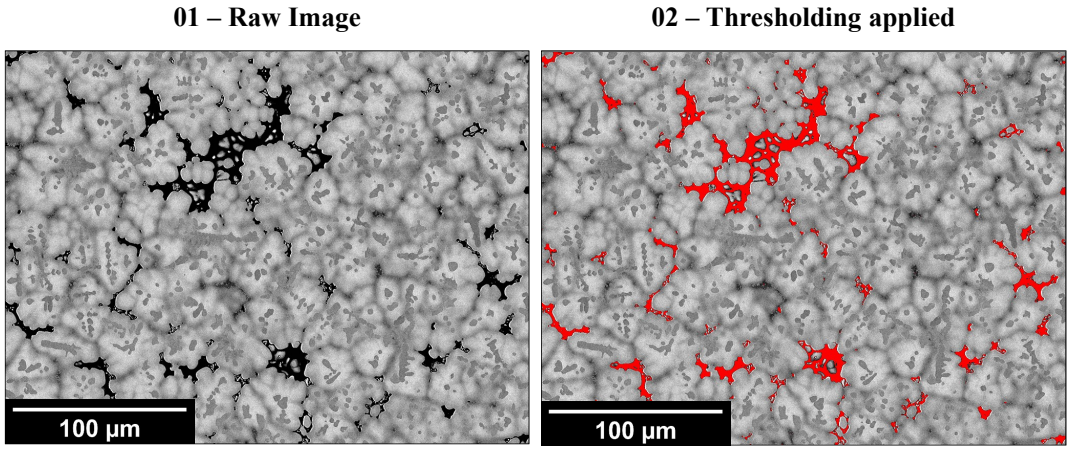

Figure 6.12: The image on the left is a raw image taken from sample 5. The Image on the right is the result of using the in-build Fiji function ”Threshold”, with grey scale limits of 0 and 5.

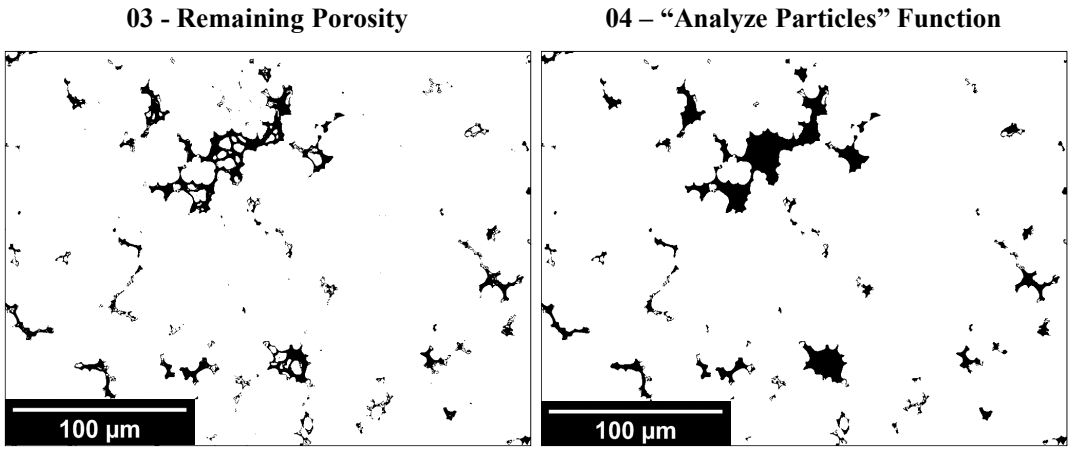

Figure 6.13: The image on the left is the what remains after the thresholding is complete, whilst the image on the right is the result of using the in-built Fiji function ”Analyze Particles” with settings to of size=20-15000 and circularity of 0.0-1.0.

The edges of the sample were found and excluded from any analysis by using a similar procedure, but thresholding at high grey scale values (between 200 and 255) in order to isolate the images of the polished sample. An example of what is excluded can be seen in figure 6.14.

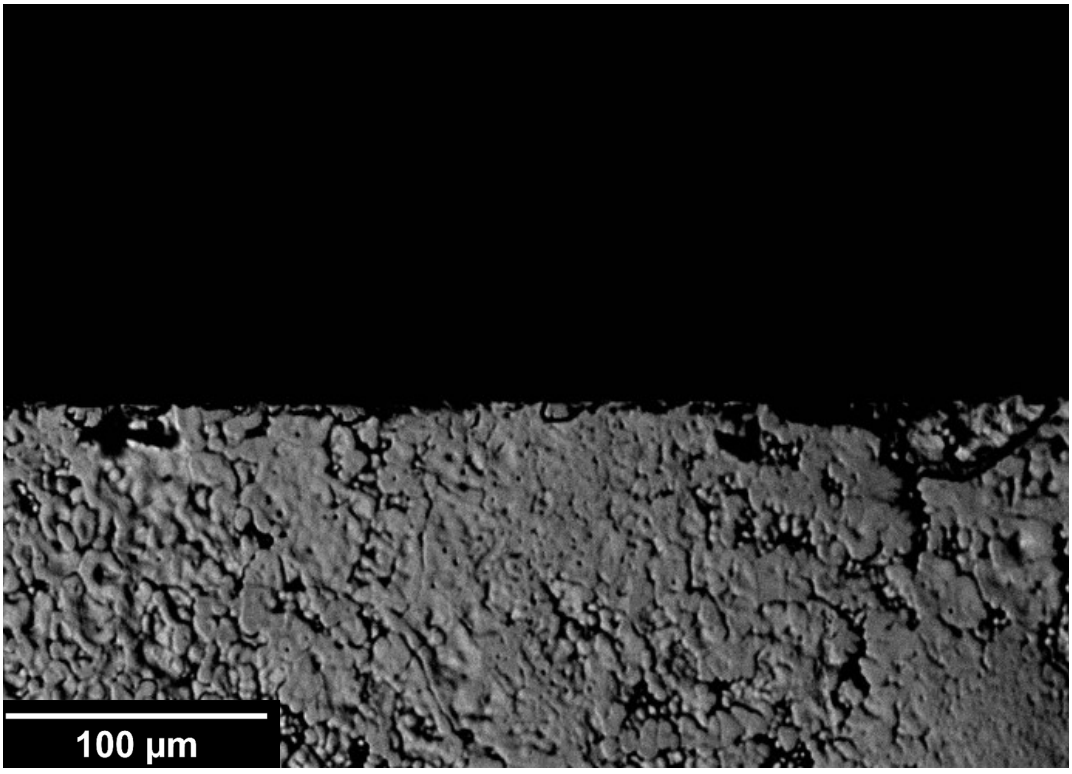

Figure 6.14: Image of the sample edge. The black region is off the sample and the grey region is the unpolished sample surface, angled due to the shape of the billet. When thresholded at high values (between 200 and 255 grey scale) none of this image remains, and so it can be excluded from pore analysis.

Due to the chemistry of the sample and nature of secondary and back-scatter electron detectors the thresholding was unable to reliably distinguish between different phases and areas of segregation. This can be seen in figure 6.15 which shows an attempt to isolate the HCP precipitates using thresholding, but has also captured the segregated regions as they share a grey scale value.

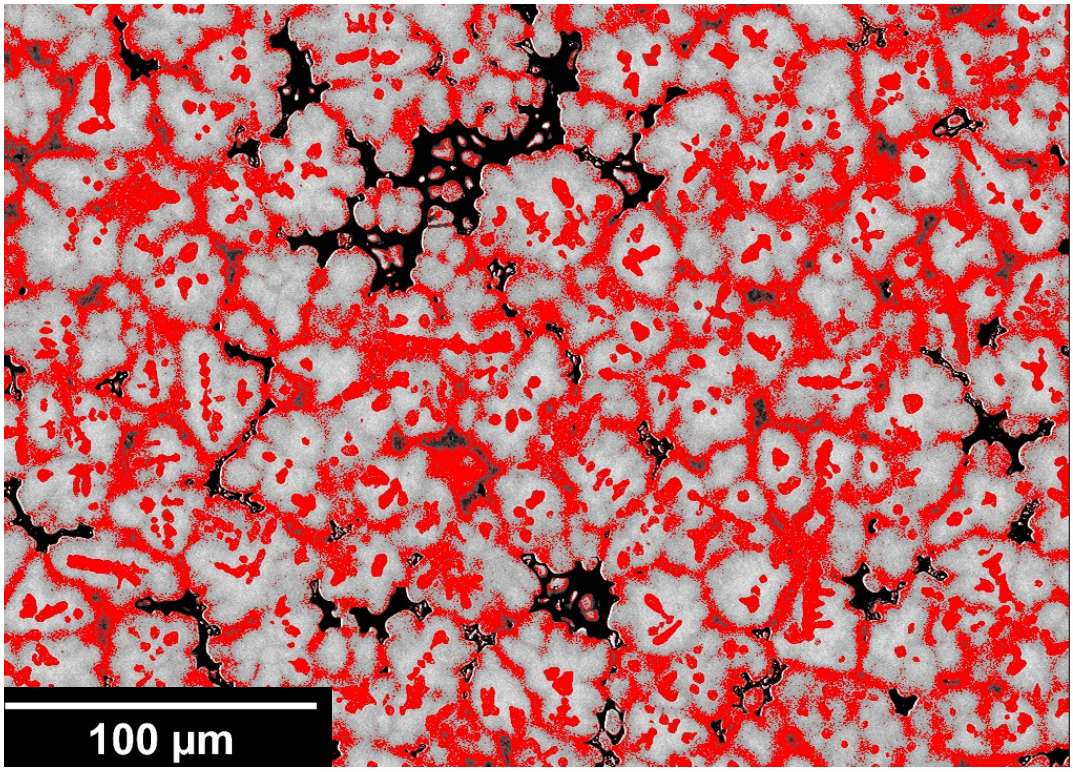

Figure 6.15: Image demonstrating an attempt to use grey scale thresholding to isolate the secondary phase in an SEM image. It can be seen that the grey scale value of the HCP precipitates and the segregated regions are the same.

Once this data was collected it was analysed to show maps of porosity and to extract statistics. Figures 6.16 and 6.17 shows heat maps of the porosity in samples 8 and 10 respectively. The colour relates to the percentage of each pixel which as been determined to be porosity.

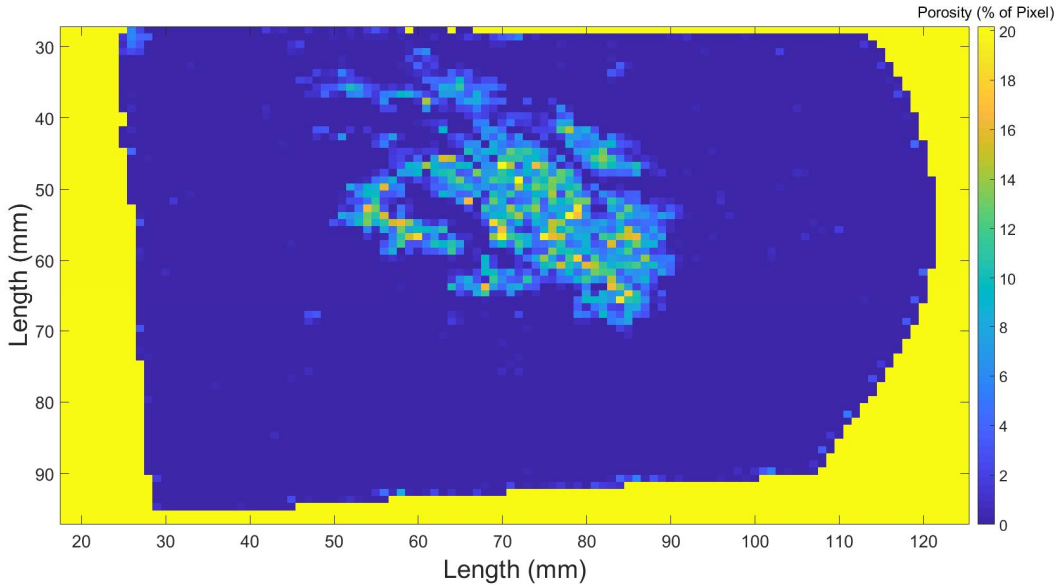

Figure 6.16: Heat map of porosity across sample 8, made by using thresholding of a mosaic backscatter SEM images of the sample. The colour of each pixel relates to the percentage of it which has been determined to be a pore.

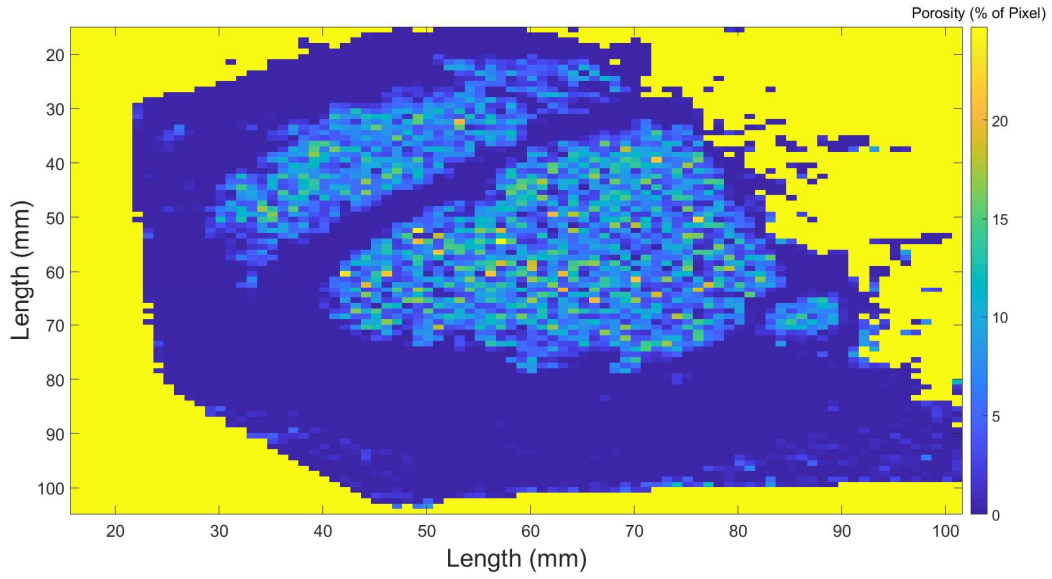

Figure 6.17: Heat map of porosity across sample 10, made by using thresholding of a mosaic backscatter SEM images of the sample. The colour of each pixel relates to the percentage of it which has been determined to be a pore. It can be seen that the unpolished regions of the sample have been ignored.

This data can also be used to extract statistics about the porosity in the billet: figure 6.18 shows the average pore size and total pore area on each sample. It can be seen that both these values increase from samples 1 through 10, but that there are a low number of large pores in sample 1, 2 and 3: the average size is high, but the raw count very low.

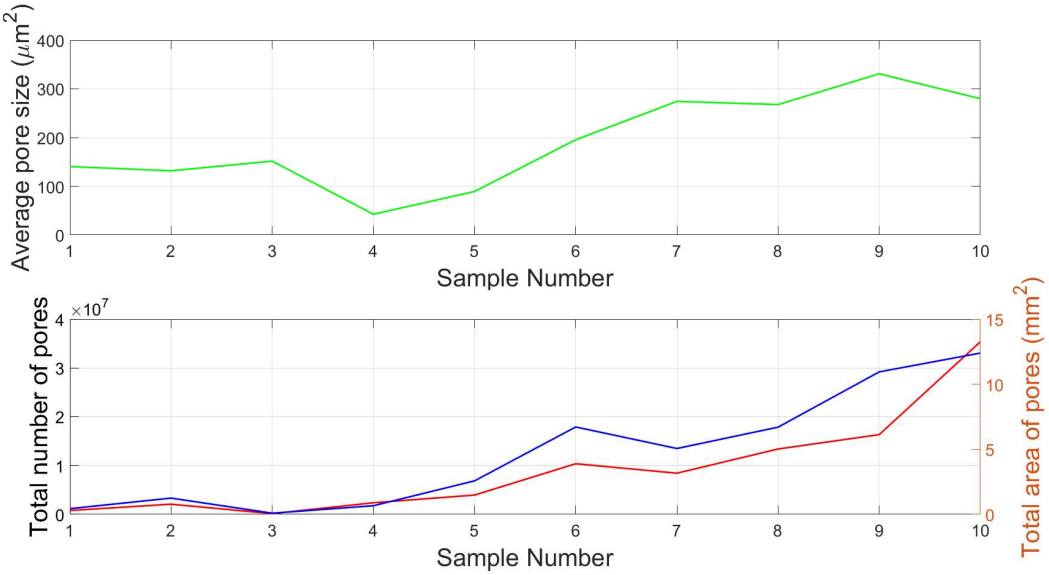

Figure 6.18: Graphs showing the average pore size, total area of porosity, and total number of pores on each sample in the Sectioned Billet. It can be seen thatall of these metrics increase from sample 1 to 10.

Almost the entire porosity in the billet it concentrated in the area which cools slowest, consistent with macro-shrinkage in large castings. Pores act as fracture initiation sites, limiting the stain range of bulk mechanical testing that can be done before failure. As porosity is not generated evenly through a billet it is essential to understand whether any is captured in tensile or compressive specimens that are machined out of billets: researchers should be clear how large their billets are, and where they extract their specimens, particularly as it is only large billets that can be used to make bulk specimens.

6.8 Discussion

A detail which is always reported in literature based on arc-melted HEAs, is the amount of billet flipping and remelting that is done (sometimes as much as eight times [188]). This step is seen as essential in order to avoid macrosegregation, which can occur if any of the raw material is not completely melted. Although the use of the crucible's electromagnetic stirrer is not standard practise this increases the turbulence in the melt pool and helps ensure complete melting and mixing. Another possible cause of macrosegregation is solute rejection ahead of a planar solidification front [189]. It was noted in chapter 5 that close to the crucible face the solidification seems to be planar in some billets; however, as HEAs are so compositionally complex constitutional supercooling will make this difficult to maintain, and the solidification front it will eventually break down into a dendritic structure [186, 190]: making them susceptible to microsegregation, but not macrosegregation.

The billet melted here is slightly different to normal HEAs, as it contains impurity elements which are much lighter than the rest. If the melt pool was stagnant then these elements would be expected to rise to the top due to convection, however in the real billet several effects work against this. Firstly, the melt pool is not stagnant, the turbulence generated by the physical force of the arc as well as its associated electric field give good mixing. Additionally, the imposed temperature gradient generated by the cooling in the crucible means there are convectional flows not based on density that are also established. The time to solidification is short ($<$3 seconds according to the FEA simulations) and so this is not enough time for the lighter elements to rise to the top of the liquid before solidification has finished. This is supported by the EDX measurements made on the slices, which show the concentrations of the

metal species to be constant from one end of the billet to the other. Of particular importance is the distribution of Zr and Hf within the billet, which as the primary reactant with C and N can act as a proxy for the distribution of the impurities.

A point which must be addressed is the change in relative peak height of the carbon signal in the EDX spectra shown in figure 6.4. There are two explanations for this effect: either the bulk concentration of carbon is higher in this slice, or surface contamination is increasing the carbon signal in the EDX measurement. The AZtec software alone is unable to accurately quantify light element concentrations, but they can be calculated using the relative peak heights and the billet's bulk concentration as provided by AMG (0.4at% C). This would mean sample 3 contains 0.72at% C, sample 4 contains 0.46at% C, while the other four samples measured would contain 0.31at%. In reality these are small variations (with a standard deviation of only 0.15at%) and could occur within the billet. However, as carbon is such a common surface contaminant, and no other light elements are seen to vary as much, it is a reasonable conclusion that the change in height of the carbon peak is a surface effect only.

As the composition of the billet is homogeneous, any other variations must be due to kinetic effects based on the differences in cooling rate. For example, in samples with lower cooling rate a larger volume fraction of carbonitride is measured, and also a lower volume fraction of HCP phase. A reasonable conclusion is that the impurities want to come out of solution as a carbonitride, but are locked in oversaturated solid-solutions in the HCP phase. In regions of the billet where cooling is slower more diffusion can occur and more of the HCP phase is converted to carbonitride, which also explains the changes in crystallite sizes that have been measured. The increase in the volume fraction of carbonitride between 5eqC and 5eqA is

marked (from 8 to 30vol% as shown in chapter 4), demonstrating that a large amount of impurities are locked in over-saturated solid-solutions in the as-cast billets. The change in phase through the billet has also led to an increase in the measured hardness of the billet, from 6.44 to 7.21GPa. That this corresponds to an increase in carbonitride and to a *decrease* in the amount of impurities in solid solution, goes against the severe lattice distortion hypothesis, which suggests maximising this in order to increase strength and hardness: for this alloy at least it is precipitation that leads to higher hardness, rather than more solid-solution strengthening.

The billet examined here is not representative of all HEAs, as the impurities have exaggerated the effect of phase separation that can occur. However, this is actually an asset: it means the variations, which will be present in all billets, are easier to measure and to demonstrate. Although a true HEA may be single phase throughout the entire billet, there will still be a change in grain size, and still be a change in porosity that can have profound effects on the measured properties of the alloy. In order to take account of this researchers should ensure that samples are taken from multiple locations within the billet, and when reporting information they should disclose which region the sample was taken from, particularly if it was adjacent to the crucible face where the most quenched microstructures are formed. Of paramount importance for researchers using arc-melted billets to prepare mechanical specimens, is understanding the distribution of porosity within them. Some machining techniques can close up near-surface porosity, making it hard to identify how much may be retained inside each specimen. If not well understood these pores can then dominate the measured mechanical properties, particularly in tension, as they can act as stress concentrators [191], rather than the properties of the alloy itself.

6.9 Conclusions

It was shown in chapter 5 that the cooling rate in arc-melted samples vary based on sample mass, and that this has knock on effects for the as-cast microstructures. It has now also been shown that the variations of cooling rate *within* a sample also alter the microstructure achieved, demonstrating that arc-melted billets are unrepresentative of any scaled up material. This is similar to the results of Molnar [110] who showed microstructure varied along melt-spun droplets, except this applies to a more commonly used technique, the samples for which are often examined in the as-cast state and are assumed to be homogeneous. In future, researchers must heat treat their samples to remove metastable phases, report the mass billets are cast in, and also disclose the location in each billet that samples are taken from for chemical analysis or mechanical testing. Without this information it is not possible to understand the effects of sample fabrication on alloy microstructure.

Chapter 7

Nanoindentation of TiVZrHfTa by CSM and Express methods

7.1 Introduction

In the previous chapters data relating to multicomponent billets containing high concentrations of impurities was analysed in order to understand the effect of arc melting on as-cast and annealed samples. In this chapter conventional nanoindentation has been uses to assess the response to ion implantation of the five component alloys, and a new nanoindentation technique has been experimented with in order to compare the mechanical properties of the various phases found in these alloys.

7.1.1 Sample Descriptions

The alloys discussed in this section are the five component alloys presented in section 4: 5eqC, 5eqA, 5optC, and 5optA. These were chosen because each has a dramatically different microstructure featuring a different combination of hard and soft phases. Each of these has been analysed in the untreated condition, and after re-

ceiving approximately 0.6dpa and 3.5dpa of ion-implantation damage, the specific conditions of which are given in chapter 3.

7.2 Implantation Results

7.2.1 Conventional Indentation

Continuous Stiffness Measurement (CSM) indents have been used to analyse the matrix phase of all the alloys as well as pure vanadium, which has been used as a control material and is shown in figure 7.1. The hardening in the vanadium at 250nm is 1GPa in the low dpa condition and 1.5GPa in the high dpa condition.

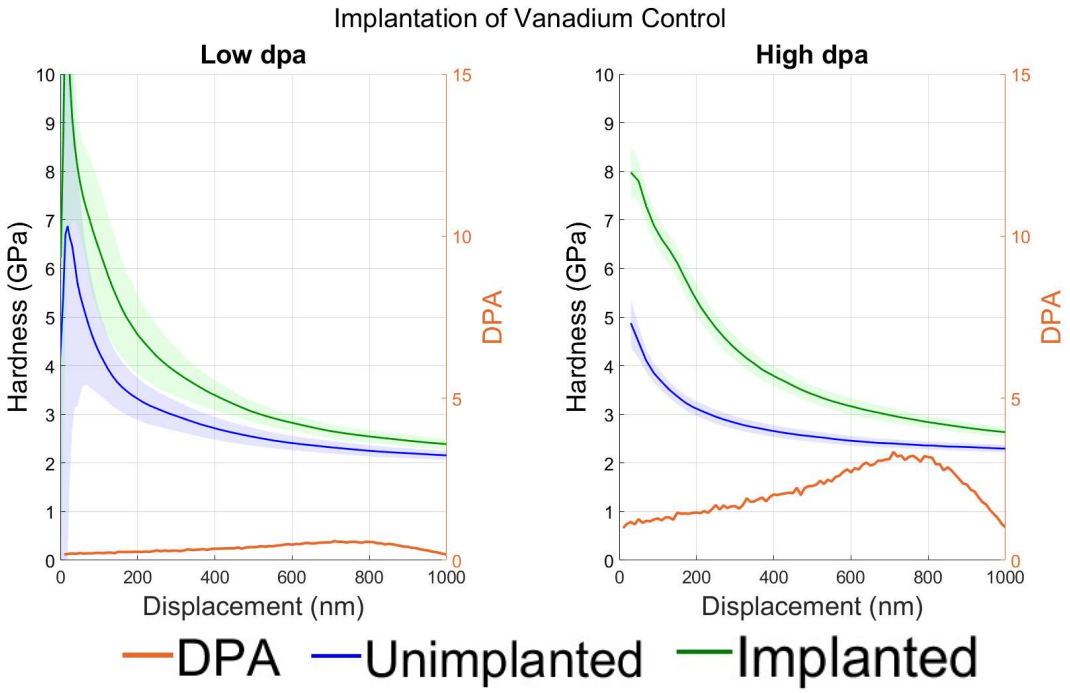

Figure 7.1: Nanoindentation results on a Vanadium control material that was implanted alongside the HEAs. Data shows hardness in implanted and unimplanted regions, along with the dpa profile calculated using SRIM. Data shown is the average of at least 32 separate indents; the errors are the standard deviations of this data.

The hardnesses of the HEA materials before and after the implantations is shown in figures 7.2 and 7.3; these show there has been no hardening in the matrix phase due to the implantation, consistent with other results of implanted HEAs, as discussed in chapter 2.

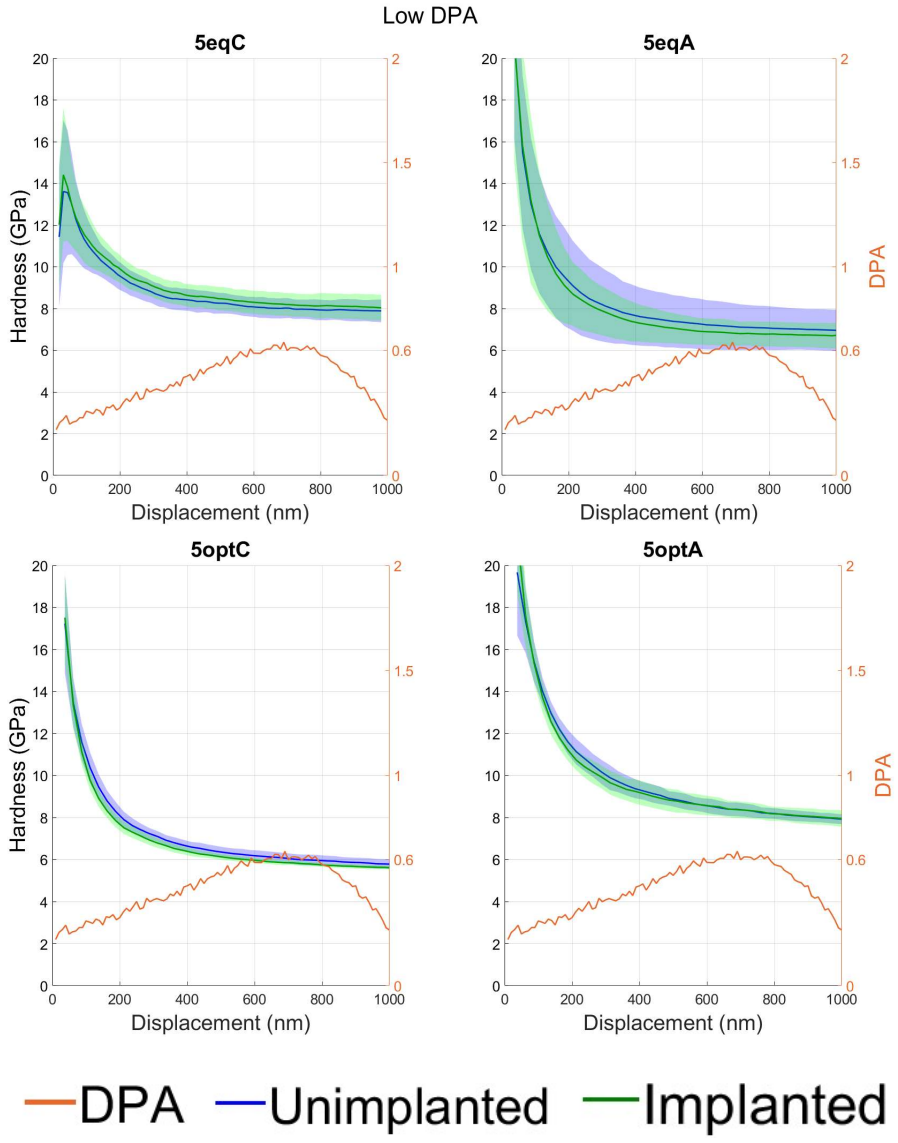

Figure 7.2: Nanoindentation results of the low dpa implantation, along with the dpa profile calculated using SRIM. Data shown is the average of at least 32 separate indents placed into the matrix of the respective materials; the errors are the standard deviations of this data. The main result is that there has been no change in hardness due to implantation.

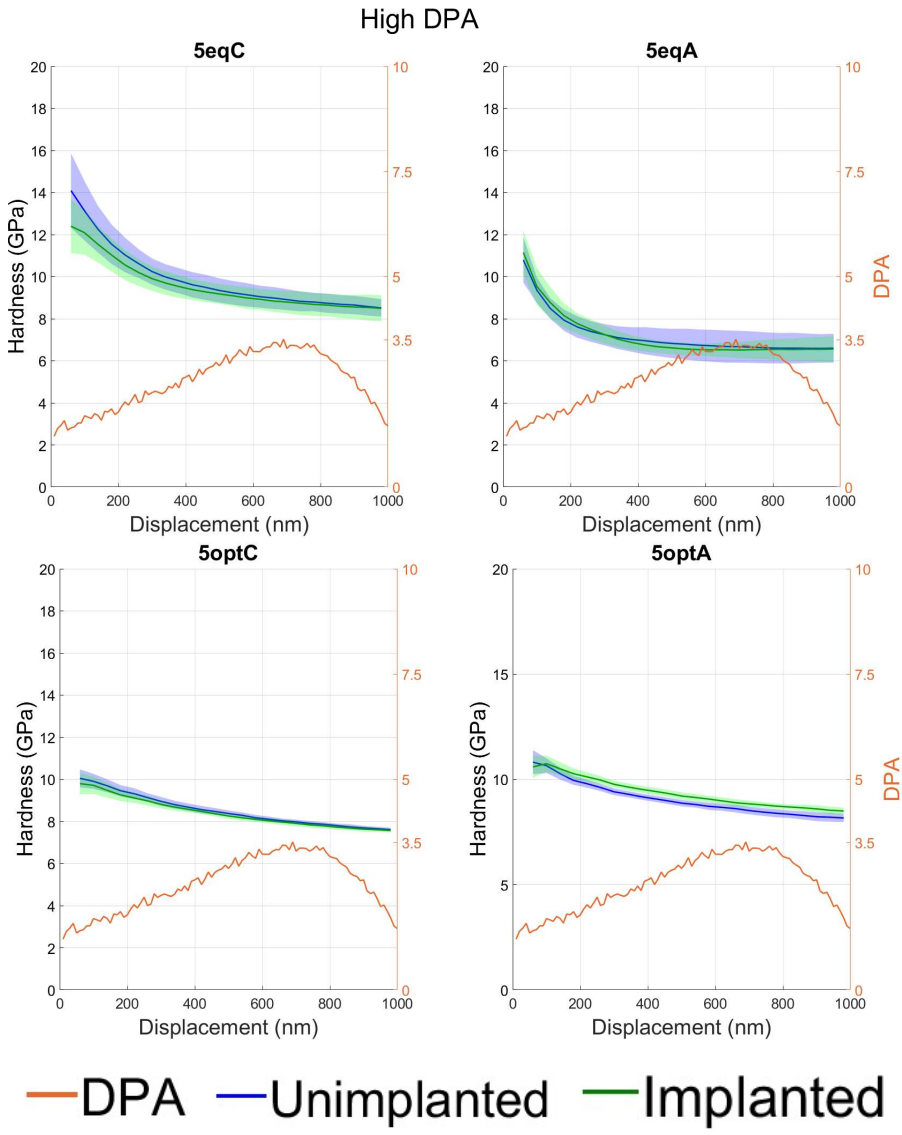

Figure 7.3: Nanoindentation results of the high dpa implantation, along with the dpa profile calculated using SRIM. Data shown is the average of at least 32 separate indents placed into the matrix of the respective materials; the errors are the standard deviations of this data. The main result is that there has been no change in hardness due to implantation.

The hardening observed in the vanadium control demonstrates that the resistance of TiVZrHfTa to implantation damage is real: the melting point of vanadium is 1910 °C, meaning its homologous temperature is 0.26 T_m; the HEA's approximate melting point is 2127 °C, meaning a homologous temperature of 0.24 T_m: if there

has been no healing in the vanadium sample then there has certainly been no healing in the HEA. Any resistance to hardening must be due to either the material's ability to resist the introduction of crystal defects, or its insensitivity to their presence on its mechanical properties.

Although it has been shown up until now that ion implantation has not caused changes in hardness across individual samples, results from all the samples can be seen to vary when plotted together, i.e. the implanted and unimplanted regions of each sample have the same hardness, but the unimplanted regions under different dpa conditions do not match each other, or even the untreated samples.

Figures 7.4 to 7.7 compare the hardness and modulus of the implanted and unimplanted regions, as well as the untreated samples. They show that the hardnesses and moduli of the as-cast material all increase after the implantation process, despite the material having been blanked and therefore not experiencing any ion damage. The annealed material shows a much smaller spread and the mechanical response does not seem to be changing. In all of the samples that were implanted to 3.5dpa, there is a very high hardness at depths lower than 200nm, this is due to slightly different procedures in calibrating indenter tips between each experiment.

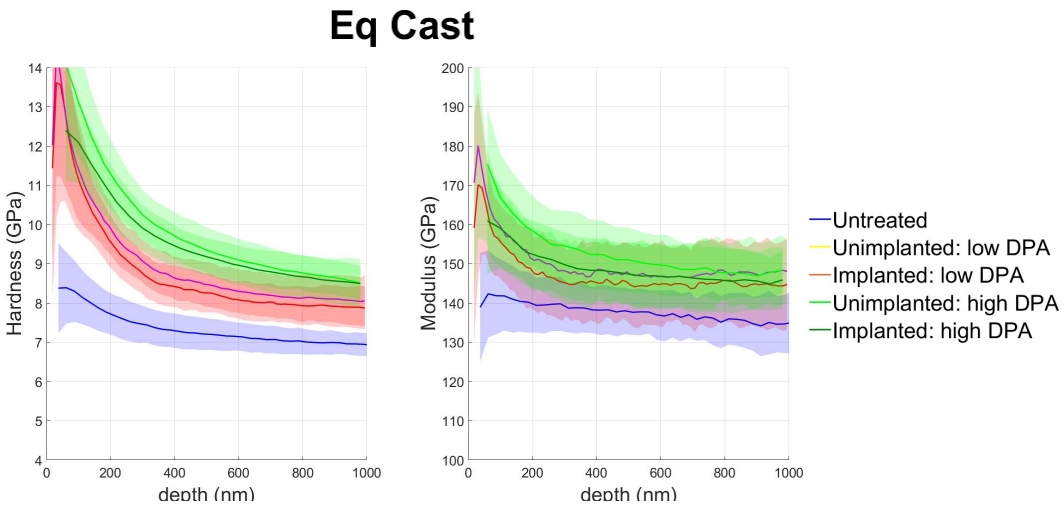

Figure 7.4: Nanoindentation results comparing the hardness and elastic modulus of the as-cast equiatomic TiVZrHfTa in the untreated condition, as well as in the implanted and unimplanted regions of both implanted samples.

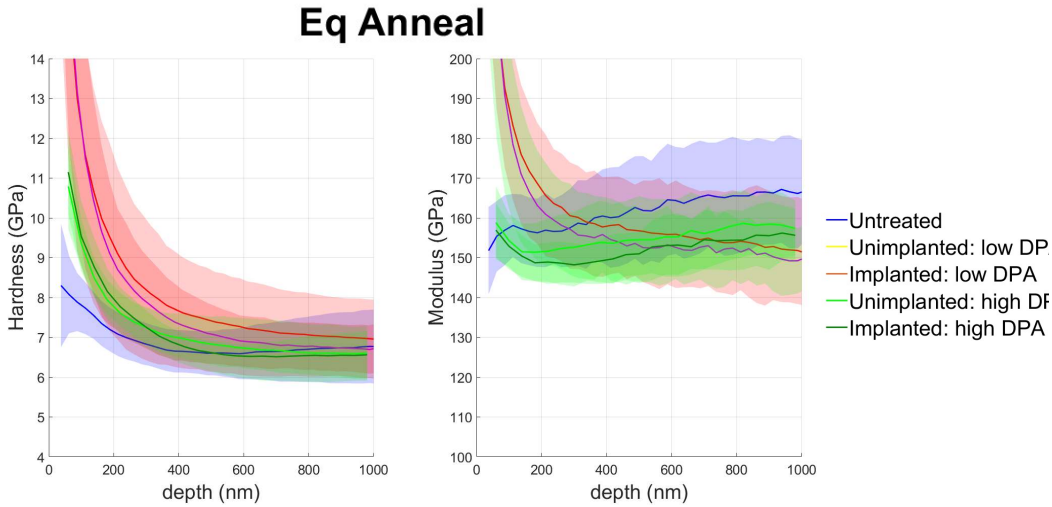

Figure 7.5: Nanoindentation results comparing the hardness and elastic modulus of the annealed equiatomic TiVZrHfTa in the untreated condition, as well as in the implanted and unimplanted regions of both implanted samples.

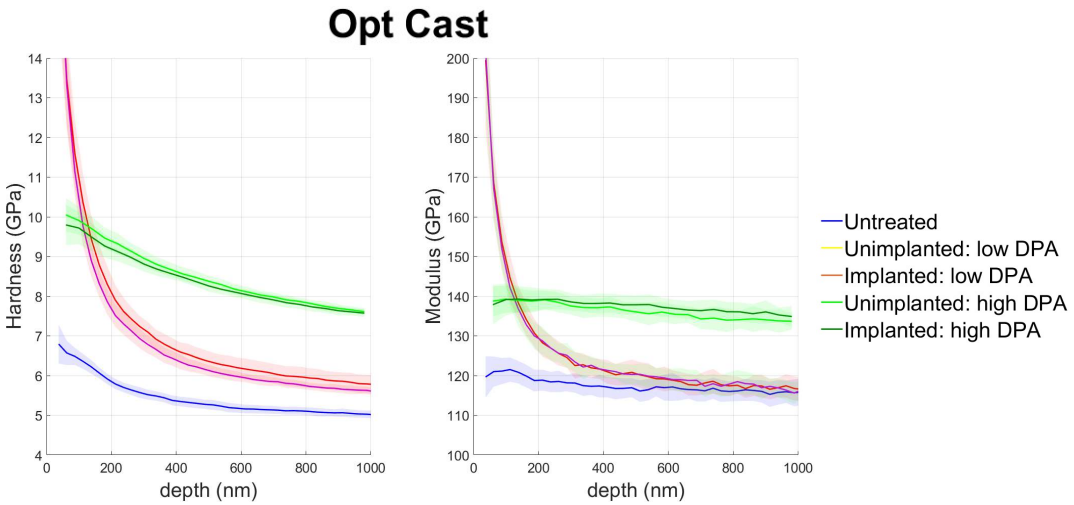

Figure 7.6: Nanoindentation results comparing the hardness and elastic modulus of the as-cast optimised TiVZrHfTa in the untreated condition, as well as in the implanted and unimplanted regions of both implanted samples.

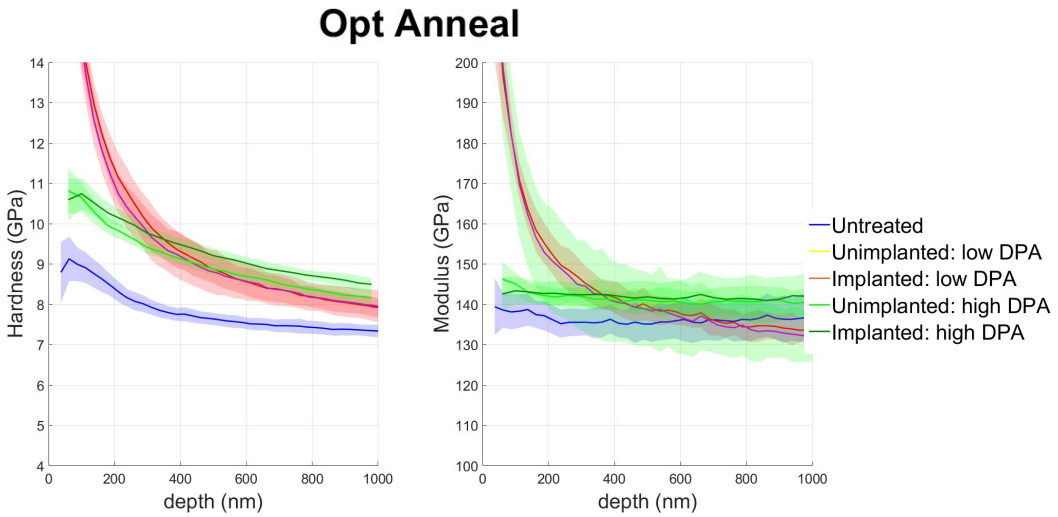

Figure 7.7: Nanoindentation results comparing the hardness and elastic modulus of the annealed optimised TiVZrHfTa in the untreated condition, as well as in the implanted and unimplanted regions of both implanted samples.

The samples which have hardened the most are the as-cast samples, in particular the optimised as-cast material discussed in section 4.3, and an image is reproduced in figure 7.8. The reason for these changes is that precipitation is occurring during

the 500 °C heat treatment that is happening during the implantation: fine-scale precipitates were observed in the 5optC samples, although could not be found in the 5eqC ones, as their starting microstructure is already prohibitively complicated, see image B in figure 7.8.

The supporting evidence for this conclusion is that there is no easily observable increase in hardness or moduli in the material that was annealed before implantation, as the precipitation which was suppressed by the rapid cooling of the samples has already occurred; figure 7.5 shows a large spread in hardness and modulus measurements due to the multiple phases in the material, but these values do overlap.

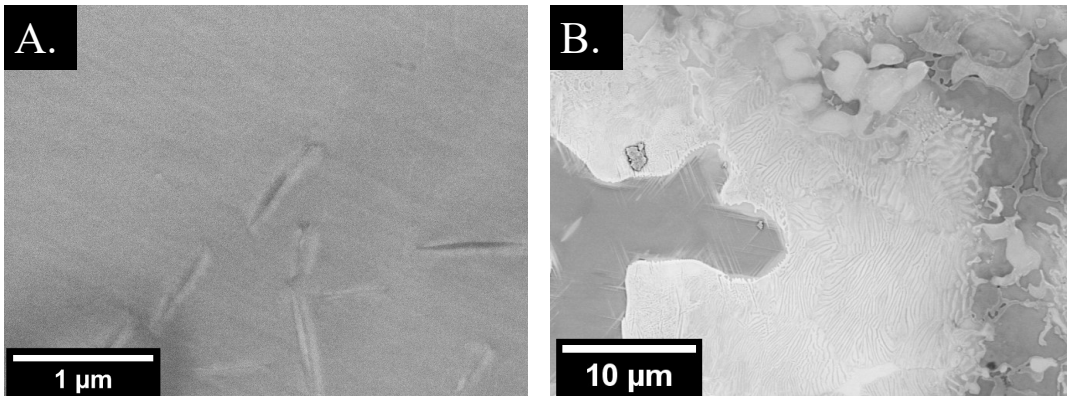

Figure 7.8: Back-scatter SEM images reproduced from chapter 4. Image A is from the unimplanted region of 5optC after being implanted to 0.7dpa, sub micron precipitates can be seen. Image B is taken from an untreated sample of 5eqC; the microstructure is much more complicated and it can be seen that "new" phases would be difficult to find or recognise.

Up until now the only mechanical data that has been presented is from the matrix of the alloys, the reason for this is that many of the the precipitates in these samples are either too small, too brittle, or too sparse, to be analysed with CSM indentation; figure 7.9 shows CSM indents in 5eqC and 5optA. It can be seen that the indents are too large for the precipitates, and that fracture has also occurred, preventing properties being extracted for depths greater than $\sim$300nm, meaning that useful data could

not be extracted with CSM indentation. Even when indents are placed shallowly in a precipitate, the spread in results can be between 15 and 50GPa, and the difficultly in getting a dataset large enough to be statistically significant made CSM indentation unsuitable for this purpose.

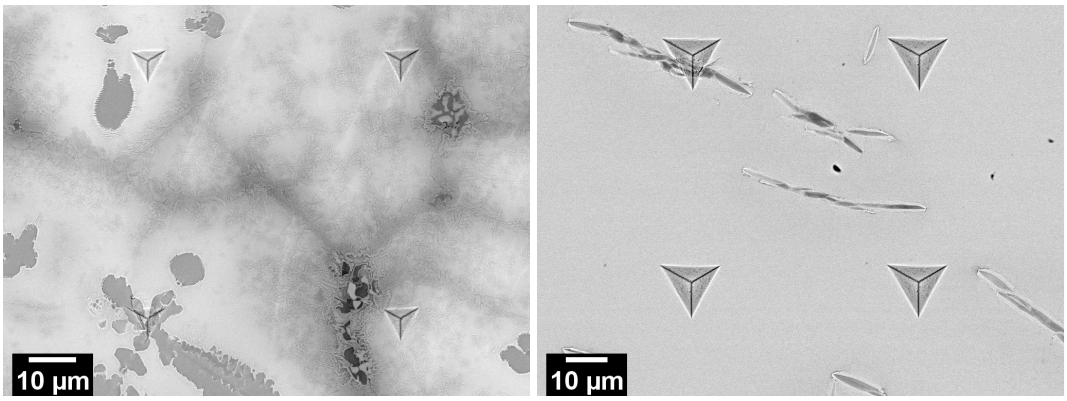

Figure 7.9: Back-scatter SEM images of indents in 5eqC (left) and 5optA (right). It can be seen that non-matrix phases are often too brittle to indent or too small to analyse with CSM indentation.

7.2.2 Implantation Conclusions

Ion implantation has not altered the mechanical response of the matrix phase in the alloys tested, although the 500 °C heat treatments have allowed precipitation to occur in the as-cast alloys. However, the main conclusion is that these alloys have resisted mechanical degradation due to ion implantation, particularly when compared to the vanadium control which has shown substantial hardening.

The microstructures of these alloy system are extremely complex due to the effects of the contamination on the composition and phases present in the alloys, and so understanding the additional complexity of ion implantation on their microstructure and properties is beyond the scope of this thesis. However, these samples do pose an interesting challenge: measuring the mechanical response of phases with a

variety of morphologies and a wide variation in mechanical response. For this reason these alloys have been used to understand and explore a new indentation technique called Express Indentation.

7.3 Express Indentation

Express indentation is a relatively new technique whereby shallow indents (<500nm deep) are rapidly placed across a material in a grid fashion [192]. Using the nanopositioning stage on the G200 machine, indent spacings can be decreased to submicron levels, allowing for dense maps of mechanical properties to be built. The dimensions of Express arrays are defined in two ways: first the user defines the "bundle" dimensions (e.g. width, height, load, number of indents), the user then defines the number and locations of the bundles, which follows the same procedure as when defining a batch of CSM indents; a schematic of an Express array is shown in figure 7.10. Throughout this section the nomenclature of bundles and batches is important, and so it is explained here; the best way of visualising this distinction is that the bundle defines the patches, whilst the batch defines how the patches become a patchwork quilt.

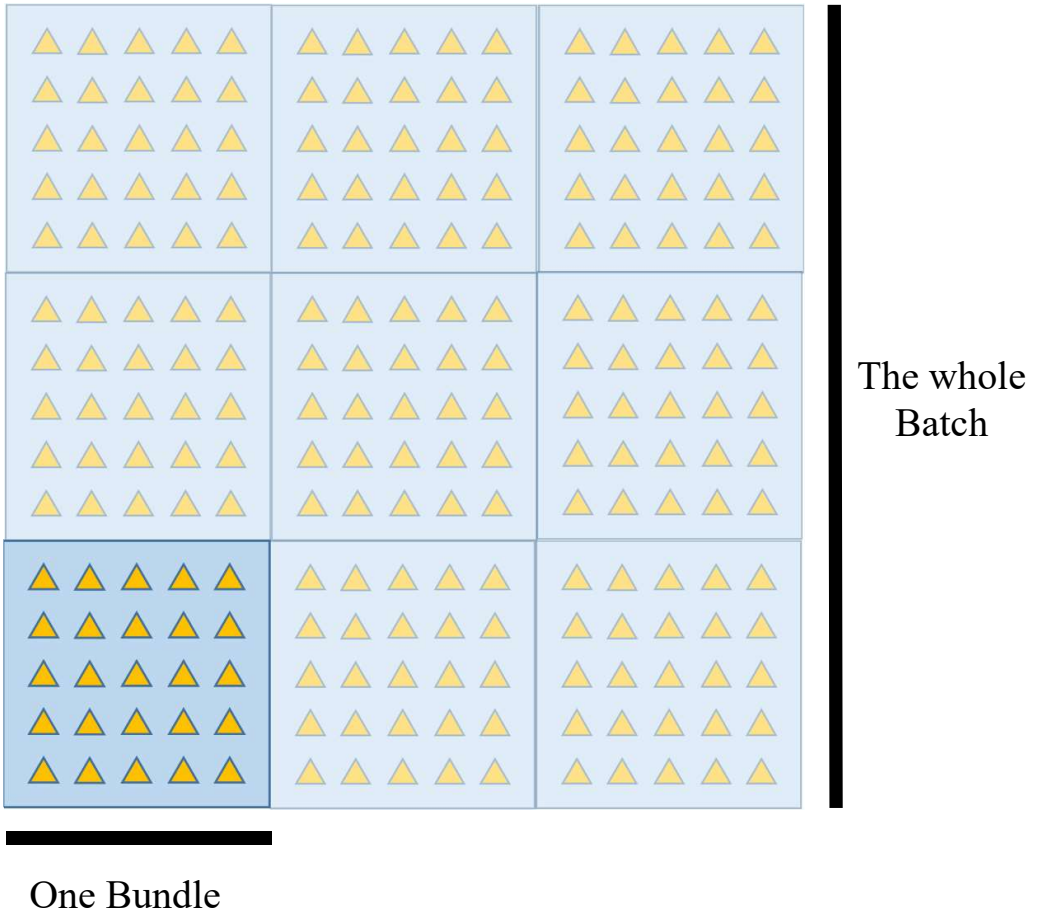

Figure 7.10: Schematic showing the layout of an Express array, demonstrating the difference between a bundle and a batch, which are both components of an Express array.

7.3.1 Implementation

The main difference between the results of CSM and Express indentation is that in the latter, results are not calculated as a function of depth, rather a single value of hardness and modulus is calculated for each indent based on single values of load and indentation depth. Removing this requirement allows the rate of indentation to be increased: a 2000nm deep CSM indent takes around 10-20 minutes, a single Express indent takes around 3 seconds. This means that express data collected in a single sitting can comprise tens of thousands of data points, while retaining a high

spatial resolution allowing for a high number of data points in lower volume fraction phases than is possible with conventional indentation techniques.

7.3.2 Technique troubleshooting

The following section is aimed at readers interested in this technique, and what follows is a description of some early problems and how they were overcome on the G200 system: although other indenter machines use different software similar problems may be encountered.

7.3.2.1 Indent Digging

When the control software encounters a problem during an Express test, it records an error and stops logging data. However, instead of terminating the tests and cancelling the remaining indents the array continues to run, but going to much greater depths than was originally planned; an SEM image of this effect is shown on the left in figure 7.11. Based on the width of these indents the machine is going to depths of at least 2 µm, far in excess of the Express methods limit of 500nm. Once the digging begins it continues until the end of the batch. The most worrying part of the digging phenomena, is that the tip does not retract properly between indents, and so it scratches through the material, as seen on the right in figure 7.11). Indent digging is a major concern as it causes damage to tips that mean they must be thrown out, because afterwards they cannot be recalibrated to account for their change in shape.

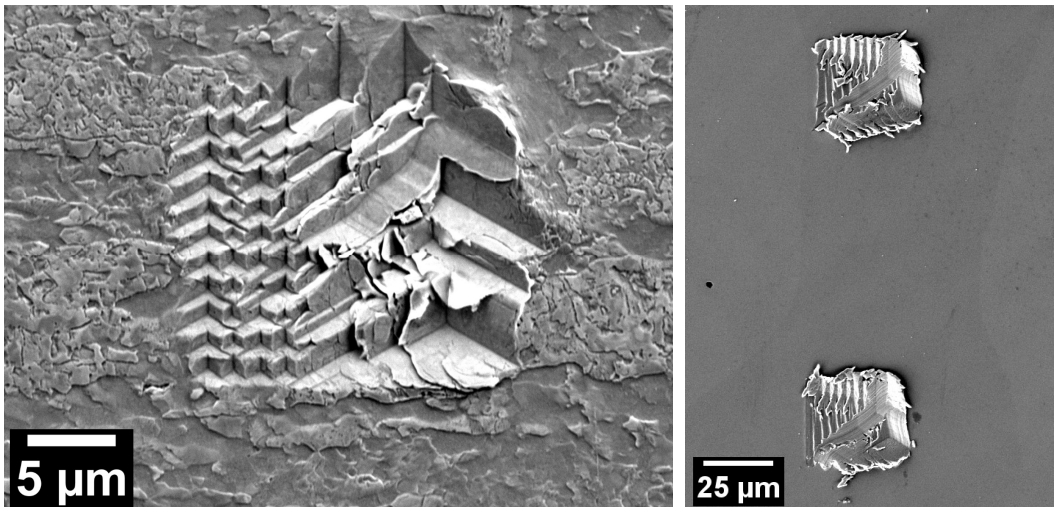

Figure 7.11: Back-scatter and secondary electron image of an Express arrays which have failed and resulted in a digging effect. The left hand image is a bundle which has glitched partway through, while the image on the right shows the "dragging" effect caused when the tip is not fully retracted.

7.3.2.2 Displacement-control versus Load-control

Operating the Express method using displacement control has advantages: primarily that it allows for more direct control of the plastic zone size of each indent, which is related to indentation depth. However, displacement control is implemented by running the first few indents in load control so as to determine the correct load for the target depth, then simply operating the remainder of the batch in load control. This works reasonably well in a homogeneous material but when testing a multiphase material with varying mechanical properties it can fail. When the indenter encounters a change in phase whilst operating in displacement control the load and target displacement values stop matching, and the indenter responds by digging, causing the batch to fail and potentially the indenter tip to be ruined. This issue was only discovered through trial and error and took several weeks to overcome reliably.

7.3.2.3 Surface-finds and sample tilt

In the initial stages of a CSM indent the tip approaches the surface at a slow speed until it meets resistance, at this point the test begins and data is logged: this is known as the surface-approach segment. This process is too time consuming to run on every indent in an Express array, and so only one surface-approach segment is run for each batch, and then the same value is used for each indent. If a batch is large (and they can span tens of millimetres), then the surface height of the sample can change due to bevelling or poor mounting: a 1° tilt will change the surface height by 17 µm over 1mm in the XY plane. If the surface height deviates too much from the one determined at the start of the batch then the software can glitch and begin digging.

7.3.2.4 Main stage versus nanopositioning stage

The nanopositioning stage uses piezoelectric crystals in order to achieve very high spatial accuracy, the limitation of this being the range of movement is only 100 µm in X and Y. The main stage uses a mechanical movement in order to cover a much wider area but with a lower accuracy. When running an Express array, intra-bundle movement is via the nanopositioning stage, inter-bundle movement is via the main stage. This means that sometimes there are visible offsets between bundles, as shown in figure 7.12, where although the array was set up to be square there are errors in position which can be as high as several microns.

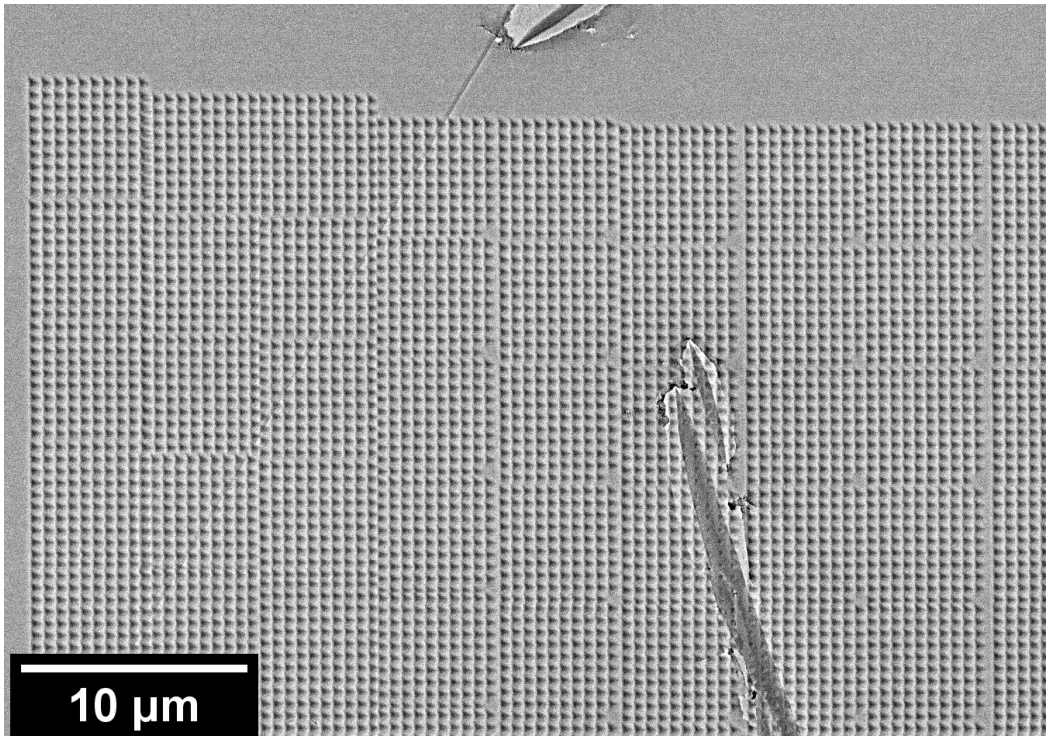

Figure 7.12: Back-scatter SEM image of an Express array in 5optA. The batch was set up to be square, but deviations in the movement between bundles has resulted in offsets between them.

The movement of the nanopositioning stage is also imperfect, particularly at the edge of its 100 µm range, which can mean that an entire row or column of indents may be out of position by around a micron.

The best operating procedure found to date is to maximise the number of indents in each bundle, but not allowing it to become bigger than 90 microns in any direction. If an Express array larger than this is required then use as few individual bundles as possible so as to minimise the use of the main stage.

7.3.2.5 Modulus measurements

When an Express indent is made the indenter goes directly to the specified load and records the displacement achieved into the material. This results in single values

of load and displacement for each indent. Indentation hardness can be calculated from this data using equation 3.2, however the method of calculating modulus is not clear, as calculating modulus with conventional CSM indentation requires additional stages, such as an unloading measurement or an oscillation in the tip displacement. The values of hardness and modulus do not correlate perfectly (i.e. two indents in the same material can have the same load-displacement, the same hardness, yet have different moduli). Despite examining the Express array subroutine and having discussions with the manufacturers of the G200 machine, no answers to this have been provided. It is still not known how modulus is being calculated in Express indentation, which is a concern, as until this is understood the reliability and validity of the method cannot be assessed. Instead benchmarking on well-characterised materials must be undertaken.

7.4 Benchmarking the Express Method

In order to assess the accuracy of the hardness and modulus measurements of Express arrays, it was benchmarked against two well understood materials: fused silica and tungsten.

7.4.1 Calibration in the Express method

Nanoindentation requires tip calibration in order to generate quantitative results. This is achieved by indenting fused silica, which has a well defined modulus of 72GPa, and adjusting the tip area function until the data reflects this. These values are strongly affected by the position of the surface marker. The default position for the surface marker is where the indenter first encounters a non-zero load during its surface-approach segment; however this means that the first 10-20nm of the test are

simply the tip coming into full contact with the surface, and is more related to debris on the tip and surface roughness of the sample than the actual mechanical response of the material. For this reason it is common practise to redefine the point in the data where the surface is marked, so as to better capture the data which is actually representative of the material; the point which is usually chosen is where the harmonic contact stiffness becomes linear. The modulus and harmonic contact stiffness of the same data set, but with different surface markers is shown in figure 7.13. It can be seen that if the surface marker is moved inward by 30nm before the data is calibrated then the modulus is flat and consistently 72GPa. If the surface marker is left in its default position during calibration, then the modulus value peaks at a depth of 100nm and then slowly decreases with depth until it is below the theoretical value.

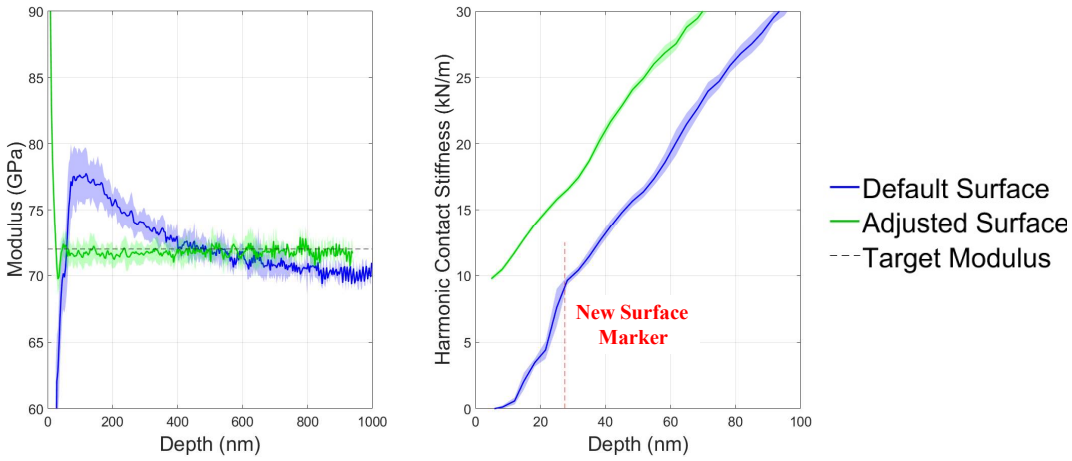

Figure 7.13: Comparison of Modulus and Harmonic Contact Stiffness with different surface marker positions

The reason this happens is the software is trying to fit a polynomial that describes the tip shape such that the modulus is always 72GPa; it cannot reliably do this for the data where the tip is not in proper contact with the surface *and* for data at greater depths. For CSM indentation this effect does not cause any problems, as the user can be consistent with where they place the surface marker. For express indentation this

is not possible, as the surface marker cannot be moved in post and the user simply has to accept the default position. The effect of this on Express data is striking, figure 7.14 shows CSM and Express data taken on fused silica, but calculated using two calibration files shown in figure 7.13.

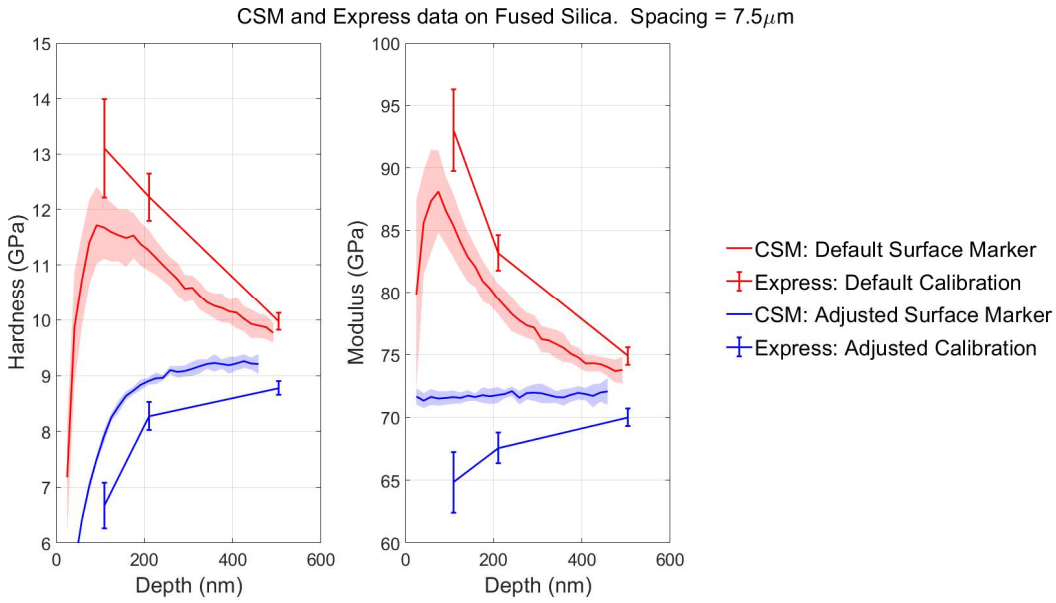

Figure 7.14: Comparison of CSM and Express data on fused silica, calculated with two different calibration files: one with the default surface marker and one with an adjusted surface marker.

The CSM data using the default surface marker is poor: the modulus and hardness both peak unphysically at 100nm and then decrease at greater depths, while the CSM data for the adjusted surface marker is more accurate. However, despite the adjusted surface marker giving good CSM data it gives poor Express data, consistently underestimating modulus and hardness. The Express data calculated with the default surface calibration on the other hand is poor, but poor in the same way as matching CSM data.

Similar data but for tungsten is shown in figure 7.15. As with the fused silica case, the default surface marker may give incorrect data, but it does at least give

CSM and Express data that is similarly incorrect, rather than divergent.

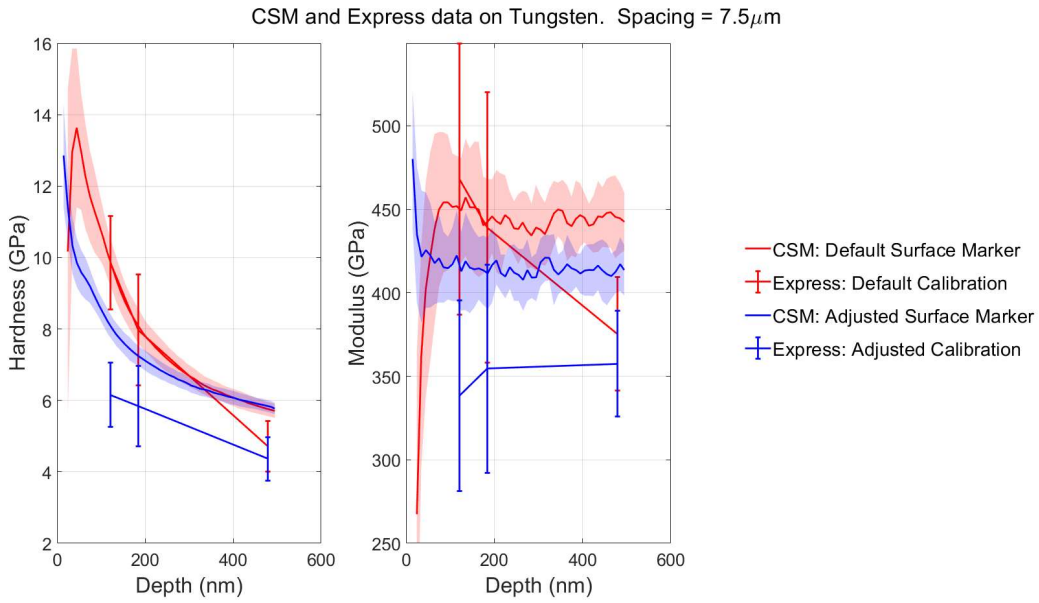

Figure 7.15: Comparison of CSM and Express data on tungsten, calculated with two different calibration files: one with the default surface marker and one with an adjusted surface marker.

Based on this it was decided that the surface marker should always be left in the default position when calibrating a tip before running an express array, but that it should not be calibrated for shallow data ($\sim$<50nm).

7.4.2 Results on fused Silica

Both CSM and Express arrays have been made in fused silica at depths of 100, 200, and 500nm; spaced out by 15x, 10x, 8x, and 5x their maximum depths. This has been done in order to study how sensitive Express data is to size-effects and overlapping plastic zones. Figures 7.16 shows CSM and Express data with indents spacings that are 15x the maximum depth. These indents are far enough apart to guarantee there is no overlap in plastic zones [193]. The CSM data is close to the theoretical values, while the Express arrays slightly overestimate the hardness and

modulus values.

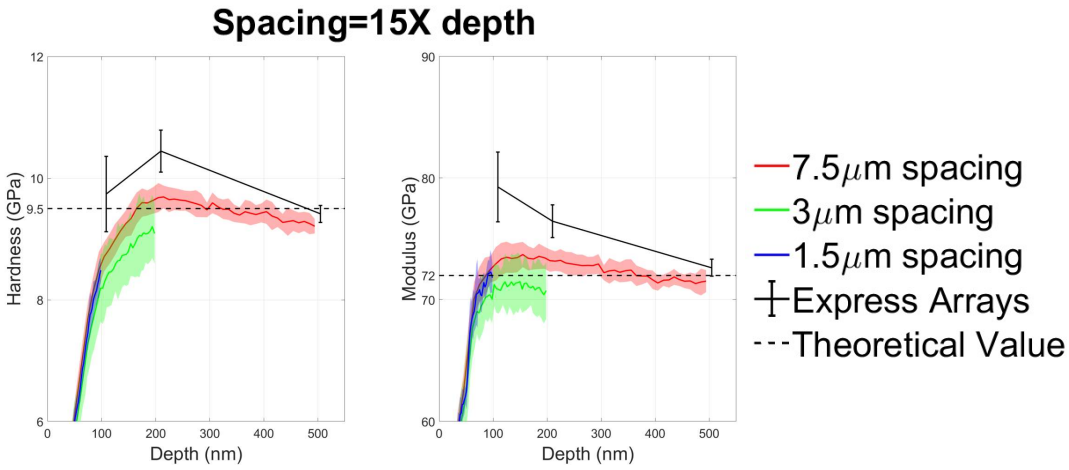

Figure 7.16: Nanoindentation results on fused silica showing hardness and modulus from CSM and Express arrays with the spacings shown in the legend: these are all 15x the maximum indent depth. The CSM data is averaged from nine indents, while the Express arrays contain 100 indents. The errors are the standard deviation of this data.

These trends continue as the indent spacing decreases: figures 7.17 to 7.19 show the similar data but for indent spacings that are 10x, 8x, and 5x the maximum depths. At 8x and 5x spacing it can be seen that the CSM data is showing slight increases in modulus and hardness, reflecting that the plastic zones of each indent are overlapping, meaning the later indents are probing material which has partially exhausted its plastic capability. In contrast, the Express data is consistent as indent spacing decreases: it is not sensitive to the overlapping plastic zones. The reason for this is that plastic processes such as dislocation flow are rate sensitive [194, 195], and the strain rates achieved in Express indents are ∼35x higher than in CSM indents, leading to the plastic zone being more confined, and less likely to overlap with neighbouring indents: displacement rates in Express tests are 170 nm s^{-1} as a conservative estimation, compared to 4.5 nm s^{-1} in CSM indentation. As there is less plasticity possible during the Express indents, the values of hardness and modulus are higher *and* less sensitive to indent spacing. Modulus should not be rate sensitive, but as the method

of calculating modulus is unknown, there is no way to determine which externality is affecting the measurement.

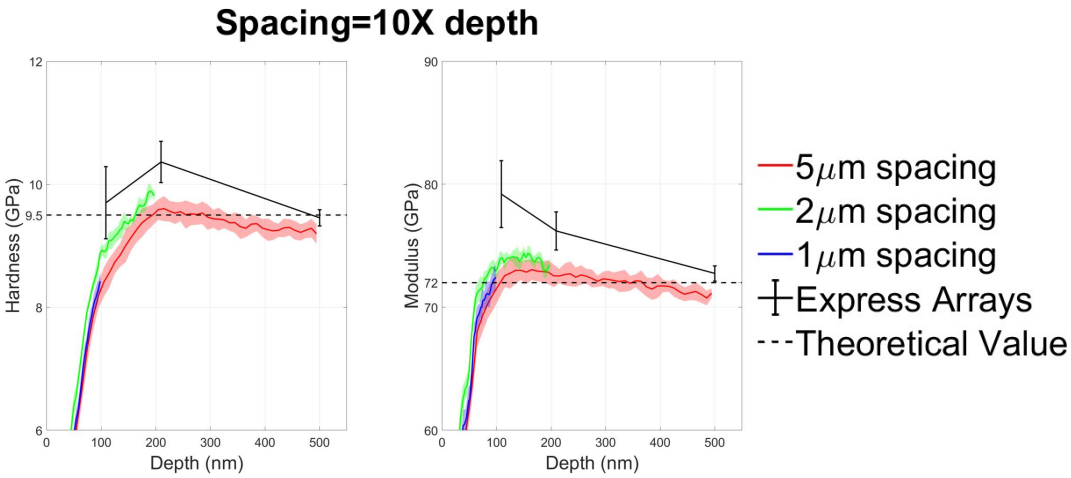

Figure 7.17: Nanoindentation results on fused silica showing hardness and modulus from CSM and Express arrays with the spacings shown in the legend: these are all 10x the maximum indent depth. The CSM data is averaged from nine indents, while the Express arrays contain 100 indents. The errors are the standard deviation of this data.

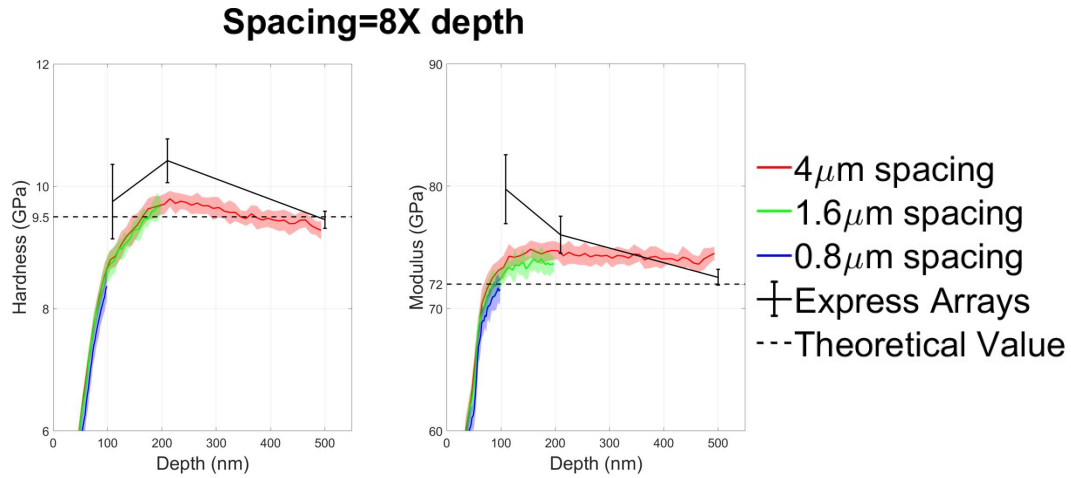

Figure 7.18: Nanoindentation results on fused silica showing hardness and modulus from CSM and Express arrays with the spacings shown in the legend: these are all 8x the maximum indent depth. The CSM data is averaged from nine indents, while the Express arrays contain 100 indents. The errors are the standard deviation of this data.

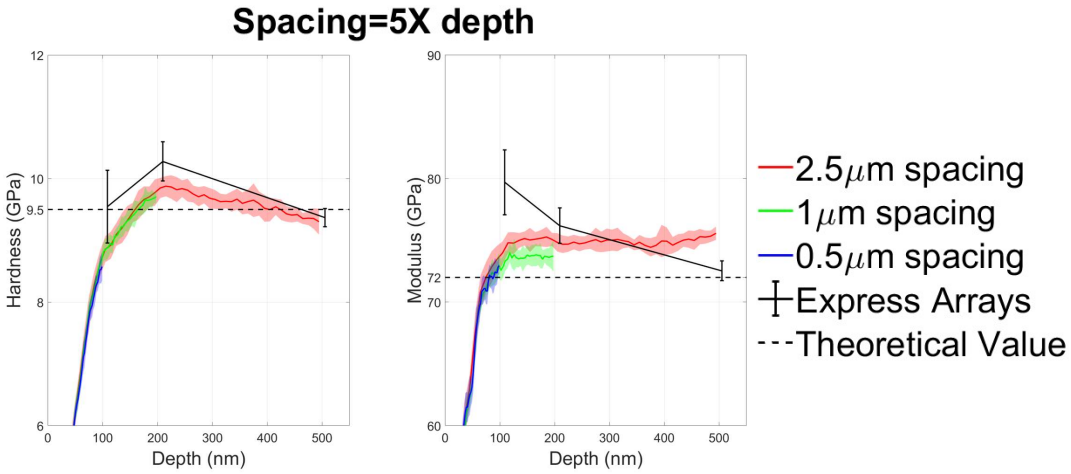

Figure 7.19: Nanoindentation results on fused silica showing hardness and modulus from CSM and Express arrays with the spacings shown in the legend: these are all 5x the maximum indent depth. The CSM data is averaged from nine indents, while the Express arrays contain 100 indents. The errors are the standard deviation of this data.

7.4.3 Results on Tungsten

The exact same tests have been run for tungsten, and the results are shown in figures 7.20 to 7.23. The CSM data is close to theoretical values, with measured hardness and modulus increasing as indent spacing decreases. The Express data is very similar to the CSM data, although at 500nm it underestimates hardness and modulus. In tungsten the express data does show a slight increase in measured hardness and modulus as indent spacing is reduced, although these increases are still lower than that seen in the CSM data. The reason there is this response in tungsten but not in fused silica is that tungsten has a lower yield stress ($\sim$ 2GPa versus nearly 6GPa in fused silica [196, 197]) and therefore tungsten will have larger plastic zones as a wider volume is required to accommodate the stress generated by the indent.

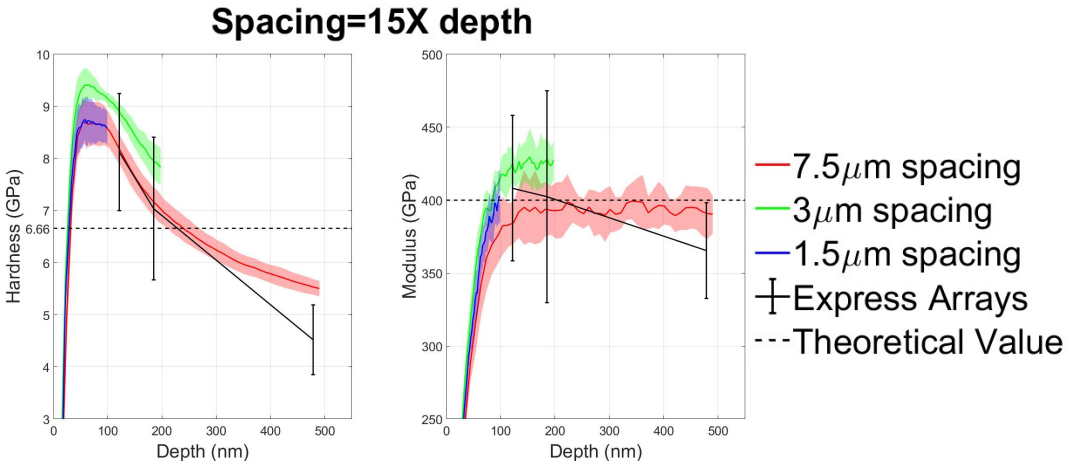

Figure 7.20: Nanoindentation results on tungsten showing hardness and modulus from CSM and Express arrays with the spacings shown in the legend: these are all 15x the maximum indent depth. The CSM data is averaged from nine indents, while the Express arrays contain 100 indents. The errors are the standard deviation of this data.

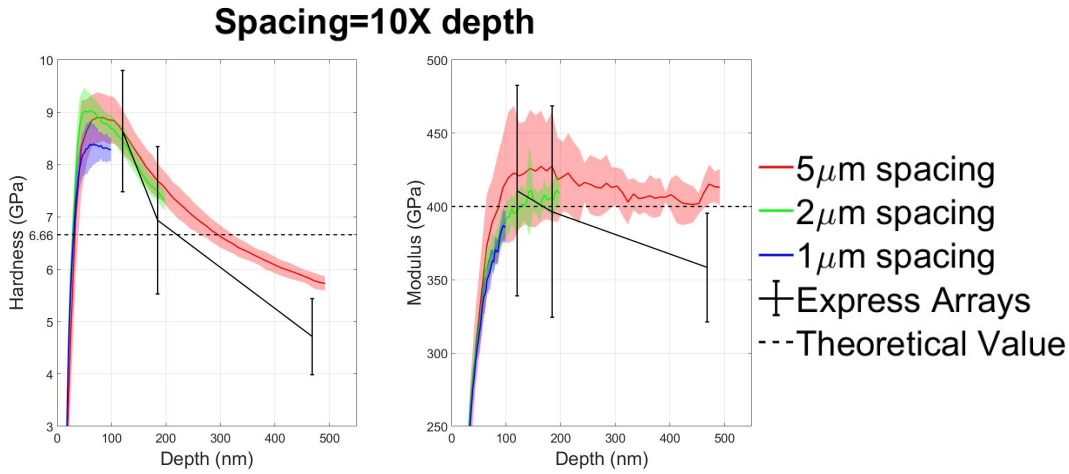

Figure 7.21: Nanoindentation results on tungsten showing hardness and modulus from CSM and Express arrays with the spacings shown in the legend: these are all 10x the maximum indent depth. The CSM data is averaged from nine indents, while the Express arrays contain 100 indents. The errors are the standard deviation of this data.

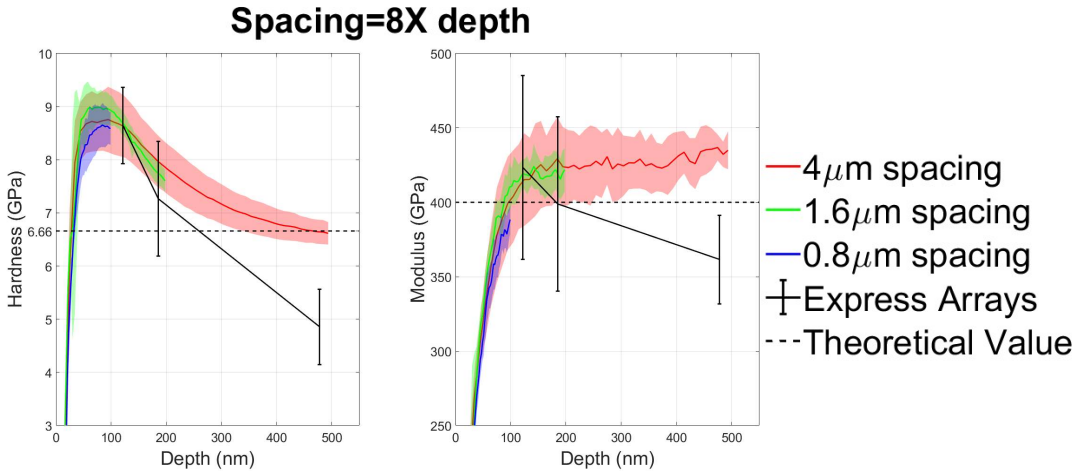

Figure 7.22: Nanoindentation results on tungsten showing hardness and modulus from CSM and Express arrays with the spacings shown in the legend: these are all 8x the maximum indent depth. The CSM data is averaged from nine indents, while the Express arrays contain 100 indents. The errors are the standard deviation of this data.

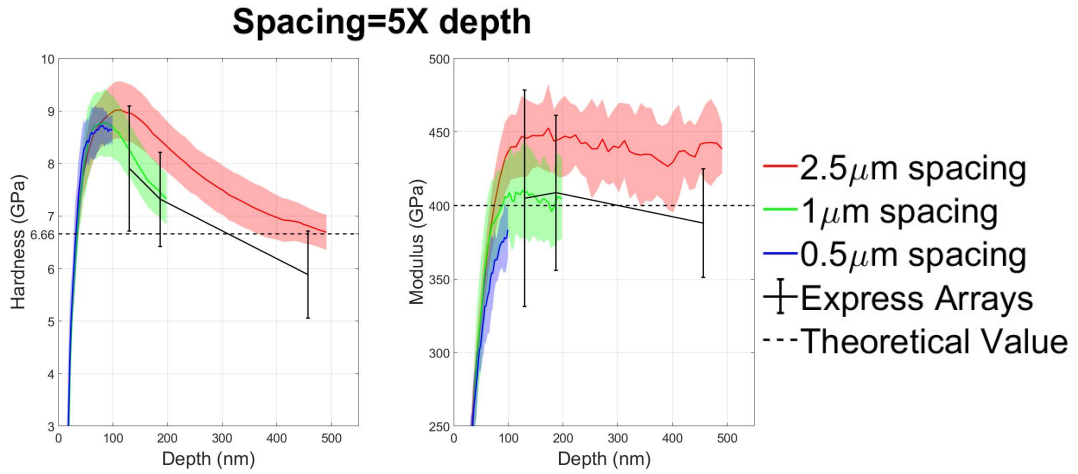

Figure 7.23: Nanoindentation results on tungsten showing hardness and modulus from CSM and Express arrays with the spacings shown in the legend: these are all 5x the maximum indent depth. The CSM data is averaged from nine indents, while the Express arrays contain 100 indents. The errors are the standard deviation of this data.

7.5 Separating phases in Express data

Benchmarking against fused silica and tungsten has shown that the Express arrays can be used to get accurate values of hardness and modulus, although this is very sensitive to where the surface marker is placed during tip calibration. The next step was to use Express arrays to measure the properties of multiphase materials. All scans were completed in load control, and the indent spacings used are specified. The primary goal is to be able to intelligently sort indents by phase. As only mechanical information is available the main method used is to compare the distributions of hardness, modulus, and indentation depth. The materials tested are the alloys of TiVZrHfTa discussed previously.

7.5.1 Results on a quasi single-phase alloy

As shown in chapter 4, 5optC is the closest alloy to being single phase, with only a limited amount of precipitation. Express arrays of different sizes have been used to measure modulus and hardness, and these results are higher than with CSM indentation. Figure 7.24 shows the results of these express arrays in two different forms. The first is a scatter plot of hardness against modulus, which is usually a good method of separating out materials with different mechanical responses. The lines on this graph are a contour plot showing the density of data points, in order to better demonstrate most common values of the data: for example in 5optC it can be seen the highest density of data points and therefore most likely the mean is at a hardness of $\sim$ 7.75GPa and a modulus of $\sim$125GPa. This clustering of data is also demonstrated in the individual histograms of hardness, modulus, and depth data shown below. The results from the 5optC sample show the material to be single phase as the data shows only one discernible population of data. The mean (with

standard deviation) and median values of hardness, modulus, and depth are shown in table 7.1.

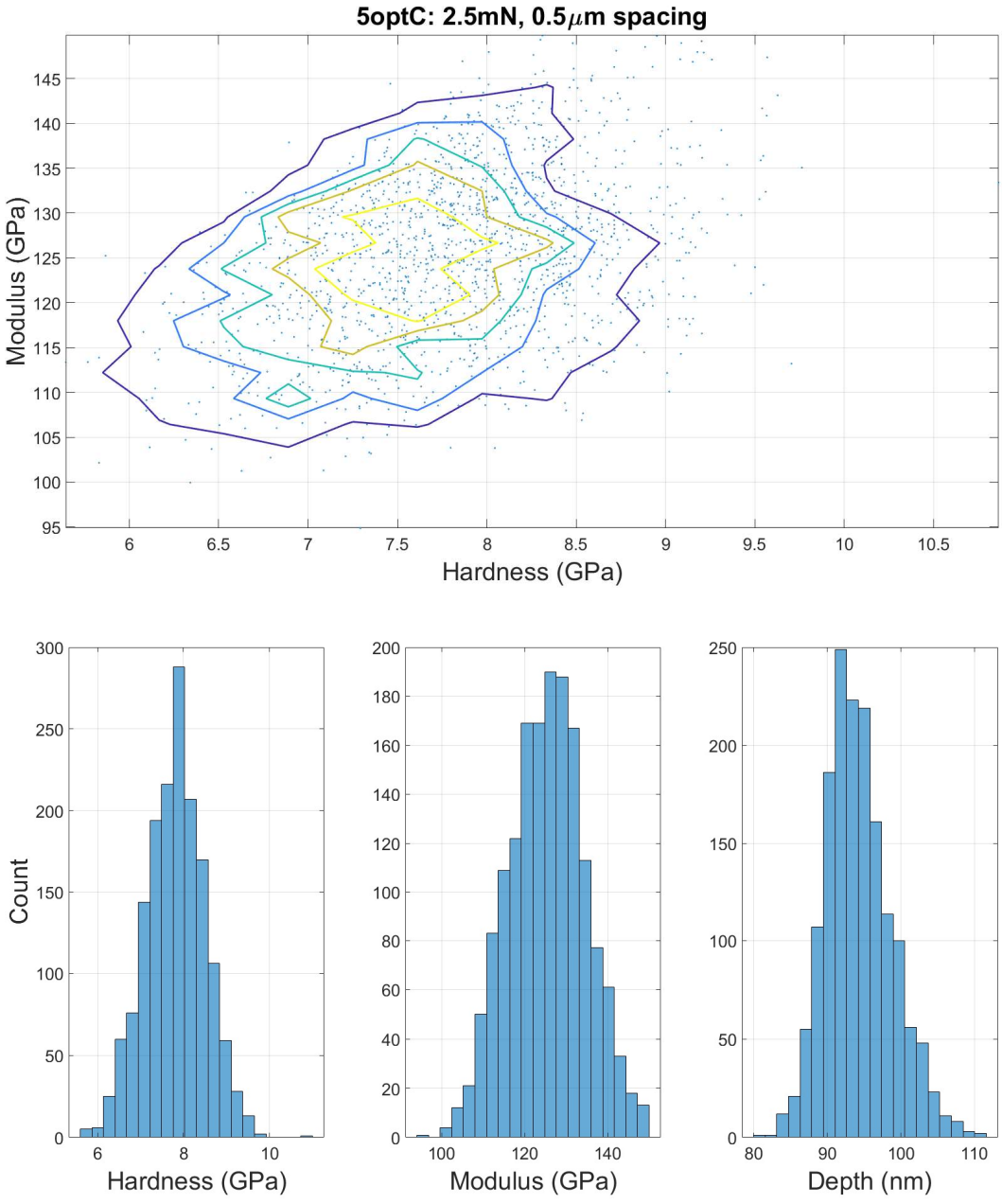

Figure 7.24: Data from Express indentation of 5optC, shown in a scatter graph of hardness against modulus with contours showing data point density, as well as histograms of hardness, modulus, and indent depth. The data is for 2.5mN indents made 0.5 µm apart.

Element	Hardness (GPa)	Modulus (GPa)	Depth (nm)
Mean	7.81 ± 0.7	125.48 ± 9.1	94.28 ± 4.5
Median	7.82	125.57	93.77

Table 7.1: Table comparing the mean and median values of hardness, modulus, and depth for 5optC, as calculated by from 2.5mN intents spaced 0.5 µm.

7.5.2 Results on a material with fine precipitates

Annealed optimised TiVZrHfTa (5optA) is a useful material to analyse with Express indentation as it pushes the spatial resolution of the Express arrays to their limit. The largest precipitates are only a couple of microns wide, and so in order to maximise the number of indents in the precipitate phase a large Express map was made with the minimum possible indent load and the minimum possible spacing (2.5mN and 0.5 µm respectively). It is possible that this spacing is close enough to incur size effects, however when tests were done gradually decreasing indent spacing no change in hardness was found, indicating size effects were not an issue. Figure 7.25 shows a section of the hardness map alongside a back-scatter SEM image taken after the array was made. It can be seen that only 1-2 indents can be placed along the width of these precipitates.

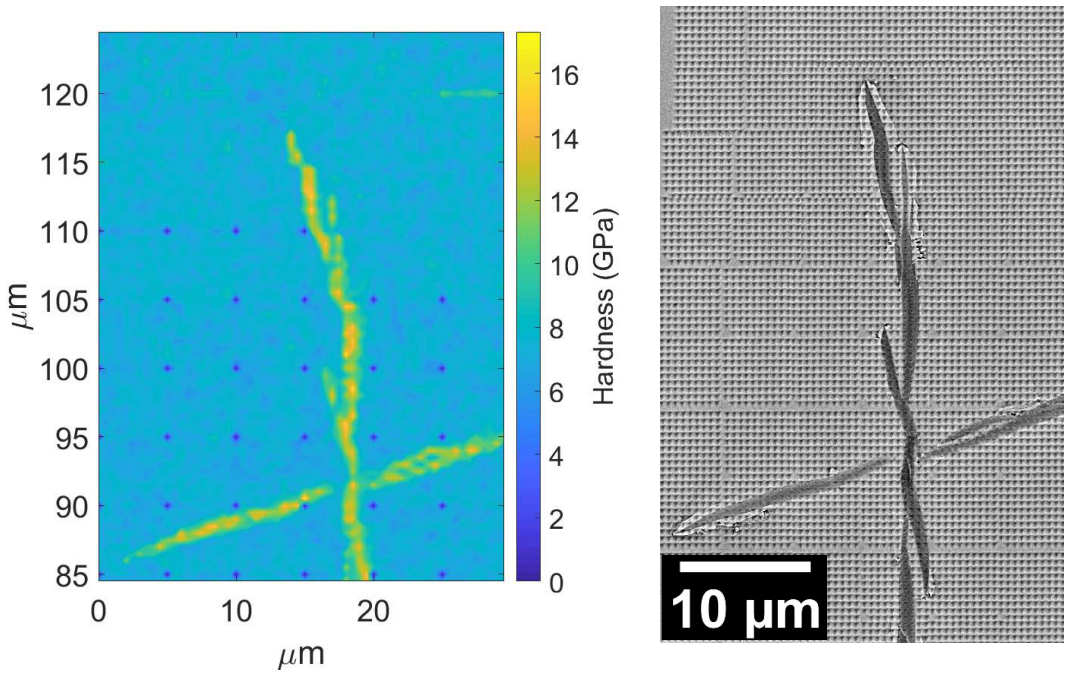

Figure 7.25: Hardness map of 5optA made with an Express array, alongside a back-scatter SEM image of the same area. Due to the narrow width of the precipitates only one or two indents could be made across their width, limiting the volume fraction that could be made in this phase. The array is for 2.5mN intents spaced 0.5 µm apart

The data from this large dense array is also presented in the same way as for for the quasi-single-phase material (5optC): as a scatter plot with contours showing density and also three separate histograms. Both the single-phase and precipitated materials have a main cluster of data points at a hardness of ∼7.5GPa and modulus of ∼120GPa, but in the two-phase material there is a tail of harder and stiffer data points coming off this main peak: these relate to indents made on or near the precipitates. If the size and volume fractions of the precipitates were larger it is possible that a second clustering of data points would emerge, and the contour plot would show where modal values of hardness and modulus overlap; with this data set however the contour plot shows there is no area within the tail that has a higher density of data points than any other, and so no single values of hardness and modulus can be extracted for the precipitates, only a broad range which is given in table

7.2. The histograms also support this observation, there is a peak representing the matrix phase, and then a broad tail of data but with no discernible peak. In summary, the Express method has not been able to evaluate the mechanical response of the precipitates in 5optA, although if a larger fraction of indents could be placed in the secondary phase it is possible that values could be obtained.

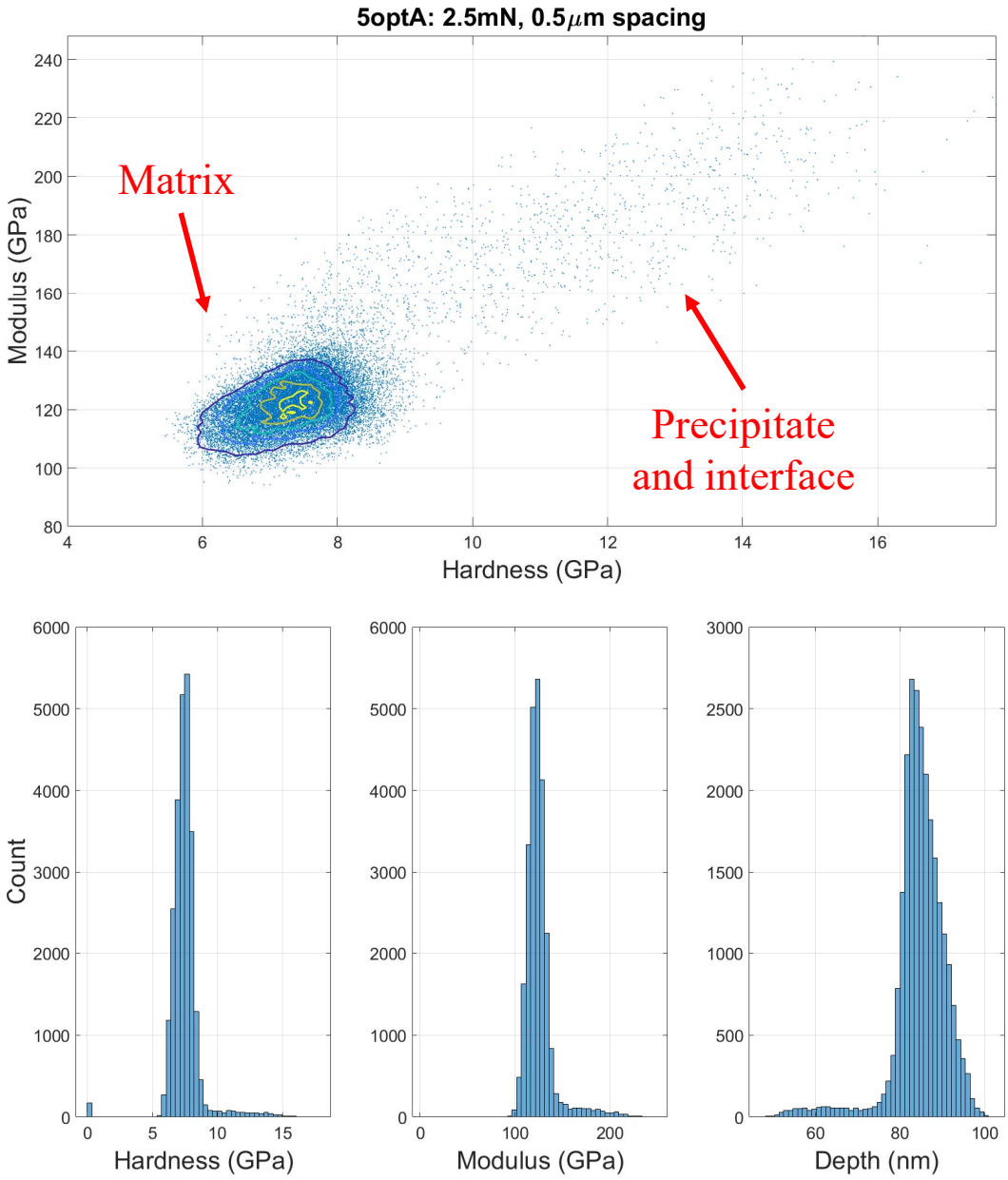

Figure 7.26: Data from Express indentation of 5optA, shown in a scatter graph of hardness against modulus with contours showing datapoint density, as well as histograms of hardness, modulus, and indent depth, as calculated by from 2.5mN intents spaced 0.5 µm.

Element	Hardness (GPa)	Modulus (GPa)	Depth (nm)
Approximate means of matrix phase	7.63 ± 0.9	123.24 ± 8.9	89.32 ± 4.2
Ranges of values for precipitate phase	9 - 16	150 - 240	50 - 75

Table 7.2: Table comparing the approximate mean properties of the matrix phase of 5optA and the ranges of values determined for the precipitates. This data is taken for Express arrays calculated with 2.5mN indents spaced 0.5 µm apart.

7.5.3 Results on a material with high volume fractions of different phases

The most complicated microstructure analysed with Express indentation is that of 5eqA. All the data discussed in this section relates to a large map of 18,000 indents made to a load of 2.5mN and spaced 0.5 µm apart. A map of hardness as well as a back-scatter electron image is shown in figure 7.27, and it can be seen there are three different phases with distinct mechanical responses. The phase with darkest contrast in the SEM image has the highest hardness (this is to be expected as this phase has previously been identified as a carbonitride), while the matrix phase is the softest part of the material.

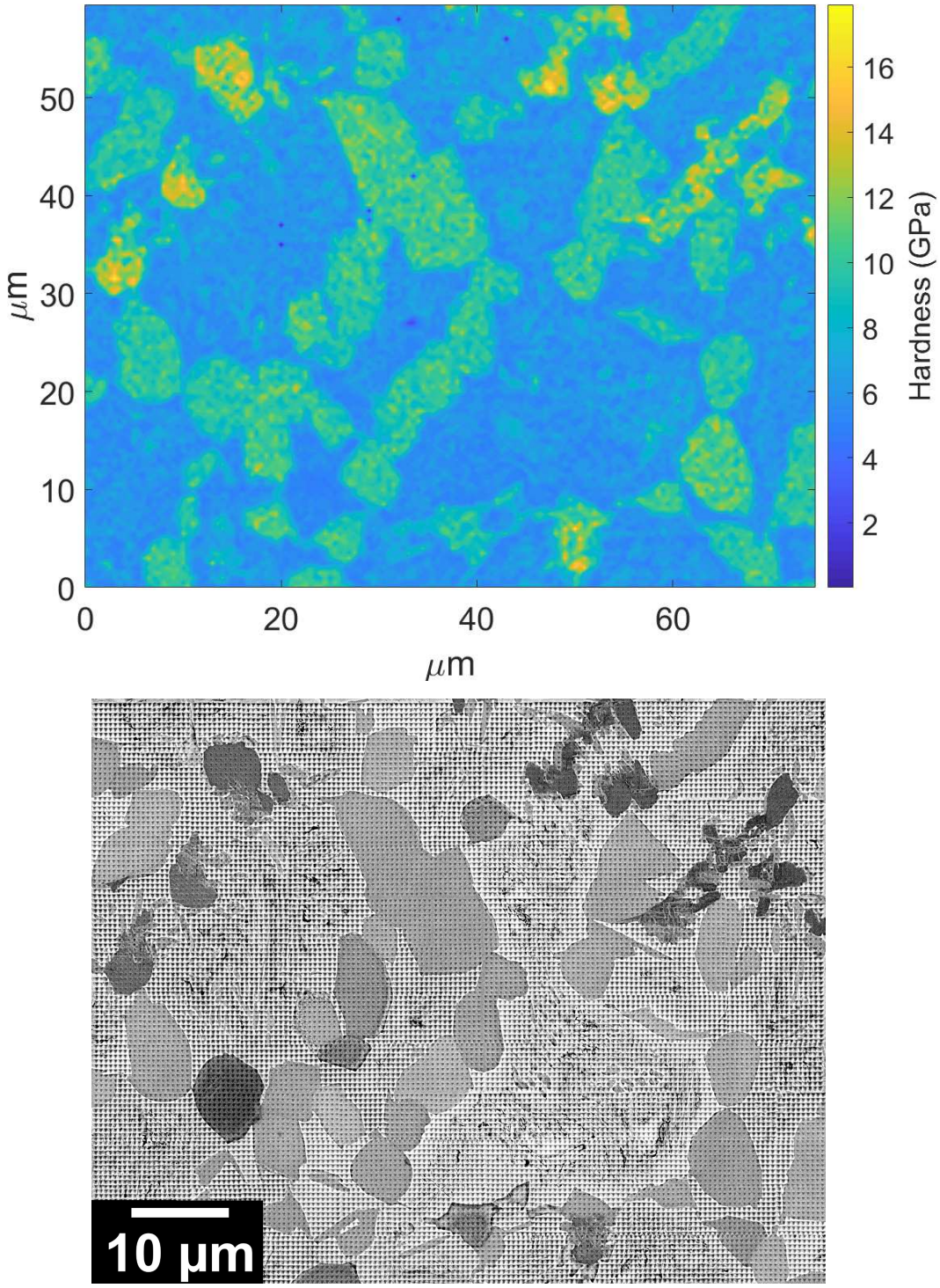

Figure 7.27: Hardness map of 5eqA made with an Express array, alongside a back-scatter SEM image of the same area. Three distinct mechanical responses can be seen in the hardness map, and these seem to relate to the carbonitride phase, the HCP precipitates, and the matrix phase which can all be seen in the SEM image.

An attempt has been made to group the indents according to their mechanical response. A scatter plot of hardness against modulus shows a familiar effect whereby there is a main cluster of data points relating to the matrix, and then a tail of data points which relate to the precipitates. Although there is a second peak in the hardness/modulus contour plot, it cannot be resolved any better with different contour parameters. However, if depth is plotted against modulus instead, then a second cluster at modulus of 160GPa and indentation depth 65nm is visible: these two scatter plots are shown in figure 7.28.

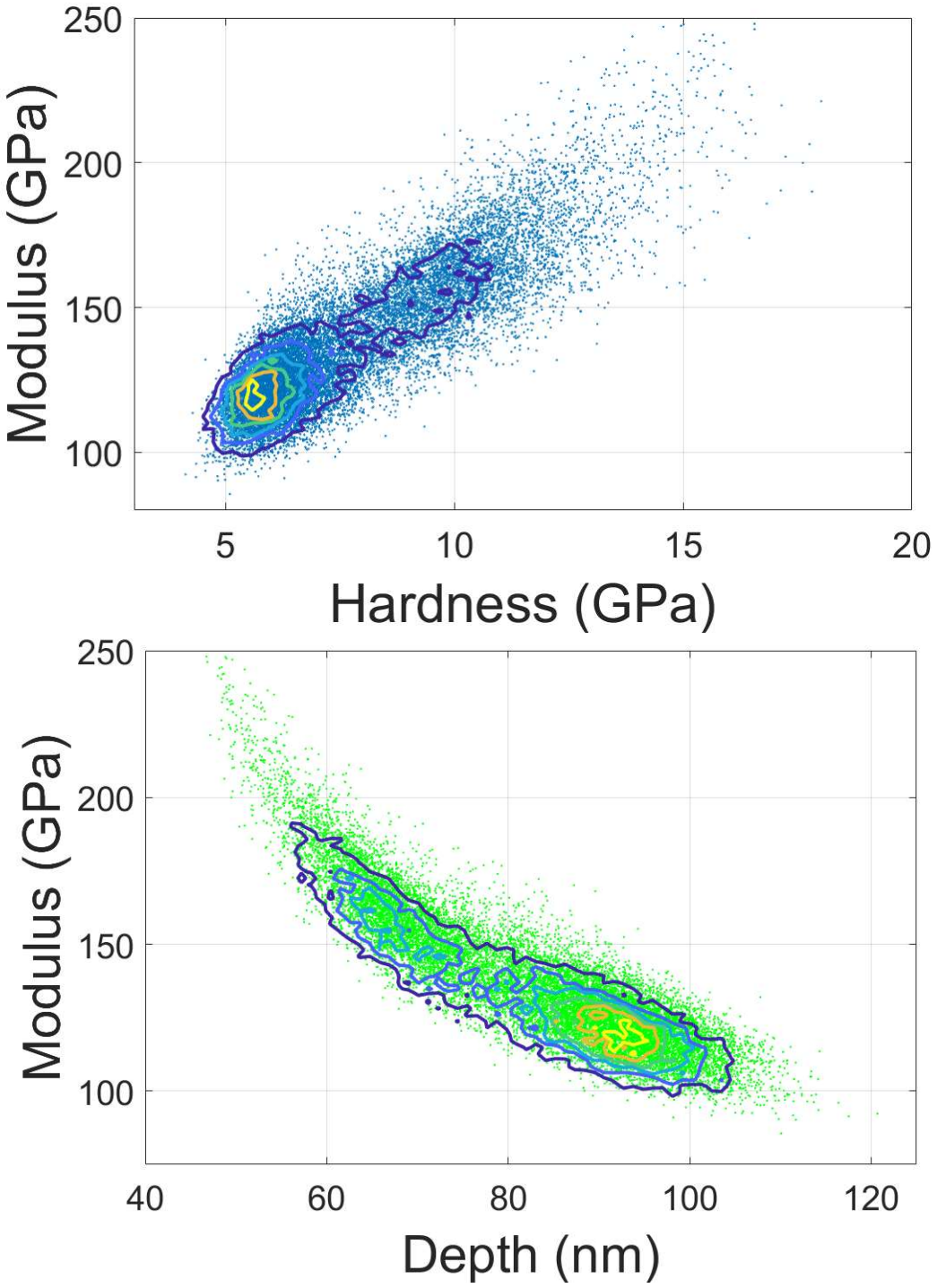

Figure 7.28: Scatter plots of hardness against modulus and indentation depth against modulus, both taken from the same array on 5eqA. The scatter plots show contours which relate to the density of data points: the densest area relates to the matrix phase while the second peak relates to the HCP precipitates.

In order to try and extend this analysis and separate out the populations, Gaussian curves have been fitted to the histograms of hardness, modulus, and indentation depths. Figure 7.29 shows two sets of histograms, those on top have been fitted for three Gaussian distributions, while those on the bottom are fitted for only two. The black curves show the summation of all of the Gaussian distributions for each graph.

It can be seen that although the distributions relating to the matrix (blue) and HCP precipitates (red) are easy to identify due to clear peaks in the histogram, the carbonitride's distributions (green) have a low number of counts and overlap strongly with the other phases, making its fitting parameters difficult to be certain of.

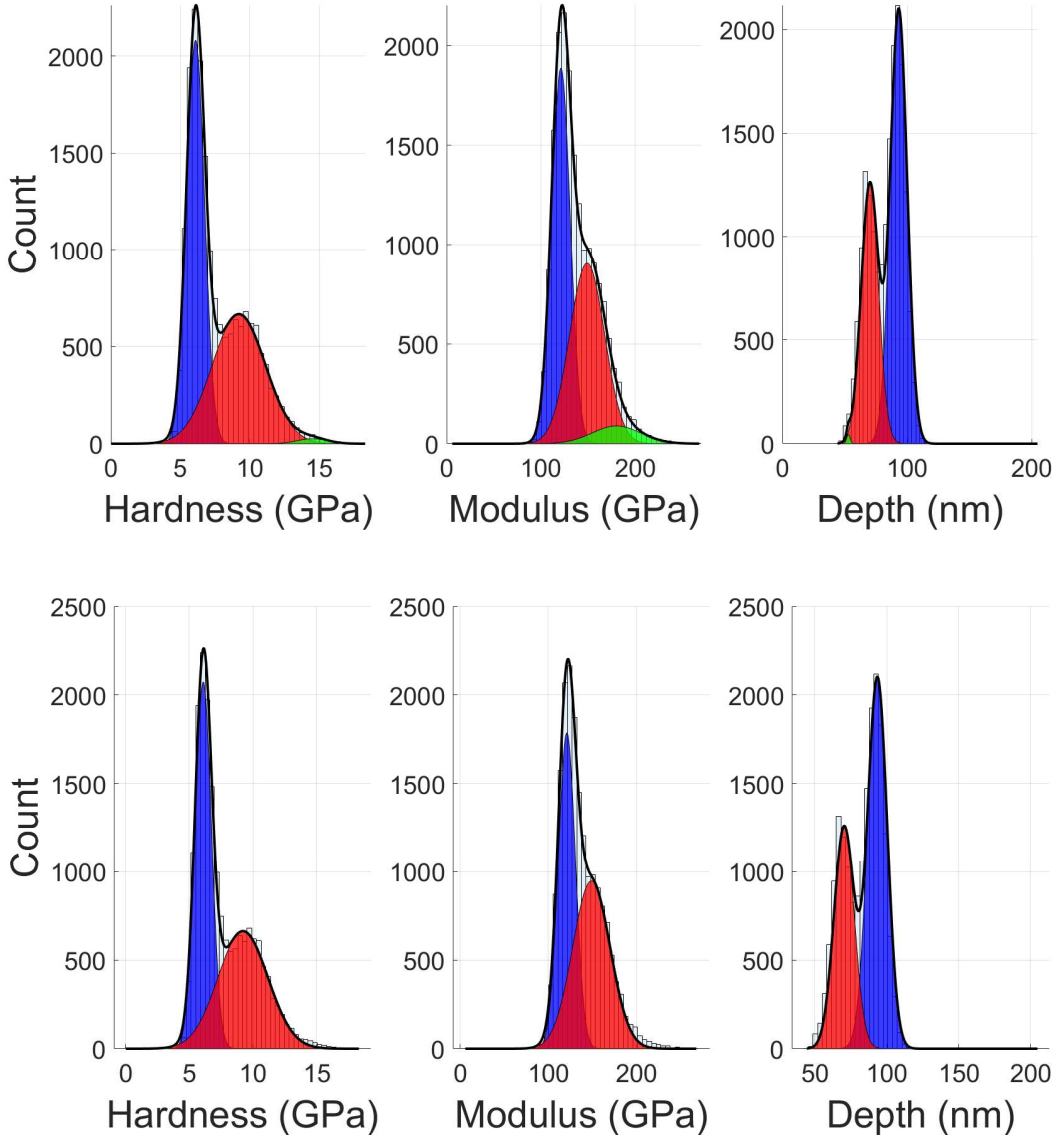

Figure 7.29: Histograms of hardness, modulus, and depth with Gaussian distributions fitted on them. The top three graphs all have three populations fitted, while the second three have only two. It can be seen that the green population makes very little difference to the red and blue ones which both represent a much greater number of indents.

Plots of the residual value can help to assess the accuracy of fitted data, and to this end the residuals of the modulus data for the two and three-population fits are shown in figure 7.30. The third population represents the carbonitride, the stiffest of the three phases, and so the residual value when the modulus $\geq$200GPa is most

relevance when trying to determine if Express Indentation has successfully captured the mechanical properties of the carbonitride. It can be seen from the plot that the three-population fit is more accurate in this range than the two population fit, demonstrating that Express indentation is capturing this phase, even if the technique is not easily able to separate them out for further statistical analysis at this point in its development.

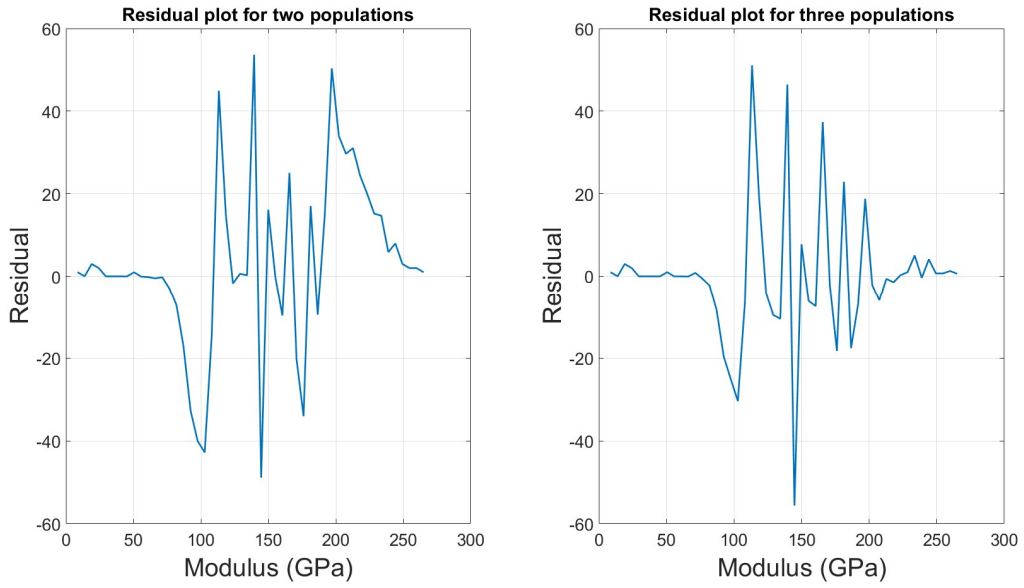

Figure 7.30: Residual plots of the two and three populations fits for the modulus histograms made from the Express data on 5eqA. This data is from 2.5mN indents spaced 0.5 µm apart. It can be seen that the three-population fit has a lower residual, particularly at stiffer values of modulus where the third population is present.

7.5.3.1 Results on a material with chemical segregation

As-cast equiatomic TiVZrHfTa (5eqC) has similar precipitation to 5eqA, but is unique in the amount of interdendritic segregation that it shows. An express array was made over an area containing segregation and precipitates: a map of modulus as well as a back-scatter SEM image of the same area is shown in figure 7.31. It can be seen that the interdendritic region, which appears darker in the SEM image

has a measurably stiffer mechanical response. This shows that Express indentation is capable of resolving small changes in mechanical response, broadening its possible applications away from materials that contain ceramic phases within metallic matrices.

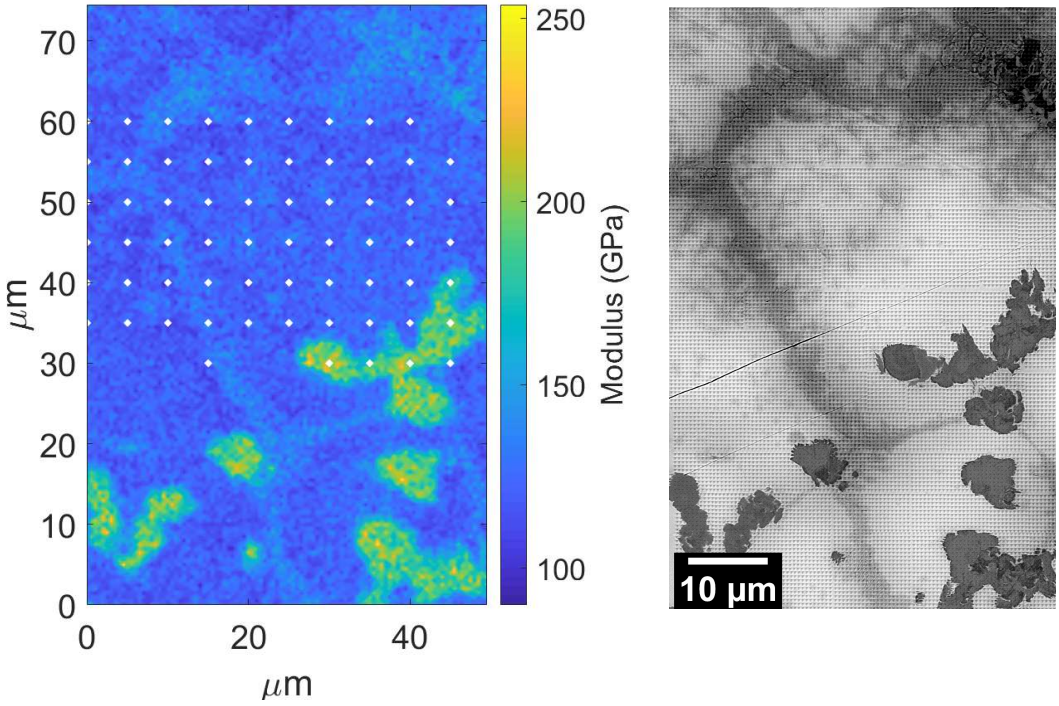

Figure 7.31: Map of modulus made in 5eqC using Express indentation next to a back-scatter image of the same area taken after the array was made. The indents are made to a load of 2.5mN and are spaced 0.5 µm apart

7.5.4 Summary of Express testing of multiphase materials

In summary, the Express indentation on the TiVZrHfTa alloys has shown many of the technique's capabilities but also its limitations. The practical limits of load and indent spacing have been identified, but it has been shown to be able to measure the properties of three different phases in 5eqA. The next stage of technique development will be to integrate SEM techniques with Express indentation, so that EBSD, EDX, or even back-scatter contrast can be used to to group indents by phase into

separate populations, alloying better and more accurate statistics to be calculated.

7.6 Conclusions

The mechanical properties of the alloys analysed in this project show that the rocksalt-structured phase is very hard, exceeding 20GPa in hardness, while the matrix is much softer, at around 6-8GPa. Hardness and modulus measurements made in the material matrices have not been able to detect any changes after ion implantations of up to 3.5 dpa. Despite the tested material being contaminated, the metallic matrix phase was still shown to exhibit better resistance to radiation damage than a pure material: further tests of clean material, combined with TEM analysis of defect structures, will help to answer what gives them this resistance to hardening and whether a low-activation refractory HEA will indeed be suitable for application in a fusion reactor.

Express testing has been benchmarked against fused silica and tungsten, and then used to try and analyse the various phases in the TiVZrHfTa alloys. Express indentation is a challenging technique to use, but the results presented here demonstrate that it can be used to map multiphase materials with a high degree of spatial accuracy, and capture the mechanical properties of even low volume fraction phases. This technique will be even more powerful once it analysis can be guided by SEM micrographs, in order better separate indents based on the phase they were made in.

Chapter 8

Future Work

The work done in this thesis has answered many questions, but have also left some unanswered. The purpose of this section is to highlight some of the work that could be done to continue this project.

To fully understand the effect of impurities, more APT and TEM data is needed. This would allow the composition and crystal structures of the different phases to be measured more accurately. Combining this information with the XRD phases will allow a more accurate assessment of how much of each phase the samples contain, and how much the composition varies. It may also be interesting to use high-resolution EBSD to calculate the orientation relationships between the HCP and rocksalt-structured phases, which are marked but were too difficult to quantify during this project.

Due to contamination it was never possible to accurately assess the efficacy of the Ω parameter or its optimisation. The one billet which was not contaminated (5opt) showed a high stability when compared to the binary phase diagrams which show relatively low solubility across multiple systems. It would be valuable therefore to

melt some equiatomic and optimised billets in the clean furnace and then to compare their microstructures, to once and for all answer the question of whether a higher Ω really leads to a more stable solid-solution microstructure.

Another area of this project that is so far unfulfilled is locating a fusion appropriate HEA. This thesis provides more evidence that these alloys are unnaturally able to resist radiation damage, and it is worth trying to optimise these and other properties. The BCC systems related to this and ongoing work is being done on TiVCrTa and other similar alloys.

In terms of HEA resistance to radiation damage there is still much work out to do in order to work out why and when the resistance comes from. This will likely require a greater range of ion implantation experiments, and more advanced characterisation such as by TEM in order to accurately measure crystal defect structures.

Express indentation has been shown to have a high potential to analyse multiphase materials, and work is ongoing in group to further improve this technique. This is focussing on better understanding how modulus measurements are made, ensuring good and consistent calibration methods, and combining the technique with SEM analysis. The aim is to be able to sort indents by phase based on data from electron microscopy, for example taking an EBSD map and using it to separate indents by grain orientation or phase, or using EDX data to sort indents by elemental concentration. This additional data will make statistical analysis of the mechanical properties more reliable.

Chapter 9

Final Conclusions

In chapter 2 five research aims were listed. Over the course of this thesis they have been answered as follows.

- **Discover the controlling factors for phase formation in refractory HEAs;**

Many of the element used in refractory HEAs, and in particular the group IV metals, are sensitive to the presence of impurities. In the alloys fabricated here carbon contamination was found in the zirconium feedstock material, while nitrogen and oxygen were introduced by a faulty door seal. The effect of this was to form a variety of carbonitrides, all with the rocksalt crystal structure. Several papers have been identified which report FCC crystal structures, that may also have formed due to contaminates during melting. Within refractory alloys there is strong sensitivity to contaminates, the cleanest billet still precipitated small carbides, and unless these can be removed they will dominate phase formation.

- **Compare whether thermodynamics or kinetics control the formation of single-phase solid-solution microstructures;**

A new method of optimising composition in order to maximise the Ω parameter was proposed. Based on the evidence of the phase-separating contaminated alloys it was then discarded, however these experiments should be repeated in order to establish whether this was in err. It was separately demonstrated that reducing the mass of an arc-melted billet from 50 to 10g was sufficient to increase cooling rate to a point which largely suppressed phase separation in TiVZrHfTa, and reduced the amount of secondary phase formation in TiVZrTa and TiVTa alloys. Based on this it is concluded that regardless of the role thermodynamics plays in the solidification of HEAs, kinetics can be easily manipulated to give single-phase microstructures that are not representative of what could be achieved if manufacturing techniques are scaled up.

- **Explore the effect of cooling rate variation in arc-melted billets;**

The cooling rate of HEAs has been shown to play a key role in determining their as-cast microstructures. It has also been demonstrated that the cooling rate in a 50g arc-melted billet varies severely enough to form different microstructures at different parts of the billet: for example the volume fraction of carbonitride phase varies from 0% to 10% when comparing the fastest cooling material to the slowest, and the total area of porosity increasing from nearly zero to 13mm^2 when polishing back from the part of the billet adjacent to the crucible and the part adjacent to the atmosphere. This has profound effects on how data from HEAs should be reported, implying that both billet mass, machining techniques, and sample location are all of importance when discussing the measured properties of arc-melted alloys.

- **Determine whether BCC HEAs are able to resist the deleterious effects of ion-implantation;**

Although the contaminated alloys are not model materials for application in a fusion reaction, nanoindentation measurements of the sample matrices show that there is no increase in hardness after ion-implantation of up to 3.5dpa. This is contrast to the behaviour of pure vanadium which hardened by over 25% under the same conditions. This is in accordance with the results in the wider literature, which have found that FCC HEAs also share a resistance to the deleterious effects of ion-implantation, although the exact mechanism of this is still unknown. The next stage of this work should be to re-test uncontaminated material, but to also try and understand how the defect structures in the implanted layer are evolving to help elucidate the origin of this seemingly innate resistance.

- **Develop a technique that can separately analyse the mechanical properties of phases in a multiphase material;**

As many of the alloys developed were multiphase, a technique was required in order to separately quantify the mechanical properties of each phase. Express indentation was used to create maps of hardness and modulus over all of the quinary alloys. It was also used to determine mean values and standard deviations for all three phases in 5eqA, which without the methodology would not have been possible. The future of Express indentation will see it combined with electron microscopy in order to better sort indents by the phase they were made into, and thus improve the statistics that can be extracted.

Appendix A

Appendix: Phase Diagrams

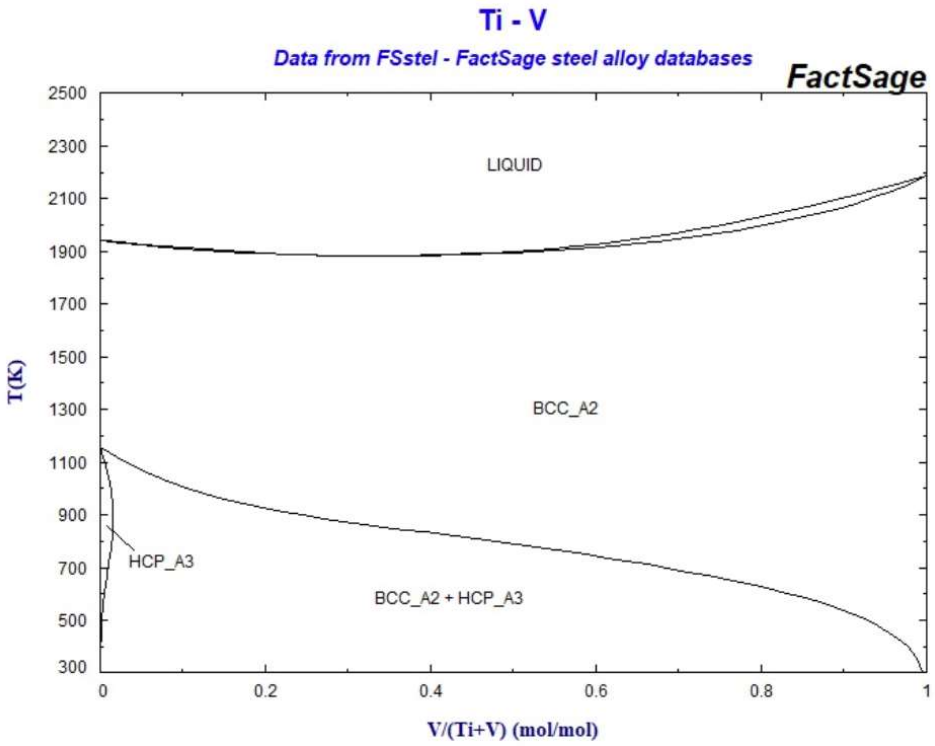

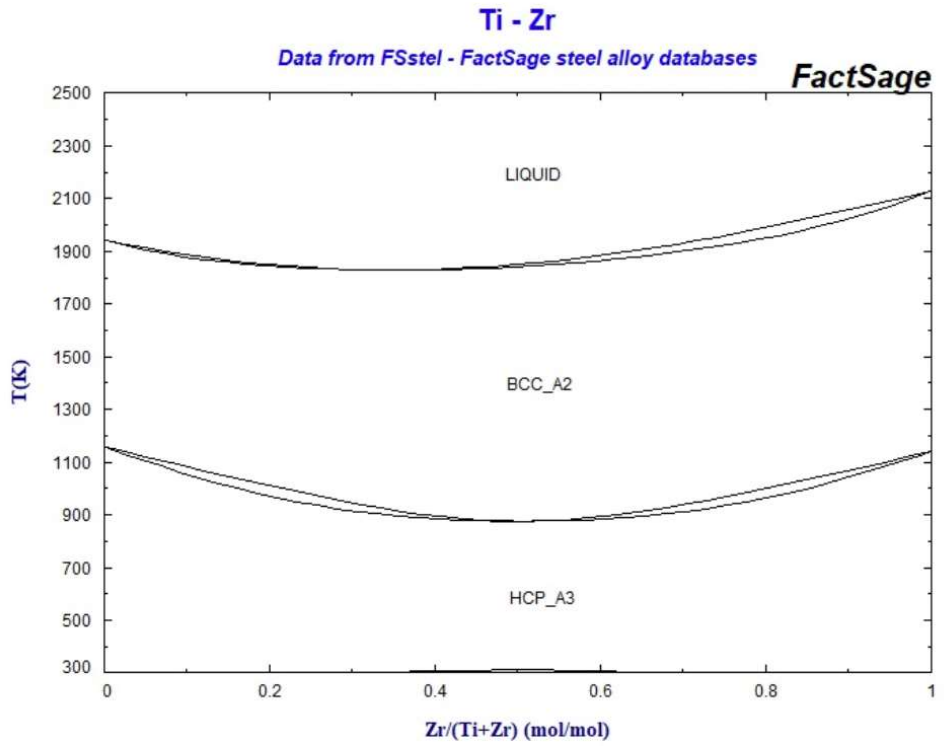
Ti - Zr
Data from FSstel - FactSage steel alloy databases
FactSage
LIQUID
BCC_A2
HCP_A3
T(K)
Zr/(Ti+Zr) (mol/mol)
2500
2300
2100
1900
1700
1500
1300
1100
900
700
500
300
0
0.2
0.4
0.6
0.8
1

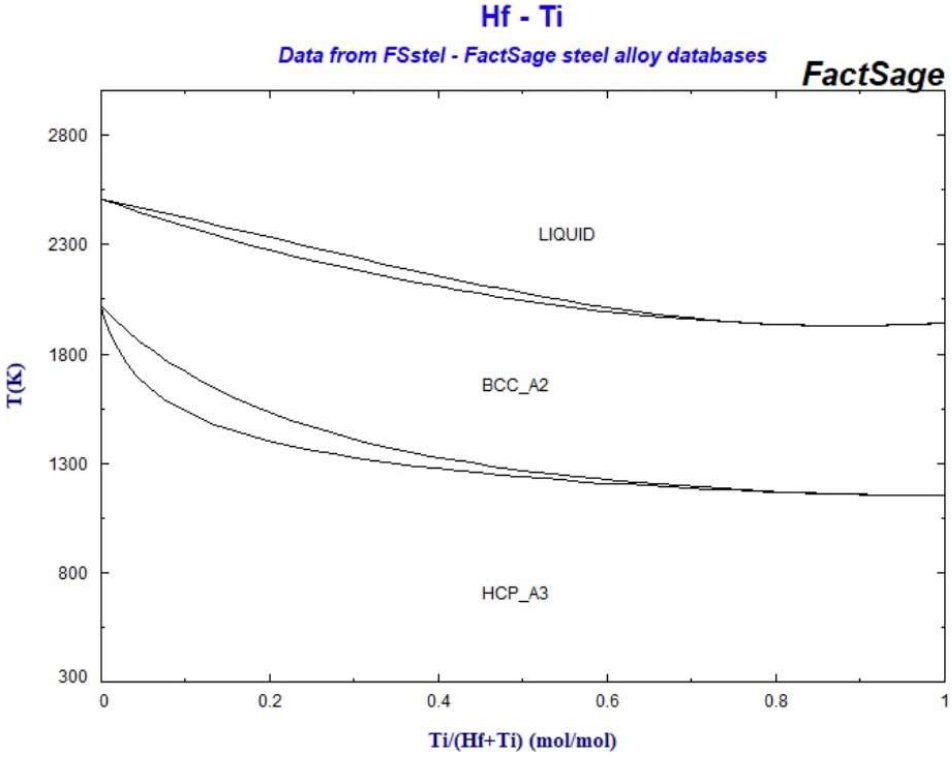
Hf - Ti
Data from FSstel - FactSage steel alloy databases
FactSage
LIQUID
BCC_A2
HCP_A3
T(K)
Ti/(Hf+Ti) (mol/mol)
2800
2300
1800
1300
800
300
0
0.2
0.4
0.6
0.8
1

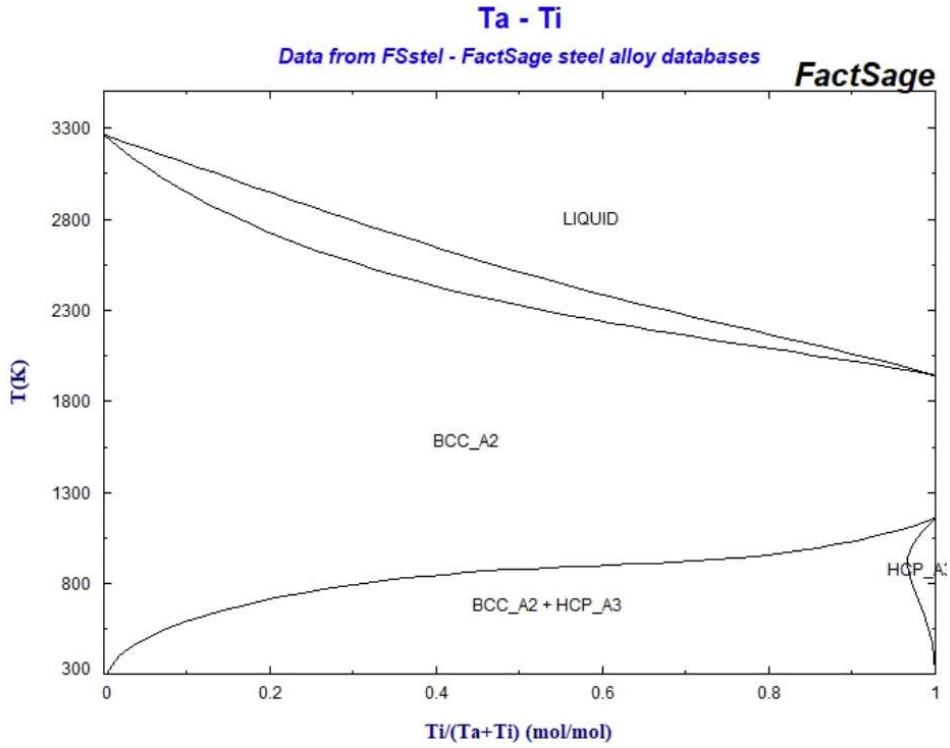
Ta - Ti
Data from FSstel - FactSage steel alloy databases
FactSage
LIQUID
BCC_A2
BCC_A2 + HCP_A3
T(K)
Ti/(Ta+Ti) (mol/mol)

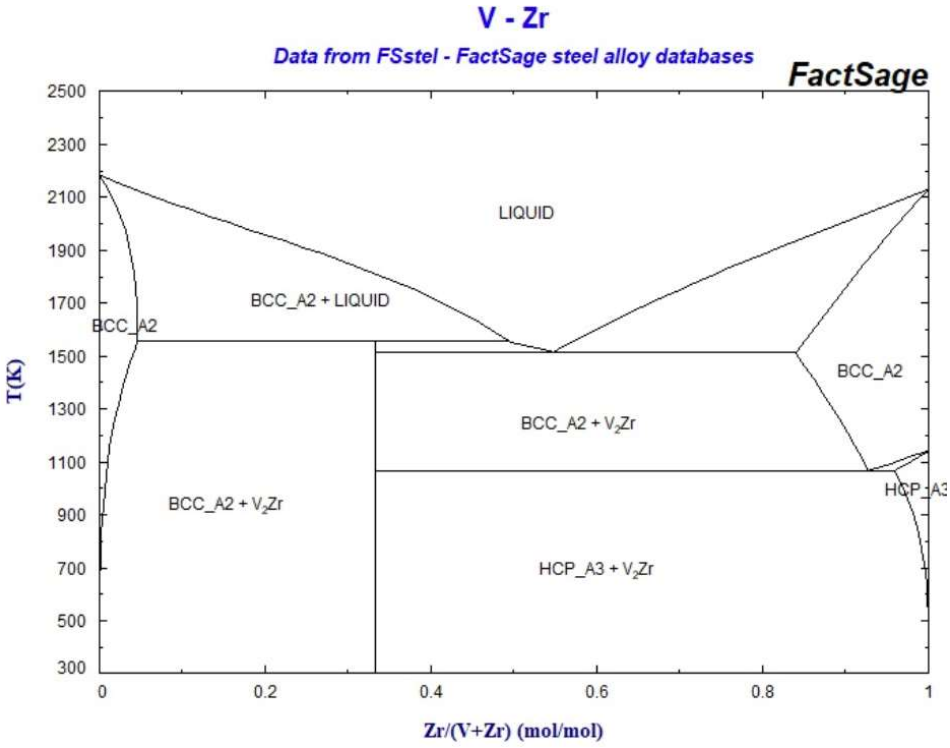
V - Zr
Data from FSstel - FactSage steel alloy databases
FactSage
LIQUID
BCC_A2 + LIQUID
BCC_A2
BCC_A2 + V2Zr
BCC_A2
BCC_A2 + V2Zr
HCP_A3 + V2Zr
T(K)
Zr/(V+Zr) (mol/mol)

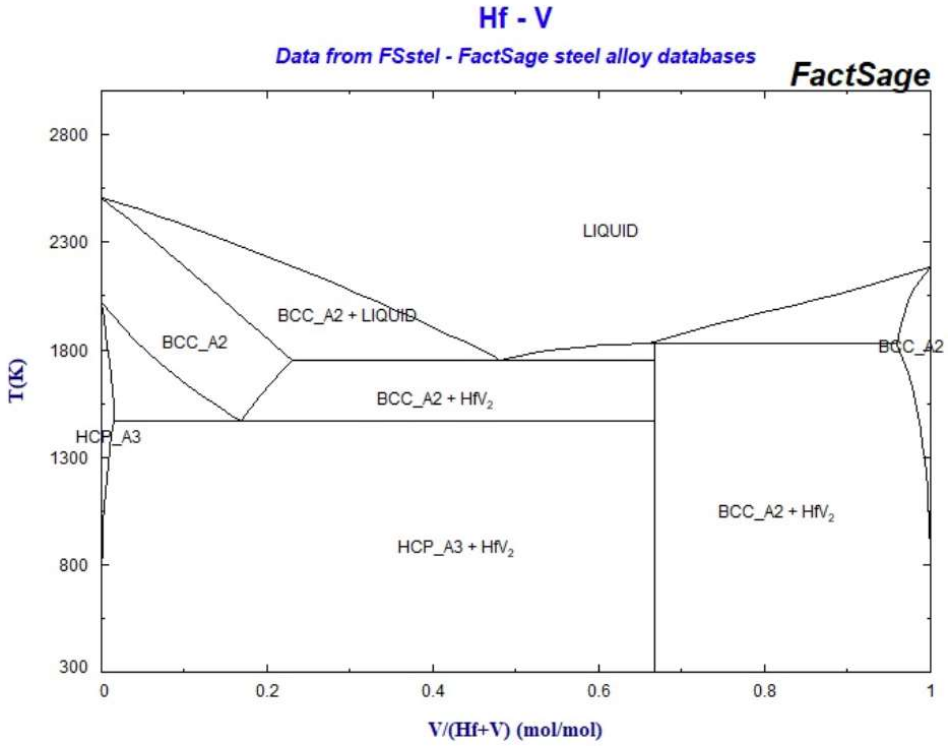
Hf - V
Data from FSstel - FactSage steel alloy databases
FactSage
LIQUID
BCC_A2 + LIQUID
BCC_A2
BCC_A2
BCC_A2 + HfV2
HCP_A3
BCC_A2 + HfV2
HCP_A3 + HfV2
T(K)
V/(Hf+V) (mol/mol)

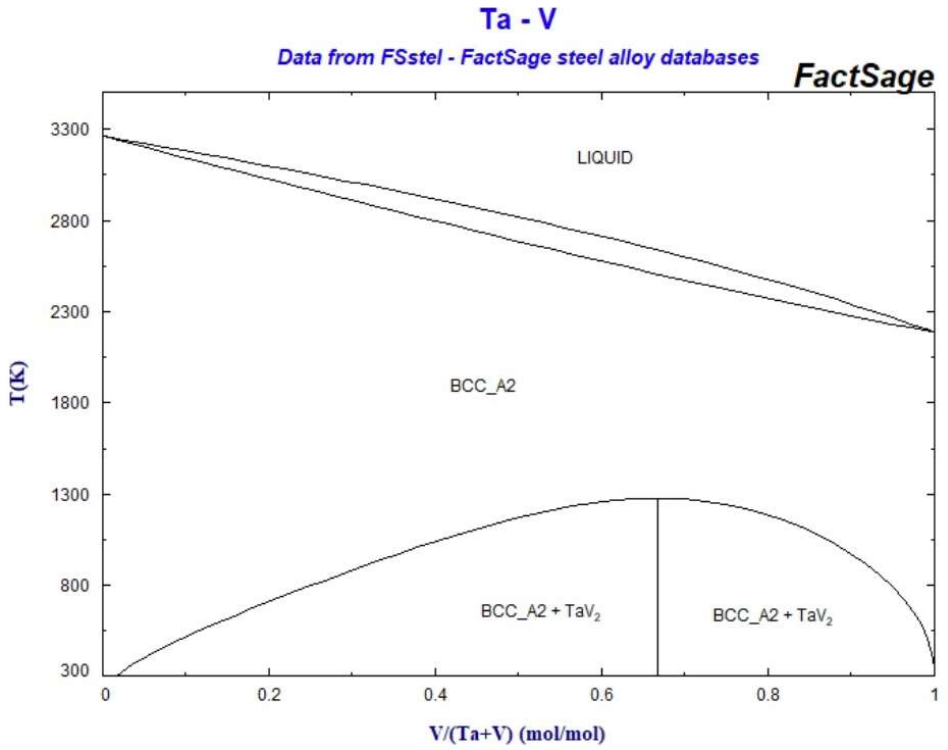
Ta - V
Data from FSstel - FactSage steel alloy databases
FactSage
LIQUID
BCC_A2
BCC_A2 + TaV2
BCC_A2 + TaV2
T(K)
V/(Ta+V) (mol/mol)

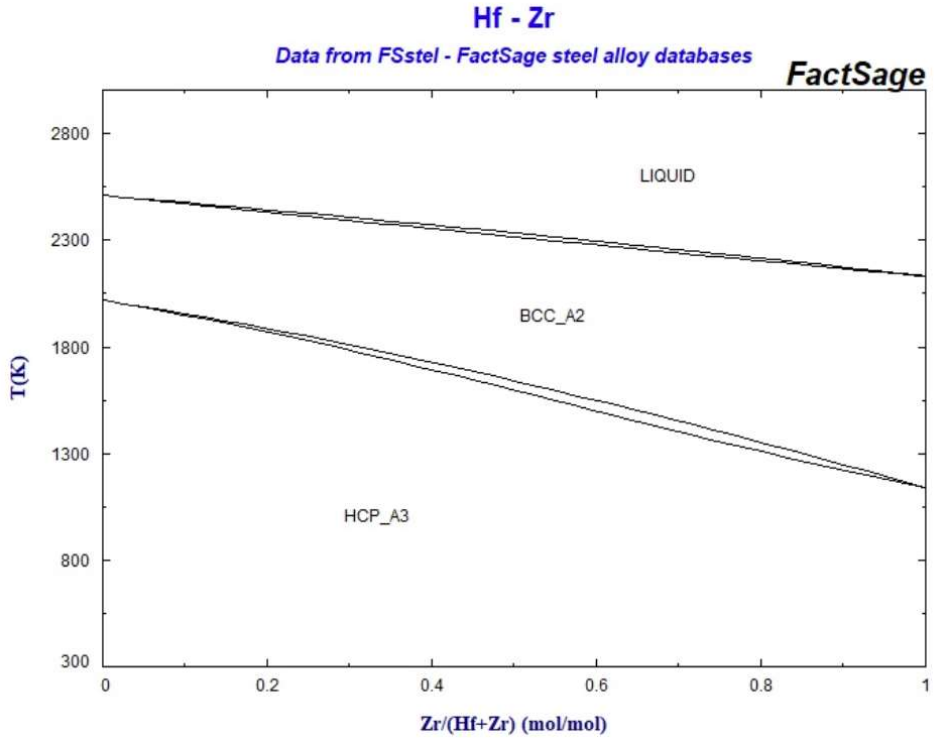
Hf - Zr
Data from FSstel - FactSage steel alloy databases
FactSage
LIQUID
BCC_A2
HCP_A3
T(K)
2800
2300
1800
1300
800
300
0
0.2
0.4
0.6
0.8
1
Zr/(Hf+Zr) (mol/mol)

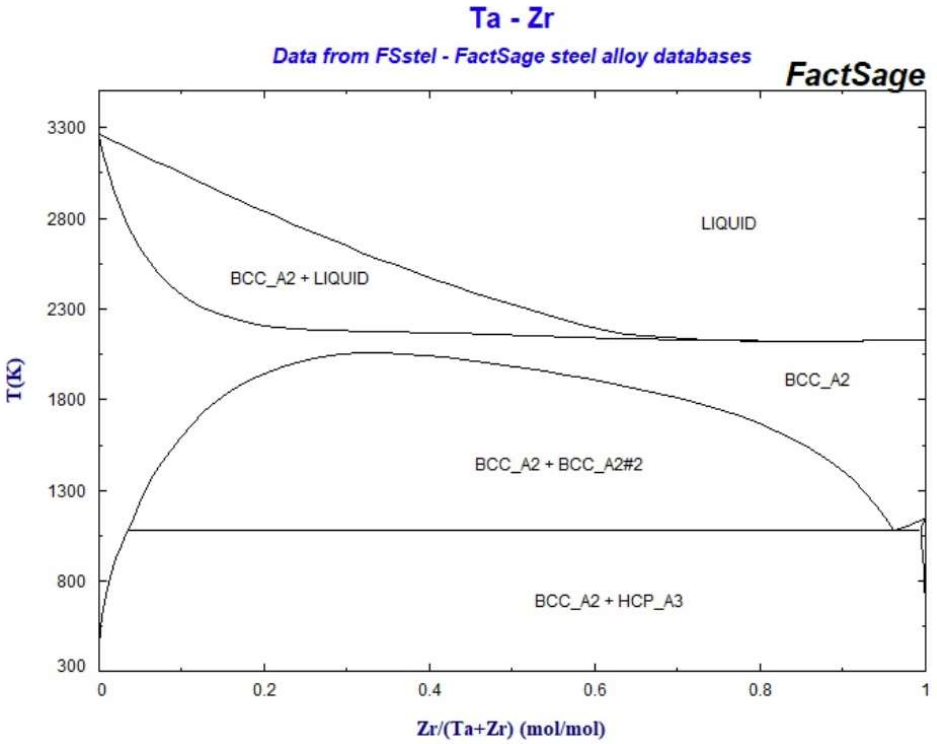
Ta - Zr
Data from FSstel - FactSage steel alloy databases
FactSage
LIQUID
BCC_A2 + LIQUID
BCC_A2
BCC_A2 + BCC_A2#2
BCC_A2 + HCP_A3
T(K)
3300
2800
2300
1800
1300
800
300
0
0.2
0.4
0.6
0.8
1
Zr/(Ta+Zr) (mol/mol)

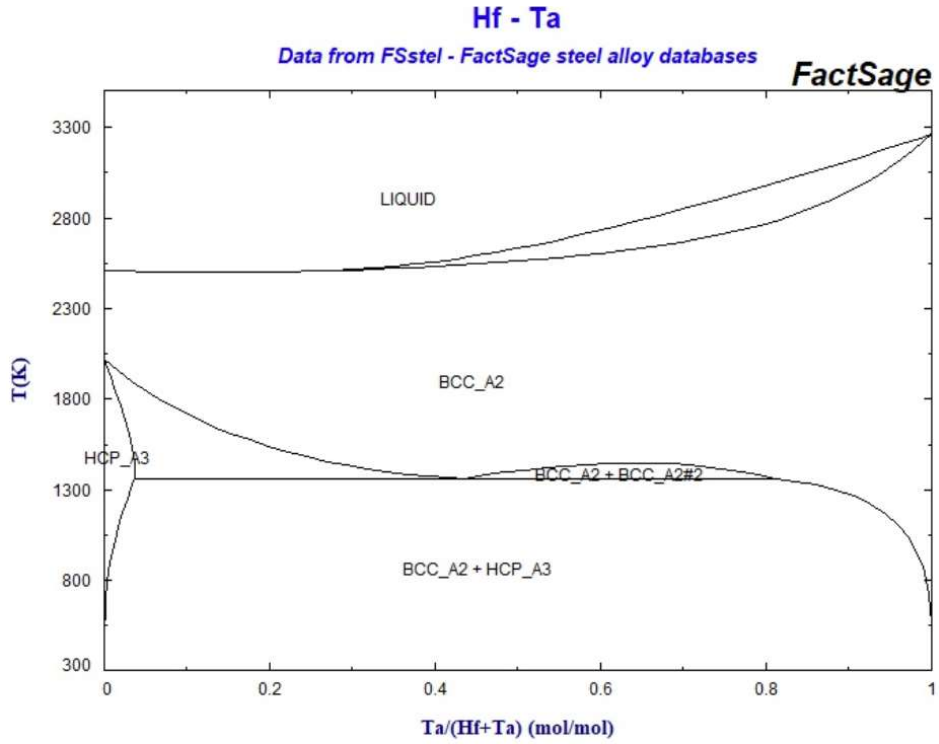
Hf - Ta
Data from FSstel - FactSage steel alloy databases
FactSage
LIQUID
BCC_A2
HCP_A3
BCC_A2 + BCC_A2#2
BCC_A2 + HCP_A3
T(K)
3300
2800
2300
1800
1300
800
300
0
0.2
0.4
0.6
0.8
1
Ta/(Hf+Ta) (mol/mol)

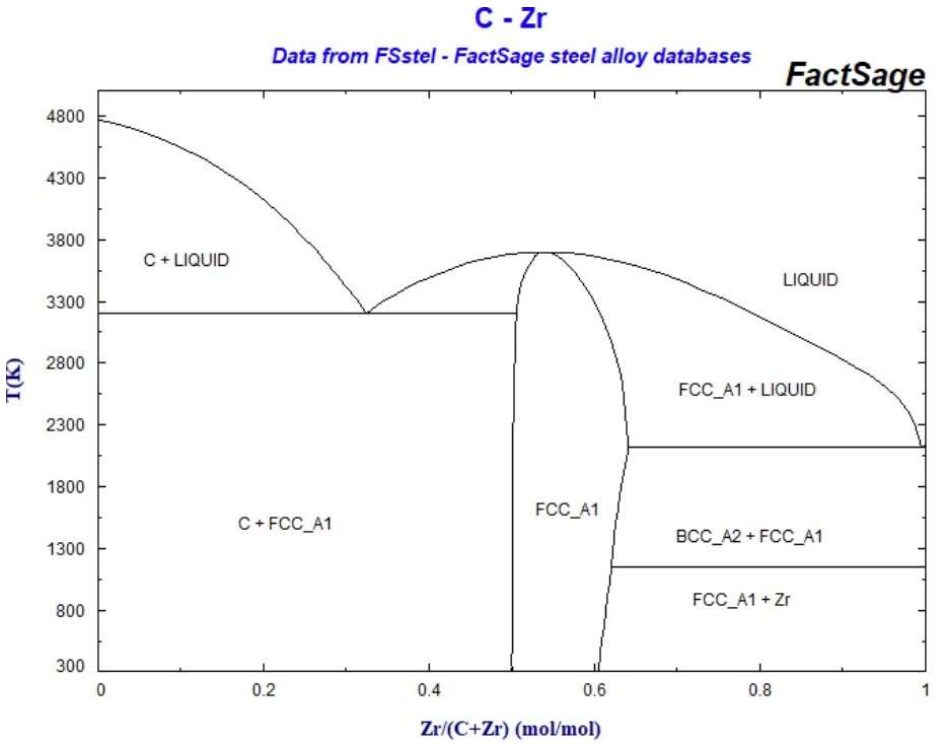
C - Zr
Data from FSstel - FactSage steel alloy databases
FactSage
C + LIQUID
LIQUID
FCC_A1 + LIQUID
C + FCC_A1
FCC_A1
BCC_A2 + FCC_A1
FCC_A1 + Zr
T(K)
4800
4300
3800
3300
2800
2300
1800
1300
800
300
0
0.2
0.4
0.6
0.8
1
Zr/(C+Zr) (mol/mol)

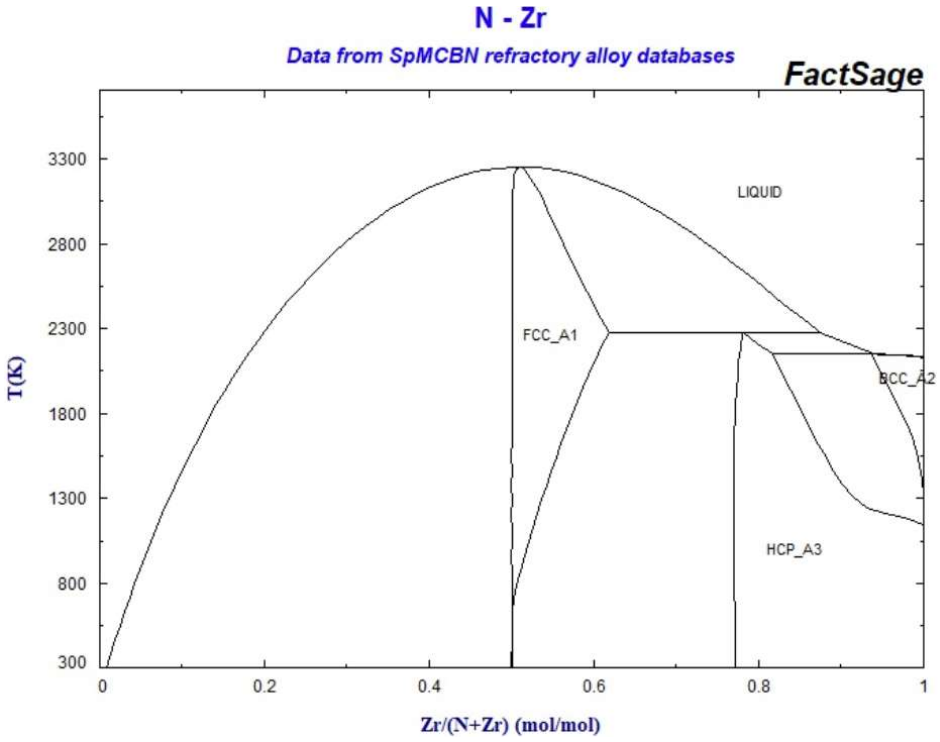
N - Zr
Data from SpMCBN refractory alloy databases
FactSage
LIQUID
FCC_A1
BCC_A2
HCP_A3
T(K)
Zr/(N+Zr) (mol/mol)

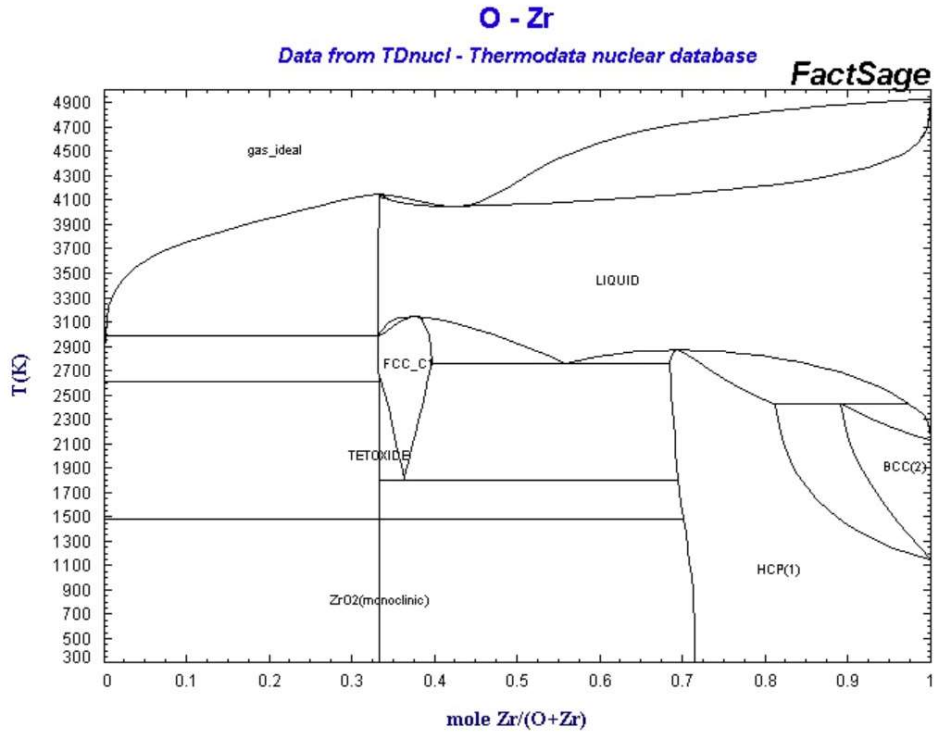
O - Zr
Data from TDnucl - Thermodata nuclear database
FactSage
gas_ideal
LIQUID
FCC_C1
TETOXIDE
BCC(2)
HCP(1)
ZrO2(monoclinic)
T(K)
mole Zr/(O+Zr)

Appendix B

Appendix: Optimisation Code

Included here are the matlab code for HEA optimisation. The final page includes two functions which are required in order to run the script. In addition to these functions several saved variables are required which list the binary enthalpies of mixing, atomic radii, and melting temperatures of the necessary elements.

```
%%%%%%%%%%%%%%%%%%%%%%%%%%%%%%%%%%%%%%%%%%%%%%%%%%%%%%%%%%%%%%%%%%%%%%%%%%%%
%%%%%%%%%%%%%%%%%%%% Written by J.C.Waite on 25/04/16 %%%%%%%%%%%%%%%%%%%%%%
%%%%%%%%%%%%%%%%%%%%%%%%%%%%%%%%%%%%%%%%%%%%%%%%%%%%%%%%%%%%%%%%%%%%%%%%%%%%
%Optimizes composition wrt Omega.  Considers Delta constraints.
%Must have omega.m, delta.m, and physical_constants.mat saved in the same folder.
%Requires at least three elements
clear()
global dHmix T r misfit_limit %Must be global so available for functions

%Set the upper and lower bounds for optimizing, as well as the misfit limit
lower_bound=0.01;
upper_bound=0.999999;
misfit_limit=6.6;

%Initial compostion in atomic % (decimal).

Li=0.;
B =0.;
Mg=0.;
Al=0.;
Si=0.;
Sc=0.;
Ti=0.326;
V =0.148;
Cr=0.;
Mn=0.;
Fe=0.;
Co=0.;
Ni=0.;
Cu=0.;
Zr=0.147;
Nb=0.;
Mo=0.;
Sn=0.;
Hf=0.173;
Ta=0.206;
W =0.;

%%%%%%%%%%%%%%%%%%%%%%  No inputs beyond this point  %%%%%%%%%%%%%%%%%%%%%%%

c=horzcat(Li, B, Mg, Al, Si, Sc, Ti, V, Cr, Mn, Fe, Co, Ni, Cu, Zr, Nb, Mo, Sn, Hf,↙
Ta, W);
clear('Li', 'B', 'Mg', 'Al', 'Si', 'Sc', 'Ti', 'V', 'Cr', 'Mn', 'Fe', 'Co', 'Ni',↙
'Cu', 'Zr', 'Nb', 'Mo', 'Sn', 'Hf', 'Ta', 'W');
eles={'Li'; 'B '; 'Mg'; 'Al'; 'Si'; 'Sc'; 'Ti'; 'V '; 'Cr'; 'Mn'; 'Fe'; 'Co'; 'Ni';↙
'Cu'; 'Zr'; 'Nb'; 'Mo'; 'Sn'; 'Hf'; 'Ta'; 'W '};


tot_ele=length(find(c)); %Counts the non-zero compositions
if round(sum(c)*10000)/10000~=1.0 %removes round error (MATLAB can't do simple↙
addition)
    total=sum(sum(c))
    error('Total composition does not equal 100%')
end
```

```
%Extract the non-zero elements and compositions
indic=find(c);
comp=c(c~=0);
ele=eles(indic);
eles=char(ele);

%Load the physcial constants and take the relevant slices
load('physical_constants.mat'); %imports 'H_table.mat', 'rad.mat', and 'Tm.mat'.
Updated 25/04/16
dHmix=zeros(tot_ele);   %placeholder
r=rad(c~=0);   %the radii for the element palette
T=Tm(c~=0);   %The melting point for the element palette
lb=zeros(1,tot_ele)+lower_bound;
ub=zeros(1,tot_ele)+upper_bound;
for m=1:length(indic)
    a=indic(m);
    for n=1:tot_ele
        b=indic(n); %'b' is a second dummy variable as with a. Need two as dHmix is
two-dimensional.
        dHmix(m,n)=H_table(a,b);
    end
end

%Calculate initial values of Omega and Delta
om_i=1/omega(comp);
del_i=100*(dot(comp,((1-(r/dot(r,comp))).^2)))^0.5;

%Clear the workspace
clear a b i m n all_ele elements tot_ele compositions H_table rad Tm Li B Mg Al Si Sc
Ti V Cr Mn Fe Co Ni Cu Zr Nb Mo Sn Hf Ta W
OPTIONS=optimoptions('fmincon','Algorithm','sqp');
%See @omega and @delta for details of function and constraints
[x,fval]=fmincon(@omega,comp,[],[],[],[],lb,ub,@delta,OPTIONS);

format shortG;
outputs=cell(length(x),5);
for i=1:length(x)
    outputs{i,1}=horzcat(eles(i,1), eles(i,2));
    outputs{i,2}=comp(i);
    outputs{i,3}=x(i);
end
outputs{1,4}=om_i;
outputs{2,4}=(1/fval);
outputs{1,5}=del_i;
outputs{2,5}=100*(dot(x,((1-(r/dot(r,x))).^2)))^0.5;
outputs{end,5}=sum(x)*100;

Ans________Initial_____Final_________Omega_______Delta=outputs
```

```
function [om]=omega(comp)
global dHmix T
S=-8.31*dot(comp,log(comp));    %Configurational Entropy
H=abs((4*dot(comp,(dHmix*comp')))*0.5)*1000;  %Regular Solution Parameter.  Factor of
0.5 for double counting.  Factor of 1000 to transfer to J/mol
Tbar=dot(comp,T);   %Weighted average melting point

om=H/(S*Tbar);  %Need 1/omega as fmincon is a minimizer

function [c,ceq]=delta(comp)
global r misfit_limit
d=100*(dot(comp,((1-(r/dot(r,comp))).^2)))^0.5;  %The Delta parameter for the alloy

c=d-misfit_limit;    %Constraint must be in the form of c~<0.0
ceq=sum(comp)-1;    %Maintains total compositon =100%
```

Bibliography

[1] United Nations. “World population prospects 2019: Highlights”. In: *United Nations. Department of Economic and Social Affairs. Population Division* 141 (2019), pp. 49–78.

[2] BP Energy. “BP Energy Outlook 2019 edition The Energy Outlook explores the forces shaping the global energy transition out to 2040 and the key uncertainties surrounding that”. In: *BP Energy Outlook 2019* (2019), p. 73.

[3] A. Demirbas. “Global renewable energy projections”. In: *Energy Sources, Part B: Economics, Planning and Policy* 4.2 (2009), pp. 212–224.

[4] *Key World Energy*. Tech. rep. International Energy Agency, 2015.

[5] Pushker A. Kharecha and Makiko Sato. “Implications of energy and CO2 emission changes in Japan and Germany after the Fukushima accident”. In: *Energy Policy* 132 (2019), pp. 647–653.

[6] M. Rieth et al. “Recent progress in research on tungsten materials for nuclear fusion applications in Europe”. In: *Journal of Nuclear Materials* 432.1-3 (2013), pp. 482–500.

[7] R. H. Jones, H. L. Heinisch, and K. A. McCarthy. “Low activation materials”. In: *Journal of Nuclear Materials* 271-272 (1999), pp. 518–525.

[8] M. J. Gorley. “Critical Assessment 12: Prospects for reduced activation steel for fusion plant”. In: *Materials Science and Technology (United Kingdom)* 31.8 (2015), pp. 975–980.

[9] Gary S. Was. *Fundamentals of Radiation Materials Science*. 2007, p. 852.

[10] S.G. Roberts. “Second Year Microplasticity Lecture Notes”. In: *Oxford FHS* 1 (2014), pp. 1–55.

[11] C Heintze et al. “Irradiation hardening of Fe9Cr based alloys and ODS Eurofer: Effect of helium implantation and iron ion irradiation at 300C including sequence effects”. In: *Journal of Nuclear Materials* 470 (2016), pp. 258–267.

[12] Tatsuya Hinoki et al. “Silicon carbide and silicon carbide composites for fusion reactor application”. In: *Materials Transactions* 54.4 (2013), pp. 472–476.

[13] Chenyang Lu et al. “Radiation-induced segregation on defect clusters in single-phase concentrated solid-solution alloys”. In: *Acta Materialia* 127.January (2017), pp. 98–107.

[14] K. Jin et al. “Effects of compositional complexity on the ion-irradiation induced swelling and hardening in Ni-containing equiatomic alloys”. In: *Scripta Materialia* 119.April (2016), pp. 65–70.

[15] B Cantor et al. “Microstructural development in equiatomic multicomponent alloys”. In: *Materials Science and Engineering: A* 375-377 (2004), pp. 213–218.

[16] J W Yeh. “Nanostructured High-Entropy-Alloys with Multiple Principal elements: Novel Alloy Design Concepts and Outcomes”. In: *Advanced Engineering Materials* 6.5 (2004), p. 5.

[17] J. W. Yeh. “Recent progress in high-entropy alloys”. In: *Annales de Chimie: Science des Materiaux* 31.6 (2006), pp. 633–648.

[18] E. J. Pickering and N. G. Jones. “High-entropy alloys: a critical assessment of their founding principles and future prospects”. In: *International Materials Reviews* 6608.May (2016), pp. 1–20.

[19] D.B. Miracle and O.N. Senkov. “A critical review of high entropy alloys and related concepts”. In: *Acta Materialia* 122 (2016), pp. 448–511.

[20] Jien-Wei Yeh. “Alloy Design Strategies and Future Trends in High-Entropy Alloys”. In: *Jom* 65.12 (2013), pp. 1759–1771.

[21] W. C. Wang et al. “A thermodynamic model proposed for calculating the standard formation enthalpies of ternary alloy systems”. In: *Scripta Materialia* 56.11 (2007), pp. 975–978.

[22] Richard Swalin. *Thermodynamics of Solids*. Wiley and Sone, 1972.

[23] O N Senkov et al. “Mechanical properties of Nb25Mo25Ta25W25 and V20Nb20Mo20Ta20W2 refractory high entropy alloys”. In: *Intermetallics* 19.5 (2011), pp. 698–706.

[24] Mathilde Laurent-Brocq et al. “From high entropy alloys to diluted multicomponent alloys: Range of existence of a solid-solution”. In: *Materials and Design* 103 (2016), pp. 84–89.

[25] Jien-Wei Yeh et al. “Formation of simple crystal structures in Cu-Co-Ni-Cr-Al-Fe-Ti-V alloys with multiprincipal metallic elements”. In: *Metallurgical and Materials Transactions A* 35.8 (2004), pp. 2533–2536.

[26] Duancheng Ma and Blazej Grabowski. “Ab initio thermodynamics of the CoCrFeMnNi high entropy alloy. Importance of entropy contributions beyond the configurational one”. In: *Acta Materialia* 100 (2015), pp. 90–97.

[27] Jien Wei Yeh et al. “Anomalous decrease in X-ray diffraction intensities of Cu-Ni-Al-Co-Cr-Fe-Si alloy systems with multi-principal elements”. In: *Materials Chemistry and Physics* 103.1 (2007), pp. 41–46.

[28] F. J. Wang, Y. Zhang, and G. L. Chen. “Atomic packing efficiency and phase transition in a high entropy alloy”. In: *Journal of Alloys and Compounds* 478.1-2 (2009), pp. 321–324.

[29] F. J. Wang and Y. Zhang. “Effect of Co addition on crystal structure and mechanical properties of Ti0.5CrFeNiAlCo high entropy alloy”. In: *Materials Science and Engineering A* 496.1-2 (2008), pp. 214–216.

[30] Zhi Tang et al. “Aluminum Alloying Effects on Lattice Types, Microstructures, and Mechanical Behavior of High-Entropy Alloys Systems”. In: *Jom* 65.12 (2013), pp. 1848–1858.

[31] Bo Ren et al. “Microstructure and properties of AlCrFeMnNiTi x and AlCrFeMnNiSi x high-entropy alloys”. In: *Rare Metals* 33.2 (2014), pp. 149–154.

[32] J. Y. He et al. “Effects of Al addition on structural evolution and tensile properties of the FeCoNiCrMn high-entropy alloy system”. In: *Acta Materialia* 62.1 (2014), pp. 105–113.

[33] Y. J. Zhou et al. “Solid solution alloys of AlCoCrFeNiTi[sub x] with excellent room-temperature mechanical properties”. In: *Applied Physics Letters* 90.18 (2007), p. 181904.

[34] Y. Deng et al. “Design of a twinning-induced plasticity high entropy alloy”. In: *Acta Materialia* 94 (2015), pp. 124–133.

[35] B. S. Li et al. “Effects of Mn, Ti and V on the microstructure and properties of AlCrFeCoNiCu high entropy alloy”. In: *Materials Science and Engineering A* 498.1-2 (2008), pp. 482–486.

[36] Hsuan Ping Chou et al. “Microstructure, thermophysical and electrical properties in AlxCoCrFeNi (0 ??? x ???2) high-entropy alloys”. In: *Materials Science and Engineering B: Solid-State Materials for Advanced Technology* 163.3 (2009), pp. 184–189.

[37] Yong Zhang et al. “High-entropy alloys with high saturation magnetization, electrical resistivity, and malleability.” In: *Scientific reports* 3 (2013), p. 1455.

[38] Yong Zhang et al. “Solid-solution phase formation rules for multi-component alloys”. In: *Advanced Engineering Materials* 10.6 (2008), pp. 534–538.

[39] Chung Chin Tung et al. “On the elemental effect of AlCoCrCuFeNi high-entropy alloy system”. In: *Materials Letters* 61.1 (2007), pp. 1–5.

[40] Wei Ji et al. “Alloying behavior and novel properties of CoCrFeNiMn high-entropy alloy fabricated by mechanical alloying and spark plasma sintering”. In: *Intermetallics* 56 (2014), pp. 24–27.

[41] P. P. Bhattacharjee et al. “Microstructure and texture evolution during annealing of equiatomic CoCrFeMnNi high-entropy alloy”. In: *Journal of Alloys and Compounds* 587 (2014), pp. 544–552.

[42] Yu Zou et al. “Size-dependent plasticity in an Nb25Mo25Ta 25W25 refractory high-entropy alloy”. In: *Acta Materialia* 65 (2014), pp. 85–97.

[43] Isaac Toda-Caraballo and Pedro E J Rivera-Diaz-Del-Castillo. “Modelling solid solution hardening in high entropy alloys”. In: *Acta Materialia* 85 (2015), pp. 14–23.

[44] B. Borie and C. J. Sparks. “The interpretation of intensity distributions from disordered binary alloys”. In: *Acta Crystallographica Section A* 27.3 (1971), pp. 198–201.

[45] L. R. Owen et al. “An assessment of the lattice strain in the CrMnFeCoNi high-entropy alloy”. In: *Acta Materialia* 122 (2017), pp. 11–18.

[46] C. Li; S. J. Zinkle, N.A.P. Kiran Kumar; and H. Bei. “Exploration of the Radiation Resistance of High-Entropy Alloys”. In: *Igarss 2014* (2014), pp. 1–9.

[47] Woei Ren Wang, Wei Lin Wang, and Jien Wei Yeh. “Phases, microstructure and mechanical properties of AlxCoCrFeNi high-entropy alloys at elevated temperatures”. In: *Journal of Alloys and Compounds* 589 (2014), pp. 143–152.

[48] Fuyang Tian et al. “Empirical design of single phase high-entropy alloys with high hardness”. In: *Intermetallics* 58 (2015), pp. 1–6.

[49] W. H. Liu et al. “Grain growth and the Hall-Petch relationship in a high-entropy FeCrNiCoMn alloy”. In: *Scripta Materialia* 68.7 (2013), pp. 526–529.

[50] O. N. Senkov et al. “Low-density, refractory multi-principal element alloys of the CrNbTiVZr system: Microstructure and phase analysis”. In: *Acta Materialia* 61.5 (2013), pp. 1545–1557.

[51] Bernd Gludovatz, Easo P. George, and Robert O. Ritchie. “Processing, Microstructure and Mechanical Properties of the CrMnFeCoNi High-Entropy Alloy”. In: *Jom* 67.10 (2015), pp. 2262–2270.

[52] Min-Rui Chen et al. “Effect of vanadium addition on the microstructure, hardness, and wear resistance of Al0.5CoCrCuFeNi high-entropy alloy”. In: *Metallurgical and Materials Transactions A* 37.5 (2006), pp. 1363–1369.

[53] Che-Wei Tsai et al. “Effect of temperature on mechanical properties of Al-CoCrCuFeNi wrought alloy”. In: *Journal of Alloys and Compounds* 490.1-2 (2010), pp. 160–165.

[54] G. Dan Sathiaraj et al. “Effect of heavy cryorolling on the evolution of microstructure and texture during annealing of equiatomic CoCrFeMnNi high entropy alloy”. In: *Intermetallics* 69 (2016), pp. 1–9.

[55] Y. F. Ye et al. “High-entropy alloy: Challenges and prospects”. In: *Materials Today* 19.6 (2015).

[56] K Y Tsai, M H Tsai, and J W Yeh. “Sluggish diffusion in CoCrFeMnNi high entropy alloys”. In: *Acta Materialia* 61.13 (2013), pp. 4887–4897.

[57] A. Paul. “Comments on: Sluggish diffusion in CoCrFeMnNi high-entropy alloys.” In: *Scripta Materialia* 135 (2017), pp. 153–157.

[58] Kun-yo Tsai, Ming-hung Tsai, and Jien-wei Yeh. “Reply to Comments on ”Sluggish Diffuion in Co-Cr-Fe-Mn-Ni high-entropy alloys” Acta Materialia 61 (2013) 4887-4897”. In: *Scripta Materialia* 135 (2017), pp. 158–159.

[59] Sergiy V. Divinski et al. “A Mystery of ”Sluggish Diffusion” in High-Entropy Alloys: The Truth or a Myth?” In: *Diffusion Foundations* 17 (2018), pp. 69–104.

[60] Tumpa R. Paul, Irina V. Belova, and Graeme E. Murch. “Analysis of diffusion in high entropy alloys”. In: *Materials Chemistry and Physics* 210 (2018), pp. 301–308.

[61] Witold Kucza et al. “Studies of sluggish diffusion effect in Co-Cr-Fe-Mn-Ni, Co-Cr-Fe-Ni and Co-Fe-Mn-Ni high entropy alloys that determine diffusivities of tracer species by combinatorial approach”. In: *Journal of Alloys and Compounds* 731 (2018), pp. 920–928.

[62] Yong Zhang et al. “Microstructures and properties of high-entropy alloys”. In: *Progress in Materials Science* 61 (2014), pp. 1–93.

[63] Z. P. Lu et al. “An assessment on the future development of high-entropy alloys: Summary from a recent workshop”. In: *Intermetallics* 66 (2015), pp. 67–76.

[64] X F Wang et al. “Novel microstructure and properties of multicomponent CoCrCuFeNiTix alloys”. In: *Intermetallics* 15.3 (2007), pp. 357–362.

[65] Ming Hung Tsai. *Physical properties of high entropy alloys*. 2013.

[66] Ming Xing Ren, Bang Sheng Li, and Heng Zhi Fu. “Formation condition of solid solution type high-entropy alloy”. In: *Transactions of Nonferrous Metals Society of China (English Edition)* 23.4 (2013), pp. 991–995.

[67] C P Lee et al. “The Effect of Boron on the Corrosion Resistance of the High Entropy Alloys AlCoCrCuFeNiB”. In: *Journal of The Electrochemical Society* 154.8 (2007), p. C424.

[68] Yu Jui Hsu, Wen Chi Chiang, and Jiann Kuo Wu. “Corrosion behavior of FeCoNiCrCux high-entropy alloys in 3.5% sodium chloride solution”. In: *Materials Chemistry and Physics* 92.1 (2005), pp. 112–117.

[69] Y. L. Chou, J. W. Yeh, and H. C. Shih. “The effect of molybdenum on the corrosion behaviour of the high-entropy alloys Co1.5CrFeNi1.5Ti0.5Mox in aqueous environments”. In: *Corrosion Science* 52.8 (2010), pp. 2571–2581.

[70] S. Ranganathan B.S. Murty, Jien-Wei Yeh. *High Entropy Alloys*. Elsevier Inc., 2014, p. 203.

[71] X Yang and Y Zhang. "Prediction of high-entropy stabilized solid-solution in multi-component alloys". In: *Materials Chemistry and Physics* 132.2-3 (2012), pp. 233–238.

[72] W.L. Bragg and E.J. Willaims. "The Effect of Thermal Agitation on Atomic Arrangement in Alloys". In: *Proceedings of the Royal Society of London, Series A.* 145.855 (1933), pp. 699–730.

[73] E. Ruedl, P. Delavignette, and S. Amelinckx. "Electron Diffraction and Electron Microscopic Study of Long- and Short-Range Order in Ni4Mo and of the Substructure Resulting from Ordering". In: (1968), pp. 305–328.

[74] Prashant Singh, a. V. Smirnov, and Duane D. Johnson. "Atomic short-range order and incipient long-range order in high-entropy alloys". In: *Physical Review B* 91.22 (2015).

[75] A. Takeuchi and A. Inoue. "Calculations of Mixing Enthalpy and Mismatch Entropy for Ternary Amorphous Alloys". In: *Materials Transactions, Jim* 41 (2000), pp. 1372–1378.

[76] Akira Takeuchi Inoue and Akihisa. "Classification of Bulk Metallic Glasses by Atomic Size Difference,Heat of Mixing and Period of Constituent Elements and Its Applicationto Characterization of the Main Alloying Element". In: *Materials Transactions* 46 (2005), p. 12.

[77] A. R. Miedema. "The electronegativity parameter for transition metals: Heat of formation and charge transfer in alloys". In: *Journal of The Less-Common Metals* 32.1 (1973), pp. 117–136.

[78] A. R. Miedema, R. Boom, and F. R. De Boer. "On the heat of formation of solid alloys". In: *Journal of the Less Common Metals* 41.2 (1975), pp. 283–298.

[79] A.R. Miedema. "On the heat of formation of solid alloys II". In: *Journal of the Less Common Metals* 46.1 (1976), pp. 67–83.

[80] A. R. Miedema, P. F. de Chatel, and F. R. de Boer. "Cohesion in alloys fundamentals of a semi-empirical model". In: *Physica B* 100.1 (1980), pp. 1–28.

[81] F.R. Boer et al. *Cohesion in Metals: Transition Metal Alloys*. Elsevier B.V., 1988, p. 758.

[82] A. Takeuchi and A. Inoue. "Mixing enthalpy of liquid phase calculated by miedema's scheme and approximated with sub-regular solution model for assessing forming ability of amorphous and glassy alloys". In: *Intermetallics* 18.9 (2010), pp. 1779–1789.

[83] A.P. Goncalves and M. Almeida. "Extended Miedema model: Predicting the formation enthalpies of intermetallic phases with more than two elements". In: *Physica B* 228 (1996), pp. 289–294.

[84] O. N. Senkov and D. B. Miracle. "A new thermodynamic parameter to predict formation of solid solution or intermetallic phases in high entropy alloys". In: *Journal of Alloys and Compounds* 658 (2016), pp. 603–607.

[85] M. Hillert. *Phase Equilibria, Phase Diagrams and Phase Transformations*. Second. Cambridge University Press, 2007.

[86] Y F Ye et al. "Design of high entropy alloys: A single-parameter thermodynamic rule". In: *Scripta Materialia* 104 (2015), pp. 53–55.

[87] Y. F. Ye et al. “The generalized thermodynamic rule for phase selection in multicomponent alloys”. In: *Intermetallics* 59 (2015), pp. 75–80.

[88] Devesh Kumar et al. “Microstructure and Characterization of Mechanically Alloyed Equiatomic AlCuCrFeMnW High Entropy Alloy”. In: *Materials Today: Proceedings* 3.9 (2016), pp. 2926–2933.

[89] Z.P. Lu, Y. Li, and S.C. Ng. “Reduced glass transition temperature and glass forming ability of bulk glass forming alloys”. In: *Journal of Non-Crystalline Solids* 270.1-3 (2000), pp. 103–114.

[90] Min-Rui Chen et al. “Microstructure and Properties of Al¡SUB¿0.5¡/SUB¿CoCrCuFeNiTi¡I¿¡S (¡I¿x¡/I¿=02.0) High-Entropy Alloys”. In: *Materials Transactions* 47.5 (2006), pp. 1395–1401.

[91] Y. J. Zhou et al. “Microstructure and compressive properties of multicomponent Alx(TiVCrMnFeCoNiCu)100-x high-entropy alloys”. In: *Materials Science and Engineering A* 454-455 (2007), pp. 260–265.

[92] Ker Chang Hsieh et al. “The microstructure and phase equilibrium of new high performance high-entropy alloys”. In: *Journal of Alloys and Compounds* 483.1-2 (2009), pp. 209–212.

[93] C. Li et al. “Effect of alloying elements on microstructure and properties of multiprincipal elements high-entropy alloys”. In: *Journal of Alloys and Compounds* 475.1-2 (2009), pp. 752–757.

[94] O. N. Senkov et al. “Refractory high-entropy alloys”. In: *Intermetallics* 18.9 (2010), pp. 1758–1765.

[95] Aditya Ayyagari et al. “Low activation high entropy alloys for next generation nuclear applications”. In: *Materialia* 4.September (2018), pp. 99–103.

[96] I. Toda-Caraballo et al. “Interatomic spacing distribution in multicomponent alloys”. In: *Acta Materialia* 97 (2015), pp. 156–169.

[97] F. Otto et al. “Decomposition of the single-phase high-entropy alloy CrMnFeCoNi after prolonged anneals at intermediate temperatures”. In: *Acta Materialia* 112 (2016), pp. 40–52.

[98] A. Munitz et al. “Heat treatment impacts the micro-structure and mechanical properties of AlCoCrFeNi high entropy alloy”. In: *Journal of Alloys and Compounds* 683 (2016), pp. 221–230.

[99] Li Jiang et al. “Annealing effects on the microstructure and properties of bulk high-entropy CoCrFeNiTi0.5 alloy casting ingot”. In: *Intermetallics* 44 (2014), pp. 37–43.

[100] Louis J Santodonato et al. “Deviation from high-entropy configurations in the atomic distributions of a multi-principal-element alloy.” In: *Nature communications* 6 (2015), p. 5964.

[101] E. J. Pickering et al. “Precipitation in the equiatomic high-entropy alloy CrMnFeCoNi”. In: *Scripta Materialia* 113 (2016), pp. 106–109.

[102] Mingyang Zhang et al. “FeCoCrNiMo High Entropy Alloys prepared by powder metallurgy processing for diamond tool applications”. In: *Powder Metallurgy* 61.2 (2018), pp. 123–130.

[103] Rahul B. Mane and Bharat B. Panigrahi. “Effect of alloying order on non-isothermal sintering kinetics of mechanically alloyed high entropy alloy powders”. In: *Materials Letters* 217 (2018), pp. 131–134.

[104] Owais Ahmed Waseem et al. “The effect of Ti on the sintering and mechanical properties of refractory high-entropy alloy TixWTaVCr fabricated via

spark plasma sintering for fusion plasma-facing materials". In: *Materials Chemistry and Physics* 210 (2018), pp. 87–94.

[105] G M Karthik et al. "Additive manufacturing of an aluminum matrix composite reinforced with nanocrystalline high-entropy alloy particles crossmark". In: *Materials Science & Engineering A* 679.October (2017), pp. 193–203.

[106] Yevgeni Brif, Meurig Thomas, and Iain Todd. "The use of high-entropy alloys in additive manufacturing". In: *Scripta Materialia* 99 (2015), pp. 93–96.

[107] Yan Zhang et al. "Microstructure and mechanical properties of a refractory HfNbTiVSi0.5 High Entropy Alloy composite". In: *Materials Letters* 174 (2016), pp. 82–85.

[108] X. F. Wang et al. "Novel microstructure and properties of multicomponent CoCrCuFeNiTix alloys". In: *Intermetallics* 15.3 (2007), pp. 357–362.

[109] Yukun Lv et al. "Cooling rate effect on microstructure and mechanical properties of AlxCoCrFeNi high entropy alloys". In: *Materials and Design* 132 (2017), pp. 392–399.

[110] David Molnar et al. "The effect of cooling rate on the microstructure and mechanical properties of NiCoFeCrGa high-entropy alloy". In: *Journal of Materials Science* (2018), pp. 5074–5082.

[111] Sheng Guo et al. "Effect of valence electron concentration on stability of fcc or bcc phase in high entropy alloys". In: *Journal of Applied Physics* 109.10 (2011), p. 103505.

[112] M. G. Poletti and L. Battezzati. "Electronic and thermodynamic criteria for the occurrence of high entropy alloys in metallic systems". In: *Acta Materialia* 75 (2014), pp. 297–306.

[113] M. Claudia Troparevsky et al. “Criteria for predicting the formation of single-phase high-entropy alloys”. In: *Physical Review X* 5.1 (2015), pp. 1–6.

[114] N. Saunders, M. Fahrmann, and C.J. Small. “The Application of Calphad Calculations To Ni-Based Superalloys”. In: *Superalloys 2000* (2000), pp. 803–811.

[115] O. N. Senkov et al. “Accelerated exploration of multi-principal element alloys for structural applications”. In: *Calphad: Computer Coupling of Phase Diagrams and Thermochemistry* 50 (2015), pp. 32–48.

[116] J. C. Zhao and M. F. Henry. “CALPHAD - Is it ready for superalloy design?” In: *Advanced Engineering Materials* 4.7 (2002), pp. 501–508.

[117] Chun Ng et al. “Entropy-driven phase stability and slow diffusion kinetics in an Al 0.5CoCrCuFeNi high entropy alloy”. In: *Intermetallics* 31 (2012), pp. 165–172.

[118] A. Manzoni et al. “Investigation of phases in AlCoCrCuFeNi high entropy alloy and comparison with equilibrium phases predicted by ThermoCalc”. In: *Journal of Alloys and Compounds* 552 (2013), pp. 430–436.

[119] M. Feuerbacher, T. Lienig, and C. Thomas. “A single-phase bcc high-entropy alloy in the refractory Zr-Nb-Ti-V-Hf system”. In: *Scripta Materialia* 152 (2018), pp. 40–43.

[120] Soumyadipta Maiti and Walter Steurer. “Structural-disorder and its effect on mechanical properties in single-phase TaNbHfZr high-entropy alloy”. In: *Acta Materialia* 106 (2016), pp. 87–97.

[121] N. D. Stepanov et al. “Aging behavior of the HfNbTaTiZr high entropy alloy”. In: *Materials Letters* 211 (2018), pp. 87–90.

[122] S.Y. Chen, W.D. Li, and R. Feng. "Phase transformations of HfNbTaTiZr high-entropy alloy at intermediate temperatures". In: *Scripta Materialia* 158 (2018), pp. 50–56.

[123] B. Schuh et al. "Thermodynamic instability of a nanocrystalline, single-phase TiZrNbHfTa alloy and its impact on the mechanical properties". In: *Acta Materialia* 142 (2018), pp. 201–212.

[124] Cheng Yang et al. "Microstructure evolution and mechanical property of a precipitation-strengthened refractory high-entropy alloy HfNbTaTiZr". In: *Materials Letters* 254 (2019), pp. 46–49.

[125] I. Manna et al. "Formation of face-centered-cubic zirconium, by mechanical attrition". In: *Applied Physics Letters* 81.22 (2002), pp. 4136–4138.

[126] Yanhong Chang et al. "The face-centered cubic titanium phase in cold-rolled commercially-pure titanium is a titanium-hydride". In: (), pp. 20–22.

[127] Tao Tsung Shun and Yu Chin Du. "Age hardening of the Al0.3CoCrFeNiC0.1 high entropy alloy". In: *Journal of Alloys and Compounds* 478.1-2 (2009), pp. 269–272.

[128] Christina M. Rost et al. "Entropy-stabilized oxides". In: *Nature Communications* 6 (2015), pp. 1–8.

[129] Zhifeng Lei and Zhaoping Lu. "Enhanced strength and ductility in a high-entropy alloy via ordered oxygen complexes". In: *Nature* 563.7732 (2018), pp. 546–550.

[130] Hynek Hadraba et al. "Oxide dispersion strengthened CoCrFeNiMn high-entropy alloy". In: *Materials Science and Engineering A* 689.December 2016 (2017), pp. 252–256.

[131] Joshua Gild et al. “High-Entropy Metal Diborides: A New Class of High-Entropy Materials and a New Type of Ultrahigh Temperature Ceramics”. In: *Scientific Reports* 6.October (2016), pp. 2–11.

[132] Pranab Sarker et al. “High-entropy high-hardness metal carbides discovered by entropy descriptors”. In: *Nature Communications* 9.1 (2018), pp. 1–10.

[133] Jieyang Zhou et al. “High-entropy carbide: A novel class of multicomponent ceramics”. In: *Ceramics International* 44.17 (2018), pp. 22014–22018.

[134] Ping Jiong Yang et al. “Mechanism of hardening and damage initiation in oxygen embrittlement of body-centred-cubic niobium”. In: *Acta Materialia* 168 (2019), pp. 331–342.

[135] R. W. Hayes. “Oxygen embrittlement and time-dependent grain-boundary cracking of ALLVAC 718PLUS”. In: *Metallurgical and Materials Transactions A: Physical Metallurgy and Materials Science* 39.11 (2008), pp. 2596–2606.

[136] A. Poulia et al. “Phase segregation discussion in a Hf25Zr30Ti20Nb15V10high entropy alloy: The effect of the high melting point element”. In: *Materials Chemistry and Physics* 210 (2018), pp. 251–258.

[137] Marcio Gustavo di Vernieri Cuppari and Sydney Ferreira Santos. “Physical properties of the NbC carbide”. In: *Metals* 6.10 (2016).

[138] O. N. Senkov and C. F. Woodward. “Microstructure and properties of a refractory NbCrMo0.5Ta0.5TiZr alloy”. In: *Materials Science and Engineering A* 529.1 (2011), pp. 311–320.

[139] N. A P Kiran Kumar et al. “Microstructural stability and mechanical behavior of FeNiMnCr high entropy alloy under ion irradiation”. In: *Acta Materialia* 113 (2016), pp. 230–244.

[140] Chenyang Lu et al. “Enhancing radiation tolerance by controlling defect mobility and migration pathways in multicomponent single phase alloys”. In: *Nature Communications* In press.December (2016), pp. 1–8.

[141] S. Q. Xia et al. “Irradiation Resistance in Al x CoCrFeNi High Entropy Alloys”. In: *Jom* 67.10 (2015), pp. 3–7.

[142] Takeshi Nagase et al. “In-situ TEM observation of structural changes in nano-crystalline CoCrCuFeNi multicomponent high-entropy alloy (HEA) under fast electron irradiation by high voltage electron microscopy (HVEM)”. In: *Intermetallics* 59 (2015), pp. 32–42.

[143] F Granberg et al. “Mechanism of Radiation Damage Reduction in Equiatomic Multicomponent Single Phase Alloys”. In: *Phys Rev Lett* 116.13 (2016), p. 135504.

[144] Lance L Snead and J.C Hay. “Neutron irradiation induced amorphization of silicon carbide”. In: *Journal of Nuclear Materials* 273.2 (1999), pp. 213–220.

[145] Nan Li et al. “He ion irradiation damage in Al/Nb multilayers”. In: *Journal of Applied Physics*. Vol. 105. 12. 2009.

[146] N. A. P. Kumar et al. “Ion Irradiation Effects on High Entropy Alloy”. In: *Fusion Reactor Materials Program* 54 (2013), p. 9.

[147] N Li et al. “Outstanding radiation resistance of tungsten-based high-entropy alloys”. In: *Science Advances* 5 (2019), pp. 1–10.

[148] Dilpuneet S. Aidhy et al. “Point defect evolution in Ni, NiFe and NiCr alloys from atomistic simulations and irradiation experiments”. In: *Acta Materialia* 99.February (2015), pp. 69–76.

[149] A. D. Pogrebnjak et al. “Nanostructured multielement (TiHfZrNbVTa)N coatings before and after implantation of N+ ions (1018??cm???2): Their structure and mechanical properties”. In: *Nuclear Instruments and Methods in Physics Research, Section B: Beam Interactions with Materials and Atoms* 385.September (2016), pp. 74–83.

[150] Yanwen Zhang et al. “Atomic-level heterogeneity and defect dynamics in concentrated solid-solution alloys”. In: *Current Opinion in Solid State and Materials Science* 21.5 (2017), pp. 221–237.

[151] G Davies et al. “Large scale cooling systems using mains water”. In: *Journal of Chemical Information and Modeling* 53.9 (2013), pp. 1689–1699.

[152] AMG. *AMG Analysis*. 2019.

[153] L Margetts, L.M. Smith, and D.V. Griffiths. *Programming the Finite Element Method*. Wiley, 2013.

[154] *MATLAB*. Natick, Massachuesetts, 2019.

[155] Matlab. *Find minimum of constrained non-linear multivariable function*. 2019.

[156] Matlab. *Choosing the Algorithm*. 2019.

[157] Christopher Hammond. *The Basics of Crystallography and Diffraction*. 1997, p. 432.

[158] S.E. Palmer and D.C. Palmer. *CrystalDiffract*. Oxford, 2019.

[159] MalvernPanalytical. *HighScore+*. Malvern, 2019.

[160] Oxford and Instruments. *AZtec*. 2017.

[161] Sales (Horiba Scientific). *Wavelength Dispersive XRF*. 2019.

[162] Thomas F. Kelly and Michael K. Miller. “Invited review article: Atom probe tomography”. In: *Review of Scientific Instruments* 78.3 (2007).

[163] Brian P Geiser et al. “M icroscopy M icroanalysis Spatial Distribution Maps for Atom Probe Tomography”. In: *Microsc.Microanal* 13 (2007), pp. 437–447.

[164] A Cerezo and T.J. Godfrey. “Application of a position-sensitive detector to atom probe microanalysis”. In: *Review of Scientific Instruments* 59.6 (1988), pp. 862–866.

[165] Baptiste Gault et al. “Spatial Resolution in Atom Probe Tomography”. In: *Microsopy and Microanalysis* 16 (2010), pp. 99–110.

[166] Andrew J. London, Daniel Haley, and Michael P. Moody. “Single-Ion Deconvolution of Mass Peak Overlaps for Atom Probe Microscopy”. In: *Microscopy and Microanalysis* 23.2 (2017), pp. 300–306.

[167] Andrew J. London. “Quantifying Uncertainty from Mass-Peak Overlaps in Atom Probe Microscopy”. In: *Microscopy and Microanalysis* 25.2 (2019), pp. 378–388.

[168] W.C. Oliver and G.M. Pharr. “Measurement of hardness and elastic modulus by instrumented indentation: Advances in understanding and refinements to methodology”. In: *Journal of Materials Research* 19.01 (2004), pp. 3–20.

[169] James Ziegler. *Stopping Range of Ions in Matter*.

[170] G Sattonnay, F Rullier-Albenque, and O Dimitrov. “Determination of displacement threshold energies in pure Ti and in gamma-TiAl alloys by electron irradiation”. In: *Journal of Nuclear Materials* 275.1 (1999), pp. 63–73.

[171] Byeongwon Park, William J. Weber, and L. Rene Corrales. “Molecular dynamics study of the threshold displacement energy in Vanadium”. In: *Nuclear Instruments and Methods in Physics Research, Section B* 166 (2000), pp. 357–363.

[172] M. Griffiths. “Displacement energies for Zr measured in a HVEM”. In: *Journal of Nuclear Materials* 165.3 (1989), pp. 315–317.

[173] G. Youngblood, S. Myhra, and J. W. DeFord. “Measurements of the threshold displacement energy in Ta and Nb”. In: *Physical Review* 188.3 (1969), pp. 1101–1107.

[174] M D Vaudin. “Pseudosymmetry in EBSD Patterns”. In: *Microscopy and Microanalysis* 11.S02 (2005), pp. 510–511.

[175] William Lenthe, Saransh Singh, and Marc DeGraef. “Prediction of potential pseudo-symmetry issues in the indexing of electron backscatter diffraction patterns”. In: *Journal of Applied Crystallography* 52 (2019), pp. 1157–1168.

[176] C.N. Rao and G.V. Rao. *Transition Metal Oxides*. U.S. Department of Commerce, 1974.

[177] Bruce W. Davis and Richard G. Varsanik. “A study of crystalline titanium carbide”. In: *Journal of Colloid And Interface Science* 37.4 (1971), pp. 870–878.

[178] Nils Schonberg and W. G. Overend. “An X-Ray Investigation on Ternary Phases in the Ta-Me-N Systems”. In: *Acta Chemica Scandinavica* 8 (2008), pp. 213–220.

[179] E. K. Storms and R. J. McNeal. “the Vanadium-Vanadium Carbide System 1”. In: *The Journal of Physical Chemistry* 66.8 (2007), pp. 1401–1408.

[180] Charles P. Kempter and R. Jay Fries. “Zirconium Carbide”. In: *Analytical Chemistry* 32.4 (1960), p. 570.

[181] Roberto J. Guerrero-Moreno and Noboru Takeuchi. “First principles calculations of the ground-state properties and structural phase transformation in CdO”. In: *Physical Review B - Condensed Matter and Materials Physics* 66.20 (2002), pp. 1–6.

[182] Qingfeng Zeng et al. “Prediction of stable hafnium carbides: Stoichiometries, mechanical properties, and electronic structure”. In: *Physical Review B - Condensed Matter and Materials Physics* 88.21 (2013), pp. 1–13.

[183] K. Aigner et al. “Lattice parameters and thermal expansion of Ti(CN), Zr(CN), Hf(CN) and TiN from 298 to 1473 K as investigated by high-temperature X-ray diffraction”. In: *Journal of Alloys and Compounds* 215 (1994), pp. 121–126.

[184] V. Valvoda. “X-ray diffraction study of Debye temperature and charge distribution in tantalum monocarbide”. In: *Physica Status Solidi (a)* 64.1 (1981), pp. 133–142.

[185] S. Music, N. Filipovic-Vincekovic, and L. Sekovanic. *Introduction to Energy Dispersive X-Ray Spectrometry (EDS)*. 2011, pp. 1–12.

[186] D.A. Porter and K.E. Easterling. *Phase Transformations in Metals and Alloys*. 2nd Editio. Chapman & Hall, 1992, p. 510.

[187] A. K. Niessen and F. R. De Boer. “The enthalpy of formation of solid borides, carbides, nitrides, silicides and phosphides of transition and noble metals”. In: *Journal of The Less-Common Metals* 82.C (1981), pp. 75–80.

[188] J. Y. He et al. “High-temperature plastic flow of a precipitation-hardened FeCoNiCr high entropy alloy”. In: *Materials Science and Engineering A* 686.November 2016 (2017), pp. 34–40.

[189] J. D. Verhoeven et al. “Macrosegregation during convection-free plane front solidification. I. Rectilinear geometry”. In: *Journal of Crystal Growth* 89.2-3 (1988), pp. 189–201.

[190] Hong Bao Cui et al. “Microstructure and Microsegregation in Directionally Solidified FeCoNiCrAl High Entropy Alloy”. In: *Advanced Materials Research* 189 (2011), pp. 3840–3843.

[191] R. W. Rice. “Comparison of stress concentration versus minimum solid area based mechanical property-porosity relations”. In: *Journal of Materials Science* 28.8 (1993), pp. 2187–2190.

[192] Ian McCue et al. “Local heterogeneity in the mechanical properties of bicontinuous composites made by liquid metal dealloying”. In: *Applied Physics Letters* 109.23 (2016).

[193] Christopher D. Hardie, Steve G. Roberts, and Andy J. Bushby. “Understanding the effects of ion irradiation using nanoindentation techniques”. In: *Journal of Nuclear Materials* 462.15 (2015), pp. 391–401.

[194] H. Mecking and U. F. Kocks. “Kinetics of flow and strain-hardening”. In: *Acta Metallurgica* 29.11 (1981), pp. 1865–1875.

[195] L. B. Freund and J. W. Hutchinson. “High strain-rate crack growth in rate-dependent plastic solids”. In: *Journal of the Mechanics and Physics of Solids* 33.2 (1985), pp. 169–191.

[196] Alan Xu et al. “Ion-irradiation-induced clustering in W-Re and W-Re-Os alloys: A comparative study using atom probe tomography and nanoindentation measurements”. In: *Acta Materialia* 87 (2015), pp. 121–127.

[197] B.A. Proctor, I Whitney, and J.W. Johnson. “The strength of fused silica”. In: *Proceedings of the Royal Society of London. Series A. Mathematical and Physical Sciences* 297.1451 (1967), pp. 534–557.